



# New lightweight structural blade designs and blade designs with build-in structural couplings

D. J. Lekou (CRES), K. Bacharoudis (CRES), A. Makris (CRES), J.P. Dekker (Knowledge Centre WMC), G.D. de Winkel (Knowledge Centre WMC), A. Croce (PolIMI), D. Wang (TUD), A. Brinkmeyer (UBRISTOL), M. Capuzzi (UBRISTOL), Neil Buckney (UBRISTOL), P. Weaver (UBRISTOL), T. P. Philippidis (UPAT), G. A. Roukis (UPAT), K. Branner (DTU), R. Montejo (CENER), I. Nuin (CENER)

## Deliverable 2.22

October, 2015

Agreement n.:	308974
Duration	November 2012 – October 2017
Co-ordinator:	Mr Peter Hjuler Jensen
Supported by:	EU 7th Framework Programme



The research leading to these results has received funding from the European Community's Seventh Framework Programme under grant agreement 308974

---

### PROPRIETARY RIGHTS STATEMENT

This document contains information, which is proprietary to the "INN WIND.EU" Consortium. Neither this document nor the information contained herein shall be used, duplicated or communicated by any means to any third party, in whole or in parts, except with prior written consent of the "INN WIND.EU" consortium.

---

## Document information

<b>Document Name:</b>	New lightweight structural blade designs and blade designs with build-in structural couplings
<b>Confidentiality Class</b>	PU
<b>Document Number:</b>	D2.22
<b>Author:</b>	D. J. Lekou, K. Bacharoudis, A. Makris (CRES), J.P. Dekker, G.D. de Winkel (Knowledge Centre WMC), A. Croce (PoliMI), D. Wang (TUD), A. Brinkmeyer, N. Buckney, M. Capuzzi, P. Weaver (UBRISTOL), T. P. Philippidis, G. A. Roukis (UPAT), K. Branner (DTU) R. Montejo, I. Nuin (CENER)
<b>Review:</b>	D. Lekou
<b>Date:</b>	5 October 2015
<b>WP:</b>	WP2: Lightweight Rotor
<b>Task:</b>	Task 2.2: Lightweight structural design

## TABLE OF CONTENTS

<b>TABLE OF CONTENTS</b> .....	<b>3</b>
<b>EXECUTIVE SUMMARY</b> .....	<b>5</b>
<b>1 INTRODUCTION</b> .....	<b>8</b>
<b>2 NEW STRUCTURAL SOLUTIONS</b> .....	<b>12</b>
2.1 INTERNAL SPACE TRUSS STRUCTURE (UPAT-CORE TEAM) .....	12
2.1.1 <i>State of the art and motivation</i> .....	13
2.1.2 <i>Brief description of the concept</i> .....	13
2.1.3 <i>Anticipated PROS and CONS</i> .....	15
2.1.4 <i>Assessment of the structural integrity of the proposed design</i> .....	15
2.1.5 <i>Conclusions and recommendations</i> .....	21
2.2 GRID STIFFENED STRUCTURE (TUDELFT) .....	21
2.2.1 <i>State of the art and motivation</i> .....	21
2.2.2 <i>Brief description of the concept</i> .....	22
2.2.3 <i>Anticipated PROS and CONS</i> .....	23
2.2.4 <i>Assessment of the structural integrity of the proposed design</i> .....	23
2.2.5 <i>Conclusions and recommendations</i> .....	28
2.3 RIB REINFORCED BLADE (CRES).....	29
2.3.1 <i>State of the art and motivation</i> .....	29
2.3.2 <i>Brief description of the concept</i> .....	29
2.3.3 <i>Anticipated PROS and CONS</i> .....	30
2.3.4 <i>Assessment of the structural integrity of the proposed design</i> .....	30
2.3.5 <i>Conclusions and recommendations</i> .....	38
2.4 TOPOLOGY OPTIMIZATION WITH OFFSET SPAR CAPS (UBRISTOL) .....	38
2.4.1 <i>State of the art and motivation</i> .....	38
2.4.2 <i>Preliminary Topology Optimisation</i> .....	39
2.4.3 <i>Structural efficiency analysis of the DTU Reference Blade</i> .....	42
2.4.4 <i>Offset Spar cap concept analysis</i> .....	53
2.4.5 <i>Conclusions</i> .....	62
<b>3 STRUCTURAL SOLUTIONS WITH BUILD-IN COUPLINGS</b> .....	<b>64</b>
3.1 POLIMI'S 10MW BEND-TWIST-COUPLING SOLUTION SC+05 (POLIMI) .....	64
3.1.1 <i>State of the art and motivation</i> .....	64
3.1.2 <i>Brief description of the concept</i> .....	65
3.1.3 <i>Anticipated PROS and CONS</i> .....	68
3.1.4 <i>Assessment of the structural integrity of the proposed design</i> .....	69
3.1.5 <i>Conclusions and recommendations</i> .....	78
3.2 PASSIVE GUST LOAD ALLEVIATION USING EMBEDDED BEND-TWIST COUPLING (UBRISTOL) .....	78
3.2.1 <i>State of the art and motivation</i> .....	78
3.2.2 <i>Definitions</i> .....	79
3.2.3 <i>Structural design and power performance</i> .....	80
3.2.4 <i>Response to Gust-Induced Loads</i> .....	88
3.2.5 <i>Gust response for 11.5 m/s wind (at rated)</i> .....	93
3.2.6 <i>Conclusions</i> .....	95
3.3 PASSIVE CONTROL STRATEGIES FOR WIND TURBINE BLADES (DTU) .....	96
3.3.1 <i>State of the art and motivation</i> .....	96
3.3.2 <i>Brief description of the concept</i> .....	97
3.3.3 <i>Models Description, Baseline Wind Turbine and DLB</i> .....	99
3.3.4 <i>Description of the Workflow</i> .....	100
3.3.5 <i>Results</i> .....	101
3.3.6 <i>Conclusions and recommendations</i> .....	107
3.4 STRUCTURAL BLADE DESIGNS WITH BUILD-IN STRUCTURAL COUPLINGS (CENER).....	108

3.4.1	<i>Karaolis approach</i> .....	109
3.4.2	<i>Blade design with Build-In Structural Couplings</i> .....	122
3.4.3	<i>Blade Design effect on loads and energy production</i> .....	134
<b>4</b>	<b>INTEGRATED STRUCTURAL DESIGN SOLUTIONS</b> .....	<b>138</b>
4.1	STRUCTURAL SOLUTION FOR LOW INDUCTION ROTOR (LIR) BLADE (CRES) .....	138
4.1.1	<i>State of the art and motivation</i> .....	138
4.1.2	<i>Brief description of the concept/solution</i> .....	138
4.1.3	<i>Anticipated PROS and CONS</i> .....	139
4.1.4	<i>Assessment of the structural integrity of the proposed design</i> .....	139
4.1.5	<i>Conclusions and recommendations</i> .....	143
4.2	INTEGRATED STRUCTURAL OPTIMIZATION USING FOCUS6 (WMC) .....	143
4.2.1	<i>State of the art and motivation</i> .....	143
4.2.2	<i>Brief description of the concept/solution</i> .....	144
4.2.3	<i>Anticipated PROS and CONS</i> .....	144
4.2.4	<i>Assessment of the structural integrity of the proposed design</i> .....	144
4.2.5	<i>Conclusions and recommendations</i> .....	146
4.3	POLIMI 10MW 182M BTC SC+05 (POLIMI) .....	146
4.3.1	<i>State of the art and motivation</i> .....	146
4.3.2	<i>Brief description of the concept/solution</i> .....	146
4.3.3	<i>Anticipated PROS and CONS</i> .....	147
4.3.4	<i>Assessment of the structural integrity of the proposed design</i> .....	147
4.3.5	<i>Conclusions and recommendations</i> .....	152
4.4	POLIMI 10MW BTC SC+05 IPC (POLIMI) .....	152
4.4.1	<i>State of the art and motivation</i> .....	152
4.4.2	<i>Brief description of the concept/solution</i> .....	153
4.4.3	<i>Anticipated PROS and CONS</i> .....	153
4.4.4	<i>Assessment of the structural integrity of the proposed design</i> .....	153
4.4.5	<i>Conclusions and recommendations</i> .....	158
4.5	POLIMI 10MW 188M BTC SC+05 + IPC (POLIMI) .....	158
4.5.1	<i>State of the art and motivation</i> .....	158
4.5.2	<i>Brief description of the concept/solution</i> .....	159
4.5.3	<i>Anticipated PROS and CONS</i> .....	159
4.5.4	<i>Assessment of the structural integrity of the proposed design</i> .....	159
4.5.5	<i>Conclusions and recommendations</i> .....	164
<b>5</b>	<b>CONCLUSIONS</b> .....	<b>167</b>
<b>6</b>	<b>REFERENCES</b> .....	<b>169</b>
	<b>APPENDIX A; STRENGTH PLOTS FOR CONFIGURATIONS OF SECTION 3.3</b> .....	<b>173</b>
	<b>APPENDIX B; ESTIMATED PROPERTIES FOR DTU REFERENCE BLADE (CENER)</b> .....	<b>176</b>

## EXECUTIVE SUMMARY

The report includes the description of structural blade designs developed/ modified, etc. within the INN WIND.EU project under WP2 “Lightweight Rotor” Task 2.2 “Lightweight structural design”, as well as the analysis results regarding the compliance with the specifications developed in InnWind.Eu work-package WP1. The purpose is to report on new structural blade designs that are developed within the INN WIND.EU WP2, Task 2.2, and subtask 2.2.2, which will be further evaluated regarding the impact of the solution on the overall cost of the wind turbine within INN WIND.EU WP1 “Conceptual Design”. The objective is to define and assess innovative structural concepts for achieving lightweight rotor blades with adequate stiffness and strength. Information included for the structural concepts and designs with potentially lower blade mass and favourable adaptive and aeroelastic characteristics that are developed by the partners participating in the frame of Task 2.2, will be forwarded to INN WIND.EU WP1 partners for their further assessment and evaluation relevant to the cost of the overall wind turbine.

To assure comparability of the solutions each partner is comparing its new solution against results of the reference blade. The benchmark on structural design methods for blades that was performed within the INN WIND.EU project under WP2 “Lightweight Rotor” Task 2.2 “Lightweight structural design” and reported under Deliverable D2.21 “Benchmarked aerodynamic-structural design methods” includes all simulation results of the partners regarding the reference blade used. The benchmark was based on the reference wind turbine and the reference blade provided by DTU [1]. “Structural Concept developers/modellers” of WP2 were provided with the necessary input for a comparison numerical simulation run. Output was compared in terms of weight, stiffness, natural frequencies, deflection (extreme load), strength & stability (extreme load) and fatigue (variable load). Each of the partners involved in Task 2.2 applies tools developed in-house. For each conceptual idea that is presented in this document, the partner shows feasibility of solution under comparison with the properties and response of the reference blade.

The structure of the report comprises three distinct parts. It starts with the description of the new structural concepts used to replace the traditional internal structure of the blade, then proceeds with the solutions that are exploiting structural couplings of the blade to alleviate the loading on the rotor and concludes with solutions obtained carrying out an integrated design taking into account both aerodynamic/aeroelastic effects as well as the structural integrity of the blade.

In essence, results in **chapter 2** including the **Innovative internal structural solutions** for the blade are based on the reference geometry of the blade and reference loading, as that used during the benchmark. Although for all solutions a reduction of the mass of the blade has been achieved the loading was not adapted to comply with it, but rather kept the same as for the reference blade. This in turn indicates that it is possible that due to the lighter blade design obtained, running full simulation to estimate the aeroelastic response, the loading on the blade will be reduced, allowing further mass reduction. However, as discussed in the subsequently the solutions proposed are not mature enough, since details of the structural design, especially relevant to joints, required in a real manufacturing scenario have not been performed. This is also outside of the scope of the work performed. The solutions discussed relevant to wind turbine blade have a **technological readiness level of 4 to 5**. That means that although they have been estimated as feasible, their adequacy has never been verified. Three solutions are presented in chapter 2 in addition to a numerical topology optimization study. The first, employing an internal truss structure to replace the traditional shear webs of the blade was performed by University of Patras (UPAT). The second solution was performed by Technical University Delft (TUD) and studies the possibility of replacing the sandwich structure usually employed in the trailing edge of the blade with a grid stiffened panel. The third solution resembles the solution by UPAT in that truss members are used to carry the load, yet instead of replacing only the shear webs, it was studied whether it is possible to replace the entire load carrying structure of the blade with truss members while the aerodynamic surface of the blade is to be constructed with a light cloth resembling material. This option was investigated by CRES. The chapter closes with the topology optimization study performed by University of Bristol (UBRISTOL) relevant to the offset of the shear webs.

**Chapter 3** includes the solutions for passive alleviation of the loads by taking into advantage **bend-twist coupling of the blade**. To this end, the structural design of the blade has to be performed suitably placing the composite materials to “design” the needed couplings in the blade’s response under load. To evaluate the final result aeroelastic estimations have been performed, therefore,

in reality the work is intermediate between integrated design (shown in chapter 4) and independent structural design (presented in chapter 2). A solution for load alleviation designing a blade with bend twist coupling and complying with all structural design specifications is presented by Politecnico di Milano. The result in terms of mass savings is in the order of 4%, while using the cost estimator developed within INN WIND.EU WP1 the reduction on the Levelized Cost of Energy (LCOE) is minimal. Work regarding the structural design of the blade to achieve passive load alleviation has also been performed in the frame of the INN WIND.EU project by Denmark's Technical University (DTU), University of Bristol (UBRISTOL) and CENER. The efforts of the institutes are also reported under Chapter 3. DTU evaluated the concepts of a conventional bend-twist coupling solution, similar to the one presented by PoliMi, against the solutions of having a blade with a single shear web, thereby reducing the torsional stiffness of the blade, as well as the solution of the swept blade. The studies relevant to the load alleviation have been performed individual for the three cases, as well as for their combination. The work concentrated to evaluating the load reduction achieved through each solution and as a minimum complying with the constraints of tower clearance (maximum deflection) and the strength of the blade under extreme loading. UBRISTOL evaluated the solution of achieving an optimized bend-twist coupling through varying the fiber orientation along the blade length, thus, achieving different levels of coupling along the blade. The solution was compared against the traditional blade structure (without bend-twist coupling) and the option of a conventional bend-twist coupling design (with off-axis fibres to induce the coupling oriented at a constant angle along the blade length). Results show that there is no significant gain in the Annual Production Energy, yet there are significant load alleviations, which might lead to savings in other parts of the wind turbine. While the introduction of bend-twist coupling by offsetting the fibres orientation with respect to the blade axis at a constant angle along the blade length is feasible from a manufacturing point of view and does not affect significantly the manufacturing cost. This is because the fibre orientation can be preselected (and ordered), similar to the biaxial and tri-axial layers used in the blade structure. On the contrary the solution proposed by UBRISTOL raises the manufacturing cost, since the requirement is for a variable angle along the blade length. Therefore, it has to be proven that the cost increase counteracts the advantages of the solution. Finally, CENER focused on the development of an analysis tool which can effectively estimate the response of a blade incorporating bend-twist coupling properties. Results of a study relevant to the output obtained with two identical solutions – one having structural coupling and the other not – are also compared. The **technological readiness level** for the solutions of bending-twisting coupling by offsetting the fibres (from the blade axis) is **5 to 6**, in that there have been demonstrations of the concept in laboratory conditions for smaller blades. These demonstrations had the purpose to evaluate the structural response of the blade, rather than its operation on the wind turbine. A demonstration of the performance of a scaled wind turbine with rotor incorporating bend-twist coupled blade is already planned to be performed at the wind tunnel of PoliMi within the INN WIND.EU project (Deliverable 2.24).

The **fourth chapter** of the present document discusses **integrated design solutions**. To be specific the structural solutions presented are the result of taking into account the aerodynamic configurations of the blade's geometry as well as the specific loading on the blade through an integrated aeroelastic-structural design. In Chapter 4 five solutions are presented: The structural design to accommodate the Low Induction generator Rotor (LIR) developed within Task 2.1 of the INN WIND.EU project by CRES, the integrated design optimization performed on the reference wind turbine blade by WMC and the integrated design studies performed by PoliMi, basically discussing three individual and separate structural solutions. The work performed on the LIR blade by CRES and is presented in here concerns only the structural design of the blade. The interest was to assess the possibility of having a longer blade, without a penalty on the mass, that is capable of sustaining the loads and respond in a similar behavior to the traditional blade. WMC presents an optimization procedure using the inhouse developed tool FOCUS6 on the reference wind turbine blade. The objective here is to design the internal structure (in a conventional configuration) so that it complies with all structural relevant constraints and minimizes the mass. Through this procedure a 4% mass decrease has been achieved by optimizing the material usage, while improving the fatigue behavior of the blade. This would again be only minimal affecting the LCOE. Yet, at the current development stage it is by small incremental terms that a significant LCOE reduction will be achieved. The configurations presented by PoliMi are based on the blade with the bend-twist coupling the partner presented in Chapter 3, but, this is combined with the option of extending the length of the blade to improve energy capture and/or the use of an individual pitch controller. All solutions presented by PoliMi comply with the (structural) constraints set, regarding placement of

natural frequencies, strength under extreme and fatigue loads, as well as buckling. Among the three options, the one combining blade twist coupling, increased length and use of individual pitch control is shown to be the optimal. However, the blade is about 15% heavier in comparison to the reference wind turbine, while it was shown that the tower loads increase. But, the wind turbine with this configuration produces about 4% more energy and results in a reduced by about 3% Levelized Cost of Energy. From a structural point of view the solutions presented in Chapter 4 by CRES and WMC have a high technological readiness level, while the innovation falls in this case on the overall aerodynamic concept for the LIR blade and the structural optimization method for the WMC solution. The **technological readiness level** for the solutions presented by PoliMi, relevant to the blade structure, is **5-6**, i.e. same as that for the bend-twist coupling presented in Chapter 3.

In all cases where structural integrity verification of the blade is performed, as a minimum the blade is checked against strength under ultimate loads, whereby the deflection of the blade should be kept equal or below that of the reference blade as well as against buckling under ultimate loads. Appropriateness of the solution is also verified against the dynamic response of the blade, with constraints posed on its modal properties. In some of the cases evaluation against fatigue strength is also performed.

Overall the report includes **more than 15 solutions** for the blade structure. These include studies on innovative approaches for the internal blade structure (e.g. truss structure, grid reinforced panels), studies for the support of new aerodynamic concepts (e.g. the low induction rotor blade), studies on passive load alleviation methods (bend-twist coupling, swept blade, torsional flexible blade, etc.), as well as integrated structural design studies reaching up to taking into consideration the controller of the wind turbine. Of these solutions **three are highlighted**, basically one of each group of solutions presented in chapters 2-5, to be further processed under INN WIND.EU work package WP1 (Deliverable 1.24). These are:

- The blade having an internal truss structure replacing the shear webs (UPAT)
- The bend-twist coupled blade (PoliMi)
- The structural solution for the low induction rotor (CRES)

However, at least 7 solutions were compliant with all constraints set for the blade design by work package 1.

In conclusion, new structural concepts were identified as feasible for implementation in the wind turbine blade. These have been also combined with load alleviation solutions, which in turn affect the design of more components on the wind turbine. The effect of the latter falls beyond the objectives of work package 2 and has to be investigated by other research groups and/or work packages.

## 1 INTRODUCTION

The report includes the description of structural blade designs developed/modified, etc. within the INN WIND.EU project under WP2 “Lightweight Rotor” Task 2.2 “Lightweight structural design”, as well as the analysis results regarding the compliance with the specifications developed in InnWind.Eu work-package WP1. The purpose is to report on the new structural blade designs that are developed within the INN WIND.EU WP2, Task 2.2, and subtask 2.2.2, which will be further evaluated regarding the impact of the solution on the overall cost of the wind turbine within INN WIND.EU WP1 “Conceptual Design”. The objective is to define and assess innovative structural concepts for achieving lightweight rotor blades with adequate stiffness and strength. Information included for the structural concepts and designs with potentially lower blade mass and favourable adaptive and aeroelastic characteristics that are developed by the partners participating in the frame of Task 2.2, will be forwarded to INN WIND.EU WP1 partners for their further assessment and evaluation relevant to the cost of the overall wind turbine.

The work performed under Task 2.2 and reported in here serves the INN WIND.EU project in three aspects:

### A. Introducing **new concepts** for the pure structural solutions

State of the art blades are built using the same internal configuration, comprising load carrying shell with shear webs. With increasing the blade size, other solutions, such as those used in the aeronautic sector might be more relevant. This solutions have not been systematically investigated. Previous research projects were mainly concentrated on aerodynamic/aeroelastic issues and limited structural investigations to support the ideas. For example, structurally-wise UPWIND<sup>1</sup> involved research on a sectional blade, which could be seen as a continuation of MEGAWIND<sup>2</sup> (completed in 2003) and SECBLADES<sup>3</sup> (finished in 2000), where focus was set to joining solutions of the two-part blade (both length-wise and chord-wise). Within UPWIND smart blade concepts and rotor control were investigated together with the development of new tools for improved prediction of structural behaviour, which was partly a continuation of OPTIMAT BLADES<sup>4</sup> project (completed 2006). But new concepts for the structural layout of the blade were not investigated. The exception of the European projects in wind energy is maybe one by Risoe-DTU, “Structural blade design and testing”<sup>5</sup> (completed in about 2010), where new structural solutions were investigated, but, again keeping the original layout of the blade. Findings of the latter form partly the base of the work presented in this report. The other part is stemming from the aeronautical sector, with the airplane wings having different structural solutions than wind turbine blades. For these structures the load is carried by metallic components, while a very light skin is forming the shape of the blade.

### B. Supporting smart rotor concepts

With the sizes of the wind turbine continuously increasing solutions that could help in reducing the loads on the components (and specifically on the wind turbine blade) while maintaining the power output are necessary. Past investigations, conducted in early 2000 mainly by the SANDIA National laboratories [2], [3], were based on exploiting the properties of the anisotropic composite material used in the blade structure to drive the response of the blade. Yet, these investigations, performed for at the time state of the art sizes of the wind turbine (~0.5MW), was not pursued by the industry. The question that the present investigations have to answer is: Is the size of a 10MW wind turbine now justifying the re-introduction of the concept on the blade? At present these investigations are facilitated by the confidence gained for the currently available numerical analysis tools, which are able to predict more accurately the response of the blade incorporating couplings.

### C. Supporting the newly proposed aerodynamic concepts (under Task 2.1)

Since aerodynamic and smart rotor proposed within INN WIND.EU solutions for the blade should reach a more or less final stage to define the New “InnWind” Rotor developed within WP2, specific

<sup>1</sup> [http://cordis.europa.eu/project/rcn/78583\\_en.html](http://cordis.europa.eu/project/rcn/78583_en.html)

<sup>2</sup> <http://www.cres.gr/megawind/>

<sup>3</sup> [http://www.technology.stfc.ac.uk/ERU/projects\\_wind.html](http://www.technology.stfc.ac.uk/ERU/projects_wind.html)

<sup>4</sup> <https://www.wmc.eu/optimatblades.php>

<sup>5</sup> <http://www.structural-blade-design-and-testing.dtu.dk/>

structural solutions to accommodate these innovations have to be also determined. Thus, the work reported in this report supports the aerodynamic and load control solutions regarding structural feasibility.

The organisation of the present report comprises three distinct parts. It starts with the description of the new structural concepts used to replace the traditional internal structure of the blade, then proceeds with the solutions that are exploiting structural couplings of the blade to alleviate the loading on the rotor and proceeds with solutions obtained carrying out an integrated design taking into account both aerodynamic/aeroelastic effects as well as the structural integrity of the blade.

To verify the structural integrity of the blade, as a minimum the blade is checked against strength under ultimate loads, whereby the deflection of the blade should be kept equal or below that of the reference blade as well as against buckling under ultimate loads. Appropriateness of the solution is also verified against the dynamic response of the blade, with constraints posed on its modal properties. In some of the cases evaluation against fatigue strength is also performed.

In essence, results in **chapter 2** including the **innovative internal structural solutions** for the blade are based on the reference geometry of the blade and reference loading, as that used during the benchmark. Although for all solutions a reduction of the mass of the blade has been achieved the loading was not adapted to comply with it, but rather kept the same as for the reference blade. This in turn indicates that it is possible that due to the lighter blade design obtained, running full simulation to estimate the aeroelastic response, the loading on the blade will be reduced, allowing further mass reduction. However, as discussed in the subsequently the solutions proposed are not mature enough, since details of the structural design, especially relevant to joints, required in a real manufacturing scenario have not been performed. This is also outside of the scope of the work performed. The solutions discussed relevant to wind turbine blade have a **technological readiness level of 4 to 5**. That means that although they have been estimated as feasible, their adequacy has never been verified. Three solutions are presented in chapter 2 in addition to a numerical topology optimization study. The first, employing an internal truss structure to replace the traditional shear webs of the blade was performed by University of Patras (UPAT). The second solution was performed by Technical University Delft (TUD) and studies the possibility of replacing the sandwich structure usually employed in the trailing edge of the blade with a grid stiffened panel. The third solution resembles the solution by UPAT in that truss members are used to carry the load, yet instead of replacing only the shear webs, it was studied whether it is possible to replace the entire load carrying structure of the blade with truss members while the aerodynamic surface of the blade is to be constructed with a light cloth resembling material. This option was investigated by CRES. The chapter closes with the topology optimization study performed by University of Bristol (UBRISTOL) relevant to the offset of the shear webs.

**Chapter 3** includes the solutions for passive alleviation of the loads by taking into advantage **bend-twist coupling of the blade**. To this end, the structural design of the blade has to be performed suitably placing the composite materials to “design” the needed couplings in the blade’s response under load. To evaluate the final result aeroelastic estimations have been performed, therefore, in essence the work is intermediate between integrated design (shown in chapter 4) and independent structural design (presented in chapter 2). A solution for load alleviation designing a blade with bend twist coupling and complying with all structural design specifications is presented by Politecnico di Milano (PoliMi). The result in terms of mass savings is in the order of 4%, while using the cost estimator developed within INN WIND.EU WP1 the reduction on the Levelized Cost of Energy (LCOE) is minimal. Work regarding the structural design of the blade to achieve passive load alleviation has also been performed in the frame of the INN WIND.EU project by Denmark’s Technical University (DTU), University of Bristol (UBRISTOL) and CENER. The efforts of the institutes are also reported under Chapter 3. DTU evaluated the concepts of a conventional bend-twist coupling solution, similar to the one presented by PoliMi, against the solutions of having a blade with a single shear web, thereby reducing the torsional stiffness of the blade, as well as the solution of the swept blade. The studies relevant to the load alleviation have been performed individual for the three cases, as well as for their combination. The work concentrated to evaluating the load reduction achieved through each solution and as a minimum complying with the constraints of tower clearance (maximum deflection) and the strength of the blade under extreme loading. UBRISTOL evaluated the solution of achieving an optimized bend-twist coupling through varying the fiber orientation along the blade length, thus, achieving different levels of coupling along the blade. The solution was compared against the traditional blade structure (without bend-twist

coupling) and the option of a conventional bend-twist coupling design (with off-axis fibres to induce the coupling oriented at a constant angle along the blade length). Results show that there is no significant gain in the Annual Production Energy, yet there are significant load alleviations, which might lead to savings in other parts of the wind turbine. While the introduction of bend-twist coupling by offsetting the fibres orientation with respect to the blade axis at a constant angle along the blade length is feasible from a manufacturing point of view and does not affect significantly the manufacturing cost. This is because the fibre orientation can be preselected (and ordered), similar to the biaxial and tri-axial layers used in the blade structure. On the contrary the solution proposed by UBRISTOL raises the manufacturing cost, since the requirement is for a variable angle along the blade length. Therefore, it has to be proven that the cost increase counteracts the advantages of the solution. Finally, CENER focused on the development of an analysis tool which can effectively estimate the response of a blade incorporating bend-twist coupling properties. Results of a study relevant to the output obtained with two identical solutions – one having structural coupling and the other not – are also compared. The **technological readiness level** for the solutions of bending-twisting coupling by offsetting the fibres (from the blade axis) is **5 to 6**, in that there have been demonstrations of the concept in laboratory conditions for smaller blades. These demonstrations had the purpose to evaluate the structural response of the blade, rather than its operation on the wind turbine. A demonstration of the performance of a scaled wind turbine with rotor incorporating bend-twist coupled blade is already planned to be performed at the wind tunnel of PoliMi within the INN WIND.EU project (Deliverable 2.24).

The **fourth chapter** of the present document discusses **integrated design solutions**. To be specific the structural solutions presented are the result of taking into account the aerodynamic configurations of the blade's geometry as well as the specific loading on the blade through an integrated aeroelastic-structural design. In Chapter 4 five solutions are presented: The structural design to accommodate the Low Induction generator Rotor (LIR) developed within Task 2.1 of the INN WIND.EU project by CRES, the integrated design optimization performed on the reference wind turbine blade by WMC and the integrated design studies performed by PoliMi, basically discussing three individual and separate structural solutions. The work performed on the LIR blade by CRES and is presented in here concerns only the structural design of the blade. The interest was to assess the possibility of having a longer blade, without a penalty on the mass, that is capable of sustaining the loads and respond in a similar behavior to the traditional blade. WMC presents an optimization procedure using the inhouse developed tool FOCUS6 on the reference wind turbine blade. The objective here is to design the internal structure (in a conventional configuration) so that it complies with all structural relevant constraints and minimizes the mass. Through this procedure a 4% mass decrease has been achieved by optimizing the material usage, while improving the fatigue behavior of the blade. This would again be only minimal affecting the LCOE. Yet, at the current development stage it is by small incremental terms that a significant LCOE reduction will be achieved. The configurations presented by PoliMi are based on the blade with the bend-twist coupling the partner presented in Chapter 3, but, this is combined with the option of extending the length of the blade to improve energy capture and/or the use of an individual pitch controller. All solutions presented by PoliMi comply with the (structural) constraints set, regarding placement of natural frequencies, strength under extreme and fatigue loads, as well as buckling. Among the three options, the one combining blade twist coupling, increased length and use of individual pitch control is shown to be the optimal. However, the blade is about 15% heavier in comparison to the reference wind turbine, while it was shown that the tower loads increase. But, the wind turbine with this configuration produces about 4% more energy and results in a reduced by about 3% Levelized Cost of Energy. From a structural point of view the solutions presented in Chapter 4 by CRES and WMC have a high technological readiness level, while the innovation falls in this case on the overall aerodynamic concept for the LIR blade and the structural optimization method for the WMC solution. The **technological readiness level** for the solutions presented by PoliMi, relevant to the blade structure, is **5-6**, i.e. same as that for the bend-twist coupling presented in Chapter 3.

To assure comparability of the solutions each partner is comparing its new solution against results of the reference blade. The benchmark on structural design methods for blades that was performed within the INN WIND.EU project under WP2 "Lightweight Rotor" Task 2.2 "Lightweight structural design" and reported under Deliverable D2.21 "Benchmarked aerodynamic-structural design methods" includes all simulation results of the partners regarding the reference blade used. The benchmark is based on the reference wind turbine and the reference blade provided by DTU [1]. "Structural Concept developers/modellers" of WP2 were provided with the necessary input for

a comparison numerical simulation run. Output was compared in terms of weight, stiffness, natural frequencies, deflection (extreme load), strength & stability (extreme load) and fatigue (variable load). Each of the partners involved in Task 2.2 applies tools developed in-house. For each conceptual idea that is presented in this document, the partner will show feasibility of solution under comparison with the reference blade.

Assessment of the structural design for the proposed solutions has been performed in most cases, especially those that are considering only internal structural changes, keeping the same aerodynamic shape as for the reference blade and using the loading conditions applied during the benchmark. For solutions regarding passive load alleviation the loading on the blade (and other major components of the wind turbine) has been estimated through aeroelastic calculations, since this is the major focus on the optimization.

## 2 NEW STRUCTURAL SOLUTIONS

In the present chapter solutions that are keeping the external surface of the blade the same, while introducing new concepts for the internal structure are presented.

Currently all blades are built using the same (gross) internal and external layout. A shell reinforced through shear webs. Of course, each manufacturer produces this gross internal layout with slight modifications, but essentially it is the same for all. This concept has not changed since the early days of wind energy, except for some material improvements; changing polyester to epoxy, applying resin injection and lately pre-impregnated layers instead of hand layup, and lately introducing carbon fibres to replace part of the glass fibres. But structurally-wise the concept remains the same. Up to now, the structural design of the blade is performed not only keeping the requirements set for the wind turbine system (stiffness, strength, etc.) but also the requirements of the manufacturing (using unidirectional reinforcement specifically at 0,  $\pm 45$  and 90 degrees, building of external shells, building of shear webs, gluing it all together – with the exception of a manufacturer avoiding the adhesion part. Other solutions were never systematically explored due to the weight put in aerodynamic solutions and increase of blade size in quite a short time. This fact combined with the lack of knowledge in material behaviour and structural modelling issues slowed down “innovation” in the structural part.

Partly inspired by the aeronautical sector with the airplane wings being based on a different structural solution, following innovations investigated are:

- Internal truss structure; performed University of Patras (UPAT), whereby the shear webs configuration is replaced by a truss structure with composite material members, keeping the traditional design for the blade skin.
- Grid reinforced skin; performed by Technical University of Delft (TUD), whereby the sandwich panels of the trailing edge are replaced by grid stiffened panels, keeping the rest of the blade structure as per traditional designs.
- Rib reinforced skin; performed by CRES, whereby the load carrying structure of the blade is completely replaced by a truss structure having composite material members. The outer surface of the blade is no longer designed to carry the loads, but rather only to form the aerodynamic shape needed for the operation of the blade.

Each of these proposed solutions is completely new for the blade structure. In the following sections, not all aspects of the introduced innovative concepts have been covered. For example structural details such as the joints between truss members have not been considered. The objective is to assess the feasibility of the concept and validate the mass savings introduced by replacing structural parts of the blade with other manufacturing technologies.

For the structural solutions in the present section the external geometry is that of the DTU 10MW reference blade [1]. Thus, the length of blade, chord, twist and (section) thickness distribution along the blade length for the aerodynamic active part, as well as the location of pitch axis is kept the same as that provided in ref. [1] and used in the benchmark [2].

Similar the loading to verify the structural integrity of the new designs is for all cases presented the load cases, extreme and fatigue case used in the benchmark [2]. This is necessary to enable comparison between solutions without the bias of having different shapes or loading envelopes. For the solutions described in-here this might be a restriction, since recalculation of the load envelope depending on the mass savings achieved would lead to even further potential to mass reduction. This is because the gravitational loads on the blade have an important influence on the load scenarios, which is now kept frozen to allow comparisons.

### 2.1 Internal Space Truss Structure (UPAT-Core Team)

In the present section the work performed by University of Patras (UPAT) is presented regarding the structural design of the reference blade having an internal space truss structure instead of the traditional use of shear webs.

### 2.1.1 State of the art and motivation

State of the art rotor blade design indicates the use of a spar-box as the main load bearing component accompanied by a number of shear-webs depending on the size of the rotor blade. The skins and shear-webs consist of a sandwich structure while the spar caps are dominated by unidirectional fibers in the pitch-axis direction to deliver the desired axial stiffness. Since producing long (>60m) rotor blades using carbon fiber composite materials is still too expensive for commercial wind turbines, glass fiber reinforced composites (GFRP) are preferred from the manufacturers.

The need for longer blades for the new many multi-megawatt machines of the future, even for the existing (>7 MW) designs, where blade weight is a restrictive parameter calls for the need to introduce an economic solution for the use of carbon fiber composite materials in the manufacture of rotor blades. New designs that take advantage of carbon fiber composite structures made of less expensive manufacturing techniques, such as filament winding and pultrusion, have to be established. In that context, the idea to replace the original spar-box beam of the rotor blade by an internal space truss structure was investigated.

### 2.1.2 Brief description of the concept

The InnWind reference blade design recommends two spar caps that consist of unidirectional GI/Ep composite material, 3 shear-webs of a sandwich structure made of biaxial GI/Ep fabric and balsa wood and skins, sandwich structures as well, consisting of triaxial and uniaxial GI/Ep composite materials; balsa wood as core material.

In order to reduce the weight of the reference blade the conceptual design proposed by UPAT suggests the replacement of the spar-box and 3rd web with an internal space truss. This will make possible to remove the uniaxial composite material from the rotor blade's skin and reduce the thickness of the triaxial composite material. The internal truss should be able to achieve the axial stiffness and strength of the reference blade.

The truss topology initially consisted of a large number of rods/beams and the modelling of the internal truss was achieved using Beam188 elements while the skin was modelled with Shell181 elements (Figure 1) of the ANSYS commercial code.

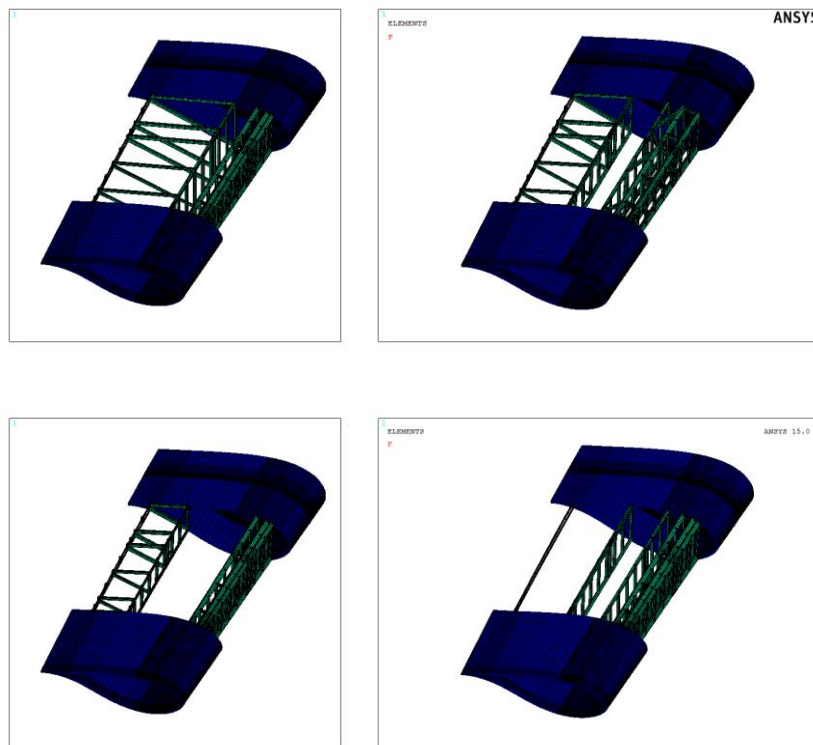
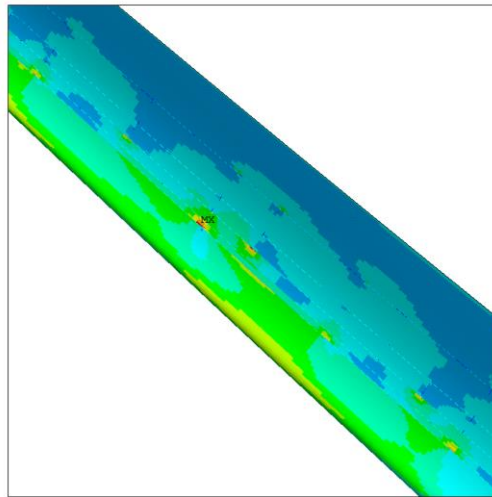


Figure 1. Examples of tested topologies of the internal truss

The investigation focused into modelling an internal space truss made of GI/Ep composite materials which would have a stiffness, strength and elastic behaviour close to those of the reference blade while keeping the weight of the blade lower. The main challenge encountered was the local failures of the blade, a numerical artefact due to concentrated forces applied in a small number of nodes (Figure 2).



**Figure 2. Local failure due to numerical artifacts**

To overcome the situation, the blade was modelled from scratch using only shell element formulation even for each individual beam component of the space truss structure (Figure 3).

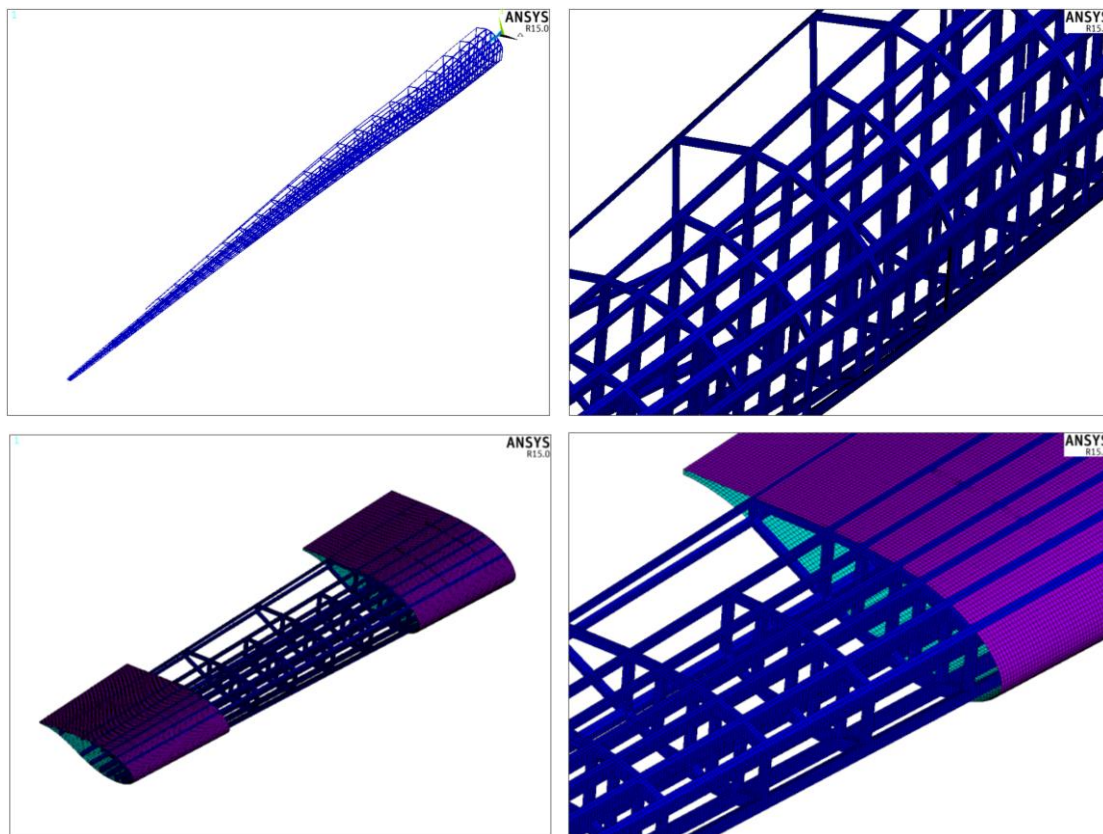


**Figure 3. Blade model using only shell elements**

The new FE model of the blade consists of 600,000+ elements and more than 3,000,000 degrees of freedom. Any change in the truss topology or layup configuration in the course of this investigation needs more than 24 hours to complete and up to 36 hours for a strength or buckling analysis run-time in fast PC servers. As a result, due to time limitations, in the final design for this report the internal truss is modelled with Beam188 elements.

### 2.1.3 Anticipated PROS and CONS

The main advantage of the conceptual design proposed by UPAT CORE Team is that offers to the manufacturer the ability to use composite materials produced by mass production techniques, e.g. filament winding and pultrusion instead of prepregs and fabrics, thus less expensive. Moreover, the control during the production of such structures is higher than in manual prepreg or fabric laying type composite materials which leads into better quality structures.

Furthermore, the modular construction of the space truss facilitates the implementation of modular blade concepts with known advantages in the transportation as well as the repair and the maintenance of the rotor blade.

The main disadvantage of the concept is the complexity in joining the various elements. More specifically, in the locations where more than 2 beams meet the joint calculation and construction is a challenging task.

### 2.1.4 Assessment of the structural integrity of the proposed design

#### 2.1.4.1 Design layout and dimensioning

Since the idea behind the implementation of a space truss instead of the traditional spar-box beam of the reference blade was to introduce an economic and efficient solution for the use of carbon fiber composite materials in rotor blades, two (2) final blade designs are presented. The first one is solely a GFRP construction along with balsa wood as core material where needed, while in the second one some of the beams of the space truss are made of C/Ep material.

The internal truss topology is kept the same for the 2 models and is presented in Figure 4. Eventually, information on beam dimensioning and their exact position into the blade might be made available upon request; due to space limitations such details are not presented in this report.

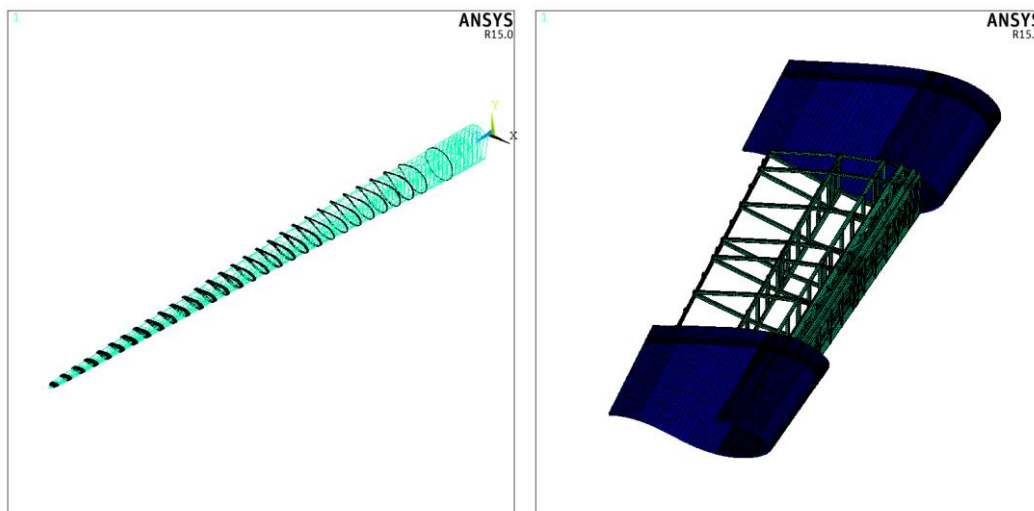


Figure 4. Truss Topology

In both cases the skin of the blade consists only of triaxial fabric and balsa wood in a sandwich form of [triax/balsa/triax].

The FE model in ANSYS is based on a Reissner – Mindlin shell formulation. The skin consists of 4-node multilayer shell181 elements while the truss consists of 2-node beam188 elements. The

triaxial, uniaxial fabric and balsa wood properties were all based on the benchmark input provided by the coordinators while the CFRP mechanical properties are presented in Table 1.

**Table 1. Typical mechanical properties of T700S C/Ep composite**

Property	Value
E <sub>1</sub>	148.51 [GPa]
E <sub>2</sub>	9.03 [GPa]
G <sub>12</sub>	5.55 [GPa]
v <sub>12</sub>	0.225 [GPa]
X <sub>t</sub>	768.84 [MPa]
X <sub>c</sub>	537.98 [MPa]
Y <sub>t</sub>	5.49 [MPa]
Y <sub>c</sub>	31.43 [MPa]
S	28.46 [MPa]
Density	1600 kg/m <sup>3</sup>

It is noted here that in the failure stress values presented in Table 1, the characteristic values are divided by a material safety factor of 2.205 according to GL design guidelines. For the elastic stability analysis a safety factor of 2.042 was applied in the elastic constants as described in the input provided by the coordinators for the structural benchmark.

The total mass of each of the materials used in the 2 blade models is presented in Table 2 while coordinates of the mass-centre of the blade are presented in Table 3.

**Table 2. Overall mass for each material**

Material	Reference Blade	Gl/Ep Blade	C/Ep Blade
Triaxial	11319.0 [kg]	8472.6 [kg]	8472.6 [kg]
Biaxial	4076.6 [kg]	-	-
Balsa	5074.8 [kg]	5411.0 [kg]	5411.0 [kg]
Uniaxial (Glass)	21908.9 [kg]	26049.0 [kg]	5367.0 [kg]
Uniaxial (Carbon)	-	-	11591.0 [kg]
<b>Total</b>	<b>42379.3 [kg]</b>	<b>39932.6 [kg]</b>	<b>30841.6 [kg]</b>

**Table 3. Coordinates of mass centre**

	Reference Blade	Gl/Ep Blade	C/Ep Blade
X coordinate [m]	-0.158	0.300	0.124
Y coordinate [m]	0.035	0.009	0.031
Z coordinate [m]	28.800	35.046	33.600

It is noted that the first section of the FE model is at 2.8 m.

#### 2.1.4.2 Structural integrity verification

The comparison between the 2 models that are presented and the reference blade in terms of load carrying capacity, elastic stability and tip deflection are presented in Table 4 while the results are presented in Figure 5 - Figure 10.

**Table 4. Mechanical performance of various blade models**

	Reference Blade	Gl/Ep Blade	C/Ep Blade
Tip Deflection [m]	20.6	24.18	11.52
Buckling critical Load factor	0.97	0.739	0.946
Strength multiplication factor	0.55	0.313	0.37

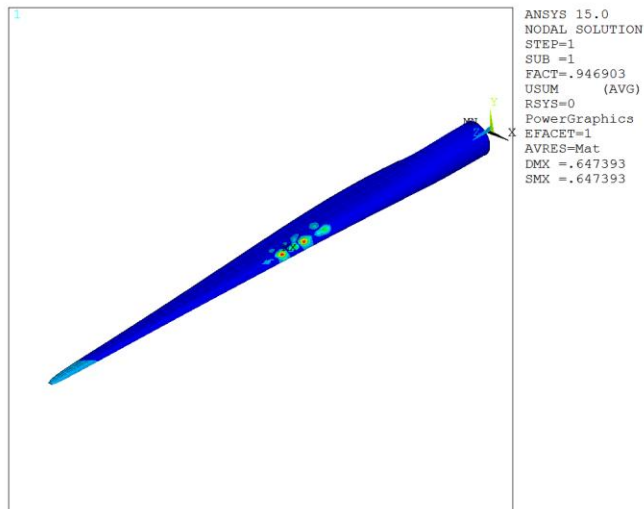


**Figure 5. 1st Buckling mode shape, C/Ep Blade**

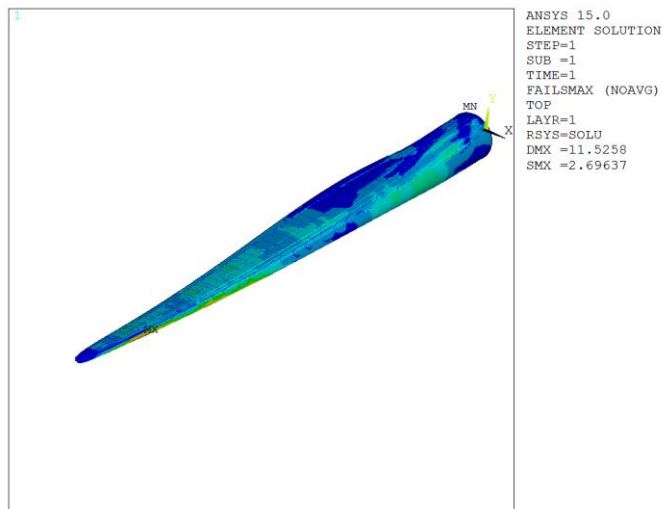


**Figure 6. Failure pattern of C/Ep blade under the reference load**

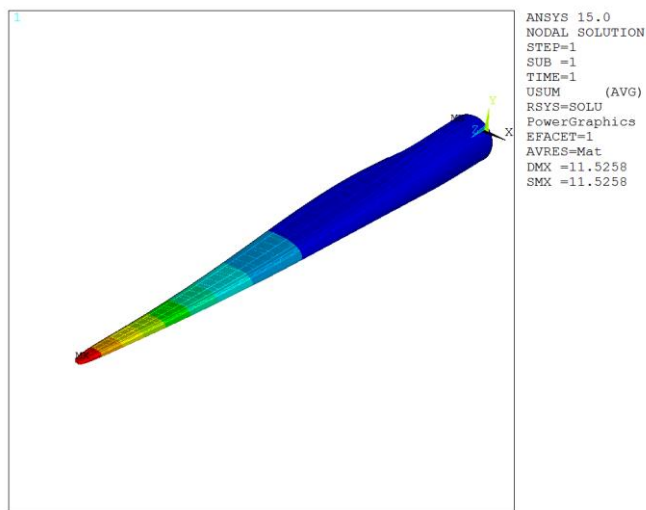


**Figure 7. Tip Deflection of C/Ep blade**

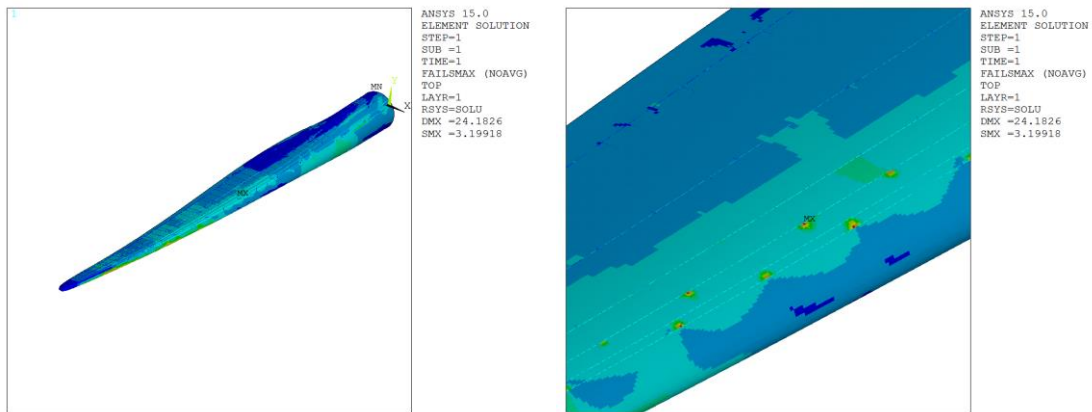


**Figure 8. Failure pattern of Gf/Ep blade under the reference load**

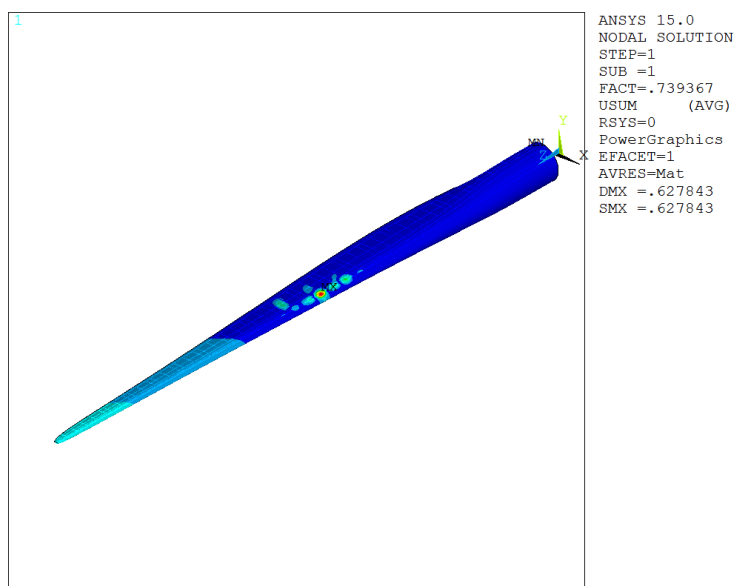


**Figure 9. 1<sup>st</sup> Buckling mode shape, Gf/Ep Blade**

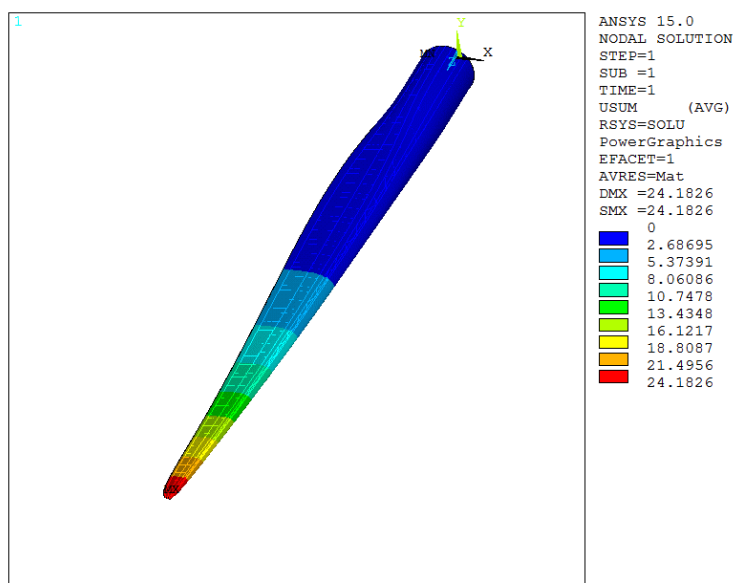


**Figure 10. Tip Deflection of GI/Ep blade**

A comparison of the natural frequencies is presented in Table 5.

**Table 5. Natural frequency comparison**

Mode Number	Reference Blade	GI/Ep Blade	C/Ep Blade
1	0.6095	0.3828	0.6767
2	0.9477	0.5470	0.7553
3	1.7486	1.2741	2.0568
4	2.8333	1.9344	2.5921
5	3.5714	2.5895	3.7984

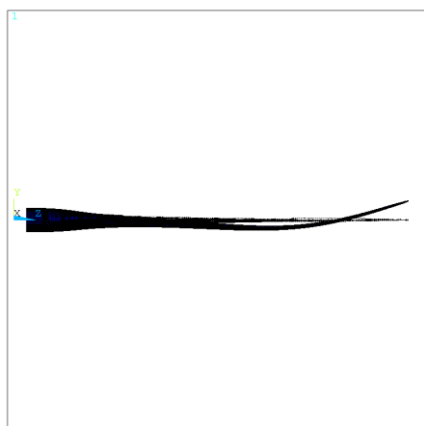
The mode shapes for the GI/Ep blade are presented in Figure 11.



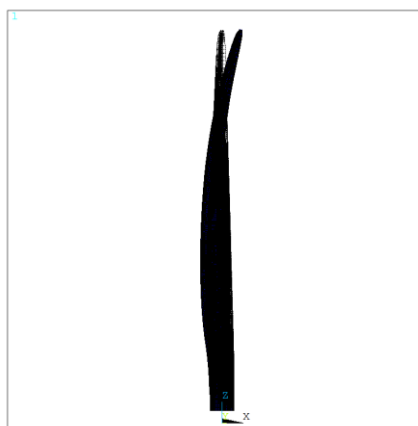
**1<sup>st</sup> Mode Shape**



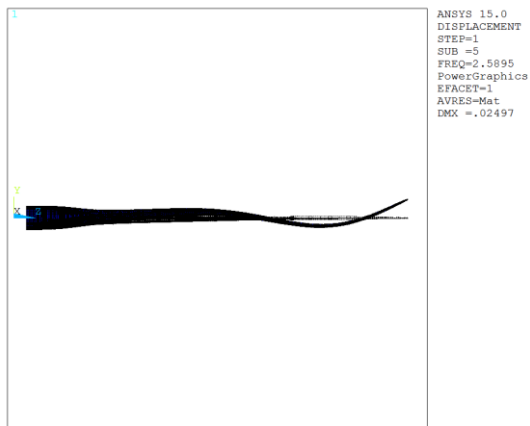
**2<sup>nd</sup> Mode Shape**



**3<sup>rd</sup> Mode Shape**



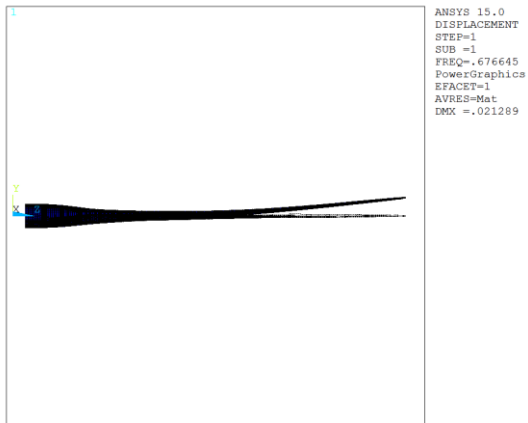
**4<sup>th</sup> Mode Shape**



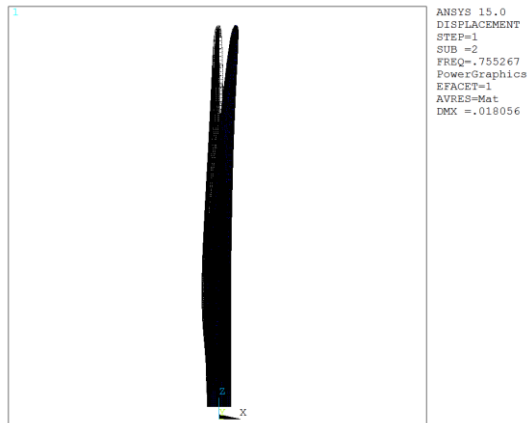
5<sup>th</sup> Mode Shape

Figure 11. 1<sup>st</sup> Mode Shape, Gl/Ep Blade

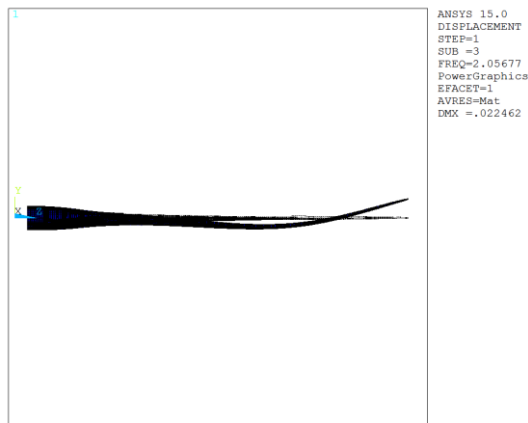
And for the C/Ep blade in Figure 12.



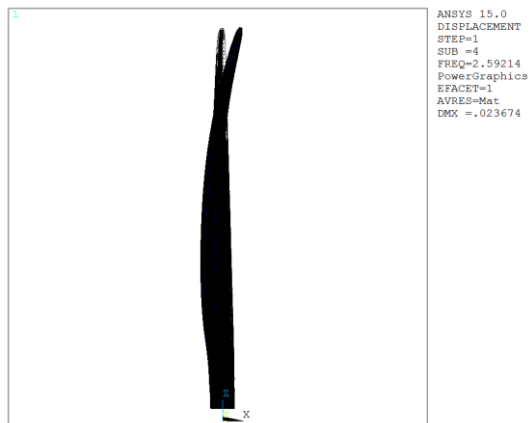
1<sup>st</sup> Mode Shape



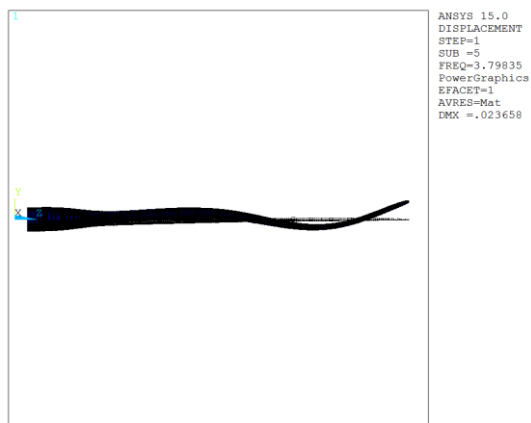
2<sup>nd</sup> Mode Shape



3<sup>rd</sup> Mode Shape



4<sup>th</sup> Mode Shape



5<sup>th</sup> Mode Shape

Figure 12. 1<sup>st</sup> Mode Shape, C/Ep Blade

### 2.1.5 Conclusions and recommendations

The structural design of an internal truss instead of the traditional spar-box faces a lot of challenges when GI/Ep materials are used. The most important one is the elastic instability of the blade's skin. A replacement of the sandwich structure with a more flexible material seems an appropriate solution to be investigated.

On the other hand, the replacement of the GI/Ep longitudinal beams with C/Ep ones improves the performance of the blade significantly. The results show that by replacing the 45% of the GI/Ep with C/Ep beams in the space truss the stiffness of the blade will improve by almost 100%, already with a ca. 27% lighter blade than the reference. This suggests that a much lighter construction might be finally achieved that will compensate for any cost increase due to material or assembly and joining complexities.

## 2.2 Grid stiffened structure (TUDelft)

In the present section the work performed by Technical University of Delft (TUDelft) is discussed regarding the use of grid stiffened panels in the blade structure to replace the traditional use of sandwich structures.

### 2.2.1 State of the art and motivation

Grid-stiffened composite structures are featured by a skin reinforced by a lattice made of fibre reinforced plastic composites. As the development of Automated Fibre Placement (AFP) technology matures, grid-stiffened composite structures can be manufactured efficiently and cheaply as an integrated structure. Nowadays, they can be up to 30% cheaper to produce than existing sandwich composite structures in addition to their other advantages, such as high damage tolerance, light weight and low moisture expansion. The aim of this work is to replace current sandwich trailing panels of the reference blade by grid-stiffened substitutions and investigate the optimal layout of stiffeners and material on the trailing panels. The design region is illustrated in Figure 13.



Figure 13. Illustration of the design region

## 2.2.2 Brief description of the concept

There are two important components of the design concept: optimization model and implementation scheme. Both of them will be introduced in the following paragraphs.

### Optimization model

In order to establish the optimization model, both the design variables, i.e. the changeable parameters, and crucial structural responses need to be selected. According to the feature of grid-stiffened composite structures, a large number of material and geometry parameters are involved, such as material selection and thickness distribution of the skin, and stiffener spacing and height distribution of the stiffeners. Actually, to insure the structural strength, the stiffener height is related to the skin thickness, which will make the optimization work complicated. By using the parametric results, the relation between stiffener height and skin thickness is set to be a fixed value in the design procedure. The stiffener spacings are determined in the same way with a linear variation of several key spacings along the span direction and a fixed spacing along the chord direction.

Another important part of the design variable selection is to separate the upper part design and the lower part design of the trailing panels in order to fully exploit the weight advantage of grid-stiffened structures by making use of the load-carrying difference in these two parts. Therefore, ten stiffener heights are chosen as design variables corresponding to five featured locations along the span direction of the blade for both the upper and lower parts of the trailing panel. Linear variations between these key stiffener heights are used to interpolate the stiffener height for an arbitrary location, as shown in Figure 14.

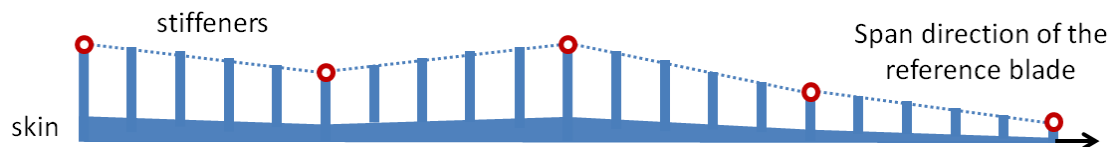


**Figure 14. Schematic diagram of the skin material and stiffener distribution of the grid-stiffened trailing panel along the span direction**

In the optimization model, four crucial structural responses of the structural weight, tip deflection, natural frequency and buckling load are included. The optimization model is implemented to minimize the structural weight with the other three responses constrained. Both tip deflection and natural frequency are bounded by the values obtained from analysis of the reference blade. Considering the differences in buckling modes between grid-stiffened structures and sandwich structures and the relatively large safety factor of buckling load (2.028) in the reference blade, the buckling load is bounded by a smaller lower value of 1.5.

In short, the optimization model is formulated as follows:

$$\left\{ \begin{array}{l} \text{Find } [h_i^{up}, h_i^{low}], \quad i = 1, \dots, 5 \\ \min \quad W \\ \text{s. t. } u_{tip}^y \leq 20.47 \\ \quad f_j \geq 0.61083, j = 1, \dots, 5 \\ \quad \lambda_k \geq 1.5, k = 1, \dots, 5 \\ \quad 0.0001 \leq h_i^{up}, h_i^{low} \leq 0.09 \end{array} \right.$$

where  $h_i^{up}$ ,  $h_i^{low}$  are the design variables denoting the  $i$ th stiffener heights of the upper and lower trailing panels at the key locations along the span direction of the blade.  $u_{tip}^y$  is the tip deflection along  $y$  direction,  $f_j$  is the  $j$ th natural frequency, and  $\lambda_k$  is the  $k$ th buckling load. The former two are bounded by the value obtained from the reference blade, while the buckling load is bounded by a reduced safety factor 1.5. Noticeably, no safety factor is applied on the buckling load since it is applied on the constraint of the response function.

### Implementation scheme

It is very computationally expensive to implement buckling analysis on the whole blade model. The scheme becomes more unpractical when the iteration of optimization with ten design variables is involved. To increase the calculation efficiency, a series of sectional models are used in the buckling analysis instead of the whole blade model. The applied load of the sectional models are the internal section forces and moments extracted from the whole model and all these load are updated with the change of design variables. The minimum buckling load among all the sectional buckling loads will be set as the critical buckling load for the whole blade model. In practice, all the sectional buckling loads are involved in the optimization model as constraint functions instead of only using the minimum value in order to avoid the typical maximizing minimum problem in optimization. Finally, the design procedure of the grid-stiffened trailing panel is illustrated in Figure 15.

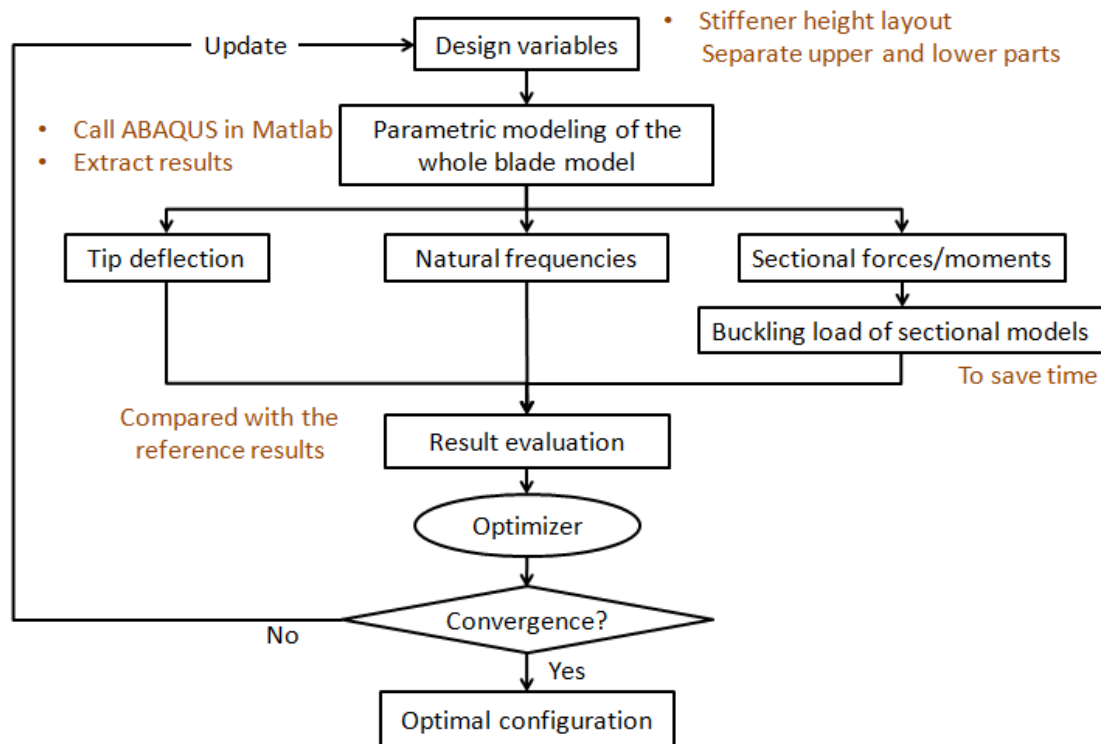


Figure 15. Design procedure of the grid-stiffened trailing panel

### 2.2.3 Anticipated PROS and CONS

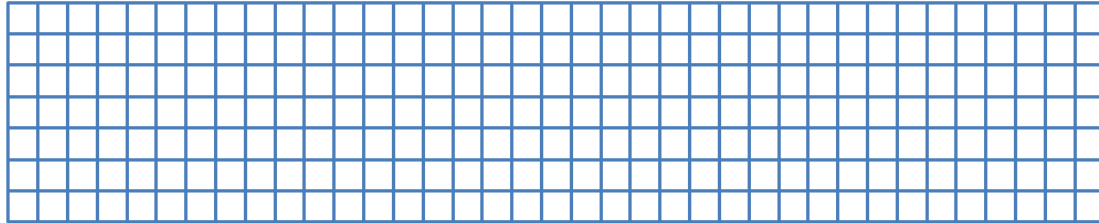
The scheme of using sectional models can efficiently reduce the computational time of buckling analysis. However, the selection of sectional dimension should be very careful. On one hand, the sectional length can't be too long to insure the accuracy of applied sectional forces and moments. On the other hand, it can't be shorter than three times of the half wave length of the local buckling mode in order to predict the same buckling model. To solve this problem, at the beginning, the sections are selected according to the existing segmentation in the previous report and then the section lengths are adjusted in the numerical test in comparing the buckling loads between the sectional models and the whole model. At the same time, a minimum skin thickness of 1.7688 mm (40% of the average face sheet thickness of the sandwich trailing panels of the reference blade) is set to avoid the local skin buckling due to the ultrathin skin.

### 2.2.4 Assessment of the structural integrity of the proposed design

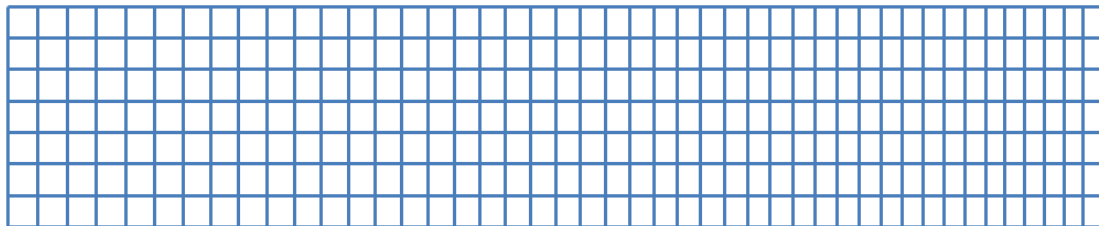
#### 2.2.4.1 Design layout and dimensioning

The key spacings along the span direction of the blade are set to be 0.4m, 0.39336m, 0.215385m, 0.22339 m, 0.4 m corresponding to the location of  $z=2.8$  m, 17.482 m, 33.892 m, 62.393 m, and

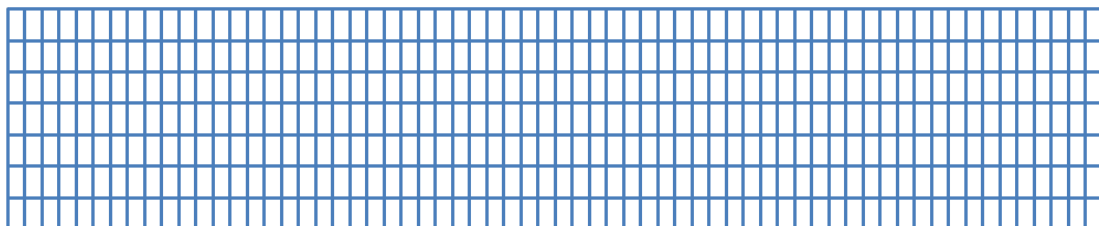
89.166 m with the stiffener spacing at an arbitrary location as a linear interpolation between two neighbouring key spacing, while the stiffener spacing along the chord direction of the blade is set to be 0.35 m. The stiffener width is 6.35 mm. The above-mentioned stiffener distribution is illustrated in Figure 16.



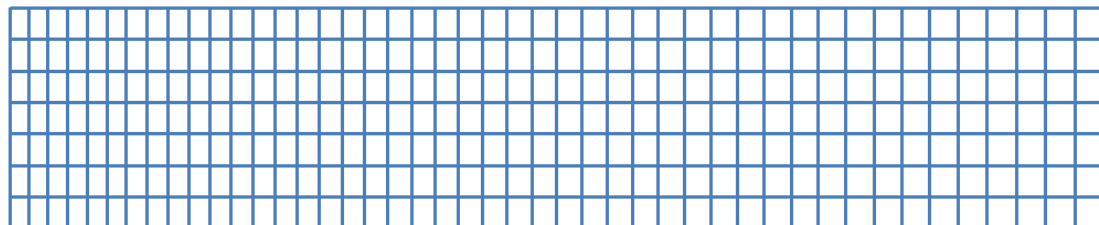
(a) From  $z=2.8$  m to  $z=17.482$  m



(b) From  $z=17.482$  m to  $z=33.892$  m



(c) From  $z=33.892$  m to  $z=62.393$  m



(d) From  $z=62.393$  m to  $z=89.166$  m

**Figure 16. Schematic diagram of the stiffener distribution**

To reduce the computational effort, the stiffener height of the lower trailing panel are optimized to be as 24.57 mm, 26.02 mm, 26.98 mm, 3.51 mm and 16.56 mm, as illustrated in Figure 17, and these values are used in the optimization of different stiffener heights for the upper trailing panel. The optimal stiffener heights for the upper trailing panel are given in Table 6 and the schematic diagrams are given in Figure 18 and Figure 19.

Table 6. *Dimensions of the optimal configurations and the structural responses*

No	$\frac{h_{stiff}}{t_{skin}}$	Optimal stiffener heights at key span locations of the upper trailing panel (mm)					Structural responses			
		$h_1^{up}$	$h_2^{up}$	$h_3^{up}$	$h_4^{up}$	$h_5^{up}$	Weight (t)	Tip deflection along y direction(m)	Natural frequency (Hz)	Buckling load
1	8	47.22	72.46	88.30	75.40	19.44	4.6768	20.00	0.6120	1.4967
2	6	8.56	77.40	88.66	67.34	10.93	5.5792	19.71	0.6127	1.5379

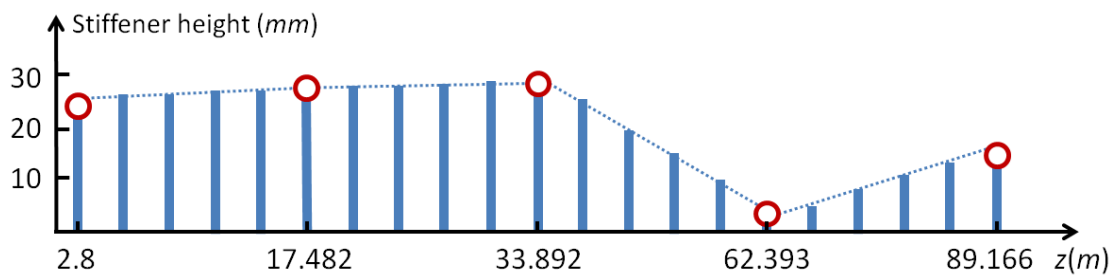


Figure 17. Schematic diagram of the optimal stiffener heights for the lower trailing panel

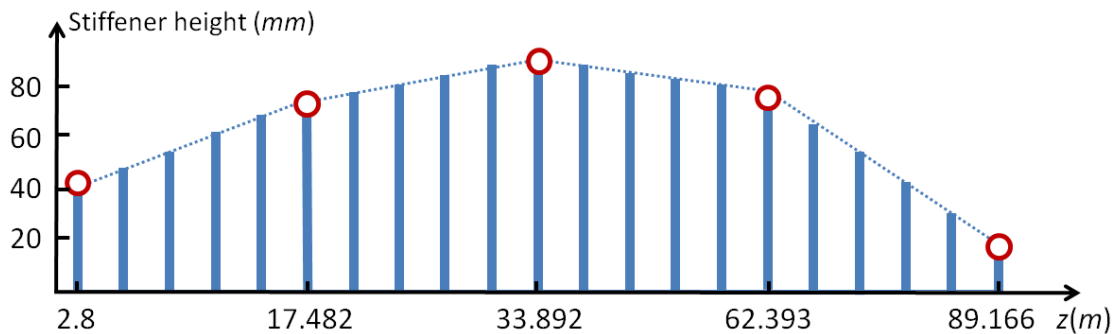


Figure 18. Schematic diagram of the optimal stiffener heights for the upper trailing panel with  $h_{stiff}/t_{skin}=8$

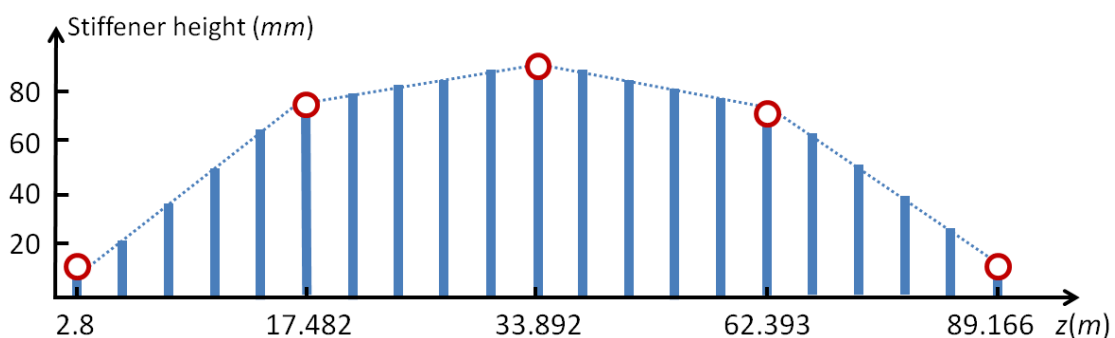


Figure 19. Schematic diagram of the optimal stiffener heights for the upper trailing panel with  $h_{stiff}/t_{skin}=6$

The skin thickness is determined by the optimal stiffener heights and the ratio between the stiffener height and the skin thickness, i.e., the skin thickness is also distributed piecewise linearly. On the other hand, same materials are used for the skin and the volume fraction for each material keeps the same. Thus, the detailed thickness for each material along the span direction of the blade is determined by the optimal skin thickness and the volume fraction of the considered material in the initial sandwich trailing panel.

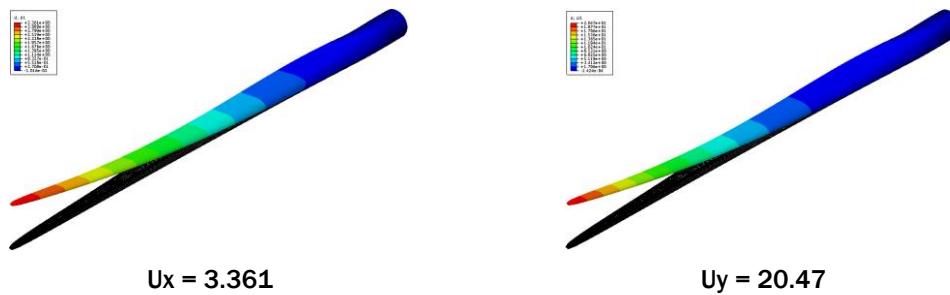
### 2.2.4.2 Structural integrity verification

The weight, tip deflection along y direction, natural frequency and buckling load of the reference blade are 6.9554 t, 20.47 m, 0.61083 Hz, 2.028, respectively. Therefore, the relative responses of the above-mentioned optimal grid stiffened trailing panels, compared with those of the reference blade are given below.

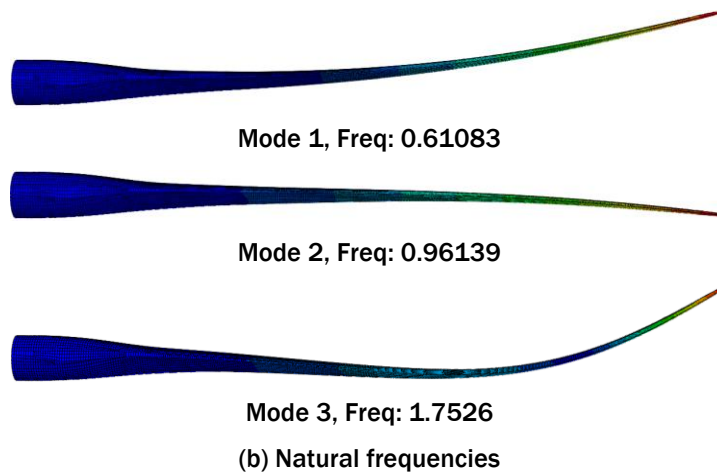
Table 7. *Relative structural responses of the optimal configurations*

No.	$\frac{h_{stiff}}{t_{skin}}$	Relative structural responses				
		Weight	Tip deflection	Natural frequency	Buckling load	
					Compared with the lower bound	Compared with the reference value
1	8	0.6724	0.9770	1.0019	0.9978	0.7380
2	6	0.8021	0.9629	1.0031	1.0253	0.7580

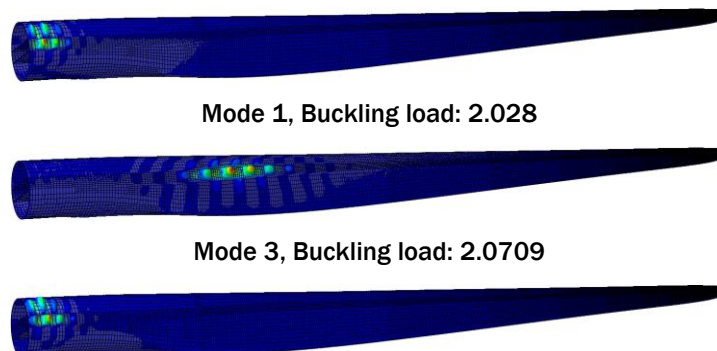
To make the comparison more clear, the corresponding figures are also provided for the reference blade and two optimal blades as follows.



(a) Tip deflections



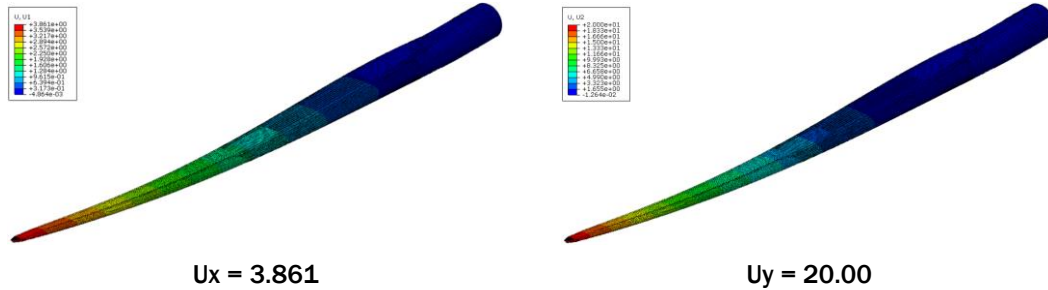
(b) Natural frequencies



Mode 5, Buckling load: 2.0933

(c) Buckling loads

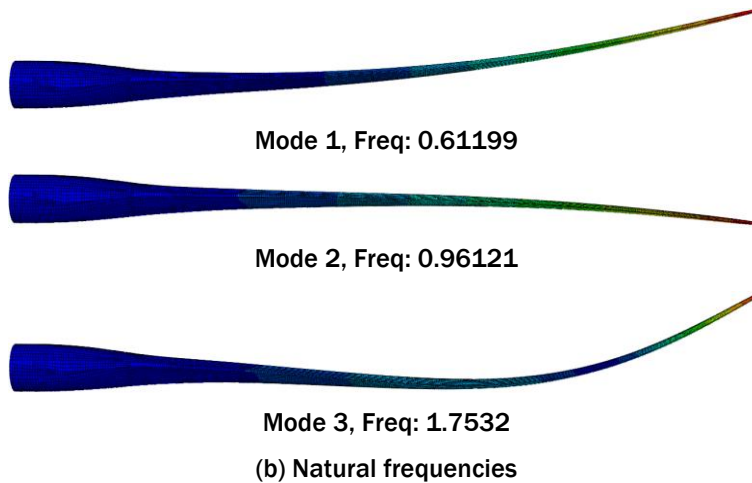
Figure 20. Structural responses of the reference blade



$U_x = 3.861$

$U_y = 20.00$

(a) Tip deflections

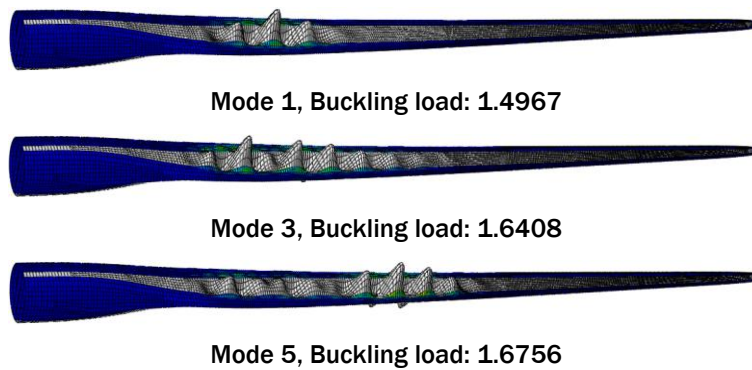


Mode 1, Freq: 0.61199

Mode 2, Freq: 0.96121

Mode 3, Freq: 1.7532

(b) Natural frequencies



Mode 1, Buckling load: 1.4967

Mode 3, Buckling load: 1.6408

Mode 5, Buckling load: 1.6756

(c) Buckling loads

Figure 21. Structural responses of the optimal blade with grid-stiffened trailing panels and  $h_{stiff}/t_{skln}=8$

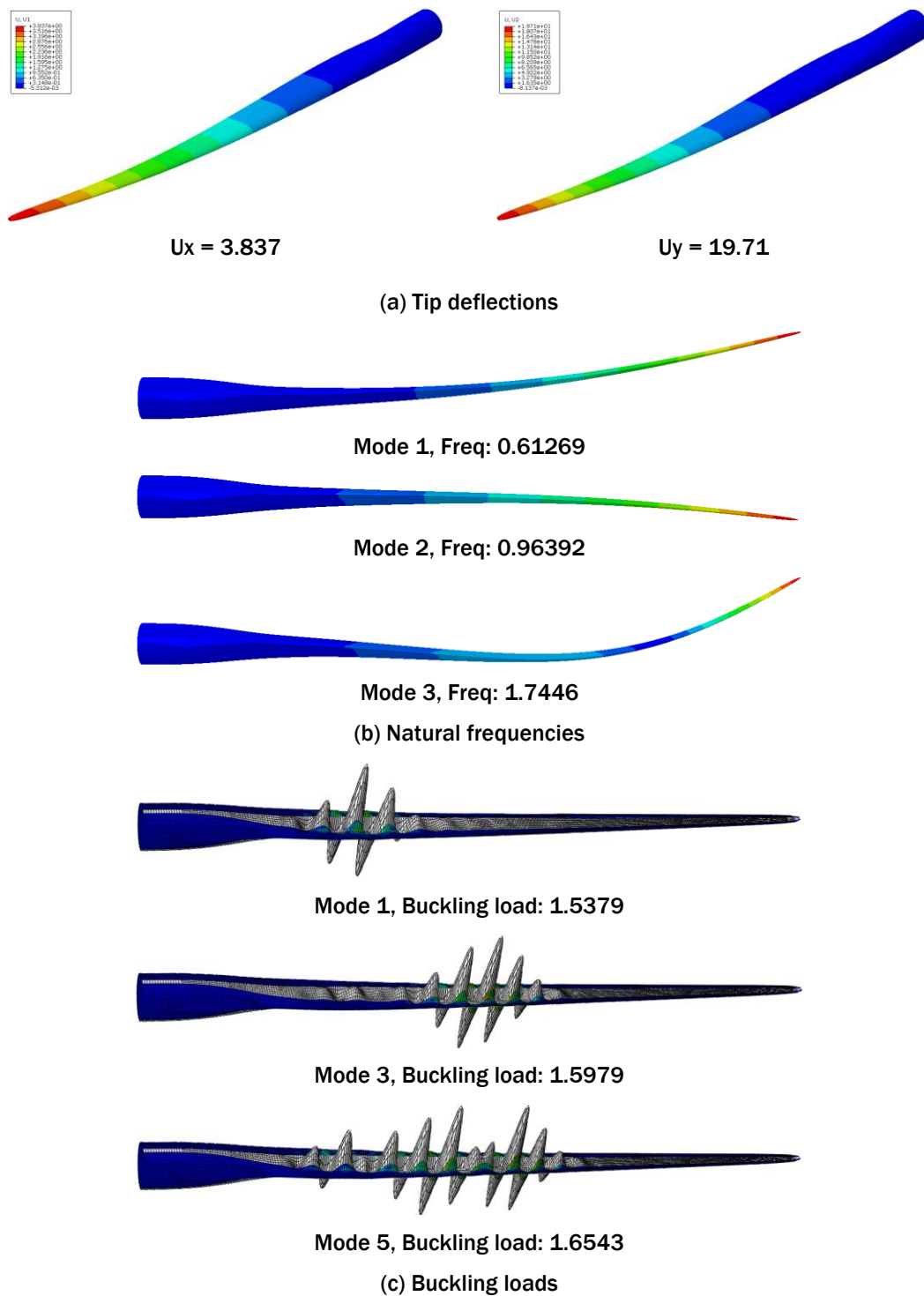


Figure 22. Structural responses of the optimal blade with grid-stiffened trailing panels and  $h_{stiff}/t_{skin}=6$

### 2.2.5 Conclusions and recommendations

With an substitution of grid-stiffened composite structure as trailing panels, the structural weight is reduced by 32.76% and 19.79% with the tip deflection, natural frequency and buckling load bounded for  $h_{stiff}/t_{skin}=8$  and  $h_{stiff}/t_{skin}=6$ , respectively, by using optimization techniques. Stiffener heights, skin thicknesses and stiffener spacings are all involved in the design, where the skin

thicknesses are bounded by values related to the stiffener heights to make the stiffener manufacturable and avoid the separation between the skin and stiffeners at the same time. It is found that the skin thickness will always reach the minimum bound in the optimization. Therefore, the skin thicknesses are not included in the optimization and determined by the user-defined ratio between the stiffener height and the skin thickness. In order to further reduce the computational effort and make the optimization affordable, the stiffener spacings are optimized before finding the optimal stiffener heights. A piecewise linearly variation between stiffener heights at the key location along the span direction of the blade is used for the final optimization.

The obtained optimal configurations are actually the local optimal which highly depends on the selection of design variables and the sequence of optimization procedure. The structural weight or other responses may be improved if a different optimization procedure is used or more design variables are involved.

## 2.3 Rib reinforced blade (CRES)

A conceptual blade design is presented in the present section, whereby the blade structure is formed by ribs. The research has been performed by CRES. The design is based on the use of beams with a circular section forming a truss structure with an external geometry identical to the reference INN WIND.EU blade [1], [3].

### 2.3.1 State of the art and motivation

Truss structures constitute a special class of structures in which individual straight members are connected at joints. Even though large scale constructions (e.g. bridges, buildings and roofs) are often designed by optimizing a truss geometry [4] there are a few design techniques available in the bibliography where special truss geometries are employed to form a wind turbine blade [5]-[6]. Unfortunately the available research in this domain is limited to the above mentioned empirical patents whereas for other types of structures sophisticated numerical tools such as finite element models and optimization algorithms are already employed leading to interesting results [7]. The recent size of the wind turbines, as well as the size anticipated for larger wind turbines justifies such schematics. In this work the possibility of finding an optimal truss geometry with the minimum mass that fulfills the requirements of the reference blade in stiffness, strength and buckling resistance using finite element models and optimization algorithms is examined.

### 2.3.2 Brief description of the concept

The proposed design uses beam elements with a circular section to form a truss and keeping the external geometry the same as the reference 10MW DTU blade [1]. To come up with the geometrical characteristics of the internal truss structure of the blade an optimization procedure is developed. A numerical optimization technique (pattern search [8]) is coupled with a parametrically built finite element model (FEM using beam element type) to find the lightest blade which accomplishes the requirements in strength, stiffness and buckling resistance. The algorithm used for the optimization is summarized in Figure 23. The procedure starts by giving initial values to the geometrical parameters. A first step completes a static and buckling analysis of the blade using identical load case with those employed in the benchmark of the reference blade [2] and automatically calculates the associated objective function. As long as the convergence criterion is not attained, the parameters are continuously updated by the optimization algorithm. When two consecutive steps do not alter the objective function by more than 0.1%, convergence is assumed and the computation stops.

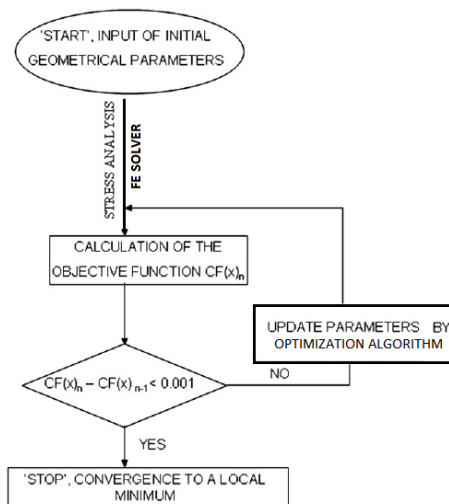


**Figure 23. Flowchart for the geometrical parameter updating**

### 2.3.3 Anticipated PROS and CONS

An optimized truss blade design can be lightweight compared to the traditional blade constructions. However, it can be expensive and time consuming to construct. Although the many supporting beams provide rigidity and robustness to the structure, truss members require careful maintenance to ensure that load carrying members, especially the joints of the members do not become damaged over time. It should be mentioned that repair of load carrying members in wind turbine blades with the traditional internal structure if damaged (e.g. through lightning strikes) is difficult to achieve and requires a rigorous certification process, with most cases ending in discarding the whole blade. The innovative solution proposed inhere allows inspection of the members, as well as replacement of the members if so needed without having to throw away the whole blade. These differences in manufacturing and maintenance of the rib reinforced blade have to be taken into account when estimating the cost of energy.

Currently, truss structures of composite materials are applied on different engineering structures. This is one of the first attempts to investigate the feasibility of such a configuration for the wind turbine blade in sizes of multi megawatt wind turbines. From the numerical point of view the optimization of a model of a truss with beam elements instead of 2D and 3D shell or solid FE model acquires less computational time and power. Yet, at the final stage it is anticipated that at a mature design stage numerical calculations with detailed representation of the structure will be necessary.

### 2.3.4 Assessment of the structural integrity of the proposed design

#### 2.3.4.1 Design layout and dimensioning

The proposed 90m blade is divided in fifty sections, see Figure 24. For the calculations the joint among the beams is assumed to be perfect and no relative movement is allowed.

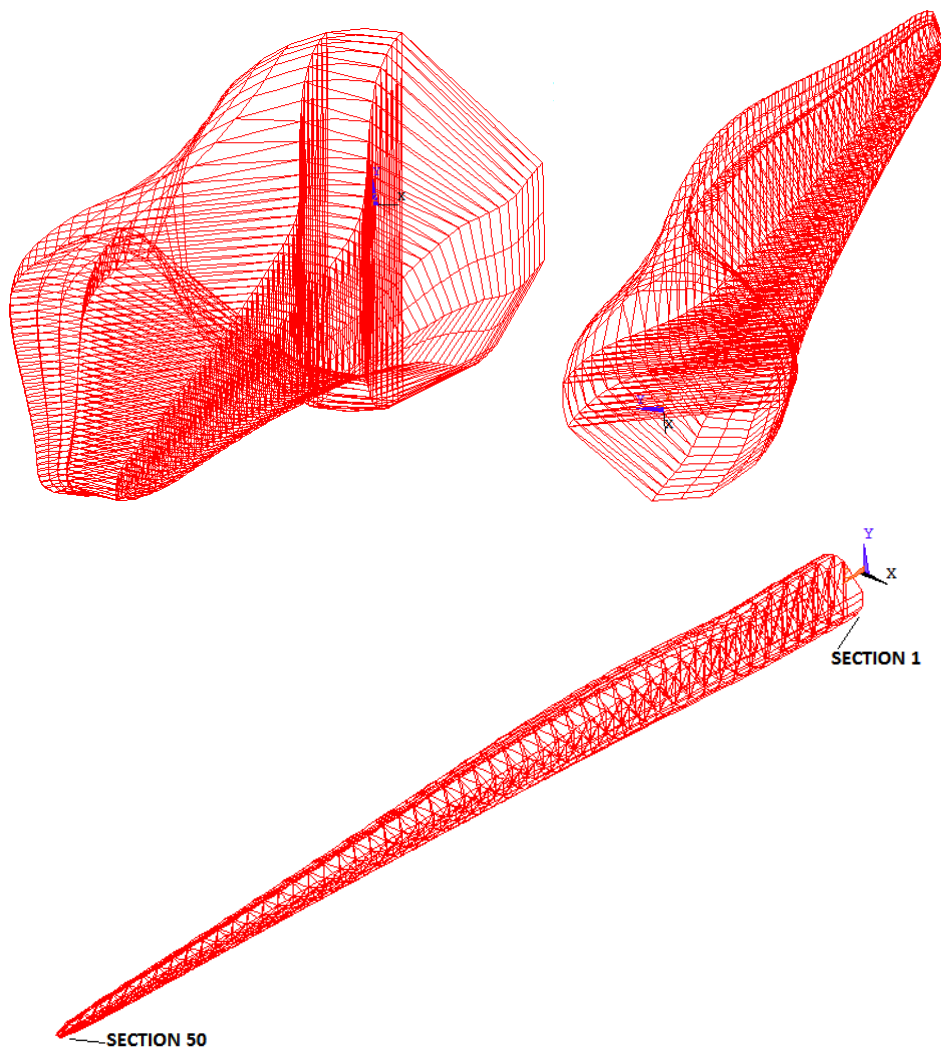


**Figure 24. 90m truss blade divided in 50 sections**

To find the optimal geometry each section is divided into five groups of beam elements as shown in Figure 25. Group 1 includes the elements running along the length of the blade (z-axis) and connects section  $i$  with section  $i+1$  (close to the edges), see Figure 26. Group 2 includes the elements which mainly reinforce the cap, see Figure 27. Group 3 consists of the elements which reinforce the shear webs in the cross direction (Figure 28), group 4 contains the elements of section  $i$  on the xy plane, as shown in Figure 29 and, finally, group 5 includes the elements of the shear web along the length of the blade, shown in Figure 30. The radius of the beams in each group from section 1 to section 50 can be degraded according to a degradation factor which is parameter of the optimization algorithm.

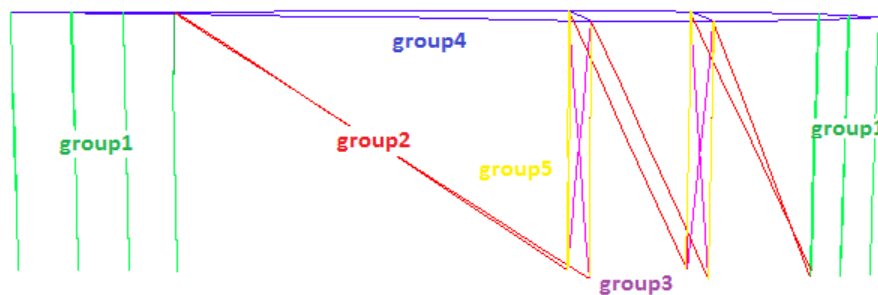


**Figure 25. Section divided in 5 groups of elements**

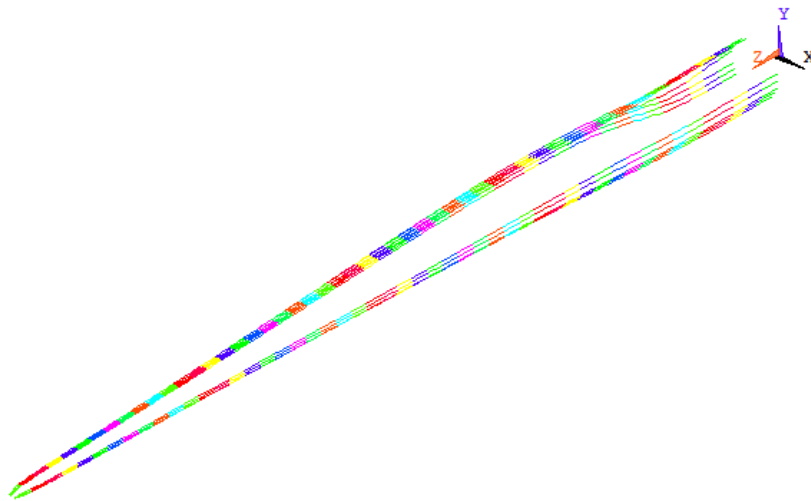


Figure 26. Group 1 elements along the blade length

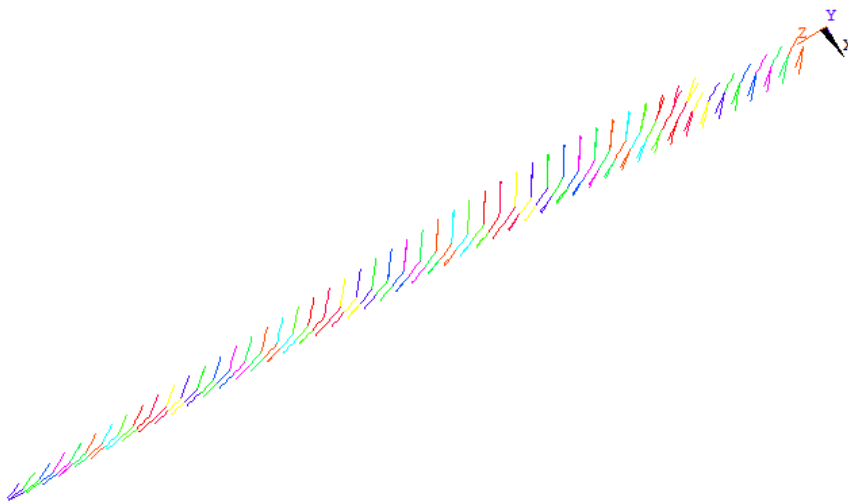


Figure 27. Group 2 cross elements of cap region

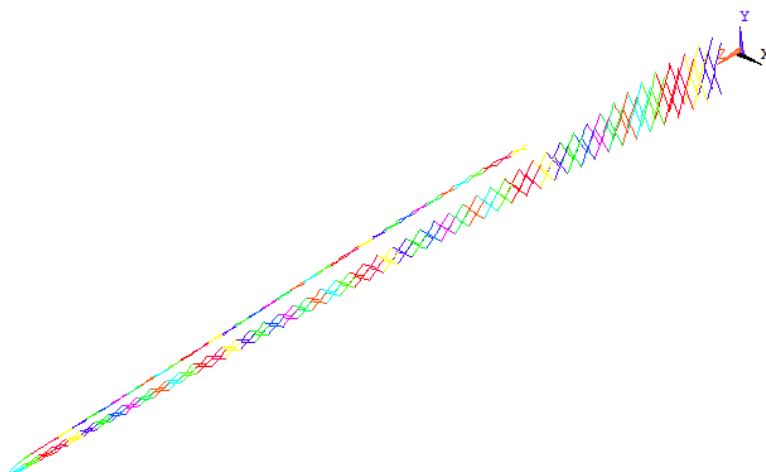


Figure 28. Group 3 elements which reinforce (form) the shear webs

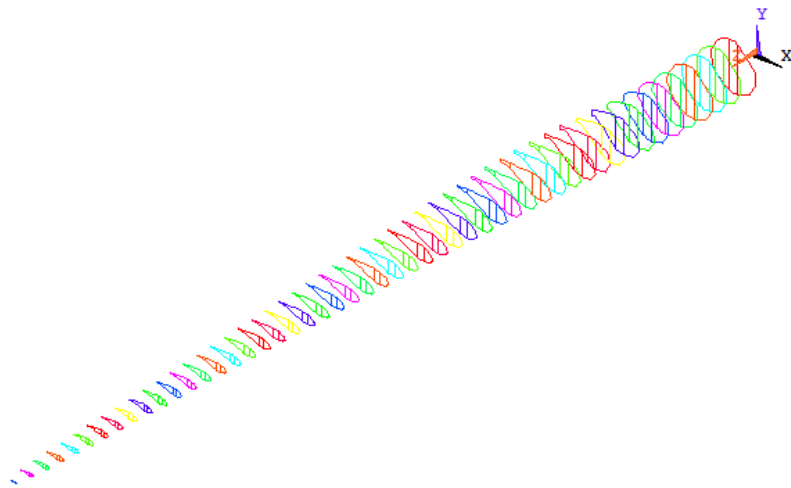


Figure 29. Group 4 elements forming the plane of each section

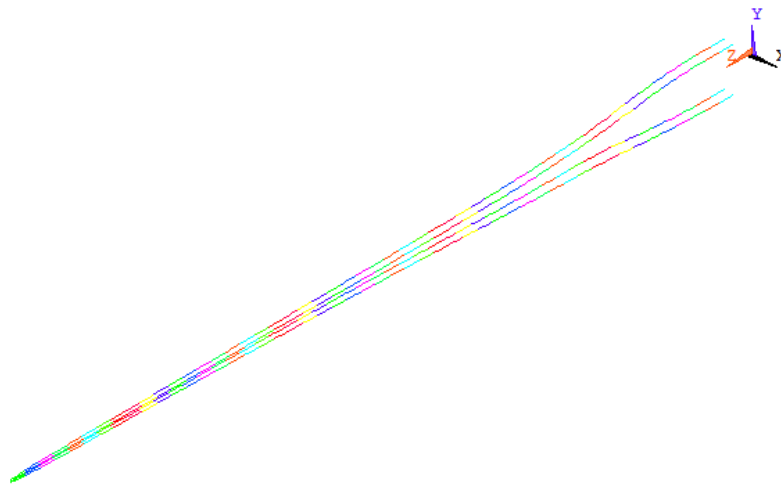


Figure 30. Group 5 elements of the shear web across the blade length

Table 8 contains the resulting values for the radius of the tubes for the five groups of elements for all the fifty sections of the blade.

Table 8. *Results for the radius of the beams with a circular section*

SECTION No	GROUP1 RADIUS (mm)	GROUP2 RADIUS (mm)	GROUP3 RADIUS (mm)	GROUP4 RADIUS (mm)	GROUP5 RADIUS (mm)
1	37.29	22.45	19.15	25.45	123.79
2	36.58	21.99	18.99	25.10	122.59
3	35.88	21.54	18.84	24.75	121.38
4	35.17	21.09	18.69	24.40	120.18
5	34.46	20.64	18.53	24.05	118.97
6	33.75	20.18	18.38	23.70	117.76
7	33.04	19.73	18.23	23.35	116.56
8	32.34	19.28	18.07	23.00	115.35
9	31.63	18.82	17.92	22.65	114.14
10	30.92	18.37	17.77	22.30	112.94
11	30.21	17.92	17.61	21.95	111.73
12	29.50	17.46	17.46	21.60	110.53
13	28.80	17.01	17.31	21.25	109.32
14	28.09	16.56	17.15	20.90	108.11

SECTION No	GROUP1 RADIUS (mm)	GROUP2 RADIUS (mm)	GROUP3 RADIUS (mm)	GROUP4 RADIUS (mm)	GROUP5 RADIUS (mm)
15	27.38	16.11	17.00	20.55	106.91
16	26.67	15.65	16.85	20.20	105.70
17	25.97	15.20	16.69	19.85	104.49
18	25.26	14.75	16.54	19.50	103.29
19	24.55	14.29	16.38	19.15	102.08
20	23.84	13.84	16.23	18.80	100.88
21	23.13	13.39	16.08	18.45	99.67
22	22.43	12.93	15.92	18.10	98.46
23	21.72	12.48	15.77	17.75	97.26
24	21.01	12.03	15.62	17.40	96.05
25	20.30	11.58	15.46	17.05	94.84
26	19.59	11.12	15.31	16.70	93.64
27	18.89	10.67	15.16	16.35	92.43
28	18.18	10.22	15.00	16.00	91.23
29	17.47	9.76	14.85	15.65	90.02
30	16.76	9.31	14.70	15.30	88.81
31	16.05	8.86	14.54	14.95	87.61
32	15.35	8.41	14.39	14.60	86.40
33	14.64	7.95	14.24	14.26	85.19
34	13.93	7.50	14.08	13.91	83.99
35	13.22	7.05	13.93	13.56	82.78
36	12.51	6.59	13.78	13.21	81.58
37	11.81	6.14	13.62	12.86	80.37
38	11.10	5.69	13.47	12.51	79.16
39	10.39	5.23	13.32	12.16	77.96
40	9.68	4.78	13.16	11.81	76.75
41	8.97	4.33	13.01	11.46	75.54
42	8.27	3.88	12.86	11.11	74.34
43	7.56	3.42	12.70	10.76	73.13
44	6.85	2.97	12.55	10.41	71.93
45	6.14	2.52	12.40	10.06	70.72
46	5.43	2.06	12.24	9.71	69.51
47	4.73	1.61	12.09	9.36	68.31
48	4.02	1.16	11.94	9.01	67.10
49	3.31	0.70	11.78	8.66	65.89
50	—	—	—	8.31	—

### Material properties

The material properties of the uniaxial glass fabric used in the INN WIND.EU reference blade are adopted herein for the truss members. The elastic properties together with the strength and density are presented in Table 9. Strength properties depicted in this table correspond to the design values and they have already been multiplied with the appropriate safety factors defined by GL [9], [2]. For simplicity reasons all the beams of the model are assumed of the same material properties and strength.

Table 9. *Material properties used for the simulations of the truss blade*

Parameter [Unit]	UNIAXIAL
$E_1$ [GPa]	41.63
$E_2$ [GPa]	14.93
$\nu_{12}$	0.24
$G_{12}$ [GPa]	5.05
$X_T$ [MPa]	396.44
$X_C$ [MPa]	283.17
$Y_T$ [MPa]	33.50
$Y_C$ [MPa]	85.69
$S$ [MPa]	25.60
$\rho$ [kg/m <sup>3</sup> ]	1915.50

### Mass

The mass of the new blade design as well as the mass of the reference blade can be seen in Table 10. In the same table the center of gravity for the proposed and the reference blade are also presented. The x, y and z axis correspond to the global coordinate system as described detailed in [2]. The proposed blade is 17% lighter than the reference one, yet, without calculating the mass that will be needed to join the beams and the mass of the fabric that will transfer the aerodynamic loads to the truss structure.

Table 10. *Mass comparison of proposed solution versus reference*

	Overall mass [kg]	C.G. z [m]	C.G. x [m]	C.G. y [m]
<b>REFERENCE BLADE</b>	42371.20	28.80	-0.16	0.04
<b>TRUSS BLADE</b>	35085.25	30.10	-0.14	0.13

### 2.3.4.2 Structural integrity verification

#### Deflection Analysis

For the static analysis the same loading case is used as the one used within the benchmark performed for the reference blade in [2]. The values of the deflection are given in Table 11 in the edge and flap direction together with the values obtained from the reference blade, with the maximum deflection naturally observed at the tip of the blade. It is observed that while the deflection in the edge direction is similar to the one of the reference blade, the deflection in the flap direction is significantly smaller. This indicates that the result of the optimization procedure lead to increased stiffness in the flap direction.

Table 11. *Deflection comparison of proposed solution versus reference*

	Ux (edge) [m]	Uy (flap) [m]
<b>REFERENCE BLADE</b>	2.322	18.529
<b>TRUSS BLADE</b>	2.066	5.202

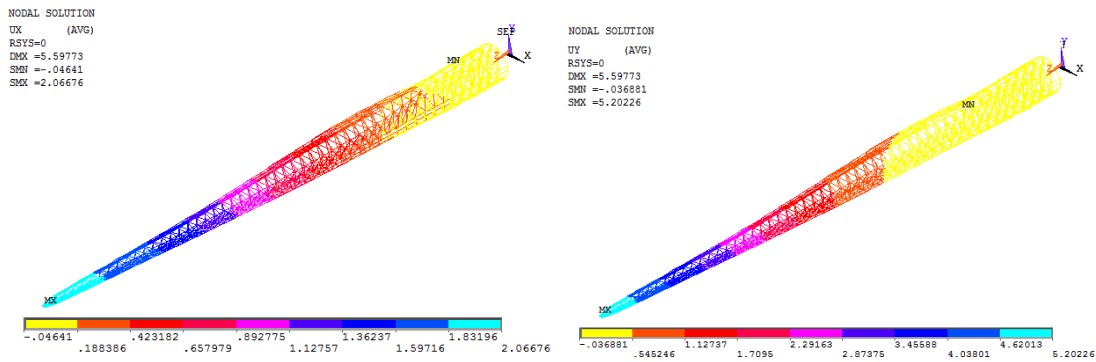


Figure 31. Deflection in edge (left) and flap (right side) directions

### Strength Analysis

Strength analysis is performed calculating the failure index according to the Max Stress failure criterion. In Figure 32 the location of all the failed elements according to Max stress failure criterion (failure index greater than 1) is illustrated. The maximum value of the failure index is 2.27 predicting failure in fiber direction due to compression approximately 23m from the root of the blade. The position of the element with the maximum failure index value is shown in Figure 33. Since the INN WIND.EU reference blade indicated a maximum Tsai-Wu failure index equal to 2.756 (using CRES calculations) [2], the current blade design is considered compliant with specifications for strength.

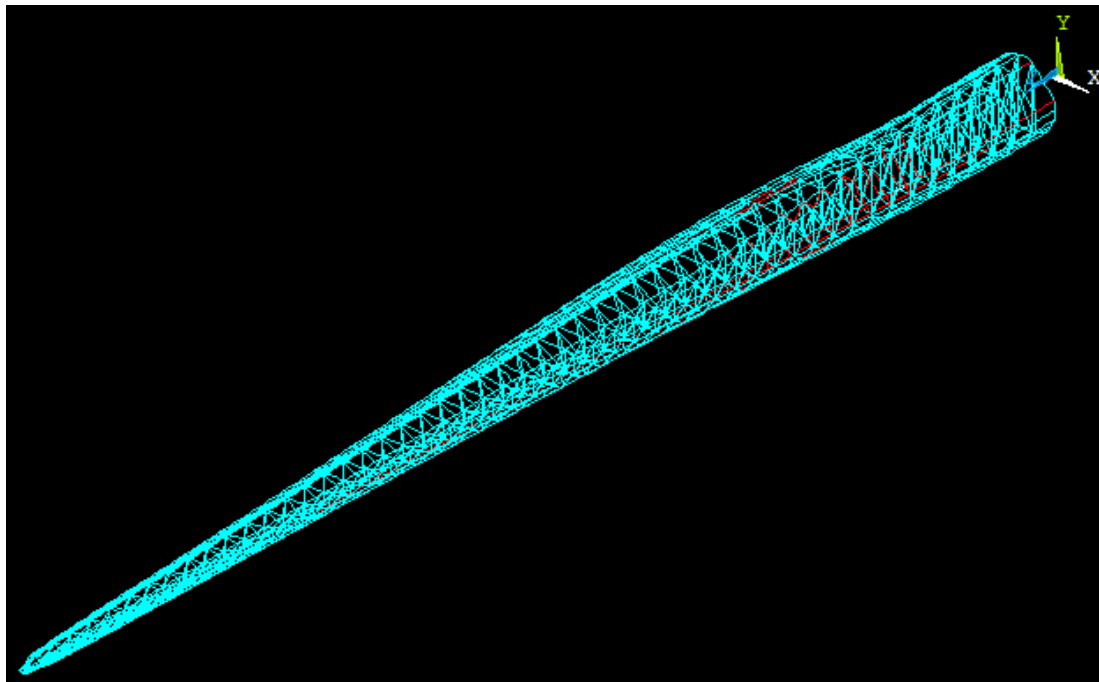


Figure 32. Failed elements according to Maximum stress failure criterion (shown in red colour)

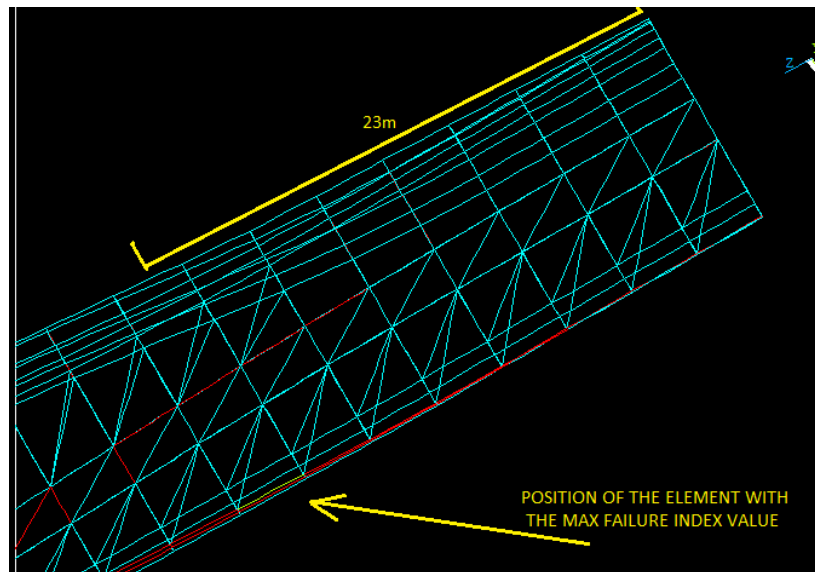


Figure 33. Position of the element with maximum failure index value (yellow colour)

### Buckling Analysis

Buckling analysis is performed considering safety factors for the stiffness properties of the composite blade. More specifically, the values of the stiffness properties of Table 9 are divided by a factor of 2.042. This safety factor is derived from [2] following GL [9] requirements. The first critical buckling load factor (BLF) is calculated equal to 0.801 while the respective eigen-mode is presented in Figure 34. A comparison with the reference blade (buckling load factor 0.875) indicates that the designed blade has a critical buckling load factor comparable to the value of the reference one. The most critical region to occur buckling is predicted close to the root (7.2m).

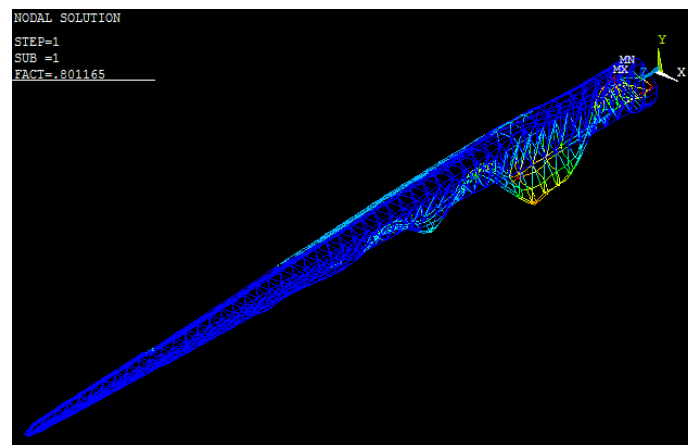


Figure 34. First eigen-mode of the proposed solution showing position of buckling

### Modal Analysis

The first six natural frequencies of the blade are presented in Table 12. A divergence is observed when comparing these results with the ones obtained for the reference blade. Further effort is needed to produce better results by adjusting the dimensions of the truss members.

Table 12. *Natural frequencies of the solution using rib reinforcement (Hz)*

MODE	TRUSS BLADE	REF. BLADE
1	0.468	0.640
2	0.619	0.897
3	1.167	1.807
4	1.248	2.686
5	1.550	3.644
6	2.019	5.469

### 2.3.5 Conclusions and recommendations

A first effort to design a wind turbine blade using a truss for the internal load carrying structure complying with strength and deflection specifications was presented. To come up with that solution for the individual truss members an optimization method was developed. The use of beam elements instead of shells and a small number of parameters (10) reduced the required computational time to solve the problem. However, this did not lead to an optimized solution for all design cases examined. The results are promising for a significant mass reduction of the blade. Yet, additional effort is needed for a more detailed design of the blade, especially in order to comply with specification of dynamic response (natural frequencies). This, nevertheless, will be conducted outside the InnWind.EU project. The simultaneous optimization constraints with respect to stiffness, strength, dynamic behaviour and buckling resistance, as well as the multitude of geometric parameters involved leads to an increased computational effort. Finally, in any case the next step of such an analysis is to go into depth regarding the joints of the truss structure. Overlooking the joint design might lead to underestimation of the blade mass, since it could be the case that the joints (and the joint strength) are design drivers.

## 2.4 Topology optimization with offset spar caps (UBRISTOL)

Within the context of the INN WIND.EU project, which aims to design next-generation 10-20MW wind turbines, UBRISTOL studied the structural efficiency of the DTU 10MW Reference Rotor Blade and developed a framework to improve its structural design. The work performed is described in this section.

The first part of this task involves a preliminary topology optimisation of a similar blade, in order to determine the ideal topology of a large wind turbine blade, subject to a variety of loads. Next, structural efficiency methods are introduced, and the structural efficiency of the DTU-10MW Reference Rotor Blade is assessed.

A design modification to the blade design, based upon the results of the structural efficiency analysis together with previous topology optimisation of wind turbine blades, is then proposed. The framework to allow a design modification to be implemented is created, and various designs are analysed. Conclusions are then drawn.

### 2.4.1 State of the art and motivation

The power generated by a wind turbine increases proportionally to the square of the rotor diameter, which explains why turbines tend to grow in size. However, the mass of the blade roughly increases with the cube of its length, which means that the blade weight grows faster than its energy output as the blade size increases [10]. Through improved design methodology, this theoretical design law is improved upon somewhat, with the blade mass of current turbines found to be growing at an average exponent of 2.3 as opposed to 3 [11]. It is thought, nevertheless, that the current blade topology may have reached maturity, and that without major changes there will be no further significant weight and cost reduction [12].

Novel lightweight designs need to be considered to satisfy the trend of growth in wind turbine size whilst minimising mass. Lightweight blade designs could not only drastically decrease blade mass but could also benefit the entire wind turbine design through decreased gravitational

loads. Indeed, although the rotor cost may only represent 20% of the total turbine cost, decreasing the mass of the blade could lead to a significant cost saving for the nacelle, tower, and foundations as well [13]. For these reasons, as the blade size increases, it becomes increasingly important to design for the highest possible structural efficiency.

## 2.4.2 Preliminary Topology Optimisation

### 2.4.2.1 Topology optimisation method

The approach undertaken here identifies novel 3D topological features from a generic medium-length blade [14] and subsequently upscales and implements them into the DTU reference blade.

Topology optimisation, also known as layout of generalised shape optimisation, is a non-parametric technique that can be used to determine the best layout to sustain loads in a given design domain for structural problems. It involves finding the features and establishing the connectivity of the domain to find the optimal material distribution [15].

In this section, 3D topology optimisation is performed on a 45 m blade from a 3 MW wind turbine. The FE-based topology optimisation has been performed using ALTAIR OPTISTRUC T [15]. The inner volume of the blade was meshed with 2.46 million TETRA4 (4-node tetrahedral) solid elements and formed the design space of the topology optimisation.

### 2.4.2.2 Materials and loads

As it is not possible to apply orthotropic properties to solid elements in OPTISTRUC T, the material properties adopted were taken as a quasi-isotropic layup of a typical high strength carbon fibre reinforced polymer with  $E = 54$  GPa,  $G = 21$  GPa, and  $\nu = 0.27$ . Despite this seemingly overconstraining limitation, relevant topologies were found that apply to orthotropic materials.

The blade loads were based on data from an industrial source and were applied as extreme individual and combined load cases. The data was available in the form of a moment distribution along the blade length for extreme forwards and reverse loads in the flapwise and edgewise directions (Figure 35). Forward flapwise bending causes compression on the suction side and forward edgewise bending causes compression on the trailing edge.

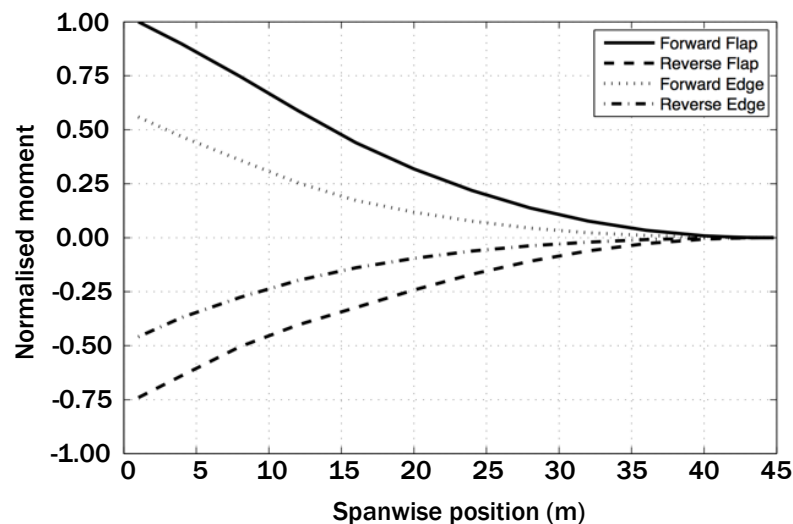


Figure 35: Normalised moment distribution for the topology optimisation analysis

A map of the combined load conditions for actual blade data is shown in Figure 36. The combined load map shows the perimeter of a cloud of data points, normalised using the maximum magnitude of moment. Seven load cases were identified for the analysis. The first four are the extreme bending moments, taken to occur independently. The other three load cases are the

extreme combined loads as shown on the load map. The load data derives from a combination of the aerodynamic, gravitational, and inertia components. This was applied in the FE model as a pressure as calculated from the moment distributions. The pressure load was then applied uniformly to both the upper and lower surfaces of the blade.

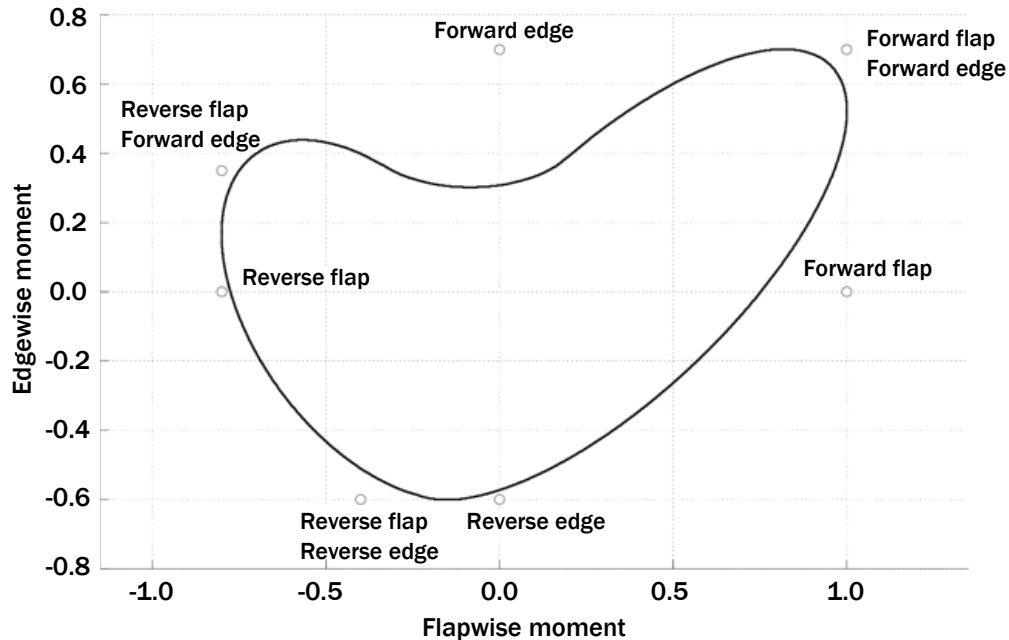


Figure 36: Normalised load cloud for the topology optimisation analysis

#### 2.4.2.3 Results of the minimised compliance formulation

Two problem formulations were used for the topology optimisation: minimised volume and minimised compliance. Only the results for minimised compliance are presented as similar results are obtained from each approach. For this optimisation, a maximum tip displacement of 9 m was applied in the flapwise direction to ensure adequate tower clearance. By setting a volume fraction constraint, this type of optimisation was found to be the stiffest for a given mass. The volume fraction was set to 12.5%, based on the volume and mass of a real wind turbine blade. The problem formulation is summarised in Table 13.

Table 13. Summary of minimised compliance problem formulation

Parameter	Value
Objective function	Minimise compliance
Volume fraction constraint	Less than 12.5%
Tip displacement constraint	Less than 9 m
Tip rotation constraint	Less than 2 degrees

A plot of the high density material is shown in Figure 37. As in a conventional design, spar caps (in red on the top surface, in yellow on the bottom surface), run along the length of the blade. Inboard, the spar caps are located near the maximum thickness of the airfoil. However, further outboard, a secondary upper spar cap forms in the outer two-thirds of the blade. The original spar cap also reduces in size, while the new spar cap grows. The overall effect is that the upper spar cap moves towards the trailing edge. This is confirmed by the minimised volume optimisation (not shown here). Additionally, a trailing edge reinforcement (TER) is seen to appear inboard, and eventually disappears at two thirds of the blade length.

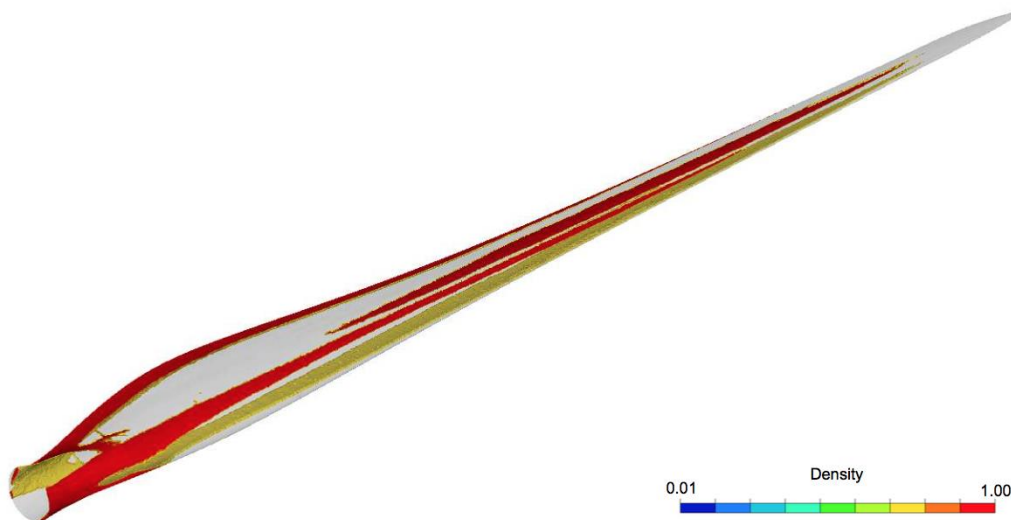


**Figure 37: Isometric view of topologically optimised blade. Element density less than 0.7 hidden.**

Figure 38 shows the top view of the blade with lower densities of material. This view clearly shows the dual spar caps, with the second spar cap offset respect to the first one towards the trailing edge. The section views at 25%, 50%, and 75% of the blade length are shown in Figure 39, which give a clearer view of the increasing offset between the upper and lower spar caps.

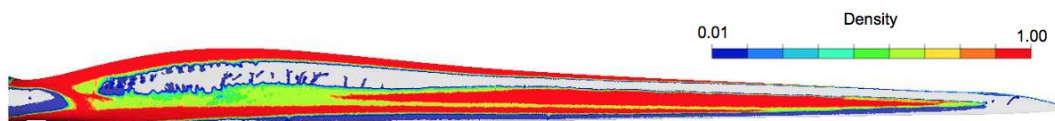


**Figure 38: Top view of topologically optimised blade. Element density less than 0.05 hidden.**

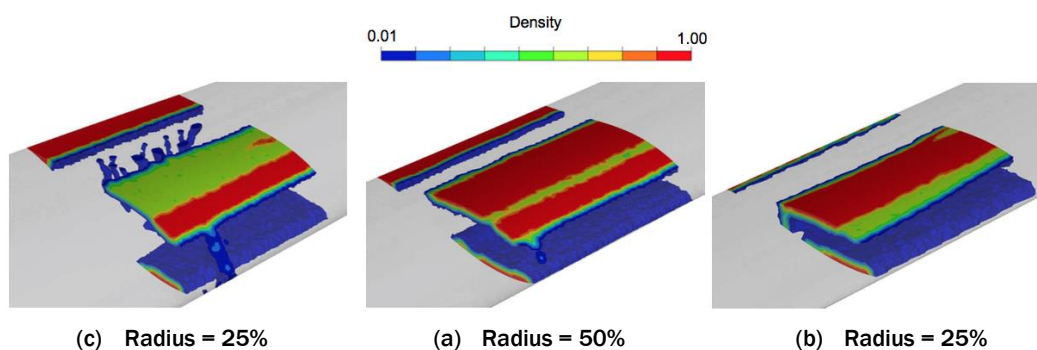


**Figure 39: Section views of topologically optimised blade, showing the progressively offset spar caps, and the disappearance of trailing edge reinforcement.**

#### 2.4.2.4 Discussion

A simple explanation for the appearance of the TER is that it increases the edgewise second moment of area. Additionally, the movement of the upper spar caps causes the centroid of the section to translate towards the trailing edge. This translation reduces the maximum distance from the neutral axis under edge-dominated loads and thereby lowers the stress at the trailing edge.

The spar caps are approximately parallel to the chord line, so the alignment of the neutral axis with the chord line means the distance to the spar caps does not vary as much as in a conventional design. The result is a more evenly distributed stress in the spar caps.

In conclusion, the topology optimisation is driven by the effort to maximise the second moment of area. The new offset spar cap topology aligns the principal second moment of area to resist the resultant moment of the combined load case. In addition to reducing the weight, the results of the topology could offer better manufacturing opportunities, although manufacturability was deliberately not considered within this deliverable.

In the next section, the structural efficiency of the DTU Reference blade is assessed and compared with a commercial blade of a similar size. The results of this topology optimisation are crucial to guide local optimisation of the DTU Reference blade, which is computationally less expensive to perform than a full 3D optimisation.

### 2.4.3 Structural efficiency analysis of the DTU Reference Blade

#### 2.4.3.1 Theory of structural efficiency

##### Structural efficiency

The goal of structural design is to produce efficient components that meet their design requirements safely. A structurally efficient design may be defined as one in which an objective function is minimised while meeting all functional requirements and constraints. The objective typically combines mass and cost, while the constraints can include strength, stability, and manufacturing requirements. The structural efficiency is determined by the choice of material and shape, so the design becomes a problem of selecting the most effective combination. Improving structural efficiency has clear benefits, such as reducing mass and material cost, while increasing performance.

The following bending convention is used throughout this report (Figure 40). In this convention, the x-axis represents the spanwise position, and the y-z plane is parallel to each section of the blade.

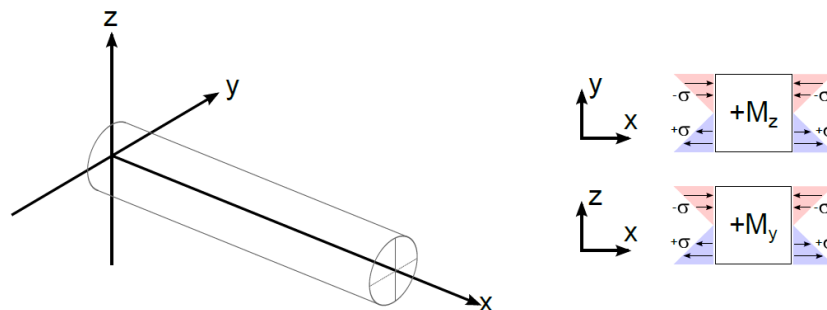


Figure 40: Bending convention

##### Shape factors

Shape factors are used to determine the efficiency of material usage in a structure [16]. They are dimensionless parameters, depending on shape and not scale, which compare the efficiency of a shaped section to that of a simple reference section of equal area, in this case a solid circular section. An efficient shape means that, for a given loading condition, it uses as little material as possible or costs the least. Structural efficiency is the ability to carry loads safely while minimising an objective, such as mass or cost.

The shape factors have been modified from those originally defined by Ashby [16] to include asymmetric bending and multiple materials. Asymmetric bending is the behaviour that occurs when a beam is not loaded along the principal axes of the second moment of area. Bending in one direction results in bending in the other, whenever the product second moment of area is non-zero; this is known as *bend-bend coupling*. Additionally, because the blade consists of layups with different materials, equivalent homogenised properties are computed, denoted by the overbar.

### Flapwise stiffness

The *flapwise stiffness shape factor* measures the efficiency of the blade for deflection in the flapwise (z) direction. This is particularly relevant for evaluating the performance of the blade for tower clearance cases. The shape factor for flapwise stiffness is given by

$$\bar{\phi}_{s,z} = \frac{4\pi M_y}{A^2} \left[ \frac{\bar{I}_y \bar{I}_z - \bar{I}_{yz}^2}{M_y \bar{I}_z - M_z \bar{I}_{yz}} \right]$$

where A is the area of the section, and the overbar denotes equivalent properties of the composite section.

### General stiffness

Although it is useful to consider the shape factor for stiffness in a particular direction, it is also important to take into account the overall stiffness of the section. A second stiffness shape factor is defined using the magnitude of the maximum deflection regardless of its direction. This is termed the *general stiffness shape factor* and is defined by

$$\bar{\phi}_{s,g} = \frac{4\pi M_{res}}{A^2} \left[ \frac{\bar{I}_{y'} \bar{I}_{z'} - \bar{I}_{yz'}^2}{M_{y'} \bar{I}_{z'} - M_{z'} \bar{I}_{yz'}} \right]$$

where  $M_{res}$  is the resultant moment applied to the section and related to the components  $M_y$  and  $M_z$  through

$$\begin{aligned} M_y &= M_{res} \cos \alpha \\ M_z &= M_{res} \sin \alpha \end{aligned}$$

where  $\alpha$  is the load angle. Figure 41 shows the load angle associated with the resultant applied moment  $M_{res}$ .

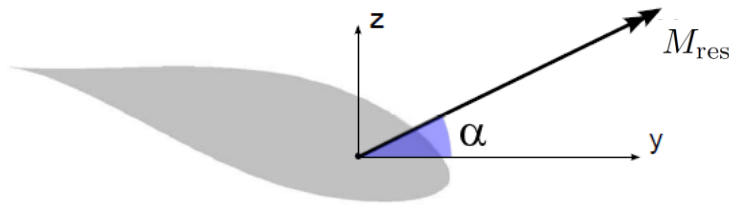


**Figure 41: Load angle defined by the angle between the resultant moment and the y-axis of the global coordinate system**

### Strain-to-failure

Finally, a strain-to-failure shape factor was derived to measure the efficiency of the structure in minimising strain, rather than maximising stiffness. This shape factor is defined as follows

$$\bar{\phi}_f = \frac{4\sqrt{\pi}}{A^{3/2}} \left| \frac{\bar{I}_{y'} \bar{I}_{z'} - \bar{I}_{yz'}^2}{\bar{I}_{z'} z' - \bar{I}_{yz'} y'} \right|$$

### Performance index

Sectional shape affects structural efficiency, but an optimal design requires selection of both shape and material. The choice of shape and material may not be simple, and two opposite designs may be equally viable solutions. For example, oil platforms can be built using sparse and complex steel space frames, or a small number of massive concrete legs [17]. When designing a structural component, the optimal material can be chosen using the material index [16], [18]. Ashby developed a method of co-selection by developing a material index that included shape, referred to as the performance index. This is particularly relevant for composite sections such as the DTU blade, as the position of each material will affect the effective stiffness of the section, even if the overall shape remains the same.

### Flapwise stiffness

By using the performance shape factor for isotropic materials and introducing effective section constants, the performance shape factor for stiffness in the flapwise (z-) direction is given by

$$\overline{M}_{s,z} = \frac{(\overline{\phi}_{s,z} \overline{E})^{1/2}}{\overline{\rho}}$$

### General stiffness

Similarly, the general stiffness shape factor is computed by

$$\overline{M}_{s,g} = \frac{(\overline{\phi}_{s,g} \overline{E})^{1/2}}{\overline{\rho}}$$

### Strain to failure

Finally, the performance index for strain is defined in the same manner, based on a critical strain-to-failure and is given by

$$\overline{M}_f = \frac{(\epsilon_x^* \overline{\phi}_f)^{2/3}}{\overline{\rho}}$$

#### 2.4.3.2 Application to the DTU Reference Blade

To assess the structural efficiency of the DTU-10 MW Reference Rotor, the cross-section stiffness properties generated by BECAS were used to generate the shape factors and performances indices outlined in Section 3.1. The data required for the analysis were the section properties, material properties, and geometry. The section data in BECAS were in a coordinate system that was aligned with the chord. Therefore, each section was rotated in order to align it with the aerodynamic twist. Modifications to the BECAS code were made in order to extract the homogenised Young's modulus, density, and second moments of area.

The results of the analysis are compared to an analysis performed on a similar large wind turbine blade. Sandia National Laboratories (SNL) is undertaking a Large Rotor Development program and have developed a 100 m blade for a 13.2 MW horizontal axis wind turbine [19], [20], [21]. Various design iterations have been produced, however the initial all-glass design, SNL100-00, is used for comparison as the DTU 10 MW blade is also all-glass. Although the SNL100-00 blade is larger than the DTU 10 MW blade, it still provides a useful point of reference.

### Flapwise stiffness

The flapwise stiffness shape factor is plotted in Figure 42 for the DTU and SNL blades with the load angle. As was defined previously, the flapwise stiffness shape factor evaluates the efficiency in

minimising the flapwise deflection arising from the application of load in a particular direction. For example, a load angle of zero ( $\alpha = 0^\circ$ ) represents a purely forward flapwise load, while a load angle of 90 degrees ( $\alpha = 90^\circ$ ) represents a purely forward edge load.

Overall, the two plots share similarities in overall trends and magnitude of shape factor. Looking at the x-axis, a characteristic *tan curve* is seen in both plots, which is a feature of the direction-specific shape factor. This phenomenon occurs when the applied load is at 90 degrees to the direction of measured deflection. Here, the shape factor becomes indeterminate near edgewise load angles ( $\alpha = 90^\circ$  and  $\alpha = 270^\circ$ ), because applying an edgewise load will result in a near-zero flapwise deflection.

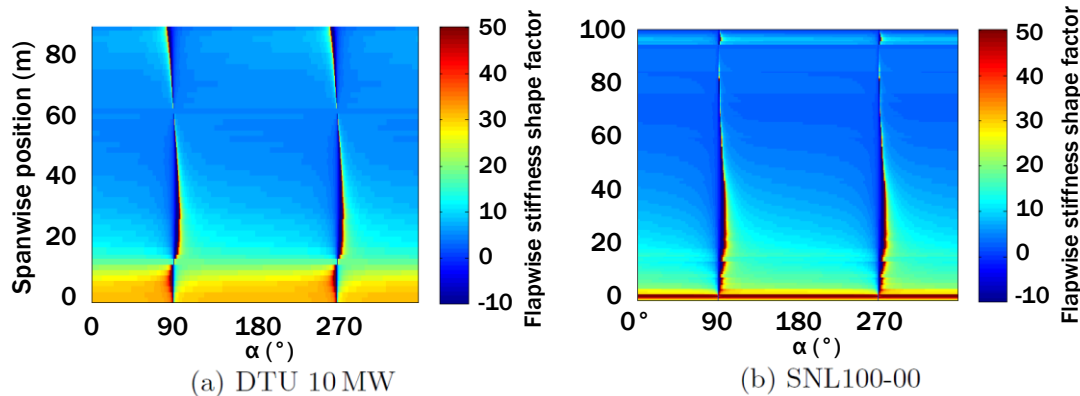


**Figure 42: Map of the flapwise stiffness shape factor**

Near the root, the DTU blade has higher shape factors for approximately the first 15% of the blade. The differences are the result of the variations between the transition from a circular root section to the aerodynamic profile as well as the differences between the start of the spar cap and webs (the webs do not appear immediately in the SNL blade). In conclusion, the reference DTU blade is more efficient at carrying loads near the root.

Further outboard, the trend and magnitudes of the shape factor are highly similar. Towards the tip, the DTU blade becomes structurally different as evidenced by different shape factors. This divergence is due to the different angles of twist between the blades in the tip region.

#### General stiffness

A *tube plot* was created to represent the general stiffness factor, shown in Figure 43. The tube plot can be thought of as a 'rolled-up' version of the map plot (Figure 44). The load angle is assigned to the angular coordinate, whilst the radial coordinate represents the magnitude of the shape factor. Finally, the axial coordinate is the spanwise position.

This plot clearly shows the axisymmetric structure of the blade near the root, which is associated with a shape factor of constant value: applying the load at different angles produces the same response.

Towards the tip, the plot becomes more asymmetric in nature. Edgewise directions ( $\alpha = 90^\circ$  and  $\alpha = 270^\circ$ ) are characterised by large shape factors, reaching a maximum at the tip. This behaviour is explained by the fact that these angles are associated with the stiffest bending direction (major principal axis). The degree of asymmetry of the plot is highly correlated to the blade geometry: as the thickness-to-chord reduces towards the tip, the asymmetry of the shape factor grows.

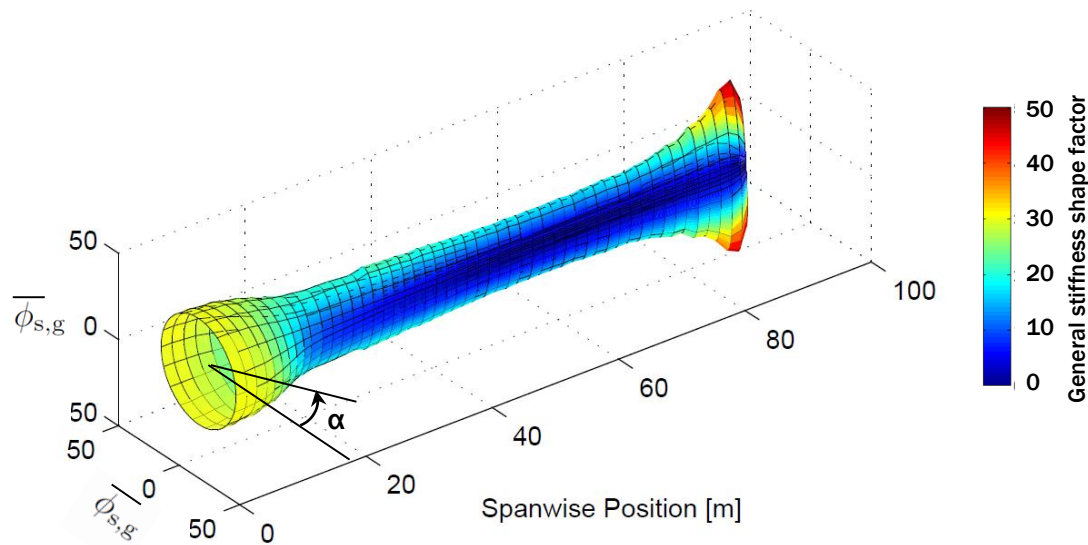


**Figure 43: Tube plot of the general stiffness shape factor. The radial coordinate represents the magnitude of the shape factor, the angular coordinate is associated with the load angle.**

The map-style plots can show more detail than the tube plot, which is more useful for a general overview of the structural efficiency behaviour. The general stiffness shape factor plots for the two blades is given in Figure 44. As with the flapwise stiffness shape factor, the DTU blade has larger shape factors in the root region, with the exception of the region immediately beside the root. Both plots show peaks in shape factors that occurs at edgewise load cases, though this occurs at decreasing values of AoA moving towards the tip.

The DTU blade has noticeably higher shape factors for the edgewise dominated load angles, indicated by the light green regions between 20 m and 80 m (not present in the SNL plot). This difference may be the result of the position of the third shear web which is located much closer to the trailing edge in the DTU blade, which leads to a higher edgewise stiffness.

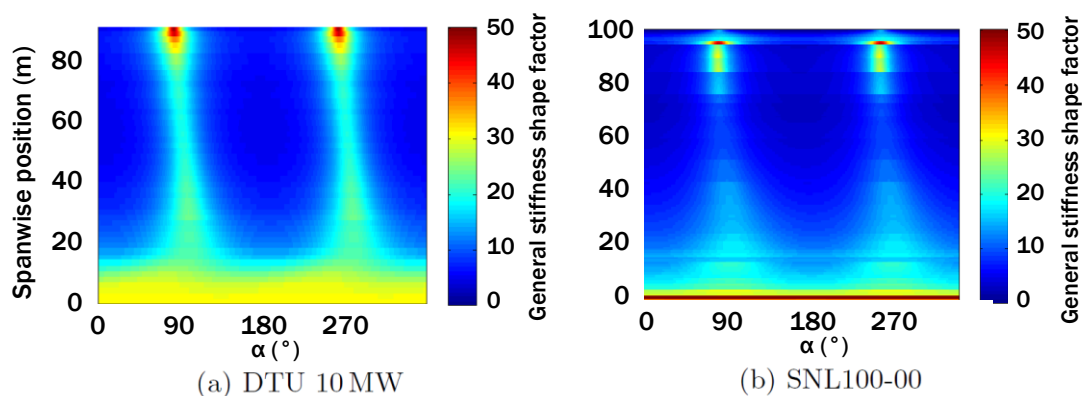


**Figure 44: Map of the general stiffness shape factor**

#### Strain to failure

The tube plot for the strain-to-failure shape factor is shown in Figure 45. In contrast to the general stiffness shape factor, the tube plot for the strain factor is more irregular. This is because the shape factor depends on the local geometry in addition to the section properties.

Similarly to the stiffness shape factor, the strain shape factor is axisymmetric in the root region. Beyond the root region, the shape factor reduces in magnitude and only increases again towards the tip. Additionally, the ‘tube’ plot is seen to rotate along the blade length. This rotation is due to the decreasing twist of the aerofoil sections with the blade length, which tends to align the principal directions of the sections with the edgewise directions of the global coordinate system ( $\alpha = 90^\circ$  and  $\alpha = 270^\circ$ ).

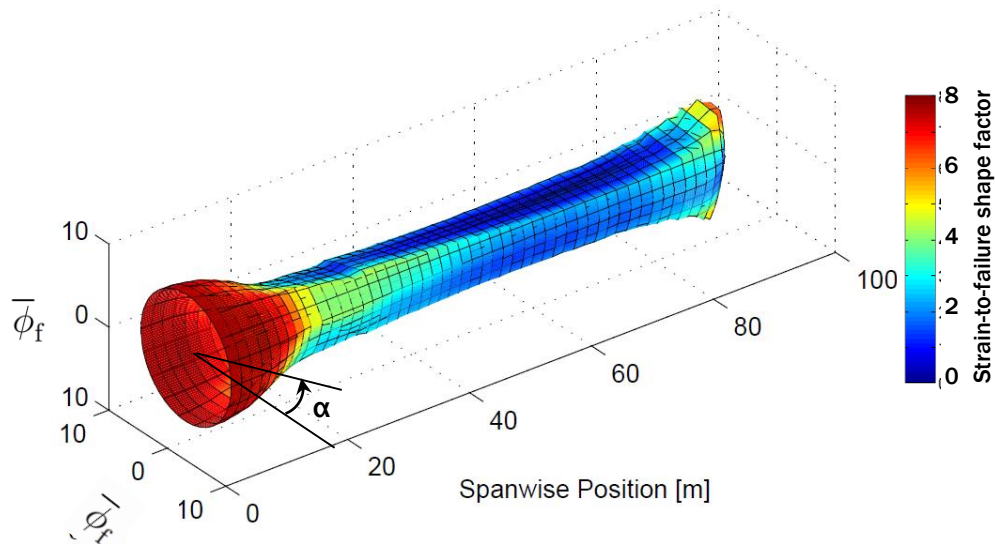


**Figure 45: Tube plot of the strain-to-failure shape factor. The radial coordinate represents the magnitude of the shape factor, while the angular coordinate is associated with the load angle.**

The strain-to-failure maps for the two blades are shown in Figure 46. The root regions are relatively similar, with both blades having large shape factor magnitudes. The SNL blade strain shape factors reduce more quickly along the blade length than the DTU blade. Further outboard, the DTU blade has generally higher shape factors, particularly for the edgewise load cases, which indicates that it is more efficient at minimising strain in these directions.

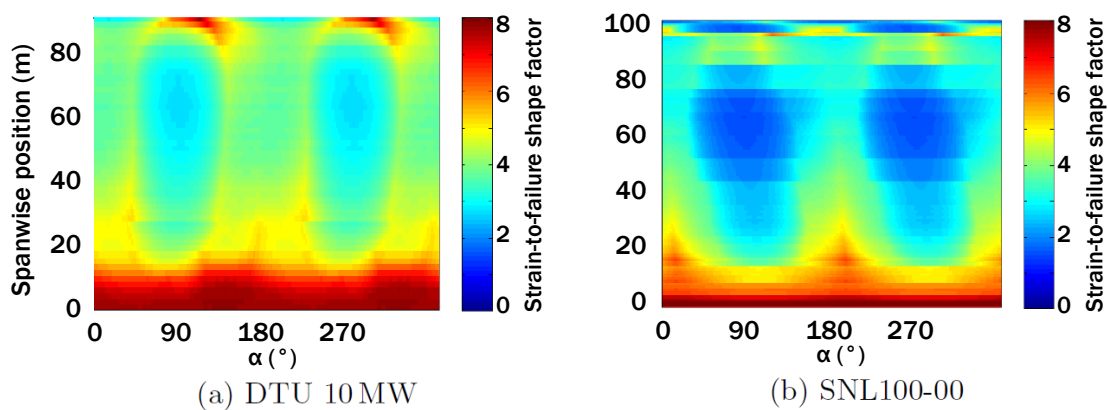


**Figure 46: Map of the strain-to-failure shape factor**

### 2.4.3.3 Performance Index

#### Flapwise stiffness

The performance index is now evaluated, with the flapwise stiffness performance index for the blade shown in Figure 47. This plot confirms that the DTU blade has a higher structural efficiency in the root region (orange area between 0 and 15 m). However, the performance index of the SNL blade is comparatively larger for spanwise positions higher than 15 m. This position coincides with the appearance of the spar caps in the SNL blade. This effect is noticeable for much of the length up to the last quarter of the blade.

These results suggest that the SNL blade sections are on the whole more efficient at maximising flapwise stiffness. As was previously shown in Figure 42, the shape factors for both blades were highly similar, which suggest that the position and use of materials in the SNL blade is more efficient than the DTU blade.

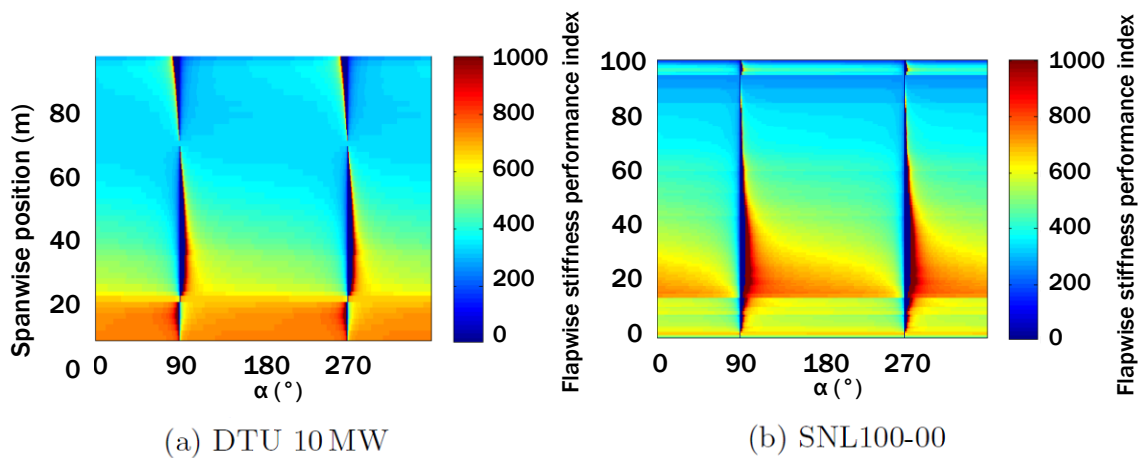


Figure 47: Map of the flapwise stiffness performance index

The tube plot for the general stiffness performance index of the DTU blade, plotted in Figure 48, illustrates better the latter argument. The placement of materials has resulted in a more uniform 'tube' that has more constant magnitudes along the blade length. The same general trends are present, but the effect of the material is seen to improve the structure at flapwise dominated load cases.

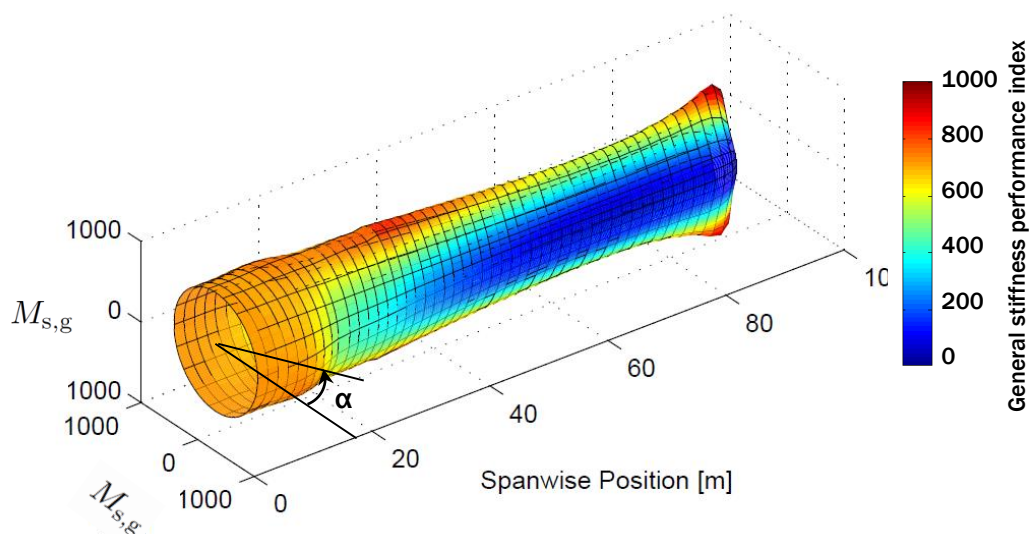


Figure 48: Tube plot of general-stiffness performance index. The radial coordinate represents the magnitude of the shape factor, the angular coordinate is associated with the load angle.

The effect of the material on the structure is seen more clearly in Figure 49. There is less variation in the performance index at a specific span position (with respect to the shape factor result). As before, the DTU blade result has a higher performance index in the root region. As with the flapwise stiffness performance index, the SNL blade has an improved performance beyond the root region. Towards the tip, the DTU blade begins to outperform the SNL blade, particularly for flapwise dominated load angles.

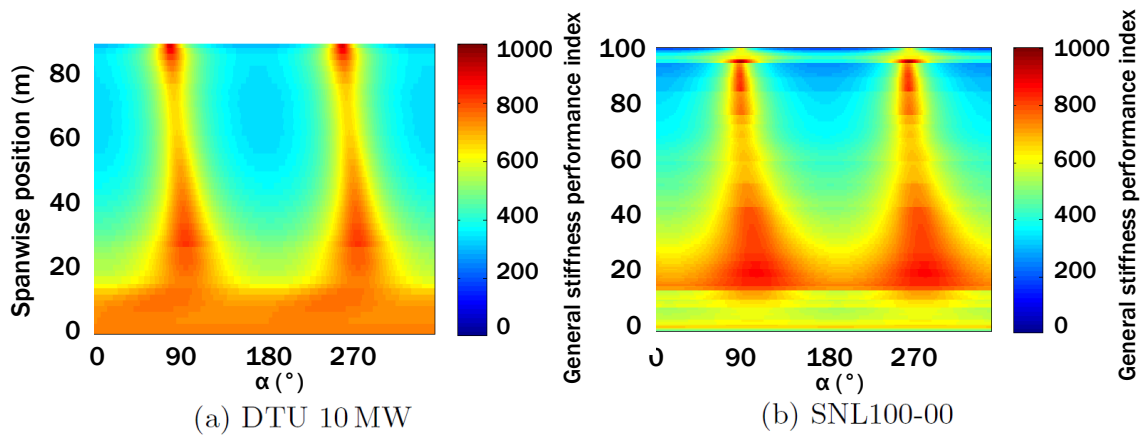


Figure 49: Map of the general stiffness performance index

#### Strain to failure

The tube plot for the strain-to-failure performance index (Figure 50) features less variation along the blade length than for the shape factor result. For the shape factor, the highest magnitude occurred at the root, before rapidly decreasing. For the performance index, the peak occurs at around one third of the blade span. This corresponds with the typical location of maximum stress. Beyond this point, the performance index decreases before briefly increasing at the tip.

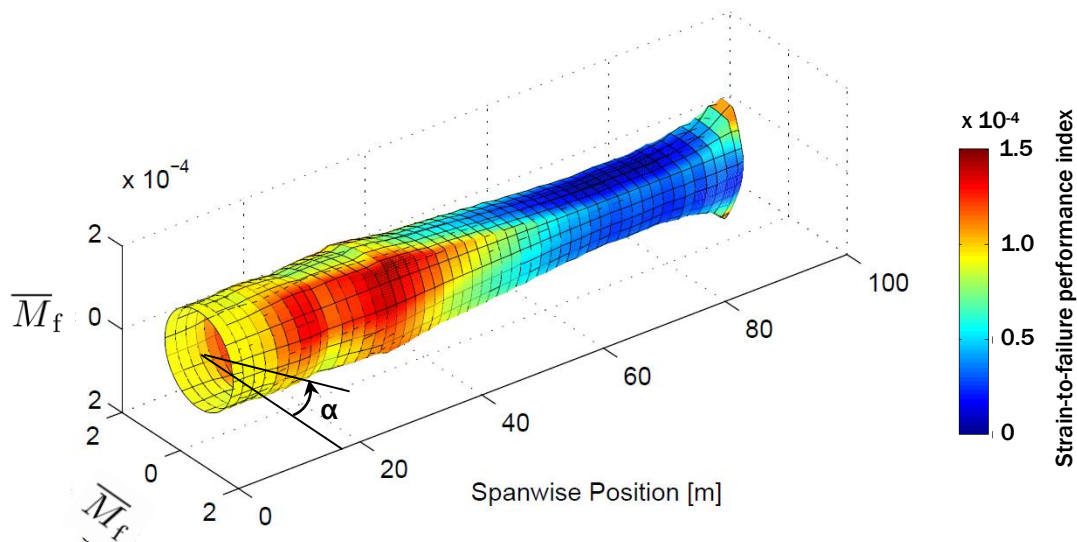


Figure 50: Tube plot of strain-to-failure performance index. The radial coordinate represents the magnitude of the shape factor, the angular coordinate is associated with the load angle.

The maps for the strain-to-failure performance index are plotted in Figure 51. In comparison to the SNL blade, the DTU blade performs better at minimising strain for most of the blade. This is particularly evident in the first half of the blade. Despite this result, the SNL blade has the maximum performance index but only in a limited region of the blade after the spar caps begin (around 15 m). The SNL blade appears to perform equally well for flapwise dominated load angles but has reduced performance for edgewise dominated loads. This may result in the SNL blade

having rapid drops in the performance index in the transition from flapwise to edgewise loads. This may be significant for combined load cases.

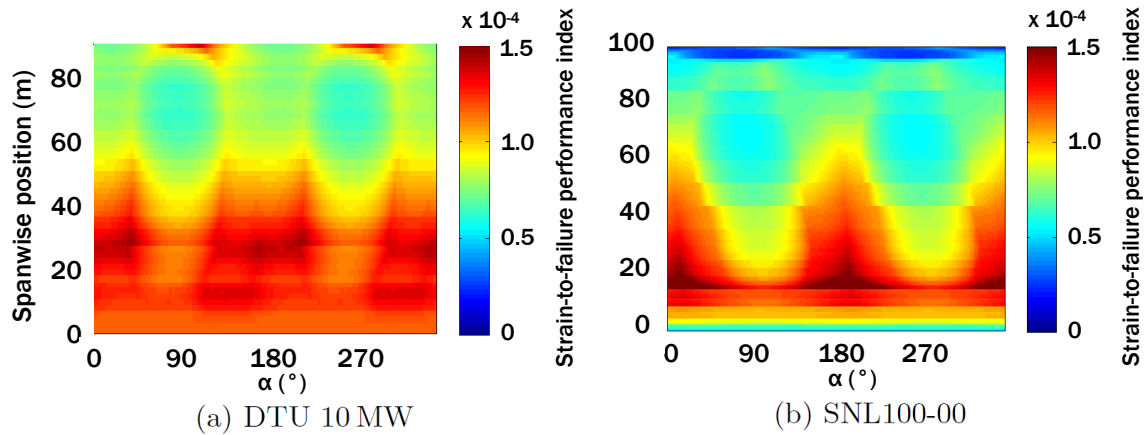


Figure 51: Map of the strain-to-failure performance index

#### 2.4.3.4 Sensitivity to load changes

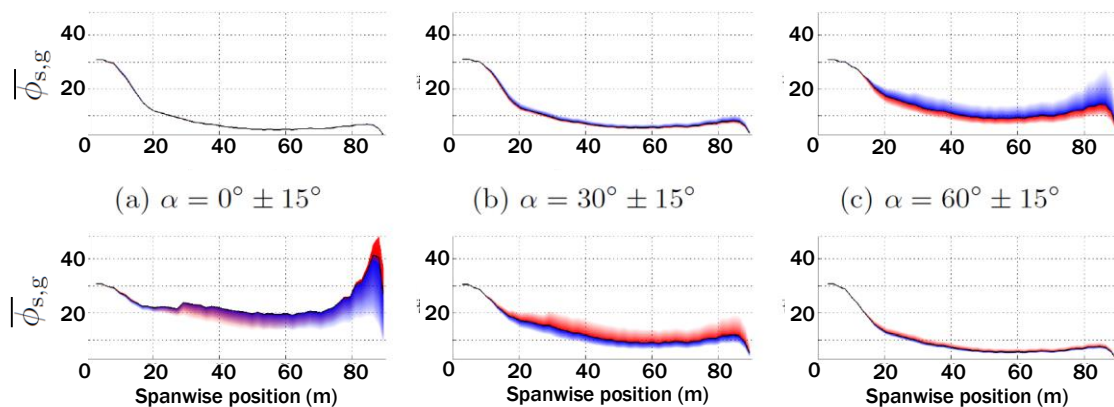
One of the benefits of the structural efficiency analysis is the ability to compute sensitivity analyses. These analyses are particularly useful to explore the sensitivity of the chosen design for load cases deviating from nominal values.

Each shape factor and performances index are plotted at various nominal load angles. Sensitivity bands are superimposed to indicate variations in shape factor or performance index for load angles of  $\pm 15$  degrees away from nominal. A red band indicates a positive change in the load angle, and a blue band indicates a negative change in the load angle. Plots with wide bands (in other words, a large variance) indicate a high sensitivity to changes in the load angle. The purpose of these plots is to be able to ascertain how the structural efficiency changes with small changes in the load conditions.

#### General stiffness

The load sensitivity for the general stiffness shape factor is shown in (d)  $\alpha = 90^\circ \pm 15^\circ$  (e)  $\alpha = 120^\circ \pm 15^\circ$  (f)  $\alpha = 150^\circ \pm 15^\circ$

Figure 52. The highest sensitivity to load change occurs around 90 degrees, or at edgewise dominated load cases, where the combined blue and red bands are the largest. This result occurs because the major principal stiffness is aligned with the edgewise direction.



(d)  $\alpha = 90^\circ \pm 15^\circ$

(e)  $\alpha = 120^\circ \pm 15^\circ$

(f)  $\alpha = 150^\circ \pm 15^\circ$

**Figure 52: Load sensitivity of general stiffness shape factor index. Red bands are associated with an increase in the load angle from the nominal value; blue bands represent a decrease in the load angle. Variance in the shape factor is given by the sum of the blue and red bands.**

The sensitivity of the general stiffness performance index to changes in the load angle is shown in Figure 53. In comparison to the shape factor results, the performance index is generally more sensitive for a wider range of angles. This plot shows that the structural sections are more sensitive to changes in load angle when the effect of material is also considered. One positive outcome of the results is that changes in the load angle do not have adverse effects for flapwise-dominated ( $\alpha = 0^\circ$ ) load cases.

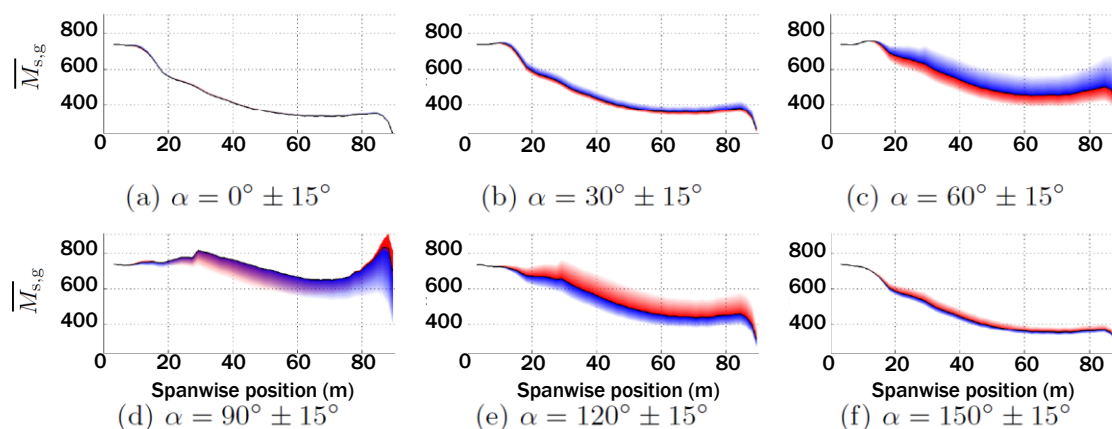


**Figure 53: Load sensitivity of general stiffness performance index. Red bands are associated with an increase in the load angle from the nominal value; blue bands represent a decrease in the load angle. Variance in the shape factor is given by the sum of the blue and red bands.**

#### Strain to failure

The load sensitivity for the strain-to-failure shape factor is plotted in Figure 54. At load angles close to  $0^\circ$  the inboard portion of the blade demonstrates noticeable sensitivity. This variation is due to the high twist and asymmetric geometry of the blade, which means the neutral axis is out of alignment with the applied load. The outboard part of the blade displays sensitivity to changes in the load angle in the vicinity of 60 degrees. The twist of the section is reduced in this part of the blade yet the direction of the load is offset from the principal directions, as manifested by large sensitivity in shape factor values. At an angle of  $120^\circ$  the blade shows significant sensitivity to changes in load angle for much of the blade span.

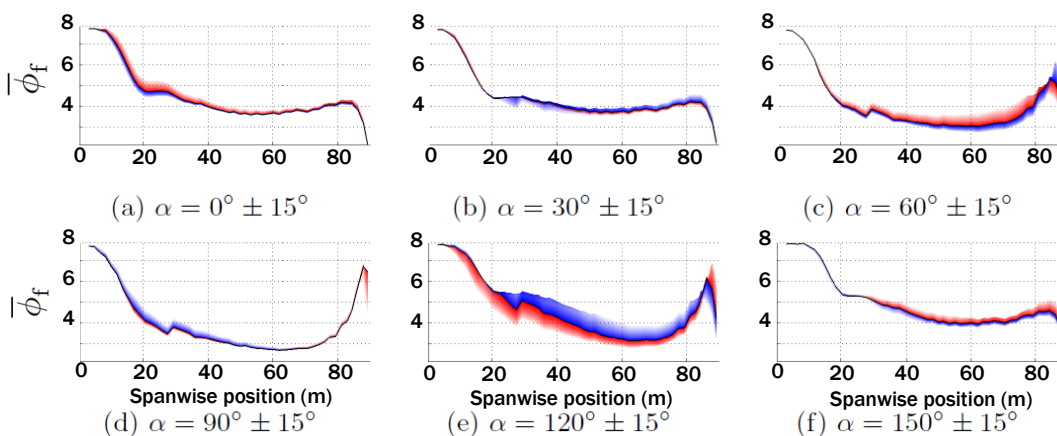


**Figure 54: Load sensitivity of strain-to-failure shape factor. Red bands are associated with an increase in the load angle from the nominal value; blue bands represent a decrease in the load angle. Variance in the shape factor is given by the sum of the blue and red bands.**

The load sensitivity for the strain-to-failure performance index is shown in Figure 55. Although the profile of the shape factor varies significantly along the span, the sensitivity of the performance index appears to remain relatively similar to that of the shape factor. This result indicates that, in this instance, the shape of the section is dominating the sensitivity of the structural efficiency, with little effect of material choice.

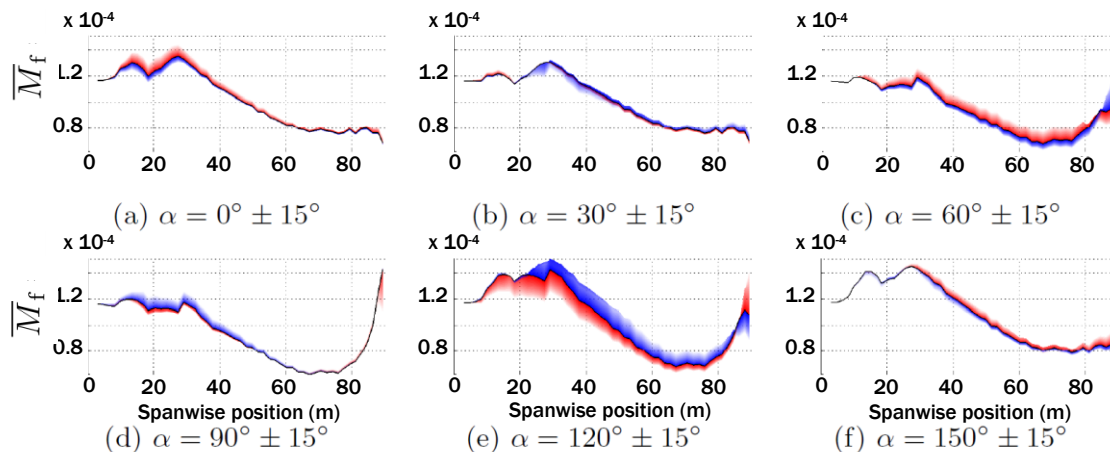


**Figure 55: Load sensitivity of strain-to-failure performance index. Red bands show an increase in the load angle from the nominal value; blue bands represent a decrease in the load angle.**

#### 2.4.3.5 Discussion

The shape factor analysis has showed that the DTU blade has particularly high structural efficiency in the root region and performs well for the remaining part of the blade, compared to the SNL blade. The flapwise stiffness results vary relatively little with load angle, yet the general stiffness results show that efficiency was greatest at edgewise dominated load cases. The fact that the edgewise dominated load shape factor is highly efficient reflects the shape of the aerodynamic aerofoil which is inherently slender. The strain-to-failure results show a similar result with high magnitudes in the root region. Further outboard, there is more variation with the load angle, with the best performing section at flapwise dominated load angles.

When the effect of material was accounted for in the performance index, the same trends were observed. Overall, the stiffness results showed less variation in the performance index for changes in the load angle. The spanwise variation in the shape factor is also different, with gradually decreasing magnitudes. For the strain-to-failure performance index, the results are significantly different compared with those from the shape factor. The first half of the blade has a consistently high performance index, which decreases in the outboard half, but with limited variations for changes in the load angle.

#### 2.4.3.6 Conclusions

The structural efficiency analysis of the DTU 10 MW Blade provided an in-depth analysis of how well the design performs, without requiring individual load cases. When compared to Sandia National Laboratories' 100m blade, the DTU reference blade was found to be more structurally efficient in terms of minimising strain-to-failure, but less efficient in terms of stiffness. In terms of absolute mass, the DTU blade is the much lighter design. The plots which show the sensitivity of the structural efficiency to change in load angles highlight the fact that a design may be efficient at very specific load cases, but the performance can change significantly with variations in resultant load angle.

## 2.4.4 Offset Spar cap concept analysis

### 2.4.4.1 Objectives

The strategy that is adopted here is to apply the knowledge gained from the global topology optimisation and the structural efficiency analysis to perform a local optimisation of the blade. An approach is taken where design modifications to the blade are explored based on the results of both topology optimisation and structural efficiency analysis. By optimising refined designs, further checks could be made in terms of realistic materials, manufacturing.

### 2.4.4.2 Pre-processing

To realise the above strategy, a process was implemented that allows a refined blade design to be readily modified. An FE blade model was first generated using Sandia National Laboratories' Numerical Manufacturing and Design tool (NuMAD). NuMAD is a versatile wind turbine design tool whereby design changes can easily be applied to a three-dimensional model of the blade, instead of constructing separate and cumbersome FEA models. NuMAD then creates an input file based on the chosen design that is then imported into ANSYS, a commercial FEA analysis package.

In this analysis, manual design changes were applied to NuMAD. Future work could include implementing these design changes in an automatic or semi-automatic manner in order to construct an optimisation process of selected design variables. The following steps were taken to prepare the NuMAD software for the analysis of the DTU 10 MW Reference Wind Turbine.

#### Aerofoil data

The aerofoil data was used in the same format. The only necessary change was to ensure the way in which the trailing edge was defined was compatible with NuMAD. This is important for modelling the different types of trailing edge (flatback, sharp and round).

#### Blade properties

The blade geometry was defined using the cubic spline representations from the Description of the DTU 10 MW Reference Wind Turbine. This data provided the chord, relative thickness, and twist. The data also provided the distance between the pitch axis and leading edge, the distance between the pitch axis and spar cap centre, and the spar caps width.

#### Laminate layups

The laminate layups, provided by INN WIND (Figure 23), were read into Matlab and checked against the published layups for the blade [20]. These layups are shown in Figure 56. For this analysis, layups and layup thicknesses are not modified; however, future work could include layup optimisation with the objective of minimising mass.

One incompatibility with NuMAD and the DTU blade was the number of layups that could be used. By default, NuMAD only allows for up to 1000 layups to be defined; however, this was judged to be insufficient for the present case. The maximum number of layups was modified in the NuMAD code, to account for the large number of sections of the DTU blade.

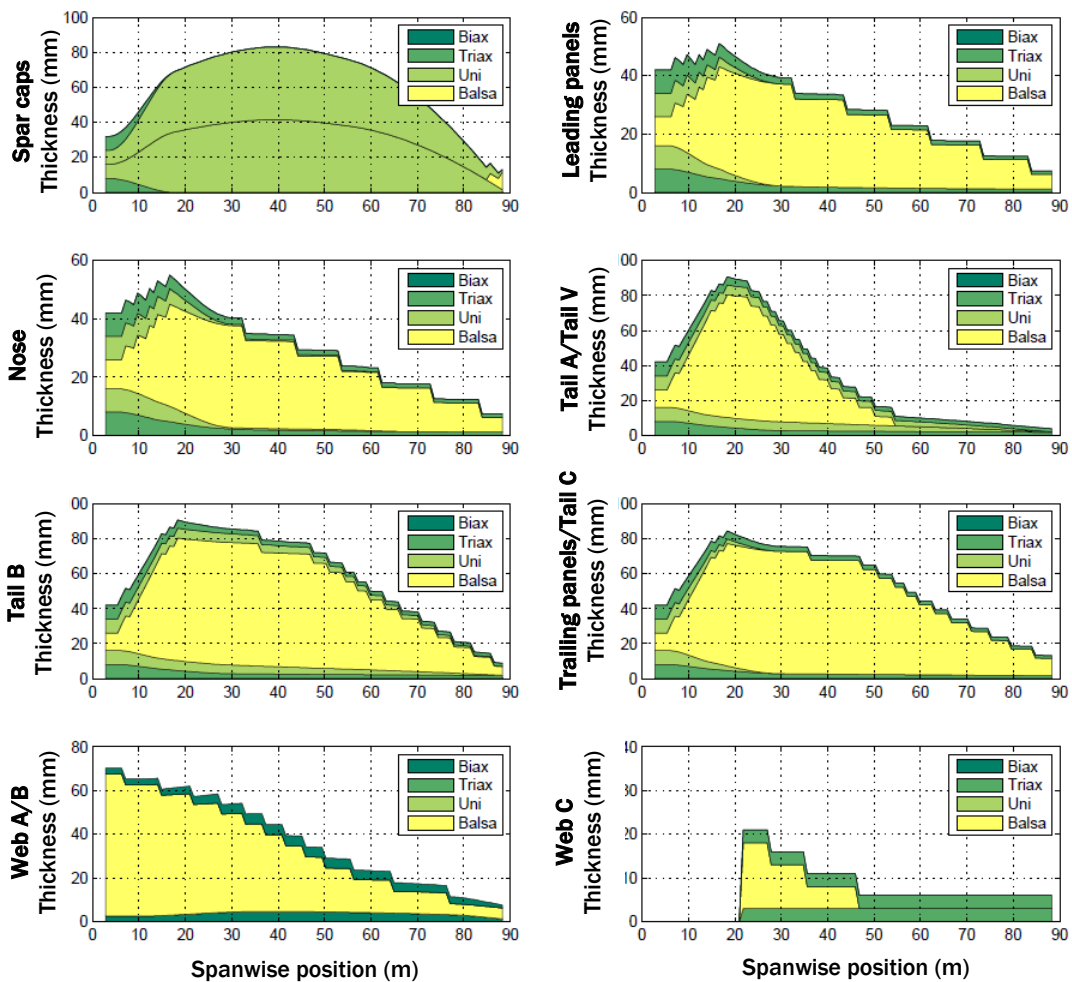


**Figure 56: Layup and thickness distributions**

### Internal geometry

The position of the spar caps was chosen as the only degree of freedom, while the remaining internal features of the blade were fixed. The reference position and width of the spar caps were constructed using cubic spline interpolation, similarly to the other blade properties.

As the spar caps initially remain perpendicular to the plane of rotation, it was necessary to find the points where the spar webs intersect the aerofoil surface to allow the spar cap edges to be defined in NuMAD. An illustration of this procedure is shown in Figure 57.

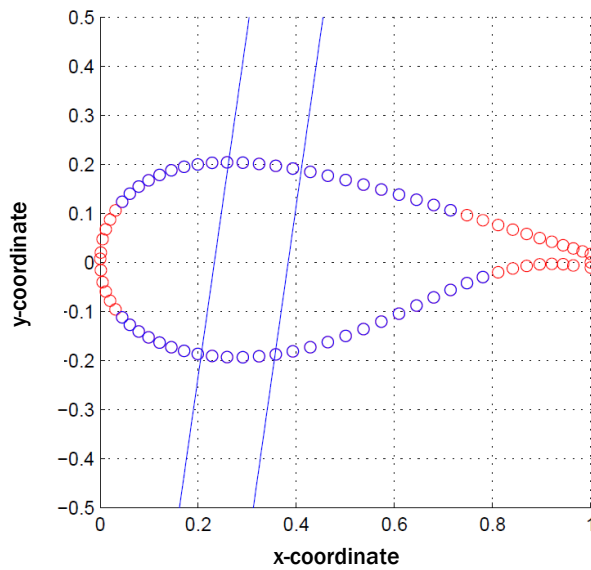


**Figure 57: Determining the position of the spar caps. The spar caps are located at the intersection between the upper and lower surfaces and the plane of rotation.**

### Material properties

Similarly to the laminate layups, the material properties were read from the text input files for the blade provided by INN WIND.

### Data flow

The data required to generate the blades in NuMAD were stored in Excel spreadsheets where designs were easily changed. These files were then imported into the NuMAD software, which creates an ANSYS input file (*shell.src*). The flow of data is represented graphically in Figure 58, where ANSYS input files have the file ending *.src*.

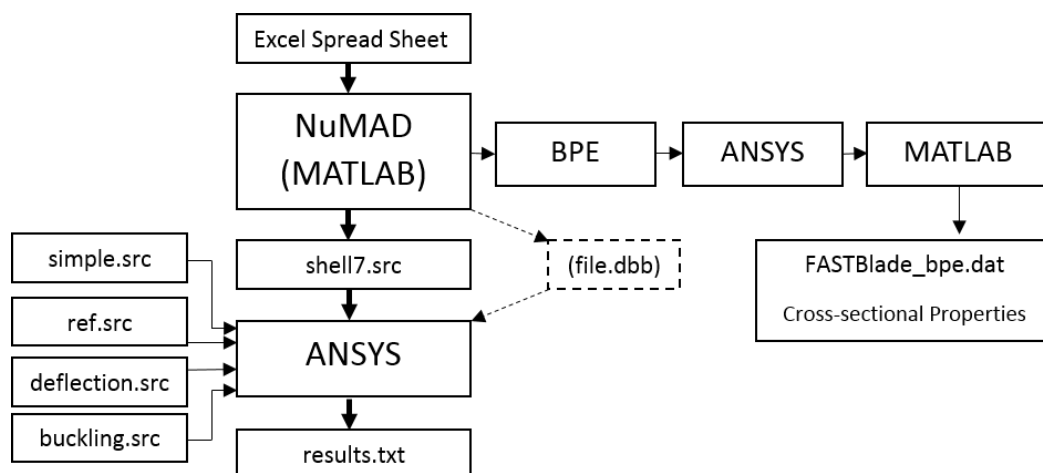


**Figure 58: Analysis flow diagram**

#### 2.4.4.3 3D blade model

The model of the DTU-10 MW Reference blade in NuMAD is shown in Figure 59. This plot shows the 101 different radial sections, defined using splining methods specified by INNWIND [1]. Each colour represents a unique layup associated with each circumferential section of the airfoil (e.g. leading edge, spar caps). The blade tip is not modelled exactly but the difference in geometry is small with respect to the real blade. This design simplification was recommended by DTU [1].

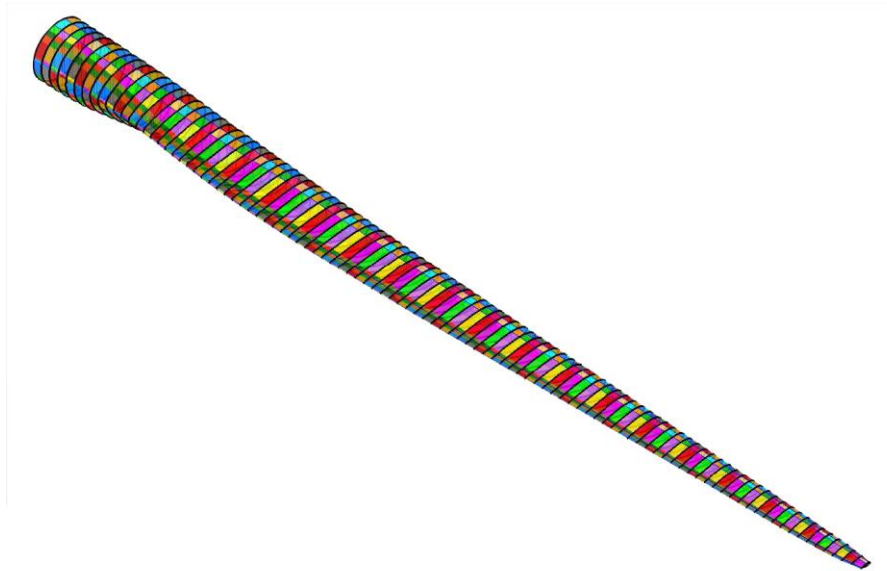


Figure 59: NuMAD model of the DTU 10MW Reference blade.

Figure 60 shows a section detail, where the different coloured lines are associated with the different layups as defined in Figure 56. The black points, referred to as *keypoints* in this report and by INNWIND [22], separate each section and are modified independently.

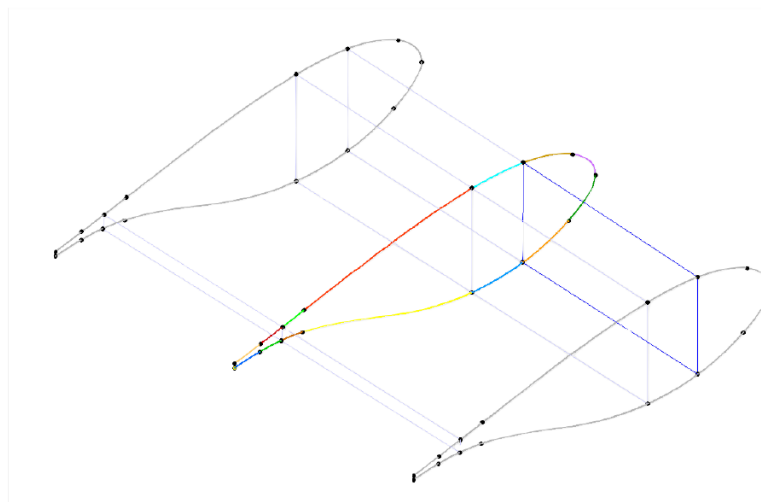


Figure 60: Blade geometry definition and representation of section keypoints

#### 2.4.4.4 Applied loads

In order to simplify the sensitivity study, the simple load case reproduced in Table 14, was used [22]. This simplified representation is statically equivalent to the reference moment distribution,

which is useful when performing sensitivity studies. Flapwise and edgewise loads are applied to nine different radial positions as shown in the following table.

Table 14. *Simple load case*

Radius (m)	Flap force (kN)	Edge force (kN)
20.07	230	-
30.44	270	-
33.03	-	290
47.71	-	180
52.03	250	-
62.39	-	130
65.85	220	-
76.21	190	18
84.85	165	25

Figure 61 shows the location of the keypoints to which the flapwise and edgewise forces are applied, using the input from Table 14. The flapwise load is divided equally between the four keypoints 5, 7, 11, and 13. Similarly, the edgewise force is split equally between keypoints 8, 9, and 10.

It is noted that the flapwise forces are applied to the extremities of each shear web, with the left shear web running between keypoints 5 and 13 and keypoints 7 and 11 forming the right shear web. The ANSYS load application file *simple.src* is defined such that the loads follow the keypoints as the move along the airfoil, rather than being applied to fixed absolute positions.

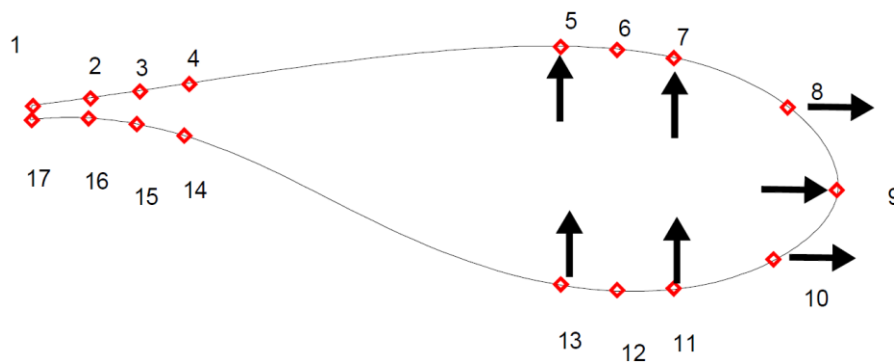


Figure 61: Location of keypoints for application of flapwise and edgewise forces

#### 2.4.4.5 Design strategy

The results of the structural efficiency assessment of the reference blade, combined with the 3D topology optimisation results of similar blades, suggested that introducing a spar cap offset could have the greatest design impact in terms of minimising the weight and improving the structural efficiency of the blade. Using this guideline, four configurations, with different variations in offset, were studied:

- 1) *Linear offset of low pressure (LP) spar cap*: the suction spar cap position is increased linearly with blade length (starting from zero offset at the root).

- 2) *Linear offset of both low and high pressure (LP and HP) spar caps*: both the suction and pressure spar cap positions are varied linearly with blade length, with the LP spar cap moving in the opposite direction to the HP spar cap.
- 3) *Constant offset on low pressure (LP) spar cap*: a constant offset is applied to the LP spar cap.
- 4) *Constant offset on both low and high pressure (LP and HP) spar caps*: a constant offset is applied to both LP and HP spar caps, with the LP spar cap moving in the opposite direction to the HP spar cap.

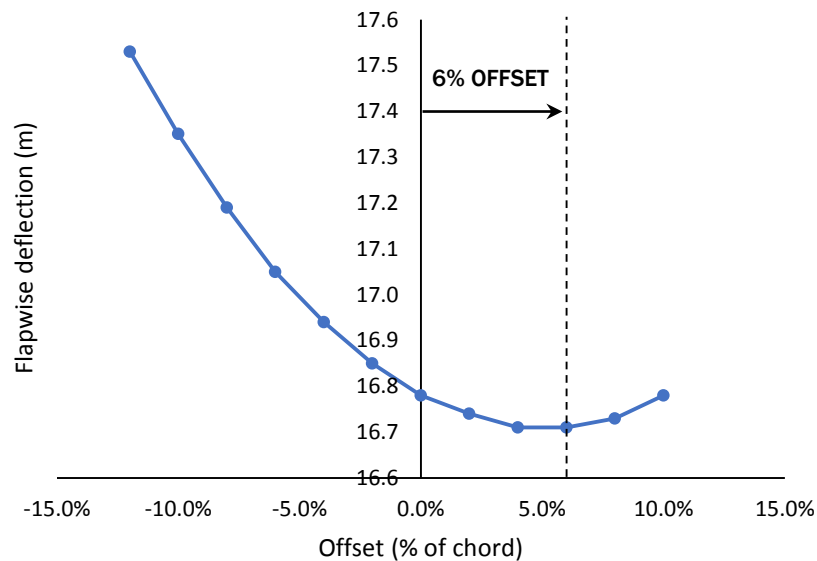
A positive offset tends to move the LP spar cap towards the trailing edge. In each case, the offset, normalized to the chord length, is measured by the relative movement of each spar cap. For example, if the LP spar cap is moved forward by 5% of the chord length, and the HP spar cap is moved backward by the same amount (configuration 4), the total offset is 10%. If only the LP spar cap is moved forward by 5% of the chord length while the HP spar cap remains fixed (configuration 3), then the applied offset is also 5%. The DTU Reference blade corresponds to 0% offset on each of the following graphs.

#### 2.4.4.6 Results

Configurations 2 and 4, outlined in the previous section are now investigated in detail, in terms of flapwise and edgewise deflections and frequencies, and blade mass. It was found that configurations 1 and 3, where the offset is applied only to the low pressure spar cap, produced results that were qualitatively similar to configurations 2 and 4, but with less improvement in performance. For this reason, the results for configurations 1 and 3 are presented herein.

##### 2.4.4.6.1 Linear offset applied to LP and HP spar cap

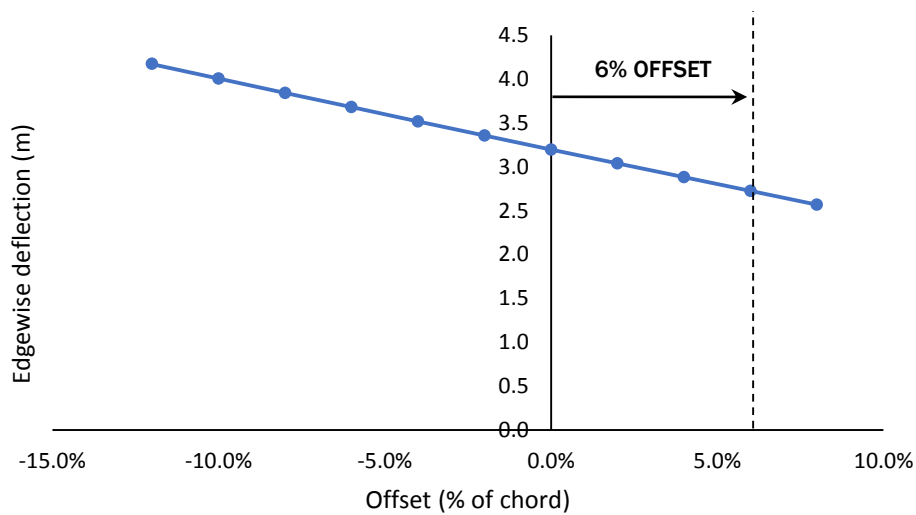
The sensitivity of the flapwise deflection to a linearly increasing offset applied to both LP and HP spar caps is plotted in Figure 62. As it stands, the DTU Reference blade is suboptimal. As the offset is slightly increased (LP spar cap moved towards leading edge), the flapwise deflection slightly decreases by 0.4% from a reference value of 16.8 m to around 16.7 m at 6% offset, suggesting that applying this offset increases the structural efficiency of the blade for this loading configuration. Figure 62 also shows that as the offset is reversed (LP spar cap moved towards trailing edge), the flapwise deflection strongly increases by 4.5% from the DTU Reference deflection of 16.8 m to 17.5 m for an offset of -12%.



**Figure 62: Sensitivity of flapwise deflection to offset, with the suggested 6% offset yielding minimum flapwise deflection.**

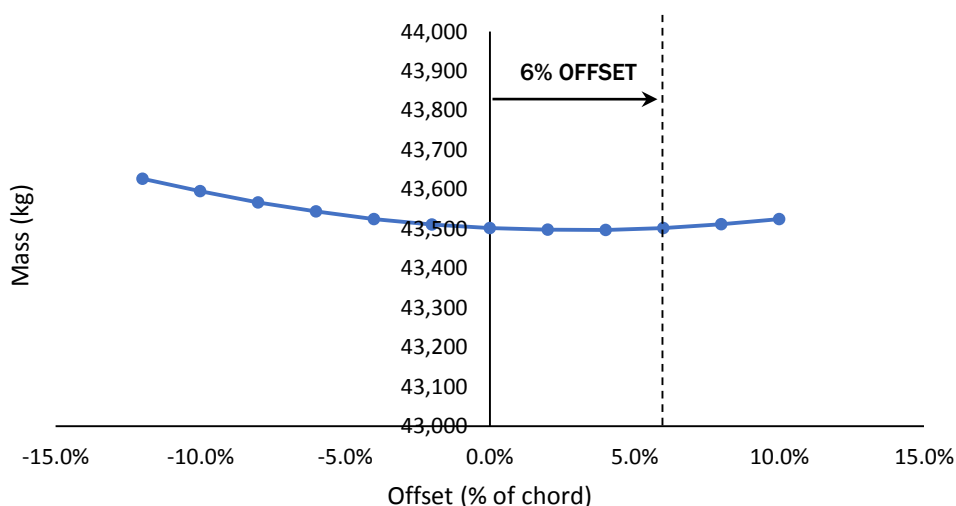
The sensitivity of the edgewise deflection to the offset (Figure 63) shows a different trend, with the deflection linearly decreasing with the offset. Applying a 6% offset decreases the edgewise deflection by 14.2%. This marked decrease in deflection is associated with the alignment of the spar caps with the resultant load. This alignment increases the effective second moment of area of the blade section in the edgewise direction, and reduces the deflection in that particular direction.

It is noted that there are decreasing returns to increasing the spar cap offset as this results in a) a decrease in the flapwise stiffness (the flapwise deflection increases again past the 6% mark), and more importantly, b) an increase in the spar web length and an associated increase in the total blade mass, which is discussed next.



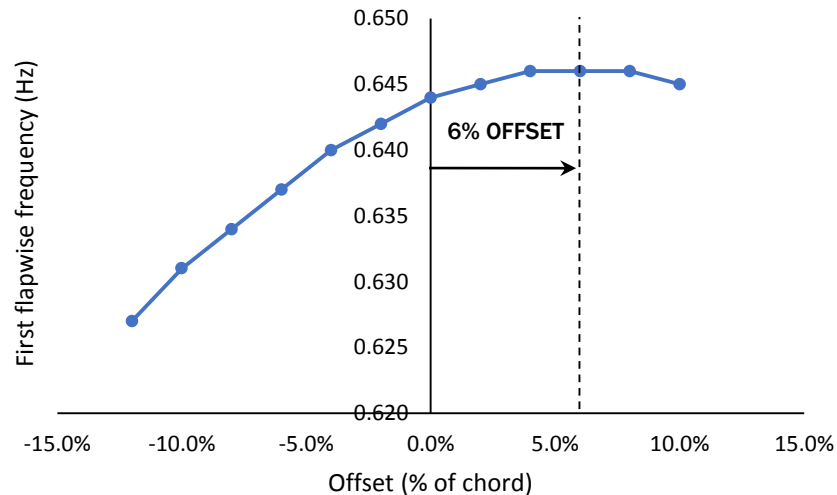
**Figure 63: Sensitivity of edgewise deflection to offset (linear offset)**

Figure 64 shows the variation in blade mass with the offset. An offset of 6% produces zero increase in mass (0.0%), therefore the stiffness gain shown in Figure 62 and Figure 63 comes at no extra (mass) cost. It is important to emphasise that this design change may incur an additional manufacturing cost, due to the complexity of designing and manufacturing a twisted spar web.



**Figure 64: Sensitivity of mass to offset (linear offset)**

Figure 65 plots the sensitivity of the first flapwise eigenvalue frequency with the spar cap offset. The increase in frequency between 0% and 6% is consistent with the lower flapwise deflection observed in Figure 62; in other words, this result confirms that the blade is stiffer in the flapwise direction with the new 6% offset design.



**Figure 65: Sensitivity of first flapwise eigenvalue frequency to offset (linear offset)**

#### 2.4.4.6.2 Constant offset applied to LP and HP spar cap

In this section, a constant offset is applied to spar caps along the whole length of the blade. Similarly to the previous analysis, a sensitivity study was conducted on flapwise deflection, edgewise deflection, mass, and frequencies.

Figure 66 and Figure 67 show the sensitivity of the flapwise and edgewise deflections to the offset, respectively. These plots are qualitatively similar to those obtained for the linearly increasing offset (Figure 62 and Figure 63); however, the effect is more pronounced. By introducing a 4% offset, the flapwise deflection decreases by 0.72% and the edgewise deflection decreases by 19.1%, while the blade mass decreases slightly by 0.032%. In other words, there is a significant return in slightly increasing the offset of the spar caps, with no or little disadvantages in terms of cost (excluding manufacturing cost).

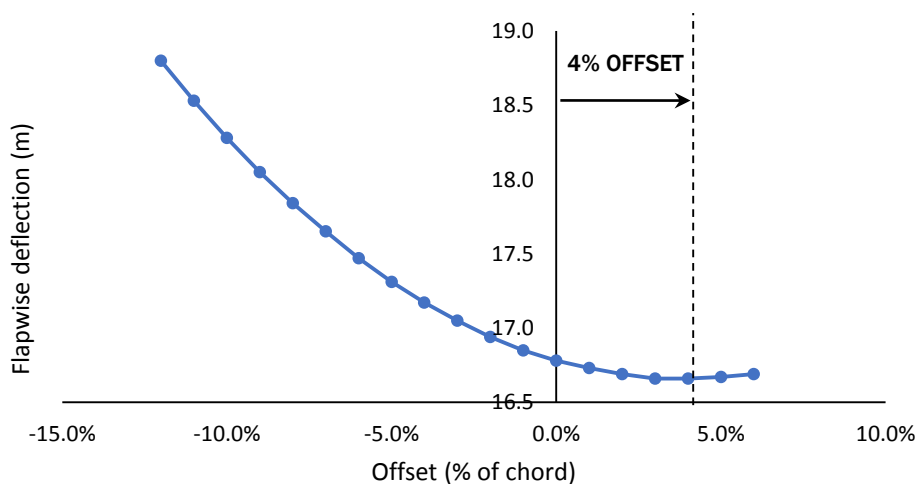


**Figure 66: Sensitivity of flapwise deflection to offset (constant offset), with the suggested 4% offset yielding minimum flapwise deflection.**

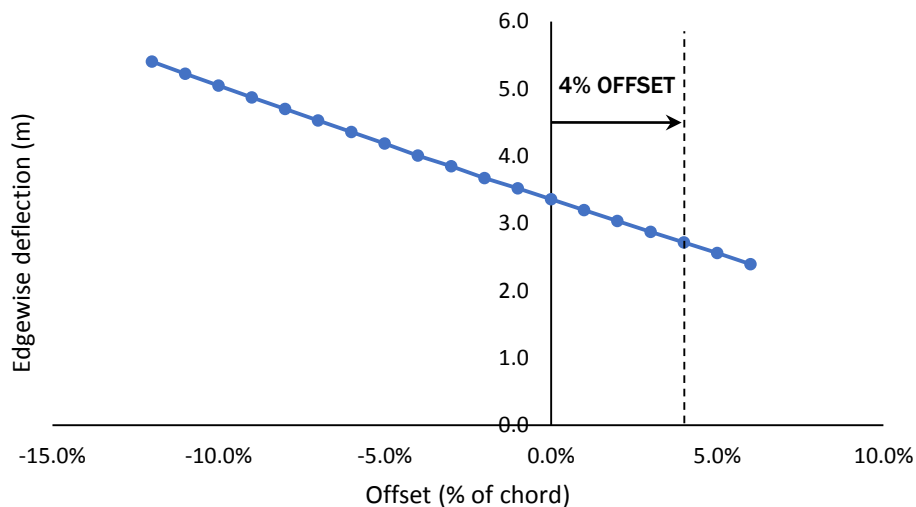


**Figure 67: Sensitivity of edgewise deflection to offset (constant offset)**

Figure 68 plots the sensitivity of the first flapwise eigenvalue frequency with the constant offset. Similarly to Figure 65, it shows a slightly higher flapwise frequency for a 4% offset (0.648 Hz as opposed to 0.644 Hz for the baseline DTU blade at 0% offset). This indicates that the structure is stiffer in the flapwise direction, as shown in Figure 66.

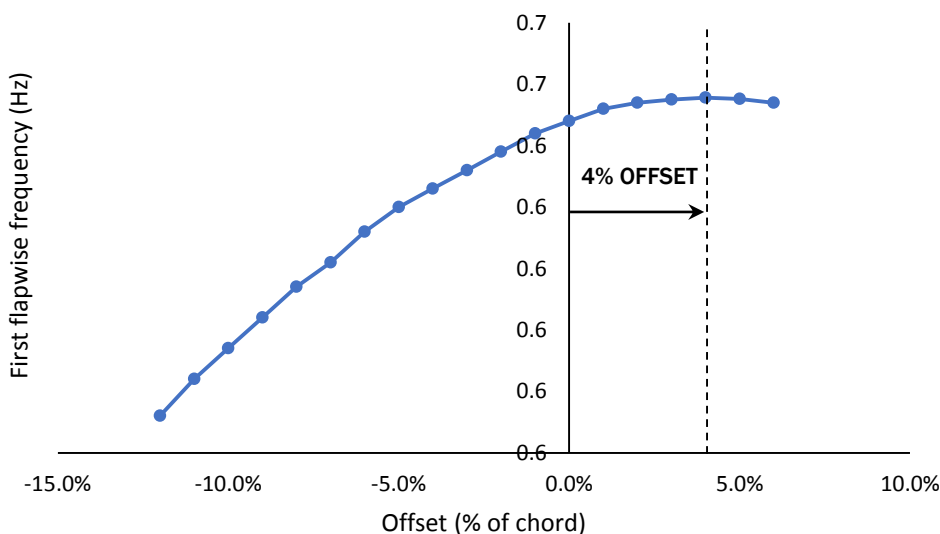


**Figure 68: Sensitivity of first flapwise eigenvalue frequency to offset (constant offset)**

#### 2.4.4.6.3 Limitations

It is noted that increasing the offset past 14% for configuration 2 (linear offset) and 8% for configuration 4 (constant offset) results in an artificial geometrical interference between the forward LP spar cap and the nose section. Towards the tip of the blade, the distance between the spar caps and the nose section reduces and increasing the offset past this value brings the spar cap past the start of the nose section, which causes a meshing error.

It is suggested, in future work, that the offset near the tip is reduced by introducing a double offset, i.e. two separate spar cap regions in the blade. The first innermost region with a constant offset

designed to minimise mass, the second outermost region with a near-zero constant offset to avoid interference between sections.

As was discussed previously, there is a significant manufacturing penalty in introducing a twisted spar cap, which would be required for either a linearly increasing spar cap offset. Implementing a single, or a double constant offset as suggested above, could minimise the manufacturing effort required to achieve this novel design.

Finally, only a simple load case was considered and this analysis may not be valid for the extensive number of load cases considered by INN WIND.EU. Further optimisation work should consider multiple load cases to represent the blade's full design life, both in and out of operation.

#### 2.4.4.6.4 Conclusions

In conclusion, two offset configurations were presented in detail, the first a linearly increasing offset, and the second a constant offset applied to the spar caps. The analysis of these new configurations, guided by the results of a generic 3D topology optimization, show how applying a spar cap offset can produce a design that is structurally more efficient than the Reference DTU Blade. For instance, setting a 6% linearly increasing offset to the spar caps results in a 0.4% and 14% decrease in the flapwise and edgewise deflections, respectively, with zero net change in blade mass. Similarly, applying a constant 4% offset reduces the flapwise and edgewise deflections by 0.7% and 19.1%, respectively, again with negligible mass change.

In future work, it is suggested to perform a local optimisation, for example using POLIMI's *Cp-max* tool, to reduce the mass of the blade, within the structural constraints outlined in the DTU Reference report [1]. It is recommended that the constant offset configuration be chosen for further investigation, as the manufacture of a straight spar (constant offset) is associated with a lower manufacturing complexity and cost compared with a twisted spar (linear offset). Finally, it is suggested to consider the option of designing multiple offsets and taking into account the complete set of load cases to further improve the structural efficiency of the blade.

## 2.4.5 Conclusions

As wind turbines grow in size to satisfy an increasing demand in wind turbine power due to economies of scale, a significant redesign of the internal structure of large wind turbine blades is needed. Blades are required to be more structurally efficient in order to curb the current trend of a cubic increase of mass. This section addresses the specific issue of structural efficiency and aims to propose a redesign of the DTU Reference Blade.

### Results

The results of the study conducted by UBRISTOL, which combines global 3D topology optimisation, structural efficiency, and sensitivity analyses, can be broadly summarised as follows:

1. The 3D optimisation study performed on a generic medium-length turbine showed that the optimal wind turbine blade consists of offset spar caps and a trailing edge reinforcement. These features are not reflected in conventional wind turbine blade design, including the DTU Reference Blade. It is suggested that applying this design strategy leads to a blade with higher structural efficiency.
2. The structural efficiency of the DTU Reference Blade was mapped using metrics such as shape factors and performance indices. The performance of the Reference Blade was compared with a similarly sized blade, the SNL100-00. Efficiency analyses show that while the DTU Reference Blade was structurally more efficient in terms of minimising strain-to-failure, it was less efficient in terms of maximising stiffness. Moreover, although the current blade design is highly efficient for specific load cases, its performance is significantly altered when considering changes in loading angles, as shown by the sensitivity studies. These results suggest that the DTU Reference Blade is suboptimal and can be further optimised.

3. Based on the insight and conclusions gathered from the 3D optimisation and the structural efficiency analyses, a local optimisation of the blade was performed by applying an offset to the spar caps. Two configurations were detailed in particular: a linearly increasing and a constant spar cap offset. Results show a significant decrease (>15%) in edgewise deflection, as well as a less substantial decrease (<1%) in flapwise deflection, at negligible mass cost.

### **Recommendations**

Introducing a spar cap offset as an alternative wind turbine blade concept proves to be a relatively simple and cost-effective solution for improving the structural efficiency of the blade. For the given load case this study found that applying a 4% constant offset to the spar caps generates a significant improvement in stiffness at no extra mass cost, while keeping incurred manufacturing costs low. A blade concept with a single or multiple constant spar cap offsets is recommended as the most effective solution.

It is recommended to pursue this solution further by performing optimisation work on the selected concept design using POLIMI's *Cp-max* tool, taking into account the structural constraints and the combined load case scenario detailed by DTU. Based on the results contained in this study, there is significant scope in optimising the DTU reference blade, with the aim of reducing its mass and achieving high structural efficiency.

### 3 STRUCTURAL SOLUTIONS WITH BUILD-IN COUPLINGS

In the present section solutions with build-in couplings are presented to achieve passive load alleviation.

For the structural solutions in the present section the external geometry is that of the DTU 10MW reference blade [1]. Thus, the length of blade, chord, twist and (section) thickness distribution along the blade length for the aerodynamic active part, as well as the location of pitch axis is kept the same as that provided in ref. [1] and used in the benchmark [2]. However, to study the effect of the coupling terms in the blade structure aeroelastic simulations are run in parallel. This allows for the estimation of the loads on the blade and the wind turbine and the evaluation of the proposed concept.

Solutions are presented by PoliMi, UBRISTOL, DTU and CENER. Each of the contributing partners provides a different solution for the structural design of the blade aiming to introduce passive load alleviation while maintaining the power output and thereupon reduce the cost of the wind turbine components, and thereupon the cost of wind energy generation.

The solution presented by PoliMi is based on designing the composite material within the wind turbine blade in such a way, in order to take advantage of the bend-twist coupling terms of the material to reduce the loads in the wind turbine by the passive response of the blade. The solution presented describes the output of the structural design which was performed assuring compliance with the design constraints of natural frequencies, stiffness and strength, including fatigue strength. In essence this forms a complete solution which enables evaluation of the cost at the wind turbine level.

The solution studied by UBRISTOL is based on the same concept of introducing bend-twist couplings, yet in this case, the angle of the fibre orientation for the drive of the coupling is not constant along the blade length, but rather varies with the radial position. Optimized coupling behaviour is achieved in this way, yet at a higher manufacturing cost.

DTU studies three individual concepts of passive load alleviation, individually, as well as their combination. The concept involves a) the introduction of the bend-twist coupling through exploitation of the composite material properties, as for the solution of PoliMi, b) the sweeping of the blade, i.e. the change of the external geometry by “pre-bending” the tip of the blade in-plane (as opposed to the pre-bend blades where the bending is performed out of plane) and c) the design of the blade with only one shear web in order to reduce the torsional stiffness of the blade. The solutions are studied relevant to the load alleviation achieved, provided that the deflection of the blade, as well as the strength under extreme loading is kept within acceptable limits.

Finally CENER focused on the development of a tool that enables accurate prediction of the blade response in the presence of bend-twist coupling terms. The incorporation of the bend-twist coupling is performed by suitably adjusting the fibre orientation of the composite material at the spar cap, as with the previous solutions. Using this tool the blade is then designed to achieve load alleviation in comparison to the reference blade design.

#### 3.1 POLIMI's 10MW Bend-Twist-Coupling solution SC+05 (POLIMI)

##### 3.1.1 State of the art and motivation

In this project PoliMI presents a structural solution based on the so called Bend-Twist Coupling (BTC), a solution aimed to achieve a particular behavior of the blade: its structure, when loaded, deforms so as to induce a load reduction. In fact BTC implies that, when the blade bends because of increased loads, the ensuing change of twist will affect the aerodynamic loading through a change in angle of attack. Passive load mitigation by BTC can be obtained by exploiting the anisotropic mechanical properties of composite materials [23], [24].

This form of load alleviation is in principle very attractive because of its passive nature: there are no actuators which may fail, no moving parts which may wear out, and no need for sensors, all characteristics that are very interesting for wind turbines where simplicity, low maintenance and high availability are key to reducing the Cost of Energy (CoE). However, as usual in the design of wind turbines or other complex engineering systems, the benefits of BTC blades may be

accompanied by other undesirable effects, such as a reduction in power production, an increase of weight and of manufacturing complexity and thus possibly cost.

Modern approach to BTC is to twist the blade sections so as to decrease the angle of attack, the so called twist-to-feather concept [25], [26]. This method showed significant fatigue damage reduction. To analyse the behaviour of such design solution, aeroelastic simulation models have been developed where the level of coupling between blade bending and twisting was obtained by directly modifying the beam stiffness sectional properties.

In order to better understand the real benefits of BTC, in this project PoliMI has followed the approach presented in [27], where parametric studies, obtained changing the coupling, have been performed within a design framework in order to compare optimal blades which simultaneously satisfy all the design constraints.

### 3.1.2 Brief description of the concept

In order to find the optimal solution for the specified blade, a series of parametric studies is done by rotating the plies of the spar caps and/or of the skin for the whole span-wise extension of the blade. For each solution the blade design is performed with a constrained optimization-based procedure that sizes the structural blade elements by minimizing a cost function [28].

All design requirements are treated as constraints, therefore all converged solutions are viable according to the conditions that have been imposed by the designer, and therefore they could all be adopted. The design optimization software, an evolution described in [29] and [28], performs the design using a multi-level approach.

The method includes 2D finite element models for sectional characterization and analysis, aero-servo-elastic multibody models for load calculation according to certification rules, and detailed 3D finite element models for detailed stress-strain, fatigue and buckling analysis. The optimizer operates at and iterates among the various levels, so as to deliver in reasonable computational times a cost-minimizing design solution that also satisfies all desired design constraints at the finest description level, i.e. the detailed 3D model.

#### Optimization-based Multi-level Method for Blade Design

Optimization tools for rotor blades have been recently developed to aid the design process of these complex structures, and a review of the literature is offered in [28]. In this work, we use the design approach developed in [29] based on the earlier results of [28], and implemented in the code Cp-Max (Code for Performance Maximization). For computational efficiency, the design is performed as a sequence of nested optimizations that operate at various description levels of the blade: a quasi-3D "coarse" representation which is made up of a 2D FEM cross-sectional model together with a spatial beam model, and a detailed "fine" 3D FEM model.

At first, the blade structural configuration and material properties are defined. Next, the sectional structural configuration is parametrized, thereby defining the design variables, which include the thickness of skin, shear webs, spar cap, and the area of leading and trailing edge reinforcements. Such variables are defined for selected span-wise stations, and interpolated elsewhere along the span using shape functions. Sectional models are defined using either 2D finite element meshes modeling the stack sequence of plies or using equivalent panels. From the sectional models, fully-populated stiffness matrices are computed using the code ANBA (Anisotropic Beam Analysis), based on the anisotropic beam theory of [30]. The stiffness matrices obtained in this way are used for defining a geometrically exact shear and torsion-deformable beam model [31]. The resulting beam is used in a complete aero-servo-elastic model of the machine, implemented here with the comprehensive non-linear finite-element-based multibody dynamics simulator Cp-Lambda (Code for Performance, Loads, Aero-Elasticity by Multi-Body Dynamic Analysis) [32], [33].

Transient design load cases (DLCs) are simulated using the aero-servo-elastic model. The results are post-processed to determine the maximum tip deflection and to extract at a number of span-wise verification sections the envelope loads, i.e. the maximum and minimum values of the internal stress resultants. At each verification section, maximum stresses and strains are computed at a number of verification spots on the cross section from the envelope loads, using recovery relations [30] obtained by the sectional analysis with ANBA. At the same verification spots, fatigue damage is computed from the stress time histories through rainflow counting and

the associated Markov matrices. The computed maximum tip deflection and the maximum stresses, strains and fatigue at each verification spot for each verification section are enforced as inequality constraints for the optimization problem, including the necessary safety factors. A Campbell diagram of the machine is computed using the aero-elastic model. A design free of resonant conditions is obtained by constraining the placement of natural frequencies away from strong harmonic excitations; here this was obtained by simply prescribing a given minimum gap between the first blade flap frequency and the three-per-rev at the rated rotor speed, enforced as an inequality constraint in the optimization. Additional inequality constraints are defined to enforce conditions on the design variables, such as a maximum thickness rate of change to account for typical values of ply tapering. From the structural configuration of the blade and its sectional description, the total mass can be readily computed, accounting also for the non-structural mass due to surface coating, foam core, resin take-up, junction adhesive, etc. The total mass defines the cost function for the optimization problem. The optimization is run until convergence, using a Sequential Quadratic Programming (SQP) algorithm with gradients computed by finite differences. For each new instantiation of the design variables, the 2D cross-sectional analysis is repeated, generating a new blade model and hence a new aero-servo-elastic wind turbine model. For each new model, the necessary analyses are repeated to update cost function and constraints. To reduce the computational cost and minimize the number of evaluations of the full set of DLCs, which is the most expensive part of the optimization, an outer iteration is used where the loads are temporarily frozen until the blade mass has converged and all constraints are satisfied; loads are then updated at the next iteration by repeating the DLCs, as explained in detail in Ref. [28].

At convergence of the blade optimization conducted at the coarse level using 2D cross-sectional and aero-servo-elastic beam-based models, a 3D CAD solid model of the blade is generated automatically by lofting the computed blade geometry. The CAD model accounts for all blade parts including webs, web core, spar caps, leading and trailing edge reinforcements, internal skin, skin core and external skin, associated with the corresponding material properties and laminate characteristics.

Finally, a non-linear buckling analysis is performed. If buckling is detected, the core thickness is increased using a heuristic approach. The modified core thickness modifies the non-structural mass of the cross-sectional model, this way again closing the loop between fine and coarse level analyses. Based on the updated constraint conditions and updated model computed at the 3D FEM analysis level, new 2D sectional models are generated which in turn define a new beam model, and the complete process is repeated. Typically, very few iterations between the coarse and fine levels are necessary for convergence.

**Short description of structural analysis tool(s) used**

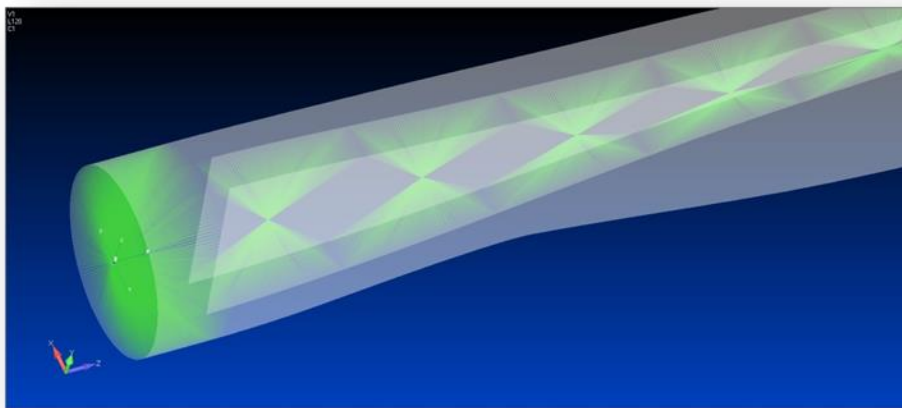
The 3D finite element model is developed in MSC Nastran 2012 format. The mesh procedure is obtained by Hypermesh while the properties definition is performed by Matlab functions. Elements are placed in mid thickness position while local lamination sequence is defined by PCOMP card. Orthotropic materials are set by MAT8 card, while isotropic materials are modelled by MAT1. Further data are reported in following table.

Table 15. *FEM constitutive elements*

Entity	Number
CTRIA3 (triangular plate element)	1196
CQUAD4 (quadrilateral plate element)	138132
RBE3 (interpolation constraint element)	29

The RBE3 elements are used to applied loads on the blade FEM model. The loads distribution is discretized and applied to 29 nodes along blade span. The RBE3 allows distributing the applied loads to elements defining the spar caps on suction and pressure side.

The first RBE3, in the root section, is also linked to all the elements, as shown in figure below. This allows to correctly redistributing the loads in the root section.



**Figure 69. RBE3 elements**

The applied constraint involve the displacements of the nodes at the blade root in direction x, y and z, while the rotations are free. This constrain set is applied for all considered analysis.

**For the analysis of the extraction of blade properties**

Sectional models are defined using either 2D finite element meshes modelling the stack sequence of plies or using equivalent panels. In this case the latter approach has been used. From the sectional models, fully-populated stiffness matrices are computed using the code **ANBA** (**Anisotropic Beam Analysis**), based on the anisotropic beam theory of [30]. From this sectional analysis code a six by six stiffness matrices and the mass matrix are obtained.

**Failure criterion used**

The failure criteria is based on the definition of a safety margin which compares the loading state in a specific point (for both stress and strain) with the allowable values defined for the material of the ply. A safety margin lower than zero means that the failure criterion is not satisfied.

**Fatigue analysis**

The RBE3 elements are used to applied static unit loads onto the structure.

The stress time histories necessary for evaluating the damage index are conveniently computed by exploiting the linear superposition of static unit load cases applied to the FE model with load histories obtained from the beam model, [34].

At each verification point, a static force or moment (in the case of shells) of unit magnitude is applied, and the full stress time history follows as:

$$\sigma_i(t) = \sum_j P_j(t) \frac{\sigma_{ij}}{P_{j,FEA}}$$

where  $P_j(t)$  denotes a load history obtained by a multibody transient simulation,  $P_{j,FEA}$  the applied unit load, and  $\sigma_{ij}$  is the static stress resultant at point i for load case j. Each time step of the loads history  $P_j(t)$ , for sake of simplicity, is discretized through the direct discretization of the internal force. This choice allows considering all the dynamic contributions included into internal forces that are provided by the multibody software. Even if the stresses  $\sigma_i(t)$  are obtained by static analysis, the effects of inertial loads and time variant aerodynamic effects are considered because they are naturally included into internal forces evaluation.

So this procedure reduces the computational cost necessary for the evaluation of the full stress time history on the comprehensive 3D FE model.

On each verification point the fatigue damage  $d_{\sigma_r}$  due to single stress component is computed according to [9]:

$$d_{\sigma_r} = \sum_{i,j,k} F_{V_k} \frac{n(\sigma_{m_i}, \sigma_{a_i}, V_k)}{N(\sigma_{m_i}, \sigma_{a_i}, \sigma_{adm}, \gamma)}$$

where  $F_{V_k}$  is given by the ratio between the time spent by the wind turbine during the entire operative life at wind speed  $V_k$  and the simulated time.  $n(\sigma_{m_i}, \sigma_{a_i}, V_k)$  is the number of cycles obtained by the rain-flow counting algorithm at mean stress  $\sigma_{m_i}$ , amplitude stress  $\sigma_{a_i}$  and wind speed  $V_k$ . The admissible number of cycles is  $N(\sigma_{m_i}, \sigma_{a_i}, \sigma_{adm}, \gamma)$ , corrected by the safety factor  $\gamma$ . From the value of  $\sigma_r$  of each stress component, a damage index is defined in agreement with [35], [36]:

$$D = d_{\sigma_r}^{2/m}$$

Considering only the longitudinal component:

$$D = d_{\sigma_L}^{2/m}$$

Where  $m$  is the inverse slope of the Wöhler curve and the longitudinal stress components is identified by indices  $L$ .

Failure is predicted if  $D > 1.0$ .

### Buckling analysis

Linear buckling analysis is performed by MSC Nastran 2012. All the dimensioning load cases used for the optimization process plus the load condition corresponding to max blade tip deflection are considered. Six eigenvalues are computed, which represent the critical load factor. A value  $> 1$  means the critical load associated to buckling is higher than the actual load.

Buckling is prevented by using balsa core in panels of skin and webs, whilst spar cap thickness is adjusted (i.e. increased) to avoid buckling all along the span.

For buckling analysis a safety factor of 2.0419 is applied reducing material capability to withstand maximum loads.

### 3.1.3 Anticipated PROS and CONS

The literature clearly shows the potential benefits of BTC. Many parametric studies have been performed using models of different levels of complexity and fidelity, yielding a good insight on what can be expected by the adoption of such a technological solution. However a comprehensive approach to the design of such complex structures is still lacking. In fact, when designing for a specific set of given conditions (e.g., rated power, wind class, rotor diameter, max tip deflection, etc.), one should be able to compare alternative solutions that all satisfy the same design constraints. Only if all alternatives are fully viable, one can then identify the one that is the most desirable according to given criteria or performance metrics. This aspect is of crucial importance in the design of blades for large modern wind turbines, given the complex couplings that exist among the various design requirements. For example, changes in bending stiffness due to fiber rotation must be compensated by increasing the thickness of spars and skin, or by using more performing materials, so as to satisfy max deflections and frequency placement constraints. However, these changes will not only influence weight, but also fatigue and buckling. In turn, the satisfaction of the fatigue and buckling constraints will again influence the sizing of the various structural members of the blade, creating a further coupling. Many other subtle effects are present: for example, different degrees of BTC will induce different mean deflected blade configurations at each mean wind speed, thereby affecting trim and hence power. To restore power to the same level, again so as to perform meaningful comparisons among different candidate solutions with different degrees of BTC, one should then change the trim pitch setting, and this will in turn modify loads, which will again induce a coupling effect in the design and can lower BTC benefits. The twist-to-feather characteristic of a BTC blade, leads to multiple benefits in terms of ultimate and fatigue loads, but at the same time, is accompanied by a higher torsion of the blade, which reflects in a lower power production. Through changing the trim pitch setting is possible to restore power to its initial value, but the potential benefits of BTC are hence mitigated.

All these aspects have been considered in the solutions presented in this project: the blades have been re-designed within an optimization design framework in order to account all these constraints. The final goal is to reduce the CoE which accounts for the mass of the blade as well as for the Annual Energy Production (AEP). All the solutions presented here are able to reduce the CoE and, in the meanwhile, some of these are also able to reduce the loads on the hub and/or on the tower. Since these components have not been re-designed in this deliverable, the real effects on the CoE of these solutions have to be further investigated.

In the following sections PoliMI presents one structural solution (named “POLIMI 10MW BTC SC+05”) which has been computed moving the direction of the unidirectional fiberglass in the spar cap away from the blade axis with an angle of 5deg. This solution has been selected between eight distinct configurations analysed with Cp-Max because it exhibits preliminarily the best CoE reduction. The other optimal blades, satisfying all the design constraints, have been obtained changing the angle in the spar cap (SC) of 3, 4, 5, 6 and 7deg and in the skin (Sk) of 5, 10 and 15deg. The following figure shows the reduction of the CoE computed preliminarily with Cp-Max with respect to the RWT.

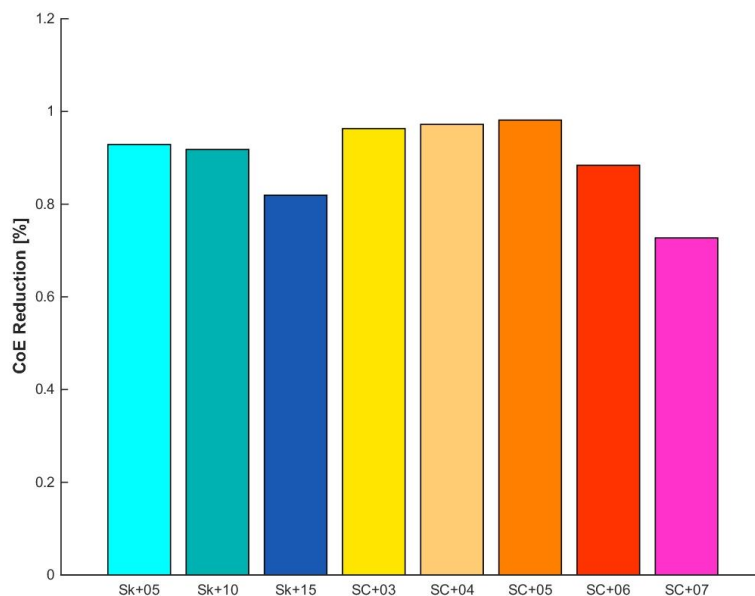


Figure 70. PoliMI BTC: CoE comparison between optimal blades

### 3.1.4 Assessment of the structural integrity of the proposed design

#### 3.1.4.1 Design layout and dimensioning

The blade structural layout uses a box-type configuration, with a single cap confined within the two shear webs. The shear webs are parallel and planar, i.e. they do not follow the twist of the airfoils. A third shear web is located at 87% of the local chord, as in the Reference wind turbine. Trailing and leading edge reinforcements are introduced to augment in-plane modal frequencies. Root reinforcement made of unidirectional fiberglass is also here used. To prevent buckling in skin and shear webs panels a sandwich with balsa core is used, while to prevent buckling in the spar caps panels the thickness of the spar caps are designed to be buckling-free.

The main blade parameters and material types used are reported in the following table, while the following figures show the adopted blade structure.

The material properties used within this task are the same of the DTU 10MW reference blade.

**Table 16. PolIMI BTC SC+05, main blade parameters and material types**

	Starting section (% span)	Ending section (% span)	Material type
Skin	0	100	Tri-axial fiberglass
Spar caps	0.025	98.12	Unidirectional fiberglass
Shear webs	0.025	98.12	Bi-axial fiberglass
Third shear web	0.22	95	Tri-axial fiberglass
Trailing and leading edge reinforcement	0.10	95	Unidirectional fiberglass
Root reinforcement	0	30	Unidirectional fiberglass

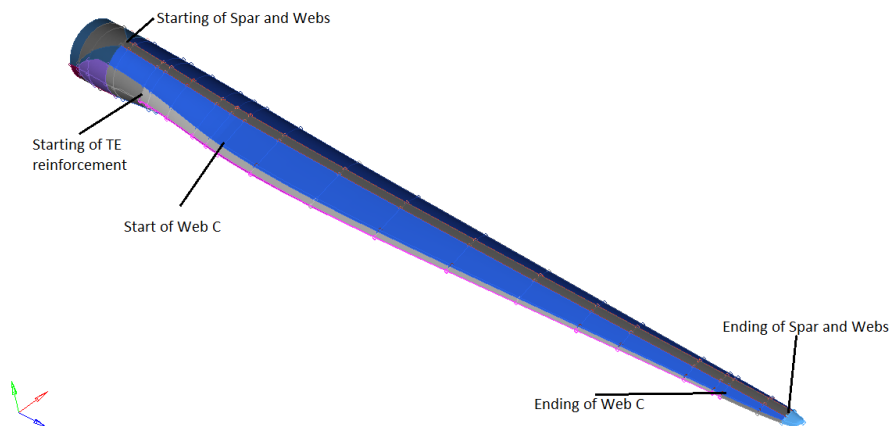


**Figure 71. PolIMI BTC SC+05, structure of the blade and position of constitutive elements**

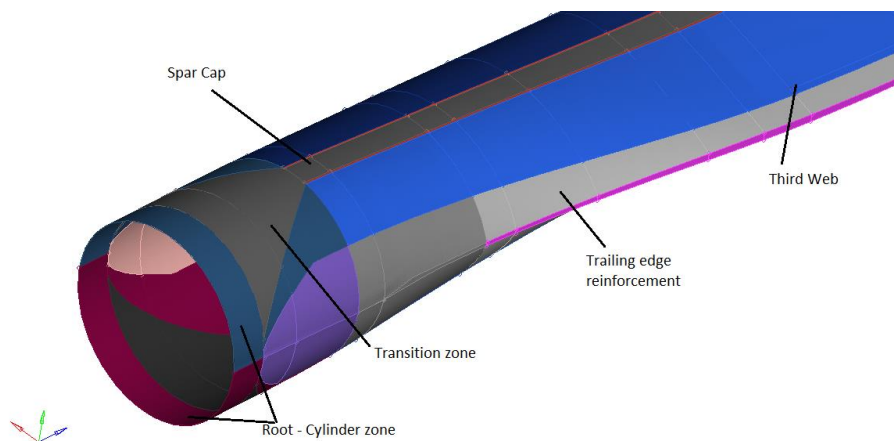


**Figure 72. PolIMI BTC SC+05, detail of root region**

The wind turbine design parameters are the same of the DTU 10MW reference blade, and are reported in the following table for completeness.

Table 17. *PolIMI BTC SC+05, design parameters*

Wind regime	IEC Class 1A
Rotor Orientation	Clockwise rotation - Upwind
Control	Variable speed, collective pitch
Cut in wind speed	4 m/s
Cut out wind speed	25 m/s
Rated wind speed	11.4 m/s
Rotor Diameter	178.3 m
Hub Diameter	5.6 m
Hub Height	119 m
Maximum Tip Speed	90 m/s
Tilt Angle	5.0 deg
Rotor Precone Angle	4.65 deg
Blade Prebend	0 m
Nacelle Mass	446.036 kg
Tower Mass	628.442 kg

The following table reports the global data of the optimal blade POLIMI 10MW BTC SC+05.

Table 18. *PolIMI BTC SC+05, design parameters*

PolIMI 10MW BTC SC+05	
Spar Caps Angle Rotation	5 deg
1st blade frequency (flap mode)	0.5587 Hz
2nd blade frequency (edge mode)	0.6173 Hz
Max Blade Tip Deflection	12.90 m
Blade Total Mass	40874 kg
AEP	46.160 GWhy
CoE	75.166 \$/kWh

The following figures reports the thickness distributions along the blade span of the internal sub-components and the mass, flapwise and edgewise stiffness. The following table reports the mass breakdown computed for each structural components including the Non-Structural Masses (NSM).

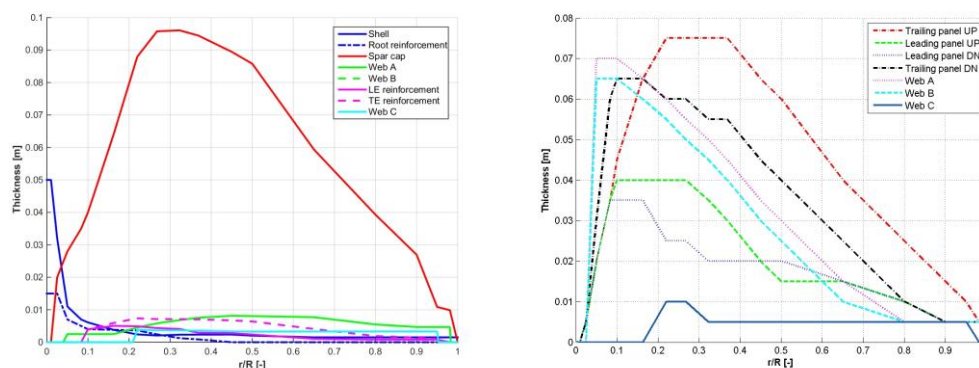


Figure 73. *PolIMI BTC SC+05, structural (left) and core (right) thickness distributions*

Table 19. *PolIMI BTC SC+05, bill of material*

Structural Component	Mass [kg]	% of total blade mass
Skin	8883	21.73

Structural Component	Mass [kg]	% of total blade mass
Spar Cap	16884	41.30
Web A + B	2413	5.90
Web C	72	0.17
LE & TE Reinforcement	1284	3.14
Root Reinforcement	2568	6.28
<b>Total Structural Mass</b>	<b>32104</b>	<b>78.54</b>
<b>NSM</b>	<b>8770</b>	<b>21.46</b>
<b>Total blade mass</b>	<b>40874</b>	<b>100.00</b>

Next is presented a comparison between the DTU 10MW RWT and the actual PoliMI 10MW BTC SC+05. The following table shows a comparison between the RWT blade and the optimal one.

Table 20. *PoliMI BTC SC+05, Comparison against RWT*

	RWT	PoliMI 10MW BTC SC+05	Difference
Blade Total Mass	42422 kg	40874 kg	- 3.65 %
Blade 1 <sup>st</sup> modal freq (flap)	0.6123 Hz	0.5587 Hz	-
Blade 2 <sup>nd</sup> modal freq (edge)	0.9124 Hz	0.6173 Hz	-
Blade Max Tip Displacement	13.04 m	12.90 m	-
CG position (spanwise direction)	26.62 m	28.56 m	-
AEP	45.760 GWhy	46.160 GWhy	+ 0.87 %
CoE	75.911 \$/kWh	75.166 \$/kWh	- 0.99 %

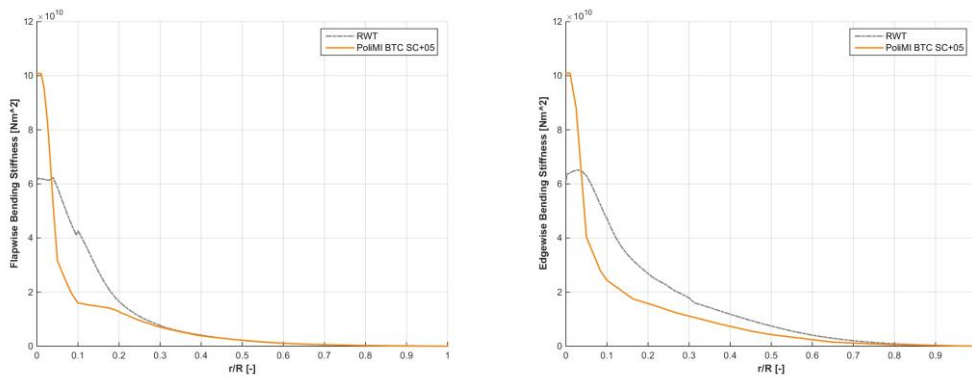


Figure 74. flapwise (left) and edgewise (right) stiffness distributions comparison

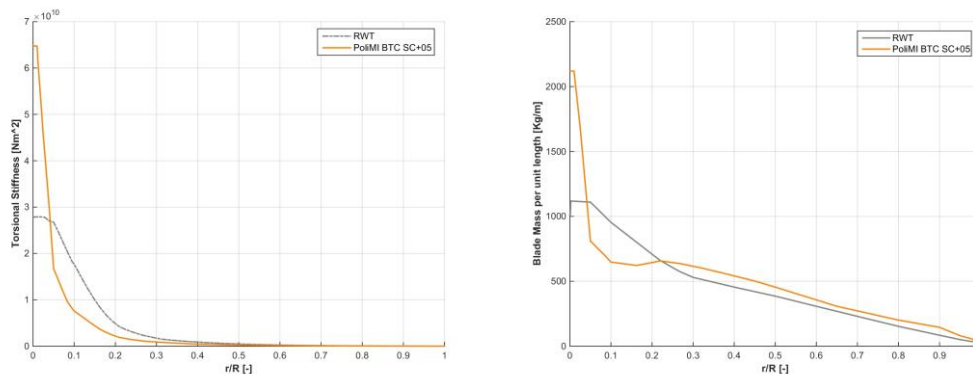


Figure 75. torsional stiffness (left) and blade mass (right) distributions comparison

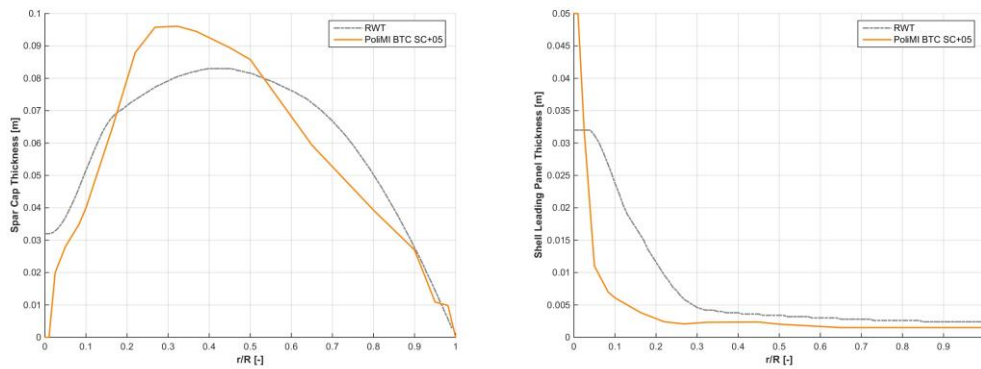


Figure 76. spar cap (left) and shell leading panel (right) distributions comparison

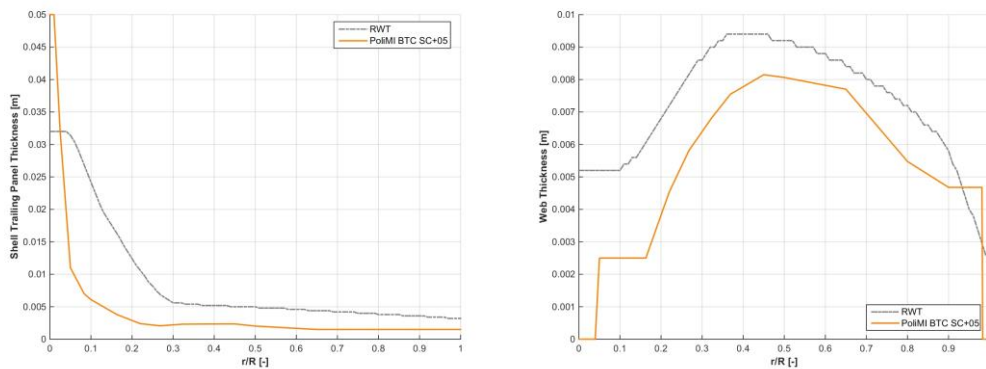


Figure 77. shell trailing panel (left) and web (right) distributions comparison

The next figures show the deflection of the blade in the out of plane direction in correspondence of the first mode of vibration (at left) and the corresponding torsion associated to the blade (at right). The PoliMI BTC 10MW SC+05 blade has, for the same flapwise deformation, a higher twist due to the BTC.

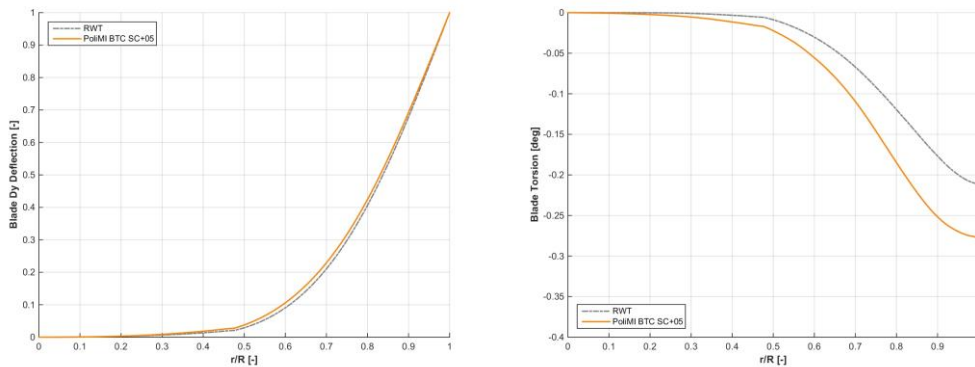


Figure 78. First flapwise mode: flapwise (left) and torsion (right) deflections comparison

### 3.1.4.2 Load cases considered

The blade is designed according to IEC 61400-1 Ed.3. The load cases selected for the design are reported in the following table.

Table 21. *PolIMI BTC SC+05, DLCs considered*

DLC number	Wind Type	Wind Speed	Yaw Misalignment	Fault	Type of Analysis	Safety factor
1.1	NTM	4 - 5:2:25 m/s	-	-	U	1.35
1.2	NTM	4 - 5:2:25 m/s	-	-	F	1
1.3	ETM	4 - 5:2:25 m/s	-	-	U	1.35
2.1	NTM	4 - 5:2:25 m/s	-	Grid Loss	U	1.35
2.3	EOG	Vr, Vr-2, Vr+2, Vout	-	Grid Loss	U	1.1
6.1	EWM	Vref (50m/s)	-8, 0, +8 deg		U	1.35
6.2	EWM	Vref (50m/s)	-180:30:180 deg	Grid Loss	U	1.1
6.3	EWM	Vref (50m/s)	-20, 0, +20 deg		U	1.1

A complete set of load cases, including also DLC 1.4, DLC 1.5, DLC 4.2, was at first considered. For computational reasons, this reduced set was taken as representative of the complete envelope loads along the entire spanwise of the blade.

### 3.1.4.3 Structural integrity verification

The proposed blade satisfies all the design constraints, as can be seen from the following figures, which report the constraint margin for stress, strain and fatigue analysis in all the structural components of the blade as described in the previous sections.

A constraint value is considered active when its value reaches 0. If  $> 1$  the constraint is violated, if  $< 0$  the constraint is non-active. As one can see, only the fatigue constraint is active in the first 3 figures, which are relatives to skin, spar cap and webs.

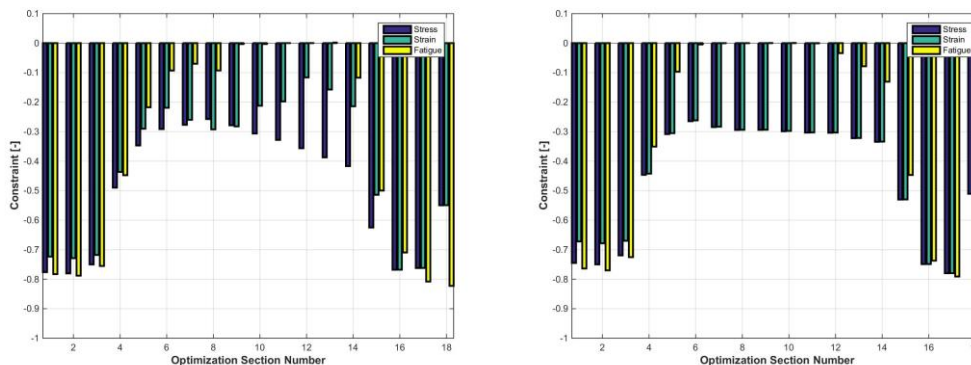


Figure 79. PolIMI BTC SC+05: skin (left) and spar cap (right) constraints

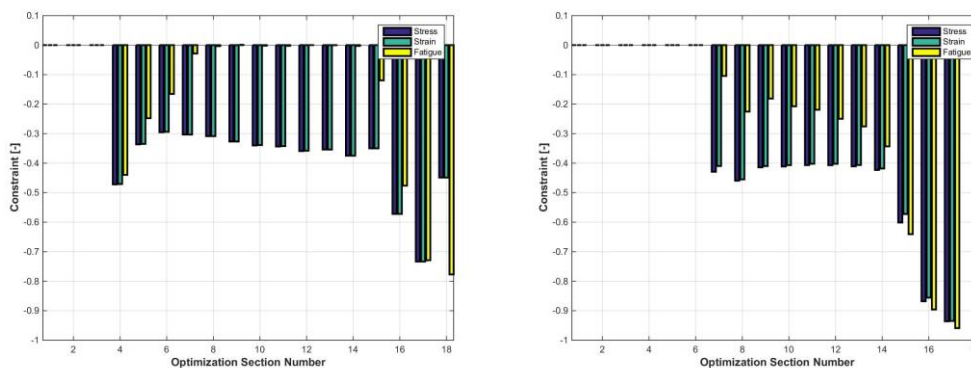


Figure 80. PolIMI BTC SC+05: web (left) and TE reinforcement (right) constraints

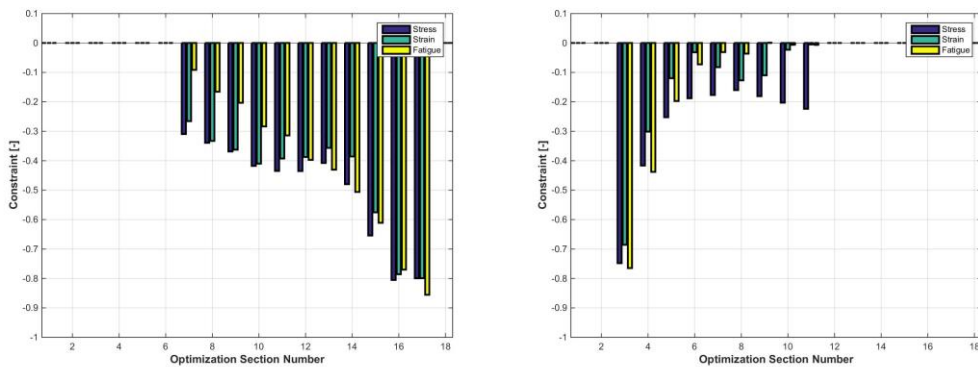


Figure 81. PoliMI BTC SC+05: LE reinforcement (left) and root reinforcement (right) constraints

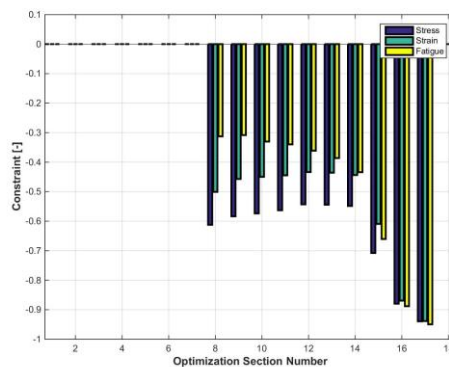


Figure 82. PoliMI BTC SC+05: third web constraints

The following table shows the ultimate loads on the hub and tower compared with the ones computed (with the same conditions) for the RWT. As one can see the BTC is able to reduce all these loads on these two subcomponents. Since these have not been re-designed in this deliverable, the real effects on the CoE of this optimal blade have to be further investigated.

Table 22. *PoliMI BTC SC+05, Comparison of ultimate loads against RWT*

	RWT	PoliMI 10MW BTC SC+05	Difference
Hub Nodding Moment	57097 kNm	53908 kNm	- 5.58 %
Hub Yaw Moment	53046 kNm	47078 kNm	- 11.25 %
Hub Combined Moment	58271 kNm	54121 kNm	- 7.13 %
Hub Axial Force	3560 kN	3121 kN	- 12.33 %
Tower Bottom Fore-Aft Moment	491819 kNm	463849 kNm	- 5.68 %
Tower Bottom Combined Moment	495794 kNm	463855 kNm	- 6.44 %
Tower Bottom Torsional Moment	59056 kNm	51513 kNm	- 12.77 %
Tower Top Fore-Aft Bending Moment	59244 kNm	54401 kNm	- 8.17 %
Tower Top Torsional Moment	58688 kNm	51270 kNm	- 12.63 %

### Fatigue loads

The next table shows the cumulative damage equivalent loads computed considering only DLC12 cases (power production in turbulent wind). A Weibull distribution has been used, with a shape factor of 2 and a mean wind speed of 10m/s. Damage Equivalent Load (DEL) are weighted with Weibull. Following parameters are chosen for the fatigue analysis, for both the blades:

- Number of bin: 100

- Number of years: 25
- Frequency: 0.012684 Hz
- $m = 3$

It can be seen that the optimal blade with BTC is able to reduce the fatigue loads of about 3 % in the hub and 2 % in tower bottom. As for the ultimate loads, since tower and hub have not been re-designed in this deliverable, the real effects on the CoE of this optimal blade have to be further investigated.

Table 23. *Polimi BTC SC+05, Comparison of fatigue DEL against RWT*

	RWT	Polimi BTC SC+05	Difference
DEL Hub Nodding Moment	27950 kNm	26884 kNm	- 3.82 %
DEL Hub Yaw Moment	26192 kNm	25270 kNm	- 3.52 %
DEL Tower Bottom Side-Side Moment	59828 kNm	58175 kNm	- 2.76 %
DEL Tower Bottom Fore-Aft Moment	136805 kNm	135267 kNm	- 1.12 %

The 3D finite element model was also used to check fatigue satisfaction of the fatigue constraint. Check of fatigue damage index D is done on the three reference section also used in the Deliverable D2.2 “Information on the Benchmark of blade structural FATIGUE models” [3] and [2]. Section number and relative position are reported in table:

Table 24. *Polimi BTC SC+05, reference sections used for FE fatigue verification*

Section	R (m)
RefSec_1	2.800
RefSec_2	26.694
RefSec_4	54.149

In the following figure is reported the fatigue damage index D on the Skin in RefSec\_2. As one can see, the suction side leading panel of the skin exhibits higher fatigue loads, but the analysis shows that the index is < 1, confirming the satisfaction of fatigue analysis. The maximum fatigue damage index computed is 0.958.

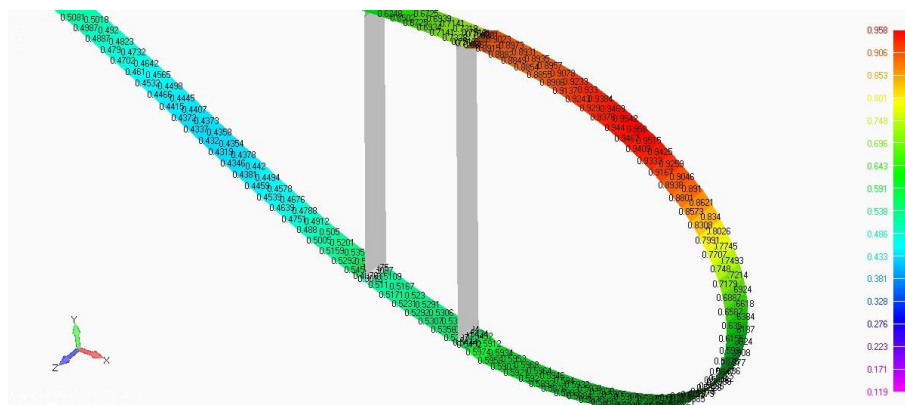


Figure 83. *Polimi BTC SC+05, fatigue damage index on skin on RefSec\_2*

In [3] the fatigue damage index was requested in some specified key (KP1, KP5, KP9, KP12) on the three reference sections selected. Even if the internal structure of the Polimi 10MW BTC SC+05 is slightly different from the RWT, these fatigue analysis has been repeated in the points which are closer to the original ones. The analysis has showed that all the fatigue constraints are satisfied (fatigue damage less than 1).

Table 25. *PolIMI BTC SC+05, fatigue damage index on RefSec\_1*

Key point No.	Layup	RefSec_1		
		Laminate	Layer 1	Layer 2
1	Tail A	0.1371	0.1371	0.1116
9	Nose P	0.1591	0.1591	0.1433
12	CAP	0.2687	0.2687	0.2273

Table 26. *PolIMI BTC SC+05, fatigue damage index on RefSec\_2*

Key point No.	Layup	RefSec_2		
		Laminate	Layer 1	Layer 2
1	Tail A	0.7296	0.7296	0.7286
5	Trailing	0.4976	0.4976	0.4475
5	CAP	0.5110	0.5110	0.4330
5	Web B	0.7628	0.7628	-
9	Nose P	0.6384	0.6384	0.6244
12	CAP	0.6725	0.6725	0.6384

Table 27. *PolIMI BTC SC+05, fatigue damage index on RefSec\_4*

Key point No.	Layup	RefSec_4		
		Laminate	Layer 1	Layer 2
1	Tail A	0.6691	0.6687	0.6691
5	Trailing	0.5107	0.5107	0.4556
5	CAP	0.5303	0.5303	0.4728
5	Web B	0.6412	0.6412	-
9	Nose P	0.4074	0.4023	0.4074
12	CAP	0.6991	0.6991	0.6803

### Buckling analysis

The first buckling eigenvalues appears at suction side between 4.0m and 10.7m from the blade root, but the critical load is higher than actual load on the blade since the minimum buckling load factor computed is 1.0232 in the spar cap and leading edge panels as showed in the next figure.

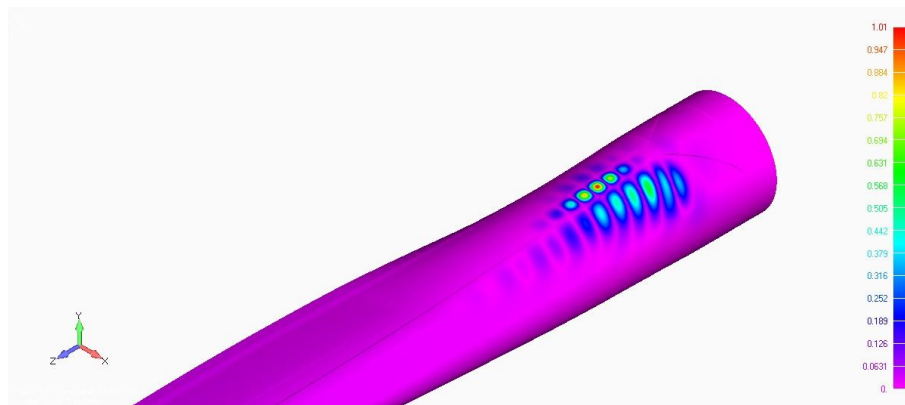


Figure 84. *PolIMI BTC SC+05, fatigue damage index on skin on RefSec\_2*

### 3.1.5 Conclusions and recommendations

In this section PoliMI has presented a structural solution based on the so called Bend-Twist Coupling (BTC), a passive load mitigation solution obtained by exploiting the anisotropic mechanical properties of composite materials. BTC implies that, when the blade bends because of increased loads, the ensuing change of twist will affect the aerodynamic loading through a change in angle of attack.

The structural solution is computed throughout a blade design procedure based on a novel comprehensive multi-level constrained optimization approach. The design process alternates between a multibody beam model augmented with a 2D FEM cross sectional sub-models and a fine scale 3D FEM detailed model of the blade. The former enables the numerous transient aero-servo-elastic analyses required to compute loads and deflections throughout the lifetime of the machine, while the latter makes it possible to conduct detailed local verifications of the design.

The use of a constrained optimization-based approach to design is crucial and allows comparing different solutions that satisfy the same design requirements, and hence permitting to choose the optimal solution.

For each optimal blade, the control set-points have been changed in order to improve the annual energy production.

The optimal blade presented has several advantages with respect to the RWT: it is lighter (mass - 3%), has a higher AEP (+0.6%) and hence the Cost of Energy is lower, about - 1%. Moreover the ultimate as well as the fatigue loads on the hub and tower have been reduced. Since these components have not been re-designed within this task the actual final effect on the CoE of this optimal blade has to be further investigated.

## 3.2 Passive gust load alleviation using embedded bend-twist coupling (UBRISTOL)

### 3.2.1 State of the art and motivation

In recent years, the cost of energy produced by alternative supplies has steadily decreased. This, together with several other socio-economic reasons, has made alternative energies increasingly competitive and, hence, a viable alternative to more traditional sources such as carbon, oil or nuclear power. This trend is confirmed by industry growth figures. The wind energy industry, in particular, has grown and is predicted to continue to grow steadily, both in terms of investments and installed capacity.

From an engineering perspective, the growth in this sector raises some interesting challenges as it creates the drive to build larger, more durable rotors that produce more energy, in a more cost efficient way. The rationale for moving towards larger rotors is that, with current designs, the power generated by wind turbines is theoretically proportional to the square of the blade length. Furthermore, taller wind turbines operate benefit from greater wind speeds because of their higher placement. Hence, there are increasing returns to scale on the harvested energy by opting for larger wind turbines.

However, larger blades are heavier, more expensive and increasingly prone to greater aerodynamic and inertial forces. In fact, it has been shown that they exhibit a cubic relationship between length and mass, meaning that material costs, inertial and self-weight effects grow faster than the energy output as the blade size increases (Figure 85) This issue is specifically addressed in section 2.4, which proposes a concept blade with higher structural efficiency, using offset spar caps/shear webs.

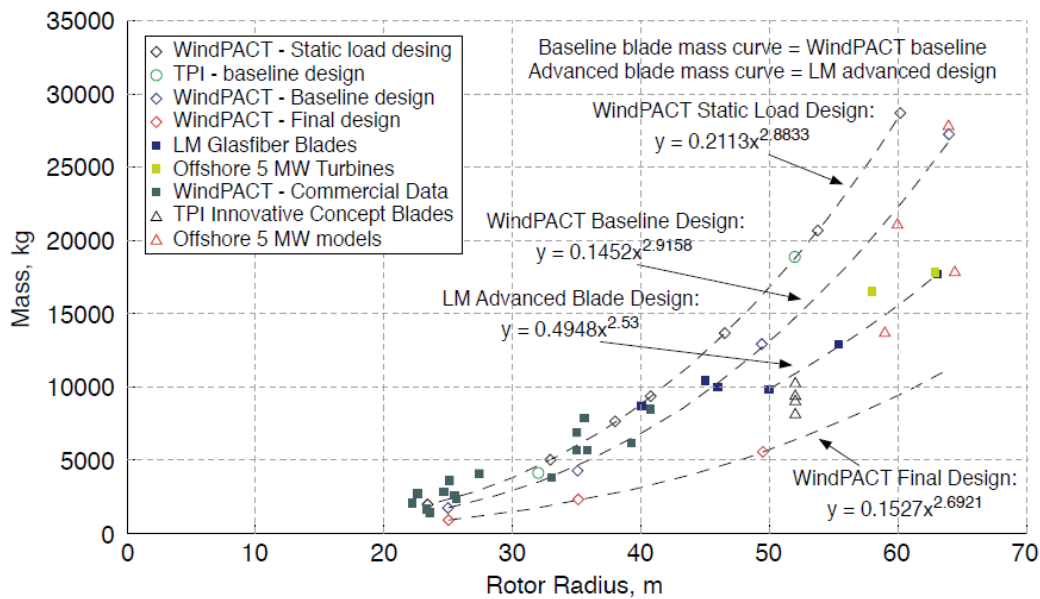


Figure 85. Wind turbine blade mass vs. rotor radius [37]

The demand for improvements in blade design is evident. The notion of lighter turbines, which are also able to harvest more energy, is indeed immediately attractive. As a consequence, this work investigates novel approaches to blade design, to improve on the global performance of the turbine system. Specifically, the study is focused on variable speed turbines.

In the context of the DTU 10MW wind turbine blade design, the aim of this work is to assess the use of tow-steered composite laminates for novel blade designs that could potentially increase the annual energy production and provide an added mechanism for passive load alleviation. The first part of this section assesses the change in power performance by introducing tow-steered laminates. The second part studies the gust response of the blade using a dynamic aeroelastic model and assesses whether the concept blade can provide passive load alleviation.

### 3.2.2 Definitions

For sake of clarity and consistency, the following terms are defined and will be adhered to throughout Section 3.2.

**Rigid blade, non-adaptive blade:** a blade that has no aeroelastic coupling and that can be controlled only through rigid pitch control. This is opposed to an adaptive blade.

**Adaptive blade** (as opposed to a rigid blade), a blade that is tailored aeroelastically with bend-twist coupling so as to provide nose-down pitch as the wind speed increases.

**Classic adaptive blade:** a blade that is tailored aeroelastically with bend-twist coupling so as to provide monotonically increasing nose-down pitch as the wind speed increases.

**Optimum blade, optimal blade, ideal blade:** a blade that is tailored aeroelastically (by changing the fibre orientation and spar layout) such that the optimised solution produces the best possible power output, regardless of any manufacturing constraints.

**Novel adaptive blade, concept adaptive blade:** a realistic adaptive blade design based on the optimum blade design.

**Pre-twist:** the geometric twist of each blade section with respect to the reference axis of the blade.

**Pitch angle:** the angle associated with the rigid pitching of the blade.

**Elastic twist, elastically-induced twist:** the twist angle associated with the bend-twist coupling of the blade with produces a nose-down pitch.

**Total twist:** the resultant twist of the blade at each section. For rigid blades, this is the sum of the pre-twist and the pitch angle; for adaptive blades, it is the sum of the pre-twist, pitch angle and elastically-induced twist.

**Conventional wind turbine:** a wind turbine design respecting a classically asymptotic distribution of angular blade speed (see Figure 86), based on the Vestas V90 wind turbine.

**AEP:** Annual Energy Production, the amount of energy produced by the blade in one year taking into account the probability of wind speed distribution.

**Rated-optimised blade:** a blade that is optimised in terms of power output at its rated speed.

**AEP-optimised blade:** a blade that is optimised in terms of power output over the whole range of operating speeds (below rated).

Short description of the state of the art for the solution and motivation for the structural concept selected.

### 3.2.3 Structural design and power performance

#### 3.2.3.1 Objectives

Section 3.2 introduces a novel aeroelastic approach to the design of large-scale wind turbine blades. In this approach, the load variation associated with different wind speeds is exploited in order to improve the aerodynamic efficiency of the turbine across its entire operating range. In order to maximise the turbine's yielded power at different wind speeds, an optimal aeroelastic twist distribution is determined, using the DTU 10MW Reference blade as a baseline case. The results of this analysis are then used to determine the adaptive behaviour that is required for improved aerodynamic performance. Finally, the desired adaptive behaviour is translated into a structural design.

Classic wind turbine design ignores aeroelastic effects and considers the blade to be torsionally rigid; as a result, the total twist distribution can be considered as the sum of pre-twist and pitch angle only. The Annual Energy Production (AEP) is then maximised by choosing an optimal pre-twist at a given wind speed, and controlling the pitch to minimise the power loss at different wind speeds. In aeroelastic approaches, however, the blade is no longer considered to be torsionally rigid, and the elastically-induced twist contribution becomes an added design variable.

In a previous study on a Vestas wind turbine, it was shown that the turbine's AEP can be significantly improved through aeroelastic tailoring [38], [39]. In this report, a similar methodology is implemented in the Innwind DTU Reference blade. By allowing the AOA of each blade section to adapt to different wind speeds, the blade's bend-twist coupling is tailored to maximise the power yielded below rated wind speed.

The adaptation consists of a nose-down rotation of the sections, but as opposed to classic adaptive blades, the elastically-induced twist is no longer a monotonic function of the radial position. Upon bending of the blade, the induced twist increases in magnitude along the blade, decreasing the AoA of each section. Outboard, the trend is inverted: the induced twist decreases and the AoA increases again. Despite the inversion of the twist rate in the second half of the blade, all sections move towards feather. As a result, this concept retains some of the load alleviation capabilities explored in literature.

#### 3.2.3.2 Angular speed distribution and optimum adaptive behaviour

Studying the angular speed distribution, it is noted that the distribution provided by Innwind is significantly different from that of the conventional variable speed wind turbine (Figure 86). For a conventional wind turbine, the angular speed quickly rises from cut-in speed, reaching a plateau in the second half of the operating range of the turbine. Instead, for the case of the Innwind design

the speed remains constant for the first 40% of the operating range before rising sharply near the rated wind speed. It is also noted that the rated wind speed for the Innwind design is significantly lower than that of a conventional design. As is shown later in this report, this unconventional angular speed distribution has a major impact on the design of the optimum blade.

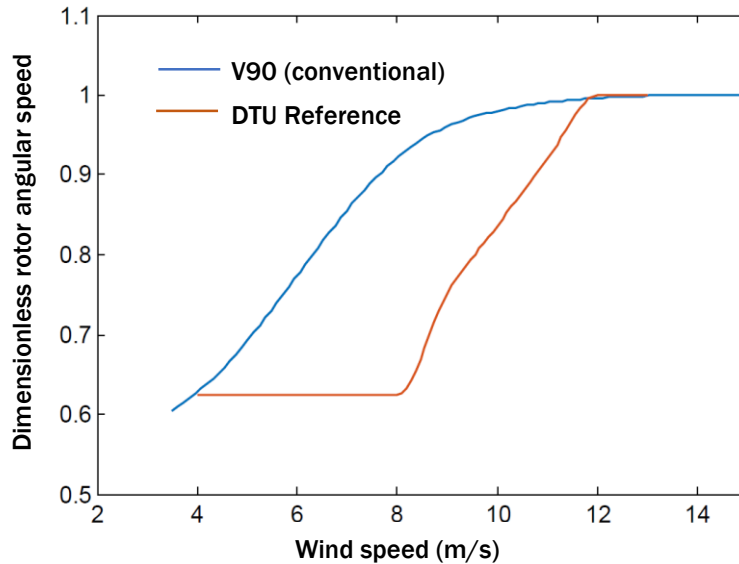


**Figure 86 : Dimensionless angular speed with wind speed for (a) a Vestas V90 conventional variable speed wind turbine and the (b) Innwind DTU wind turbine**

The total twist distributions that maximise the power output at different operating conditions are found by performing an exhaustive search from cut-in to rated wind speed, for both the conventional and the Innwind designs. At each of these operating conditions the optimised twist yields maximum power output. This search was conducted with wind speed increments of 0.5 m/s in the interval from cut-in to rated speed. During the optimisation, all other given parameters are kept constant. The aerodynamic model adopted in this work is based on the Blade Element Momentum theory [40]. The implemented aerodynamic model has been successfully validated against the WT\_PERF tool [41].

### 3.2.3.3 Conventional blade twist optimisation

#### 3.2.3.3.1 Target twist

This section presents a summary of the results of the aerodynamic optimisation of the conventional blade performed by UBRISTOL. The optimum total twist distribution at different radial locations is shown as a function of the operating conditions in Figure 87. It can be seen that on the right hand side of the plot the curves increase monotonically, and their gradients decrease with the radial position (moving from root outboard). At lower wind speeds the curves become more irregular and their slope inverts.

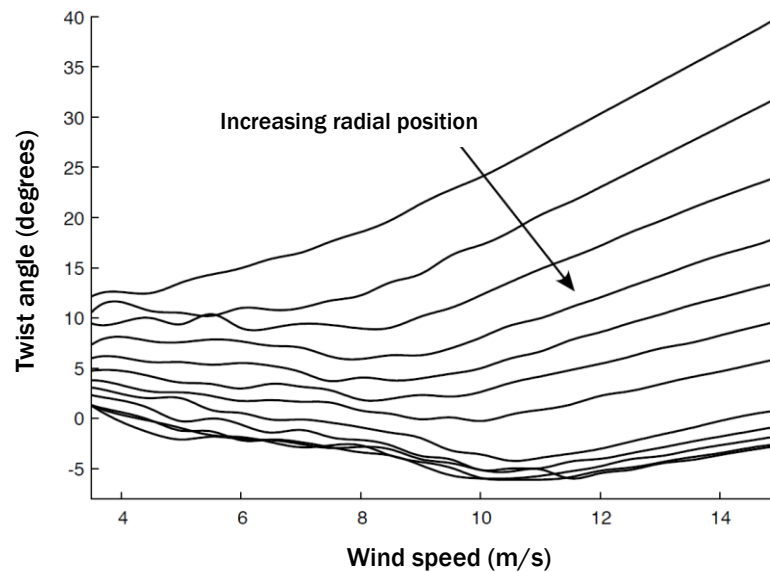


**Figure 87. Optimum twist as a function of wind speed at different radial positions**

The present aim is to identify a distribution of induced elastic twist that achieves the shape adaptation necessary to follow the optimal total twist profile at all of the operating conditions as close as possible. In other words, an aeroelastic concept is sought where the blade's twist distribution follows the curves shown in Figure 87.

If the pre-twist is chosen to match the optimum at a given operating condition, its values can then be obtained from Figure 87. For any other operating condition, in an attempt to follow the optimal curves closely, the total twist can then be adjusted using pitch control. This, however, changes its values by the same amount at all of the radial locations, thus forcing a deviation from optimal conditions. This can be seen from Figure 87, where the optimum total twist is observed to change with a different rate depending on the radial location. This approach to the aerodynamic design entails a loss of power but, in principle, it is similar to the one used in conventional turbines. This power loss can be partially overcome by exploiting an elastically-induced twist, as it allows the total twist to vary with the aerodynamic load and along the entire blade length.

It is noted, from these results, that the elastic twist would need to change sign whenever the optimum twist gradient changes sign. In other words, as the wind speed is increased the elastic twist should ideally produce nose-up to decrease the total twist, then nose-down to increase it. Because this elastic design cannot be achieved passively, the optimal curves need to be modified, by imposing a horizontal tangent where the slope is not constantly positive. The modified target curves are shown in Figure 88 at four different radial locations, for sake of clarity.

The target curves are achievable because they require the blade sections to only twist nose-down for all operating conditions. Such a combination of pre- and elastic twist allows the optimal power curves to be followed closely in the upper half of the operating wind speed range. The power that is lost in the first half can then be partially recovered by prescribing a suitable pitch variation that realises the required nose-up rotation of the blade sections.

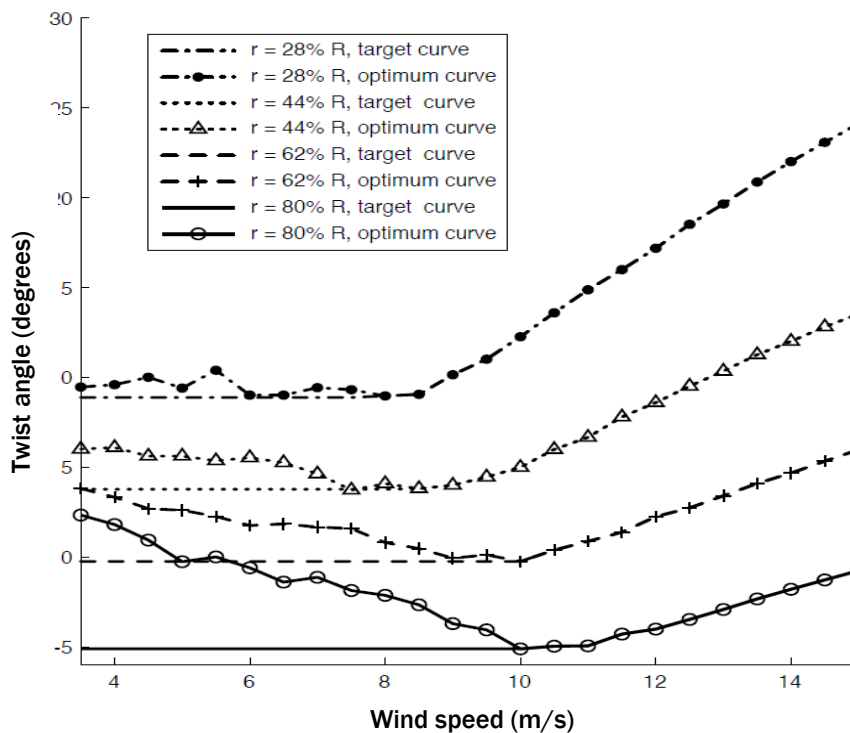


**Figure 88: Modified target twist as a function of wind speed at different radial positions**

### 3.2.3.3.2 Induced elastic twist

The targeted distribution of induced elastic twist (Figure 89) is obtained by subtracting the total target twist of blade sections at cut-in condition from the target twist at rated (Figure 88). Additionally, it has been modified to respect the boundary condition at the root, where the induced elastic twist angle must be equal to zero. Figure 89 compares the target and realised induced twist distributions. The kink in the targeted distribution visible between 80% and 90% of the blade length was smoothed out to achieve a more realistic distribution of twist, giving the 'realised distribution' of twist. In summary:

1. Compute optimum total twist distribution for different radial locations. These *ideal twist curves* represent the ideal aerodynamic solution.
2. Modify the optimum twist curves by constraining the slope of the curves to be positive, so as to produce nose-down twist only. These are the *target twist curves*.
3. Choose a design operating condition and subtract the target twist curve at cut-in speed from the target twist curve at the operating condition to obtain the variation in elastic twist.
4. Enforce zero induced elastic twist at the root due to the built-in boundary condition. This gives the *targeted distribution of elastic twist*.
5. Apply smoothing and other manufacturing constraints to the targeted distribution. The final curve is the *realised distribution of elastic twist* that can be applied to generate the concept blade.

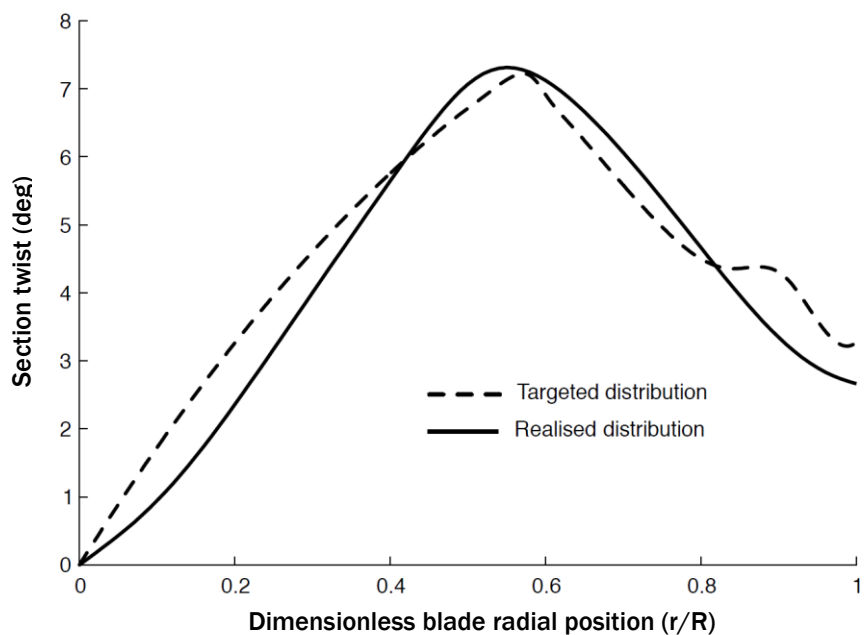
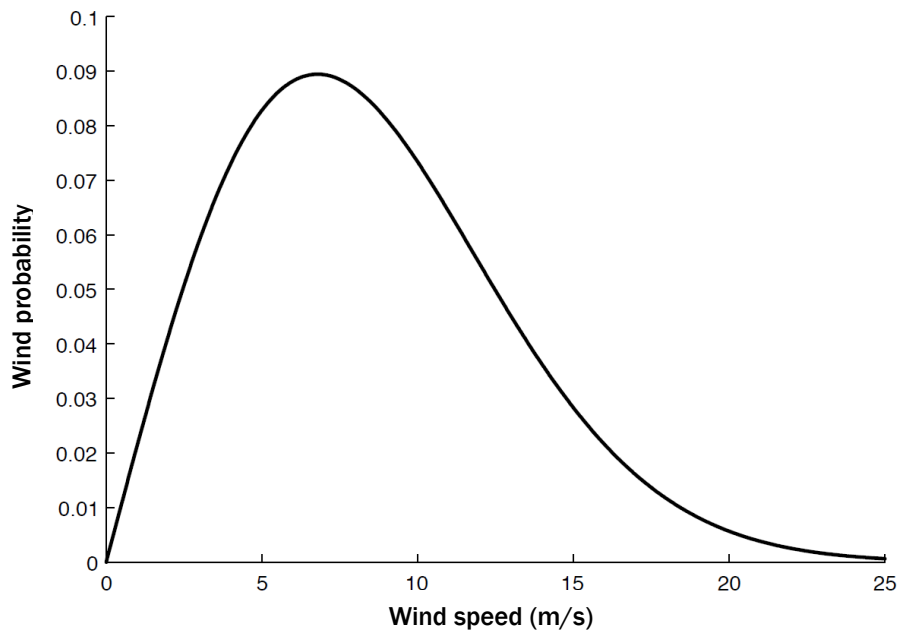


**Figure 89: Comparison between the targeted elastic twist and the actual twist distribution as a function of the radial position**

### 3.2.3.3.3 Power output of the adaptive concept blade

The power performance of the concept blade can now be assessed and compared to that of rigid blade designs. In order to represent the state-of-the-art blade design, a rated-optimised and an AEP-optimised blade are considered. The pre-twist and pitch angles of the rated-optimised blade are determined by matching the ideal twist at rated wind speed, while for the AEP-optimised blade the pre-twist and pitch angles are found by maximising the turbine's AEP.

A wind probability distribution curve with a Weibull distribution (average speed = 8.5 m/s; shape factor = 2) is adopted herein (Figure 90). AEPs are estimated taking into account below-rated speeds only. The theoretical maximum AEP is given by the ideal blade, which follows the optimal twist curves (Figure 87). This hypothetical AEP is normalised as 1 and serves as the basis for comparison of all other designs.



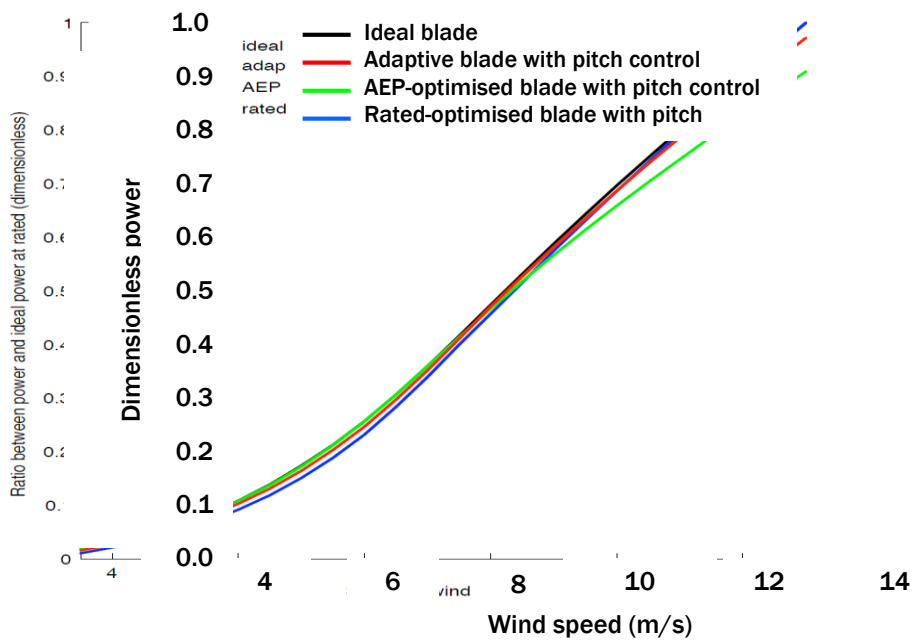
**Figure 90: Standard distribution of wind probability**

Table 28 shows the AEP loss in the classic rigid blades compared to the adaptive concept blade and reports values for blades with and without pitch control. It is noticed that the adaptive concept blade yields appreciable more power than its classic rigid counterparts, with an increase in power of around 1.7%. This conservative estimate represents a significant improvement in power which justifies a modified design of the blade.

**Table 28. AEP loss of conventional blade with respect to ideal and adaptive blade**

Blade configuration	Dimensionless AEP	Power loss w.r.t ideal blade
Ideal	1.000	0.0%
Novel adaptive with pitch control	0.976	2.4%
AEP-optimised with pitch control	0.959	4.1%
Rated optimised with pitch control	0.957	4.3%
Novel adaptive without pitch control	0.951	4.9%
AEP-optimised without pitch control	0.925	7.5%
Rated-optimised without pitch control	0.878	12.2%

Figure 91 shows the power curves of the ideal blade, the adaptive concept blade with pitch control, and the two rigid blade design with pitch control. It is straightforward to identify where the conventional design fails to follow the ideal behaviour. For instance, the rated-optimised blade loses power at all wind speeds below its design point (this is noticed in particular at wind speeds between cut-in and 9 m/s). Conversely, the AEP-optimised design loses efficiency at higher speed. On the other hand, the adaptive concept blade is closer on average to the optimum curve, which explains why it performs better overall.



**Figure 91: Power curves for ideal, rigid, AEP-optimised, and adaptive concept blades for the conventional V90 design**

### 3.2.3.4 Innwind blade twist optimisation

#### 3.2.3.4.1 Target twist

The previous analysis is now repeated for the Innwind blade. Figure 92 shows the distribution in optimum twist for the rigid blade with increasing radial position. For the rigid blade, all curves are parallel to one another as the optimum twist can be reached by rigidly pitching the blade. However, these curves yield a lower-than-optimum power curve.

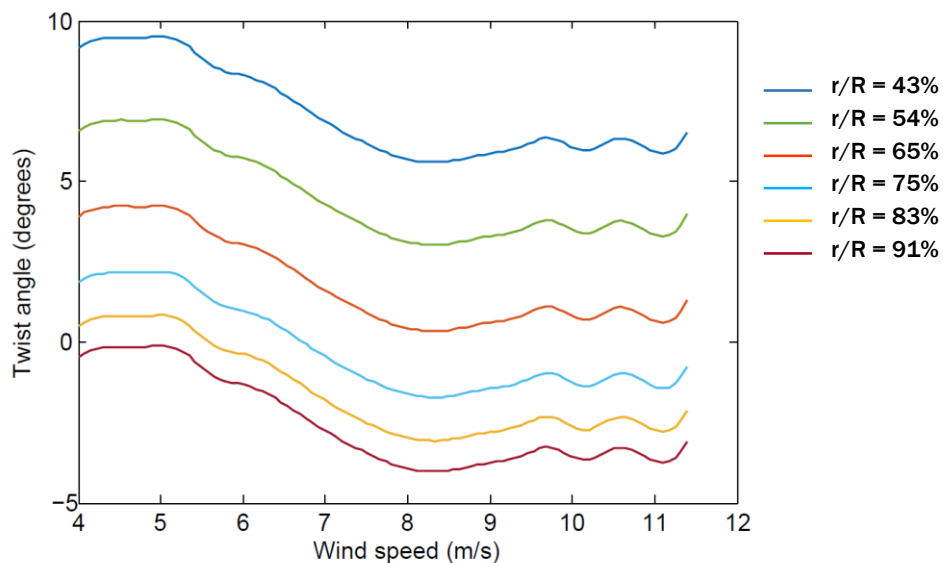


**Figure 92: Optimum twist for rigid blade as a function of wind speed at different radial positions**

Figure 93 shows the ideal optimum twist as a function of wind speed at different radial positions. It is noted that these curves are highly irregular, compared with those of the conventional blade (Figure 87). Most of the curves intersect with one another, unlike those of the conventional blade which has more clearly separated twist distributions.

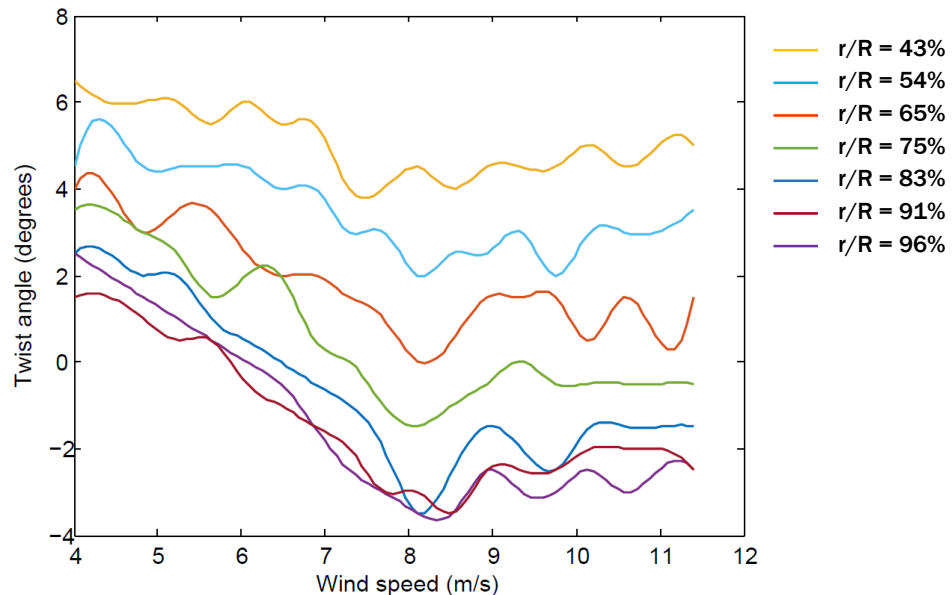


Figure 93: Optimum twist for adaptive blade as a function of wind speed at different radial positions

#### 3.2.3.4.2 Power output of the adaptive blade

Figure 94 shows the power output of the optimised DTU blade, compared with the reference rigid case. A small improvement in power near the cut-in speed region can be noticed, but overall the curves are virtually identical. In fact, the ideal power increase that could be achieved through implementing an aeroelastic design approach would be in this case be around **0.3% of AEP**, which is lower than the 1% threshold that is warranted for a design change.

This result is also significantly lower than what has been achieved in the conventional (V90) blade adaptive design (Figure 91). This is attributed to two influencing factors. The first is the difference in the operating conditions of the Innwind wind turbine, compared to conventional wind turbines. The nature of the DTU angular speed distribution (Figure 86) decreases the possibilities for power optimisation and the smaller rated wind speed decreases the width of the below-rated range. This explains in part why little improvement in power output is observed.

The second is related to differences in thickness to chord ratios the aerofoil profiles. The DTU Reference blade has relatively thick airfoil sections (high  $t/c$ ), compared to other blades, such as the Vestas V90. Thick airfoils are fundamentally less aerodynamically efficient than thin airfoils, associated with a lower  $t/c$ . Moreover, high  $t/c$  airfoils shows lower sensitivity to variations around optimum incidence, which explains the small improvement in AEP as observed in this study.

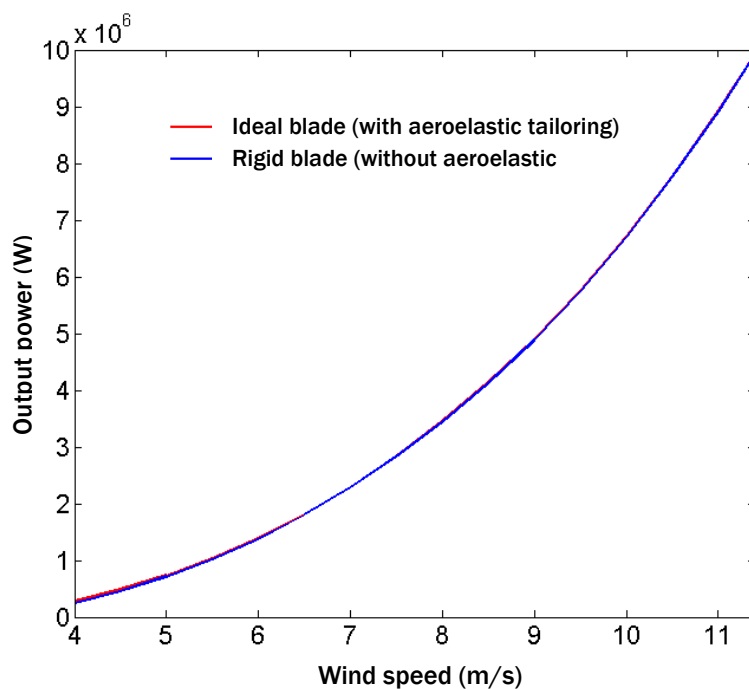


**Figure 94: Power curve for the Innwind optimum blade, compared with the DTU Reference blade with no aeroelastic tailoring**

With such a marginal theoretical improvement in the power of the blade, it is unlikely that the actual power of the wind turbine with adaptive blades can be increased, when manufacturing constraints are taken into account. The AEP of the optimised wind turbine is likely to remain constant.

To determine the target curves from the optimum curves, the following rationale is followed. Figure 93 shows that the twist of an optimised blade should increase by around 4 degrees between mid-length and tip sections, when moving from cut-in to rated wind speed. Tip sections at rated speed should have a twist that is around 4 degrees lower than at cut-in, while inboard sections should adopt a fairly constant twist. Therefore, the targeted induced elastic twist should allow for sections at mid-length to twist nose-down by 4 degrees more than the outboard sections. This is achieved by pitching the whole blade nose-up. Such a design more closely follows the ideal twist curves shown in Figure 93, but its aerodynamic performance is not analysed further, because the results of the aerodynamic optimization predict that the power improvement achieved is negligible.

### 3.2.4 Response to Gust-Induced Loads

Whereas for typical adaptive designs are consistently associated with a penalty decrease in power output, the concept adaptive blade design outlined in the previous section could provide a reduction in gust-induced loads, even though the annual energy production remains virtually unchanged.

Therefore, in this section we seek to compare the response of the adaptive concept blade when subjected to a gust. A comparison between blade designs, including the Innwind concept blade is provided by evaluating their ability to alleviate load. Although the Innwind concept blade shows no significant improvement in power performance over the reference rigid blade, it is hoped that it demonstrates an ability to reduce gust loads and, differently from classic adaptive designs, the load alleviation would come in this case without a penalty in power production.

### 3.2.4.1 Aeroelastic models

#### 3.2.4.1.1 Modelling of rotor aeroelasticity

To model the response of the wind turbine under a gust load, a three-bladed rotor spinning at constant speed is represented. Wind and angular speeds affect the dynamics of the aeroelastic system, which is obtained by coupling the three rotating blades and an unsteady aerodynamic model of the turbine. The rotor's aerodynamics are modelled via dynamic inflow (*Generalised Dynamic Wake* model), whereby the 3D aerodynamic field is determined by using a finite number of aerodynamic states [42], [43]. The output of the model is a continuous distribution of induced inflow over the rotor's surface.

Beam elements are used to mesh the blades. A *moving reference approach* captures inertial effects due to blade rotation and coupling between blade structural vibrations and rigid body motions [44]. Because the angular speed is considered to be constant, the generator's dynamics are not modelled. Effects due to variations of rotational speed are neglected, as these effects are assumed to be much slower than the structural response.

A classic aerodynamic load model is implemented based upon two-dimensional aerodynamic coefficients ( $C_L$ ,  $C_D$ , and  $C_M$ ). This aerodynamic load model is complemented with the *Boeing Vertol* model of dynamic stall [45]. The dynamic stall model captures local unsteady effects, which are mainly due to sudden variations of the Angle of Attack (AoA) around the static stall condition. Unsteady effects are caused by the growth and the shedding of vortices on the suction side of the airfoil, which significantly modify the local distribution of pressure and aerodynamic forces.

#### 3.2.4.1.2 Modelling of structure

The structural model assumes a rectangular tapered box section and neglects the aerodynamic envelope of the DTU reference blade (Figure 95). As such, this structural model is not representative of the finalised blade design. The structural design procedure could be the subject of future work [46]. It is stressed that this aeroelastic solution is based on matching the flapwise bending stiffness of the blade, as is explained in the next section, so that the tower clearance constraint is always met. However, a full aeroelastic-structural optimisation would be required to capture the final detailed solution, and additionally to verify that buckling and strength structural constraints are met.

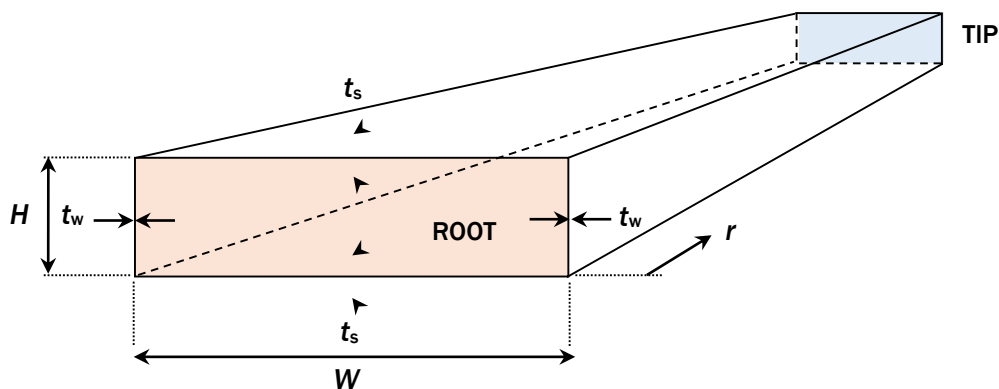


Figure 95: Simplified structural model of the wing box with design parameters

Table 29. Geometrical parameters of box section determined by pre-setting

Parameter	Root	Tip
Height (H), mm	1800	250
Width (W), mm	2500	400

Spar cap thickness ( $t_s$ ), mm	50-60	20
Web thickness ( $t_w$ ), mm	35-40	10

### 3.2.4.2 Pre-setting and structural design

#### 3.2.4.2.1 Blade design pre-setting

This section compares the gust responses of three structural blade designs, one rigid design and two adaptive designs. The first adaptive design is the classic adaptive design with a monotonic nose-down twist. The second adaptive design is the concept adaptive blade, with a non-monotonic elastic twist. In order to perform a fair comparison between gust responses, the spars are designed such that all blades have a similar flapwise bending stiffness. Because the external shape of the blade is fixed, width and height distributions of the spar sections are identical. In addition, the layup of the spars are constrained by other requirements (i.e. the desired induced elastic twist distribution), leaving the spar web and cap wall thicknesses as the only degrees of freedom.

The rigid design uses a symmetric balanced layup, while unbalanced laminates are used for the adaptive designs, producing the necessary bend-twist coupling. For the classic adaptive blade, a single fibre orientation, rotated by 7.5 degrees with respect to the blade axis, is applied to 50% of the spar cap thickness. A [0 / 90 / +45 / -45] layup is applied to the remainder of the cap thickness. For the adaptive concept blade, a variable fibre orientation via tow steering is used for over 80% of the spar cap thickness, while the [0 / 90 / +45 / -45] layup is applied to the remaining 20% of the thickness.

#### 3.2.4.2.2 Tip displacement

Using a trial-and-error approach, the spar cap thicknesses are first tuned to match a similar out-of-plane displacement for a given bending load (Figure 96). The pitch and pre-twist of the blades are then computed to match a similar flapwise bending moment at the root at the rated wind speed. This pre-setting procedure ensures that each design is compared on an equal basis in terms of induced twist.

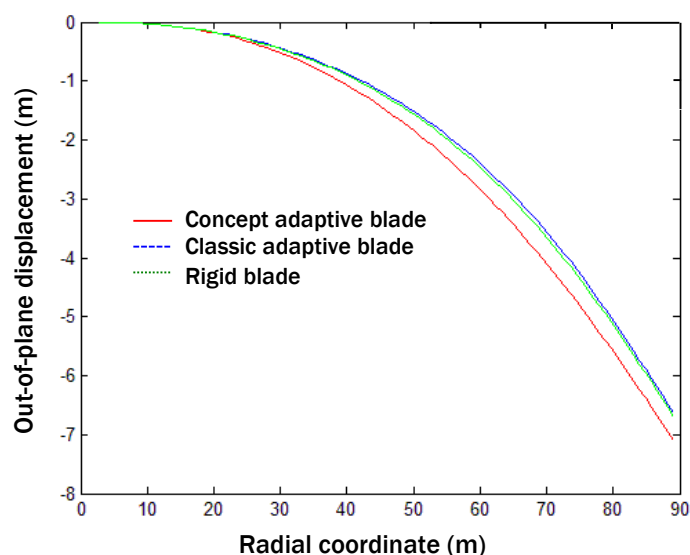


Figure 96: Comparison of the blade displacement (pre-setting at 11.5 m/s rated wind speed)

Figure 96 shows that pre-setting produces a novel adaptive blade that is slightly more flexible than the other two blades. However, the out-of-plane tip displacement error is sufficiently small (6%) to assume that all blades have similar rigidity.

### 3.2.4.2.3 Induced elastic twist and fibre orientation

The induced elastic twist distribution obtained as a result of the blade pre-setting procedure is shown in Figure 97. The twist of the novel adaptive concept has an increasing nose-down induced twist for the first half of the blade, decreasing in the second half. This distribution contrasts with the classic adaptive blade which has a monotonically increasing induced twist. On the other hand, the rigid blade has zero induced twist.

The distribution of fibre angle with radius that allows for the induced twist of the adaptive blade to be achieved is shown in Figure 98. The fibre angle first decreases to minus 15 degrees in the first 50% of the blade, before asymptotically increasing to plus 7.5 degrees towards the tip. This asymptotic behaviour is the result of the target elastic twist distribution curve obtained in the previous section.

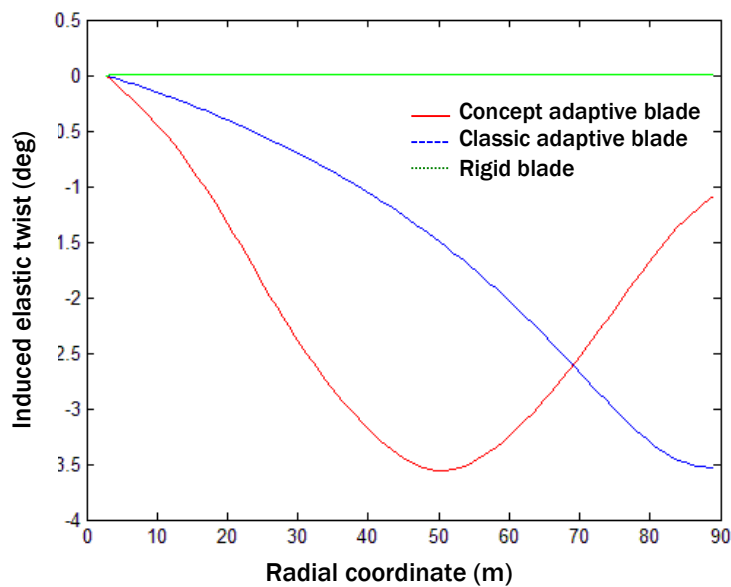


Figure 97: Induced elastic twist distribution for a steady wind speed of 11.5 m/s

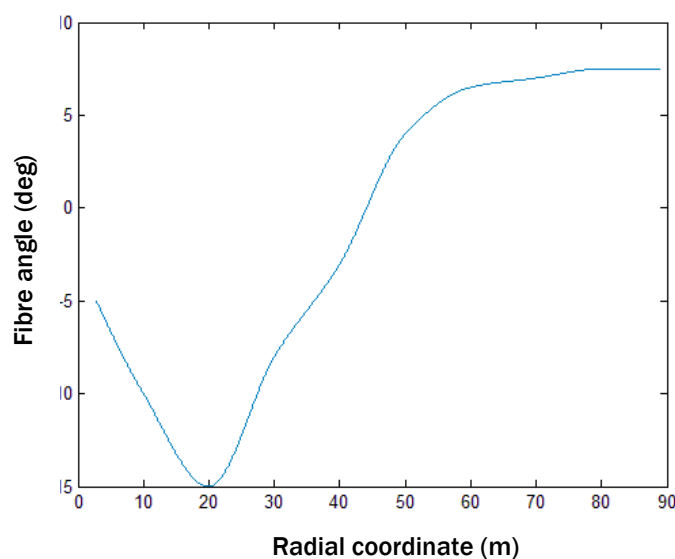
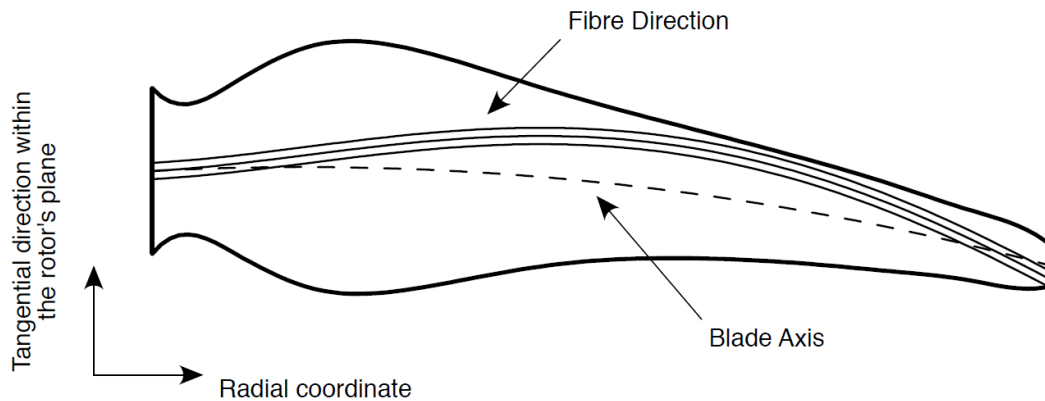


Figure 98: Distribution of fibre angle with radial position

Figure 99 shows a schematic design of the fibre path along the curved blade planform, representative of a concept adaptive blade design. As shown in the diagram the fibre angle increases positively (with respect to the blade axis) in the first half of the blade, before reducing towards a negative value in the outboard half of the blade.



**Figure 99: Schematic of the fibre path over the curved blade planform**

### 3.2.4.3 Dynamic aeroelastic analysis with gust response

The aeroelastic response of all blades, subject to gusts with average wind speeds of 8.5 m/s, 11.5 m/s, and 13.0 m/s, is now analysed.

#### 3.2.4.3.1 Gust response for 8.5 m/s wind (below rated)

Figure 100 shows the wind gust profile for a standard class I wind turbine with category A gust, relative to a hub wind speed of 8.5 m/s. For the first twelve seconds of the dynamic analysis, the wind speed is set constant to allow the model to achieve equilibrium (allowing for any transient effects to settle). This has been shown in a separate analysis which is not detailed here. Then, the gust is applied over 10.5 seconds, and the response of the structure is studied for all three designs. The numerical solution is obtained by using Matlab ODE solvers (*ode45* and *ode15s*).

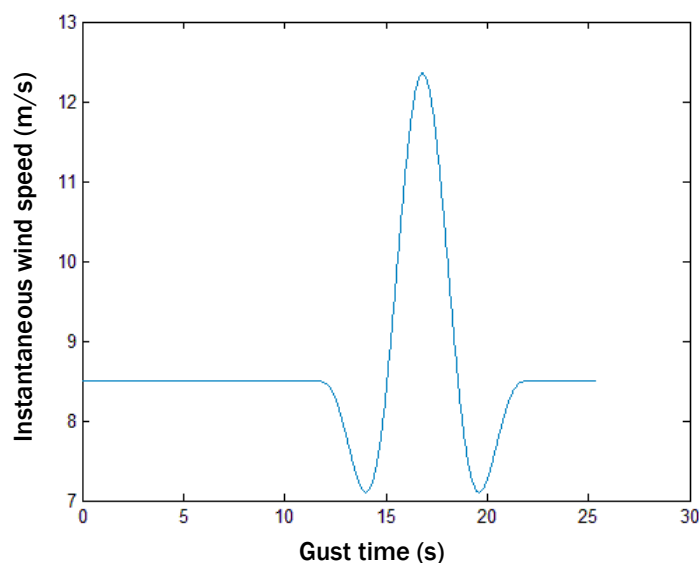


**Figure 100: Wind gust profile for a steady wind speed of 8.5 m/s.**

A gust load analysis is applied to all three blades (rigid, classic adaptive, and novel adaptive). Figure 101 shows the gust load response of the different structures to the gust, in terms of flapwise bending moment. For this wind load case, the maximum flapwise bending moments at the root for both the classic and concept adaptive blades are visibly reduced (2.6% and 2.9% reduction respectively). The concept blade notably outperforms the classic adaptive solution in terms of potential improvement in fatigue life, with an 8.6% reduction in amplitude of bending oscillations for the concept blade against 4.5% for the classic design. Table 30 summarises these findings compared to the rigid blade design.

A reduction in flapwise load oscillations is seen as more important than simply reducing the maximum flapwise bending moment [25]. Here, because the out-of-plane vibration is significantly lower than for the adaptive designs, the fatigue life of the blade is expected to increase. This also indirectly leads to weight savings upon detailed structural design, as the cap thickness can be decreased for a similar dynamic response.

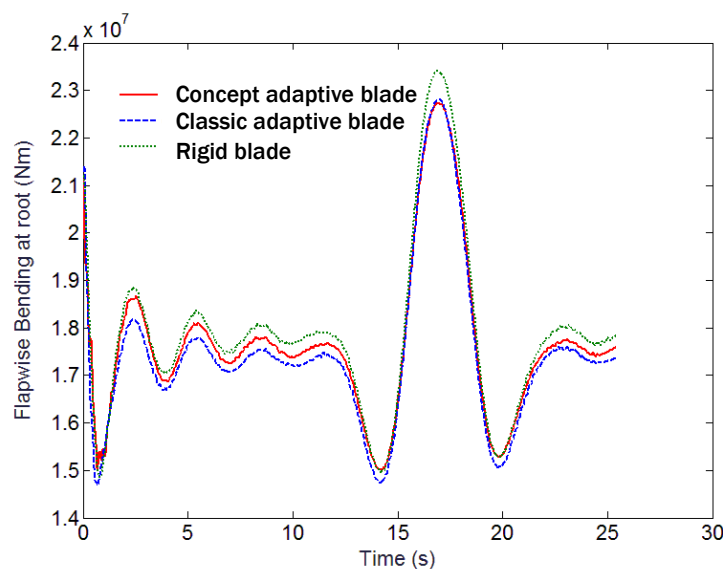


**Figure 101:** Flapwise bending moment at the root in response to a 10.5 s gust for a steady wind speed of 8.5 m/s

**Table 30. Summary of gust load alleviation results for the Innwind blade designs for a steady wind speed of 8.5 m/s**

Blade configuration	Decrease in maximum flapwise bending moment	Decrease in amplitude of flapwise bending oscillations
Rigid	-	-
Classic adaptive	2.6%	4.5%
Novel adaptive	2.9%	8.6%

### 3.2.5 Gust response for 11.5 m/s wind (at rated)

Figure 102 shows that for a gust with an 11.5 m/s steady wind (rated) speed, the concept adaptive blade significantly outperforms the other designs, with a 4.2% reduction in root bending moment, and a 16.0% decrease in the amplitude of flapwise oscillations. Table 31 summarises the findings for all three blade designs.

This wind speed is associated with the highest gust load alleviation capability. This result was expected, as the rated wind speed was chosen as the operating condition to compute the targeted induced twist. This results in a total twist which is close to the optimum solution, producing a blade that is more efficient at reducing gust loads.

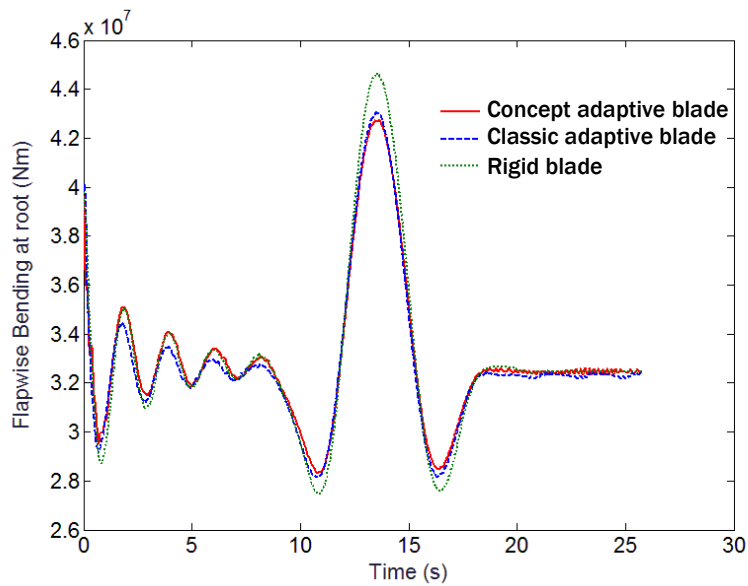


**Figure 102:** Flapwise bending moment at the root in response to a 10.5 s gust for a steady wind speed of 11.5 m/s

**Table 31. Summary of gust load alleviation results for the Innwind blade designs for a steady wind speed of 11.5 m/s**

Blade configuration	Decrease in maximum flapwise bending moment	Decrease in amplitude of flapwise bending oscillations
Rigid	-	-
Classic adaptive	3.6%	13.3%
Novel adaptive	4.2%	16.0%

### 3.2.5.1.1 Gust response for 13.0 m/s wind (above rated)

A third case, above the rated speed, is now considered (13.0 m/s). At this speed, the concept blade becomes less effective than the classic adaptive blade at reducing the amplitude of flapwise bending oscillations, as shown in Table 32. However, the novel blade design still retains the ability to decrease the root bending moment, when compared to a rigid blade design.

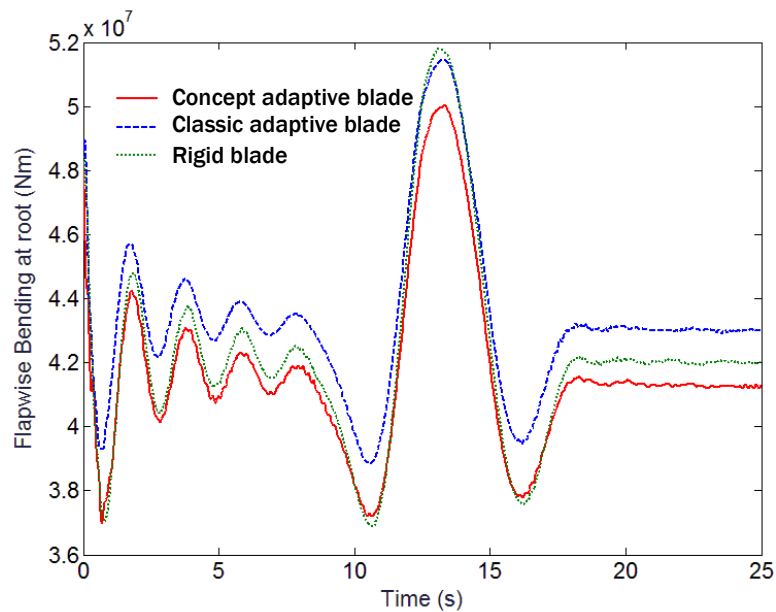


**Figure 103: Flapwise bending moment at the root in response to a 10.5 s gust for a steady wind speed of 13.0 m/s**

**Table 32. Summary of gust load alleviation results for the Innwind blade designs for a steady wind speed of 13.5 m/s**

Blade configuration	Decrease in maximum flapwise bending moment	Decrease in amplitude of flapwise bending oscillations
Rigid	-	-
Classic adaptive	0.6%	15.5%
Novel adaptive	3.4%	13.8%

### 3.2.5.1.2 Conclusions

In conclusion, the novel adaptive Innwind blade performs overall better than the reference Innwind blade in terms of reducing the flapwise bending loads and amplitudes of flapwise oscillations. It also performs better than or as well as a classically adaptive design. At the rated wind speed, the concept adaptive design reduces the amplitude in flapwise bending oscillations by 16% compared to the DTU reference blade. This is a significant result which, if implemented, could considerably enhance the fatigue life of the concept blade.

### 3.2.6 Conclusions

In conclusion the work performed by UBRISTOL and described in the current section has outlined several methods to improve the structural design of the Innwind blade by introducing a new aeroelastically tailored approach. By combining tow-steered fibres and a variation of the spar geometry and orientation, the new blade design produces an induced elastic twist which better approximates the optimum twist of the blade across its entire operating range.

Results of a previous study on a Vestas V90 blade (REF) showed a substantial improvement in Annual Energy Production (around 2%) without any active pitch control. This blade performs better than or equally as well as a classically-design blade with pitch control, suggesting that pitch control could be eliminated, potentially reducing the weight and cost of the whole wind turbine.

It was found that by applying the same methodology to the Innwind DTU Reference blade produced only a 0.3% theoretical increase in AEP. This was attributed to the marked difference in angular speed distribution, among other factors, including thickness to chord ratio of the aerofoils. It was

noted that a classically adaptive design (with monotonically increasing induced twist) carries a penalty in the AEP; therefore, the novel adaptive design represents an improvement with respect to a classic design approach.

A gust load study was then applied to the Reference DTU blade to investigate the ability of each blade technology (rigid, classic adaptive and novel adaptive) to passively reduce loads. The novel adaptive design was successful in reducing both root bending loads and the amplitude of flapwise bending oscillations at below-rated, rated, and above-rated speeds. These improvements in gust load alleviation were comparable to those of a classically adaptive blade.

A summary of the qualitative results of this study is presented in Table 33 and shows the benefits of each blade technology compared to the reference DTU blade. While a classically adaptive blade increases gust load alleviation, this comes at the expense of the annual energy production of the blade. In the novel adaptive blade, both conditions are fulfilled simultaneously.

**Table 33. Summary of benefits of each blade technology, compared to the rigid Innwind blade.**

Blade configuration	Annual Energy Production	Gust load alleviation	Overall performance
Rigid	-	-	-
Classic adaptive	Decrease	Increase	Undetermined
Novel adaptive	None or increase	Increase	Increase

Overall, these results suggest that the concept adaptive blade is able to provide both a constant or improved AEP performance and a gust load alleviation capability with respect to rigid designs. This novel concept therefore scores better overall than either the rigid or the classic adaptive blades, which are unable to fulfil both these requirements simultaneously.

### 3.3 Passive control strategies for wind turbine blades (DTU)

#### 3.3.1 State of the art and motivation

As wind turbines capacities and dimensions increase, blade designers and manufactures have taken up the challenge of designing and building blades that are stronger and lighter. The capability of efficient load mitigation on the structure during operation becomes an attractive characteristic for the design of modern wind turbine blades. To this end, different techniques have been exploited in the last two decades to achieve load reduction on wind turbines. In particular, the so-called “passive control methods” represent an interesting possibility for wind turbine blade designers. These types of methods are based on the idea of designing a structure that deforms so as to provide a load reduction during operation.

Passive control methods can be implemented by e.g. using the following mechanisms:

- employment of backward swept blades;
- bend-twist coupling (BTC) due to anisotropic properties of fiber-reinforced composite materials.

The objective of the implementation of these control strategies is the same: to introduce a structural coupling between bending toward the tower and torsion toward feather that has the effect of decreasing the angle of attack along the wind turbine blade, thus mitigating the loads on the structure.

In the last two decades, several studies have been conducted to show the passive control potential of either swept wind turbine blades [47], [48], [49], [50], [51], [52] or bend-twist coupled blades [27], [53]. So far, the research within wind energy field has been focused on the development of

blade designs that employs only a single passive control strategy at a time. The current work aims at studying the load alleviation potential for a combination of passive control methodologies with the final goal of proposing new and innovative concepts for lightweight wind turbine blade designs.

In the present investigation, several designs involving both modification of geometry of an originally straight blade and modification of the blade structure, i.e. orientation of blade materials are considered. A single-shear web design is also proposed. The initial idea related to the use of a single shear web design was to enhance the effects of backward swept blades and BTC due to a consistent decrease of blade torsional stiffness. Later analysis showed that a blade design with decreased torsional stiffness presents characteristics very similar to a blade with passive control. Due to the use of cambered airfoils, when the single-shear-web blade bends toward the tower it has the tendency of twisting toward feather, hence decreasing the angle of attack. For this reason, the single shear web design is considered as a passive control itself in this work.

Three passive control strategies are evaluated and combined in different blade designs. Blade stiffness and strength properties for each of the chosen blade design are analysed and reported. Full design load bases (DLB) are carried with the purpose of evaluating extreme and fatigue loads on the blades based on standard requirements for wind turbine construction and operation. The computed loads are compared to the DTU 10MW Reference Wind Turbine [1], which is used as a baseline for the studied passively controlled wind turbines. General observations are provided with the intention of gathering knowledge regarding the efficiency of each control strategy alone and their combinations.

Section 3.3.2 of the report describes the considered passive control methods for blade designs and the motivation behind the work. Models and tools used throughout the investigation are reported in section 3.3.3, along with a brief description of the baseline wind turbine, its controller and the DLB considered. Results for the modified blade configurations, including blade structural properties and strength characteristics, blade loads, annual energy production and tower clearance are presented and discussed in the following section. The last part of the chapter includes conclusions and future work.

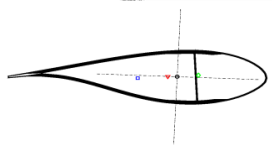
### 3.3.2 Brief description of the concept

Three passive control strategies are taken into account: blades with backward sweep, blades with BTC and blades with single shear web. The final goal is first to study the effects of each of these methods separately, and then in different combinations. Extensive load and strength analyses are performed in order to prove the possibility of exploiting the synergies between these methods. The idea is to enhance the benefits from each of the strategy applied alone and to reduce the negative effects by combining the methods. A summary of the passive methods considered here is given in Table 34.

Each column in Table 34 describes a different method, classified by a three letters code (SSW for the blade design with single shear web, SWP for the swept blade and BTC for the blade with bend-twist coupling). The rows contain information regarding:

- application zone - area where the control strategy is applied according to the span-wise position;
- mechanism of the passive control strategy;
- outcome - the qualitative effect of each control strategy;
- required design corrections - general design adjustments to be considered for implementing the method into the blades.

Table 34. *Passive control methods description*

			
	Single shear web (SSW)	Sweep (SWP)	Bend-twist coupling (BTC)
Application zone	Full Blade	Blade tip	UD layers of spar caps
Mechanism	Twist to feather due to lower torsional stiffness	Twist to feather by extra tip torque	Twist to feather due to twist generated by BTC and bending loads
Positive outcome	<ul style="list-style-type: none"> <li>• Passive load alleviation due to decreased angles of attack in operation,</li> <li>• Slightly higher tower clearance</li> </ul>	<ul style="list-style-type: none"> <li>• Passive load alleviation due to decreased angles of attack in operation</li> <li>• Higher tower clearance</li> </ul>	<ul style="list-style-type: none"> <li>• Passive load alleviation due to decreased angles of attack in operation</li> <li>• Higher torsional stiffness (potentially positive)</li> </ul>
Negative outcome	<ul style="list-style-type: none"> <li>• Lower torsional stiffness (potentially negative)</li> </ul>	<ul style="list-style-type: none"> <li>• Higher torque load along the blade</li> <li>• Higher torque load at the pitch actuator</li> </ul>	<ul style="list-style-type: none"> <li>• Lower tower clearance due to lower bending stiffness</li> <li>• Lower strength of the biased UD layers</li> </ul>
Required design corrections	Check on structural design especially for buckling of caps shear web and sandwich panels	Pitch toward stall to compensate AEP loss below rated wind speed	Pitch toward stall to compensate AEP loss below rated wind speed

The following points have to be highlighted in order to clarify some of the presented choices for the passive control strategies applied in each blade design:

- the application zones for the different methods have been chosen based on the analysis of the possible outcomes;
- the application of the SSW on the full blade span is bounded to manufacturing constraints;
- the swept blade design is selected according to a parametric study performed by the authors, taking into account load alleviation potential and a restrained increase in extreme and fatigue blade root torsional loads (to be published);
- the shape for the swept blade is chosen to be a pure backward sweep where the change in the shape starts at 80% of the blade length with the maximum sweep of around 2m at the tip;
- the application zone for the BTC is chosen after preliminary consideration of the blade strength and structural properties;
- after few design iterations, an angle of 8° was selected for biasing of the UD layers in the spar caps.

All the choices related to the control strategies are made with the general idea of exploiting the synergy between the three passive control methods. Consider for example the tower clearance: a backward swept blade is able to increase the tower clearance due to its structural properties, at the same time providing beneficial load alleviations on the blades. The BTC can reduce the loads acting on the structure, but it also decreases the bending stiffness of the blade, lowering the tower

clearance. Hence, a combination of SWP and BTC can result into a favourable load alleviation effect still maintaining the tower clearance required by the design standards.

The full list of the wind turbine blade design analysed within the present investigation is reported hereby together with their acronyms in the parenthesis:

- Baseline straight blade
- Swept blade (SWP)
- Blade with BTC (BTC)
- Straight blade with single shear web (SSW)
- Swept blade with single shear web (SWP+SSW)
- Swept blade with BTC (SWP+BTC)
- Straight blade with single shear web and BTC (BTC+SSW)
- Swept blade with single shear web and BTC (SWP+BTC+SSW)

### 3.3.3 Models Description, Baseline Wind Turbine and DLB

Linear aero-servo-elastic models are implemented in HAWCStab2 and used for closed-loop eigenvalue analysis and controller tuning. Further, nonlinear aeroelastic models, implemented in HAWC2, are used for response analysis in time domain. Structural properties of the blade cross-sections are calculated using the in-house Beam Cross section Analysis Software –BECAS.

HAWCStab2 is based on a linearization of Timoshenko beam elements in a nonlinear co-rotational formulation coupled with an unsteady blade element momentum (BEM) method. Shed vorticity, dynamic stall and dynamic inflow are included in the aerodynamic model. A detailed description of the HAWCStab2 architecture is provided by Hansen [49]. Sønderby and Hansen [53] made an exhaustive validation and analysis of the open-loop performances. A description of the linearized wind turbine controller is given by Tibaldi et al. [54].

The structural model of HAWC2 is based on a multi-body formulation using Timoshenko beam elements developed by Kim et al. [55]. The aerodynamic model, also based on the BEM method, handles dynamic inflow, dynamic stall, skew inflow, shear effects on the induction and effects from large deformation. Validation can be found in Vorpahl et al. [56], Popko et al. [57] and in Larsen et al. [58].

BECAS [59] is a group of Matlab functions used for 2D analysis of stiffness and mass properties of generic beam cross sections. Two pre-processing scripts included in the BECAS package, Airfoil2BECAS [60] and ShellExpander [61], have been used to generate the FE meshes that served as input into BECAS. They are two python scripts designed to generate 2D-meshes of blade cross-sections with specified materials and their corresponding spatial orientations in BECAS format.

The DTU 10 MW Reference Wind Turbine (RWT) [1] is used as the baseline turbine in this study. The Basic DTU Wind Energy Controller [62] is used and its description with regard to the DTU 10 MW RWT is provided by Bak et al. [1].

The DLB used is the DTU Wind Energy Design Load Basis for onshore turbines [63], which is based on the third edition of the IEC 61400-1 standard. The DTU DLB covers typical cases for assessment of extreme and fatigue loads on the turbine components. The DTU 10 MW RWT was designed before the formulation of the DTU DLB, using a slightly different IEC 61400-1-inspired load basis as reported by Bak et al. [1] in chapter 6.3 of the report. Therefore, the following modifications are made to the DTU DLB to have a load basis similar to the one used to design the baseline turbine:

- The controller dependent design case DLC 2.2 is disregarded
- The extreme values of the loading from DLC 1.1 are not determined using any statistical extrapolation, because of the uncertainty related to the choice of an appropriate method; instead, the GL approach [9], which requires a partial safety factor of 1.35, is adopted.

### 3.3.4 Description of the Workflow

A summary of the workflow used to build the analysed passive-controlled blades is provided in Figure 104. The programs and tools used for each step of the workflow and reported in the previous section have been described here they are highlighted in red boxes.

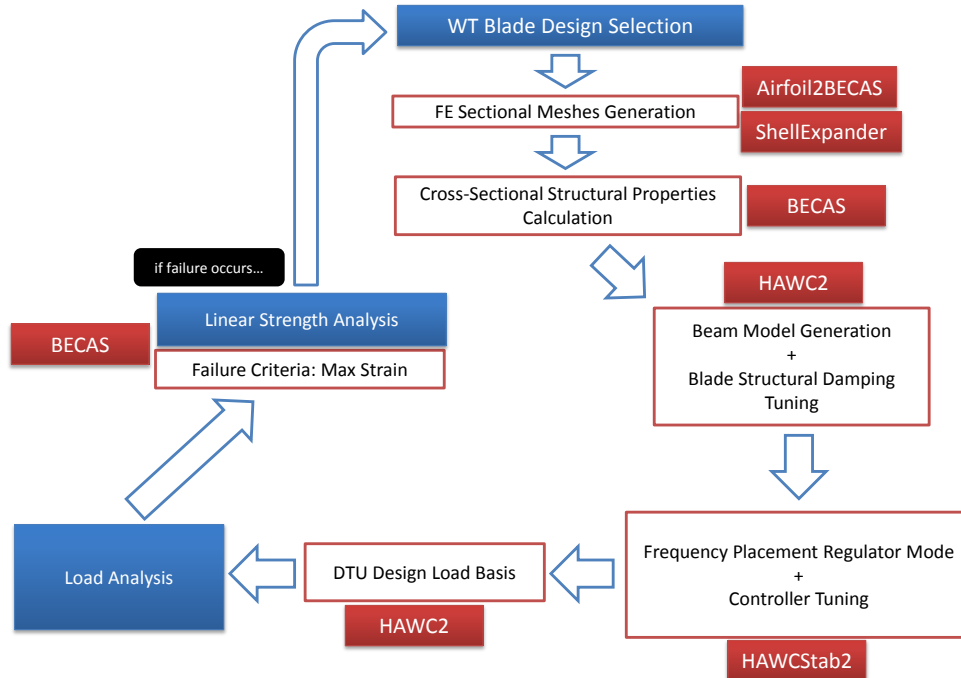


**Figure 104** Workflow diagram for input generation and analysis of selected blade designs.

After selection of a blade design is made, 2D FE meshes for 100 cross-sections along the blade span are generated using the DTU 10MW RWT input data. Cross-sectional structural properties are calculated and used for generation of the blade beam model. Structural damping of the beam is set to 3% for both flap-wise and the first edge-wise modes. Before launching the DLB and proceeding with the load analysis of the passively controlled wind turbine blades, each design is pre-processed to balance the following two negative effects associated with the chosen passive control methods:

- frequencies and damping ratios of the speed regulator mode of turbines with a passively controlled blades can be significantly different compared to the baseline, due to the changes in structural properties and dynamic behaviour;
- due to the decrease in angle of attack due to the passive control, the turbine considered to have lower Annual Energy Production (AEP) at wind speeds below rated compared to the baseline configuration.
- To overcome the first issue, tuning of the PI loop of the controller in Region 4 (constant power, torque and rotational speed) is performed with a pole placement technique. HAWCStab2 is used to perform this tuning adopting a method documented by Hansen et al. [63] and Tibaldi et al. [54]. The target damping ratio and the target frequency for the pole of the speed regulator mode at 12ms<sup>-1</sup> are respectively 70% and 0.1Hz for all the wind turbines within this study.

To compensate for the loss of annual energy production at wind speeds below rated, the passively controlled blades are pitched further toward stall compared to the baseline configuration. This is done according to the amount of twist provided by the control strategy and to compensate for the decrease in the angle of attack.

Load analysis for each wind turbine configuration is then carried out. Extreme and life time equivalent fatigue loads for the blade root and tower top are analysed for each blade configuration, verifying the AEP is close to the original values, and the tower clearance is sufficient.

### 3.3.5 Results

Results from the load and strength analyses are reported and discussed in this section. The main focus is to establish the effects of combined passive control strategies, assuming that all the analysed blade designs fulfil standard design requirements.

In the first part of the section, an overview concerning the AEP and the minimum tower clearance for the wind turbines designed is presented. A discussion regarding the computed blades structural properties and their possible impact on the loads is reported. Strength analysis is carried out in the following part of the section and analysis of the blade root and tower top extreme and life time equivalent fatigue loads for all blade configurations is given in the last part of the section.

#### 3.3.5.1 AEP and tower clearance

To keep performance and safety of the modified wind turbines at the original level, the annual energy production and minimum tower clearance are computed for each design and it is made sure they are not worse than of the baseline design.

The values of the tower clearance include the GL safety factors [9]. In the DTU 10 MW RWT report [1] the authors state that the tower clearance has enough margin for all the load cases considered. The minimum tower clearance reported in [1] is provided by DLC 1.3 and its value, including safety factors, is 5.86 m. The baseline tower clearance calculated using the workflow and tools of the present study is also provided by DLC 1.3 and its value is 5.63 m without safety factors. Therefore, the minimum clearance registered for the baseline turbine satisfies only the IEC standard requirements [64], since still clearance between blades and tower is left applying a safety factor of 1.35 indicated by the DLB used. The clearance left is 3.66 m. The guidelines given by GL [9] are not satisfied, since they require a 30% of the total tower clearance for the operation load cases (from DLC 1.x to DLC 5.x). The total tower clearance for the DTU 10 MW RWT is 18.26 m and the minimum tower clearance registered (3.66 m) for the DLB including the safety factors which is only 20% of the total. For this reason, the tower clearance required for the passively controlled wind turbines has to satisfy only the IEC standard.

A summary of the annual energy production and the minimum tower clearance computed for each of the designs considered within the present study is reported in Table 35. Results are given as variations in percent from the values for the baseline design.

Table 35. *AEPs and tower clearances compared to the baseline wind turbine*

Blade Design	AEP	Tower clearance
<b>Baseline</b>	<b>48.564 GWh</b>	<b>3.656 m</b>
SSW	- 0.3%	+ 1.3%
SWP	- 0.1%	+ 4.9%
SWP + SSW	- 0.4%	+ 8.6%
BTC	+ 0.04%	- 5.7%
BTC + SSW	+ 0.3%	- 11.6%
SWP + BTC	- 0.1%	- 4.0%
SWP + BTC + SSW	- 0.3%	- 1.0%

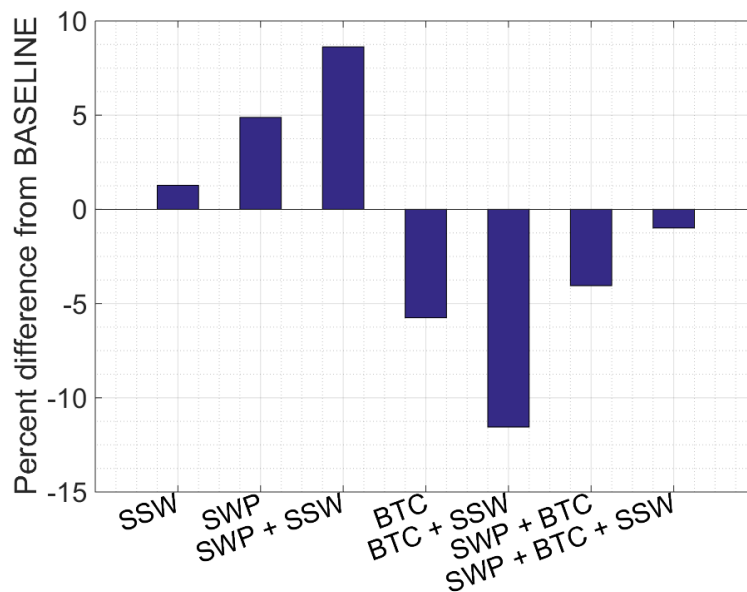


**Figure 105** Variation of the tower clearance of considered blade designs compared to the baseline configuration.

The annual energy production variations from the baseline are always lower than 0.5%. This is due to efficient strategy of pitching the blades toward stall at wind speeds below rated. Omitting this pitch angle tuning would cause a consistent drop in AEP level due to the nature of passive control mechanism to reduce the efficient angles of attack along the blade.

The tower clearance requirement according to the IEC standard is satisfied for all the passive-control designs, since none of the blades touches the tower for the implemented DLB. A diagram visualizing the differences in minimum tower clearances is given in Figure 105. The blade designs incorporating BTC generally show a substantial drop in minimum tower clearance, due to decrease in the blade flap-wise bending stiffness caused by the biasing of the fibers of the UD layers in the spar caps. As expected, the swept blades demonstrate lower tip displacements, which are reflected in a consistent increase of the minimum tower clearance. The combination of BTC and backward sweep in the blade design (SWP+BTC) helps compensating the negative effect of BTC on tower clearance, even though an increase of only 4% with respect to the baseline is registered. The combination of all three passive control methods produces a blade design with a minimum tower clearance very similar to the one of the baseline blade (difference of 1%).

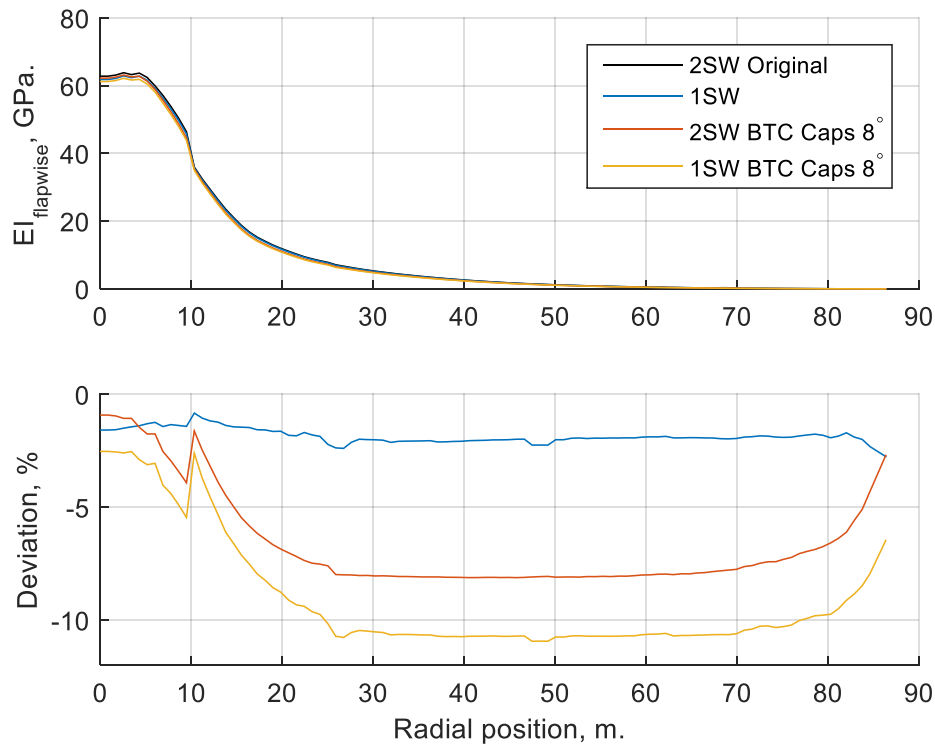
### 3.3.5.2 Blade stiffness properties

Here structural properties of the modified blades are presented. They are calculated by BECAS for each of the 100 cross-sections along the blades. Notice that stiffness properties of the swept blade configurations are not given as they are the same as for the straight blades. The sweep itself is assumed not to introduce any difference into the structural properties.

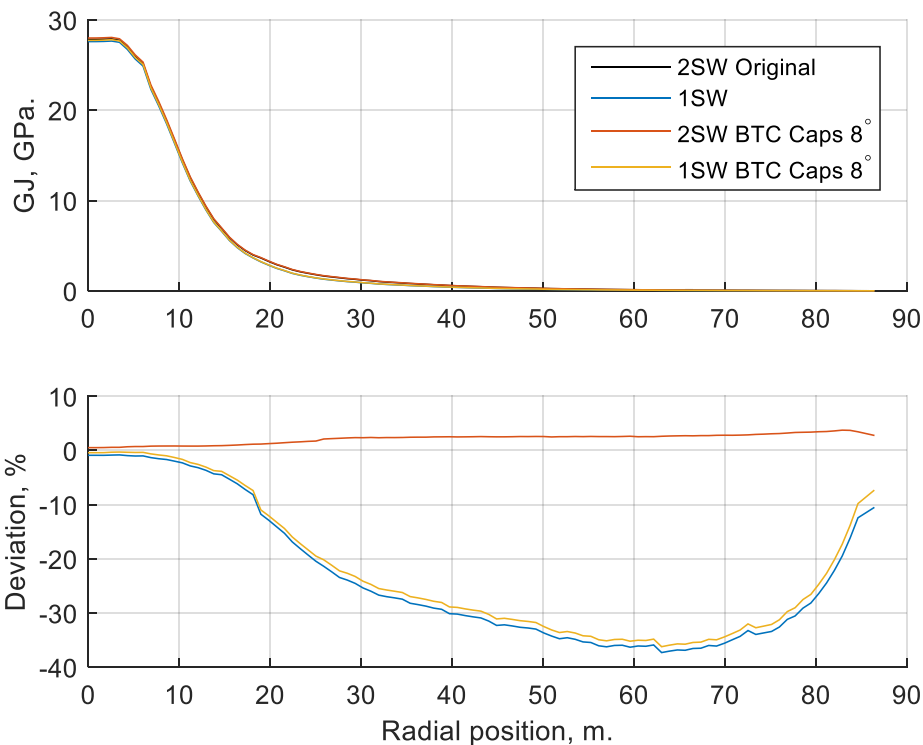
Stiffness properties of each of the considered blade configurations with passive control are compared to the ones of the baseline blade configuration. The results for flap-wise stiffness are given in Figure 106. It becomes clear that the introduction of the fiber biasing into the UD layers of the spar caps leads to significant drop in blade flap-wise bending stiffness, up to 7-8%, see the “2SW BTC” curve. While the single shear web blade design alone leads to minor reduction in the blade flap-wise bending stiffness, combination of the single shear web and fiber biasing in the same design leads to maximum drop in the bending stiffness, which is the reason for decreased tower clearance of ca. 11.6%, see Table 35.

Figure 107 demonstrates the variation of the blade torsional stiffness for different blade designs. The single shear web blade design possess much lower (up to 35%) torsional stiffness which could be a potential problem, e.g. in the runaway case where it might cause flutter, but this is not verified

in the present investigation. Another interesting fact is that the fiber biasing according to the BTC design cannot provide any reasonable recovery of the torsional stiffness in the single shear web blade design, +2...+3% at maximum. This is confirmed with the torsional stiffness growth for the BTC only blade design. It can be an indication that the UD layers of the spar caps is not the best position for fiber biasing if one wants to increase the blade torsional stiffness.



**Figure 106 Flap-wise bending stiffness for different blade designs and its deviation from baseline blade characteristics.**



**Figure 107 Torsional stiffness for different blade designs and its deviation from baseline blade characteristics.**

The next interesting plot demonstrates the amount of BTC along the blades with biased fibers in the spar caps UD layers, see Figure 108. The flap-wise bending-twist coupling coefficient  $\beta$  is calculated along the blade length in accordance to the method described in [65]. The figure shows that generally higher coupling can be achieved for the original two-shear web blade than for the modified single shear web blade. This fact agrees well with the results obtained for the coupled box- and I-beams in [65]. Thereby, the BTC and single-shear web methods for passive load control seem to interfere with each other and can unlikely be recommended for combination in the same blade design when the BTC effects are prioritized.

### 3.3.5.3 Blade strength

In order to ensure operational blade designs it is important to perform strength calculations on the blades. In the present investigation this is done for extreme load cases according to the DLB. This means that the blade strength is checked at the most critical loads expected to occur during the wind turbine lifetime, also taking into the account the safety factors prescribed by IEC standard.

Strength analysis was performed in BECAS for 27 cross-sections along the blade length. It was done for a number of critical load cases occurred in the aeroelastic simulations for each blade configuration. The failure criterion chosen for the strength analysis was the maximum strain criterion. The choice is dictated by the fact that this criterion was chosen to design the baseline DTU 10MW RWT blade. Selected results for the failure index, which shows how close is each of the sections to failure ( $FI = 1$ ), are shown in Figure 109.

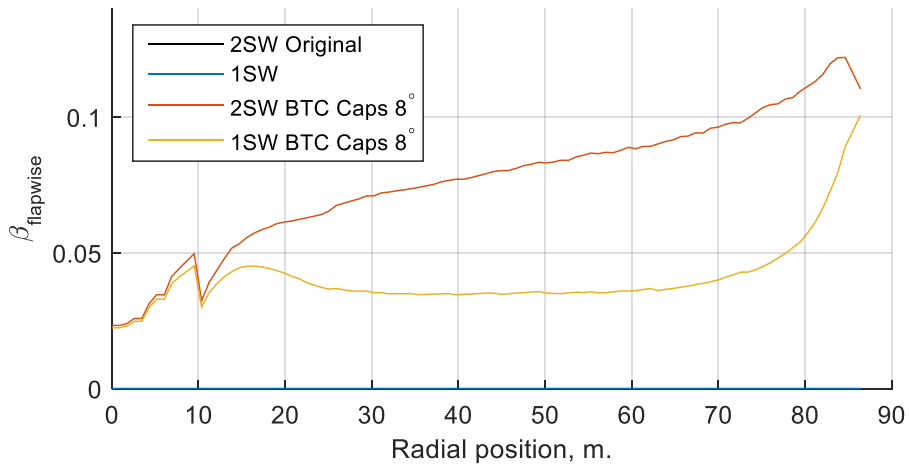


**Figure 108 Flap-wise bend-twist coupling coefficient  $\beta$  for different blade designs.**

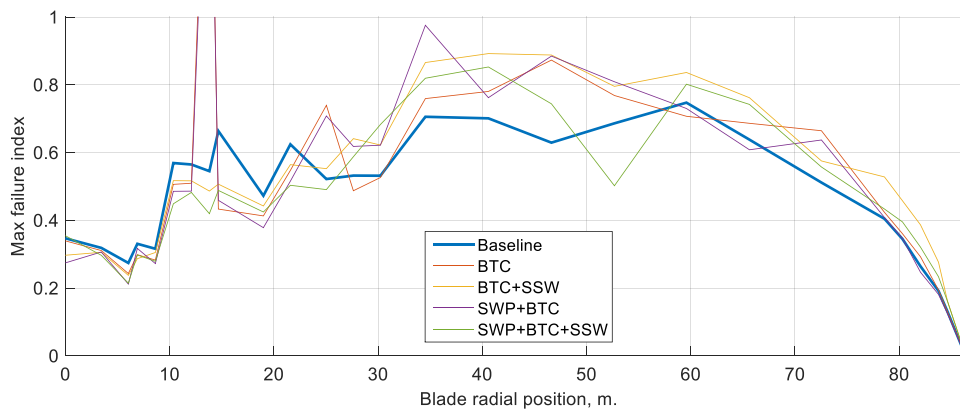


**Figure 109 Strength characteristics for some of the blade designs considered in the present investigation.**

As one can see from the results for failure indices, all the modified blade designs increase the failure index along most of the blade length, except for the blade root. This is believed to be the case due to the positive effect of the passive load control which reflects lower extreme loads at the root and generally lower strength of the blade due to introduction of BTC and single shear web concepts. Generally, all the blade modifications are shown to be strong enough to resist the extreme lifetime loads.

Figures with more details on strength of blades of different configurations are given in the APPENDIX A; Strength plots for configurations of section 3.3.

#### 3.3.5.4 Extreme and lifetime equivalent fatigue loads

Extreme and lifetime equivalent fatigue are reported in this section. The loads are calculated at two positions on the wind turbine: the blade root and the tower top.

Figure 110 and Figure 111 show blade root bending and torsional loads respectively. In general, all passive control strategies produce alleviations for both extreme and fatigue bending loads in the range between 5 and 10%.

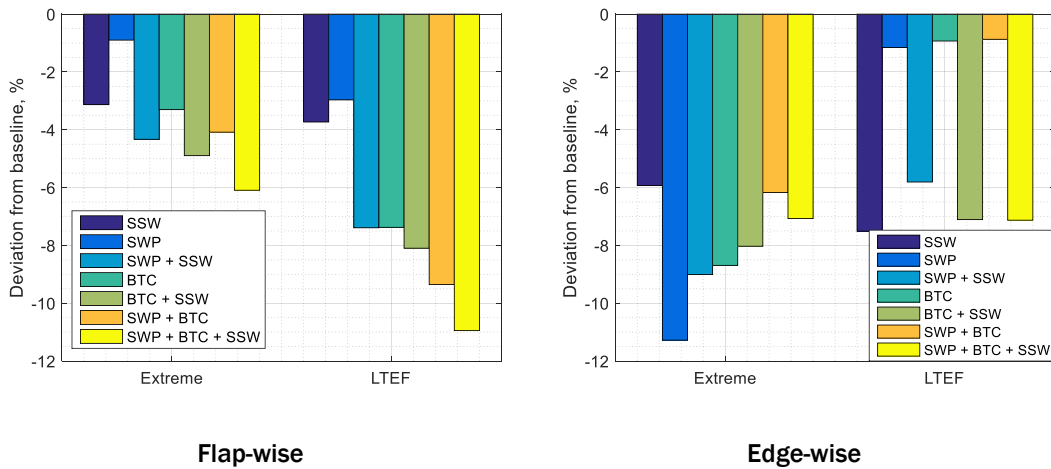


**Figure 110** Extreme and life-time equivalent fatigue (LTEF) bending moments for the blade root.

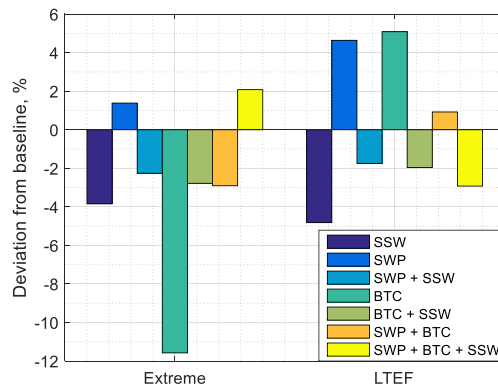


**Figure 111** Extreme and life-time equivalent fatigue (LTEF) torque values for the blade root.

In the flap-wise case, the combination of all the three control methods demonstrates the highest drop in both extreme and fatigue loads (6% for extreme and ca. 11% for fatigue values). The flap-wise load alleviation for the combined designs is stronger than for the isolated passive control designs.

The swept blade design is the most efficient for the extreme edgewise blade root loads. The single shear web design and its combinations prove to be the most effective choice for the lifetime equivalent blade root edgewise fatigue load. This outcome is due to the fact that these loads are mostly driven by gravity forces which are linked to the total mass of the blade. The SSW designs have lower blade mass, which is decreased by 7.5% compared to the DTU 10MW RWT blade due to the presence of only a single shear web against the three used for the baseline design.

It is worth mentioning here that the single shear web design will likely lead to a significantly lower buckling resistance of the blade and therefore the blades with single shear web configurations ideally have to be analyzed for this type of failure. Presently this type of analysis has not been performed as it requires modeling and computational recourses and is therefore planned for future work.

The backward swept blade has a negative impact on the blade root torsional moment (1.5% increase in extreme and 5% increase in fatigue), due to the extra torque generated by the swept tip of the blade. BTC shows a strong alleviation of the extreme blade root torque (11%) and a large increase in the lifetime equivalent fatigue load (around 5%). A clear reason for the latter is

unknown. SSW alleviates both extreme and fatigue torsional moments. In general, while the results for blade root torque for the swept design have been expected, it was not possible to define a clear trend for the other passive control strategies and, consequently, for their combinations. Further investigations regarding the blade root torsional loads need to be performed, as well as eventual evaluation of the impact on the pitch controller and the aero-servo-elastic dynamics of the system.

Figure 112 shows the extreme and fatigue loads for the tower top. This is presented to demonstrate the load alleviation potential of the passive control strategies on other wind turbine components.

The extreme fore-aft tower top moment decreases for all the considered designs. The alleviation reaches a maximum of around 9% for the case with all the three strategies combined. The result is in-line with the observations made regarding the blade root extreme flap-wise moment. The side-to-side extreme load does not show any considerable variation respect to the baseline design.

The two designs SWP+SSW and BTC have the most beneficial effects on the fore-aft tower top fatigue load, showing peak alleviations slightly higher than 9%. The combined designs are more efficient towards the side-to-side fatigue load reduction, where the SWPT+BTC+SSW and the BTC combined cases are able to reduce the lifetime equivalent load by almost 4%.

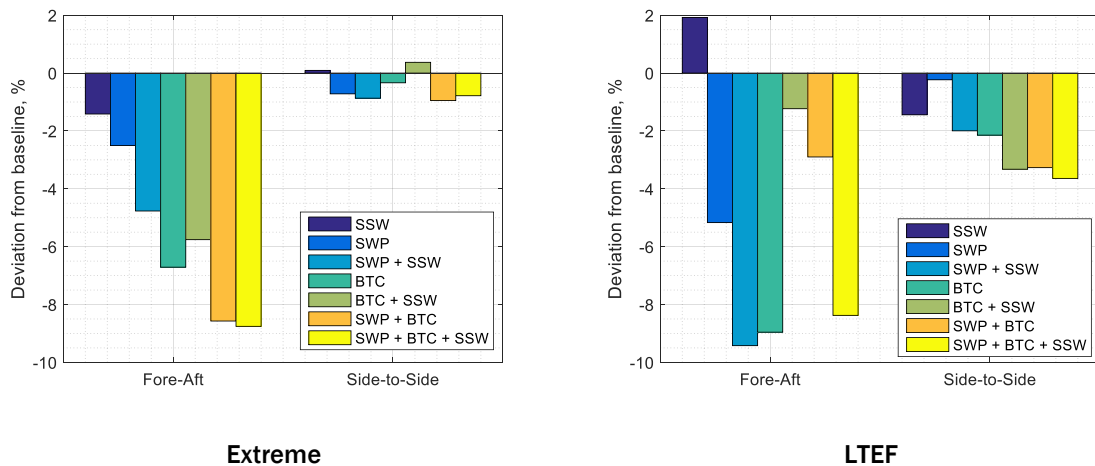


**Figure 112** Extreme and life-time equivalent fatigue (LTEF) values of the tower top fore-aft and side-to-side loads.

### 3.3.6 Conclusions and recommendations

Three passive control strategies for wind turbine blade design have been considered for the DTU 10MW reference wind turbine and the impact on loads and strength of the blades has been evaluated. The following passive control blade designs have been considered:

- backward swept blade, where change in the shape starts at 80% of the blade length with the maximum sweep at the tip at around 2m;
- BTC design, where the fibres of the UD layers in the spar caps are biased by 8°;
- single shear web design.

Several studies previously reported in the literature have already established the load alleviation potential of two of these passive control methods (blade sweep and material bend-twist coupling). Present work investigated synergies between these methods applying different combination of these passive controls strategies to a given blade design.

All the considered blade designs matched the requirements for blade strength and tower clearance. The deviation of the annual energy production from the baseline value was limited to lower than 0.5% design and it was kept at this level throughout the study.

The results showed that the right combination of passive control strategies can lead to a blade design capable of enhancing the load alleviations and diminishing negative effects from each of the passive control strategies. An example is the combination of the BTC and the backward sweep in the same blade, resulting in the blade root flap-wise fatigue loads being lower with respect to the baseline (4%) and with respect to the only-swept blade design (6% extra load alleviation) and the BTC-only design (2% extra load alleviation). At the same time, combining the swept blade design with the BTC helped to compensate the decrease in minimum tower clearance caused by the loss in bending stiffness due to the rotation of the fibres of the UD layers in the spar caps.

The single shear web design and backward sweep proved to be a good passive control combination for the reference blade. The load alleviation effects of the swept blade were enhanced by the lower torsional stiffness of the single shear web design. The blade root flap-wise life time equivalent fatigue loads for the single shear web design decreased by ca. 3.5% and the same load for the swept blade decreased by 2.5%, while combining the two designs brought a total load alleviation of 7%.

The single shear web design and BTC design combination did not produced the desired boosting in terms of load alleviation. The reason lies in the bend-twist coupling parameter  $\beta$ , which is lower along the blade span for the combined BTC+SSW design, than for the BTC-only design. The consequence of lowering the coupling coefficient  $\beta$  was observed in the tower top fore-aft extreme and fatigue loads. The BTC design has much higher load alleviation than the combined BTC+SSW case.

The blade root edge-wise fatigue loads are driven by gravity and a blade with lower mass such as the single shear web design (7.5% lower mass than the baseline) and its combination can bring a 7% decrease in lifetime equivalent moment.

The combination of all the three passive control strategies in the same reference blade is effective only with respect to the blade root flap-wise extreme and fatigue moments. For the blade root edge-wise loads and the tower top bending moments, the SWP+BTC+SSW design did not produce further load alleviations compared to the other combinations. The reason is the negative impact from the combination of BTC and single shear web design.

In general, all the passive control strategies and their combinations produced substantial changes in the structural properties of the blade. To better adapt these methods to exploiting their full potential, the blade has to be re-designed from the structural point of view, by e.g. moving materials and changing the thicknesses of the blade layups according to the needs. An optimization framework is seen to be used in the future studies to fulfil this purpose. Buckling analysis for the blade and stability analysis will also be provided in future investigations.

### 3.4 Structural blade designs with build-in structural couplings (CENER)

In this session the work done by CENER under Subtask 2.2.2 related to lightweight structural new blade designs and blade designs with build-in structural couplings is described.

Main item achieved from the work done has been the integration of structural coupling theory in the tools and methodology used by CENER for blade design. Under this work, Karaolis theory has been analyzed, validated & implemented in BASSF. BASSF (Blade Analysis Strain Stress Failure) is the analytical tool of CENER for the structural pre-design of blades. It is internally developed software based on analytical formulation available in the web-site for external users ([http://www.cener.com/en/wind-energy/en\\_signup.asp](http://www.cener.com/en/wind-energy/en_signup.asp))

In addition, a preliminary practical exercise comparing two blade designs in terms of structural performance, power production and loads has been completed:

- ✓ Conventional blade: Symmetric lay-up design using those materials of the structural benchmark [1], [22] and an internal architecture configuration based on:
  - Structural shells that integrate: the spar-cap lay-up of 800mm width from  $\approx 8\text{m}$  to  $\approx 83\text{m}$ , the leading edge reinforcement of 500mm width from  $\approx 1\text{m}$  to  $\approx 72\text{m}$ , and the

- trailing edge reinforcement of 800mm width from ≈5m to ≈63m
- Two main shear-webs located at equal distance from the PITCH axis and separated one another with a constant value of 750mm from ≈3m to ≈83m
- One additional shear web from ≈17m to ≈83m located close to the trailing edge that avoids peeling effects at the trailing edge bonded joint
- ✓ Coupled design: Obtained with an asymmetric lay-up by a 5° misalignment of the spar-cap unidirectional fibers, so that the trailing edge moves in the direction define in Figure 113 when flap wise bending moment increases.

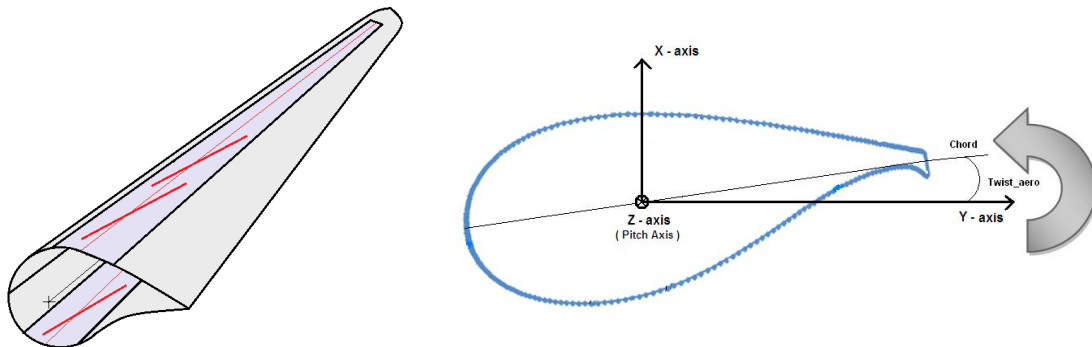


**Figure 113 Misalignment of 5° at spar-cap unidirectional fibers for structural coupling**

Further work is planned to be performed by CENER until the end of 2015 to understand in detail the influence of different asymmetric lay-ups on the structural coupling behavior and its consequences on blade holistic optimization.

### 3.4.1 Karaolis approach

#### 3.4.1.1 Theoretical basis

The basis of Karaolis coupling theory is based on the classical lamination theory, in particular on the stress-strain relation of a composite thin plate:

$$\begin{Bmatrix} \epsilon_x \\ \epsilon_y \\ \gamma_{xy} \\ \kappa_x \\ \kappa_y \\ \kappa_{xy} \end{Bmatrix} = \begin{bmatrix} a_{11} & a_{12} & a_{16} & b_{11} & b_{12} & b_{16} \\ a_{21} & a_{22} & a_{26} & b_{21} & b_{22} & b_{26} \\ a_{61} & a_{62} & a_{66} & b_{61} & b_{62} & b_{66} \\ b_{11} & b_{12} & b_{16} & d_{11} & d_{12} & d_{16} \\ b_{21} & b_{22} & b_{26} & d_{21} & d_{22} & d_{26} \\ b_{61} & b_{62} & b_{66} & d_{61} & d_{62} & d_{66} \end{bmatrix} \cdot \begin{Bmatrix} N_x \\ N_y \\ N_{xy} \\ M_x \\ M_y \\ M_{xy} \end{Bmatrix} \quad \text{Eq. 1}$$

Where:

- ✓ **N & M:** 3x1 matrices containing the forces and moments per unit width in the laminate axis
- ✓ **ε & κ:** mid-plane strains and curvature vectors
- ✓ **A<sub>ij</sub>:** extensional stiffness matrix since it relates in-plane forces to in-plane strains
- ✓ **B<sub>ij</sub>:** Coupling effect between the extensional loads with out of plane curvatures and vice-versa. It is termed the coupling matrix

Main assumptions considered by Karaolis are the following:

- ✓ Blade cross section is treated as a thin walled beam structure ( $t \ll c$ ), which means that in-plane skin bending and coupling are negligible with regard to the performance of the beam as a whole. Consequently,  $\kappa$  is negligible. Additionally, for symmetrical lay-ups  $[B_{ij}] = 0$ .
- ✓ Only elastic deformations are considered

- ✓ Stress concentrations, e.g. due to warping incompatibility or shear lag<sup>6</sup> are ignored

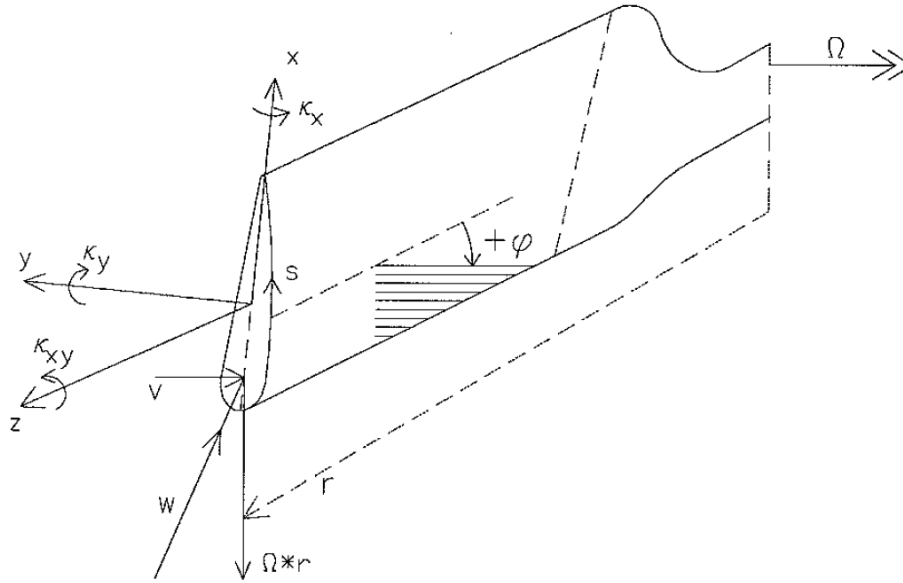


**Figure 114** Nomenclature & positive directions for rotor blade analysis

According to previous assumptions and the nomenclature & positive directions for the rotor blade analysis (see Figure 114), the equation for every of the segments in which the airfoil is divided Eq. 1 can be expressed as:

$$\Sigma \begin{Bmatrix} N_{zi} \\ N_{si} \\ N_{zsi} \end{Bmatrix} = \Sigma \left( \begin{bmatrix} A_{11} & A_{12} & A_{13} \\ A_{21} & A_{22} & A_{23} \\ A_{31} & A_{32} & A_{33} \end{bmatrix}_i \cdot \begin{Bmatrix} \epsilon_{zi} \\ \epsilon_{si} \\ \gamma_{zsi} \end{Bmatrix} \right) \quad \text{Eq. 2}$$

Where:

- ✓  $N_z = \Sigma N_{zi}$  : axial load
- ✓  $N_s = \Sigma N_{si} = 0$ : considering that the transversal force at every segment of the airfoil section  $N_{si} = 0$  because neither internal pressure, nor restraint due to a Poisson effect is considered
- ✓  $N_{zs} = M_t/2A$  : is the shear flux from torsional moments considering BREDT Theory for thin walled single - cell airfoil sections.

Additionally, the axial deformation at every point of the airfoil section can be expressed as;

$$\epsilon_z(x, y) = \epsilon_z^0 - x \cdot \kappa_y + y \cdot \kappa_x \quad \text{Eq. 3}$$

Considering both Eq. 2 and Eq. 3 and also the assumptions for  $N_z, N_s$  &  $N_{zs}$ , following mathematical expressions can be derived:

$$\begin{aligned} N_z &= S'_1 \cdot t \cdot (\epsilon_z^0 - x' \cdot c \cdot \kappa_y + y' \cdot c \cdot \kappa_x) - S'_2 \cdot M_z / 2 \cdot A' \cdot c^2 \\ \gamma_{zs} &= S'_2 \cdot (\epsilon_z^0 - x' \cdot c \cdot \kappa_y + y' \cdot c \cdot \kappa_x) + S'_3 / t \cdot M_z / 2 \cdot A' \cdot c^2 \\ \epsilon_s &= S'_4 \cdot (\epsilon_z^0 - x' \cdot c \cdot \kappa_y + y' \cdot c \cdot \kappa_x) + S'_5 / t \cdot M_z / 2 \cdot A' \cdot c^2 \end{aligned} \quad \text{Eq. 4}$$

Where:

<sup>6</sup> In a box girder, a large shear flow is transmitted from vertical webs to the horizontal flanges, which causes in-plane shear deformation of the flanges and results in unpredicted extra longitudinal displacement at the web-flange junction. Shear Lag effect is relevant to any slender box element that is loaded laterally such as airplane wing structure and box girder bridges.

$$\begin{aligned}
 \checkmark \quad S'_1 &= A'_{11} + (2A'_{12}A'_{13}A'_{23} - A'^2_{12}A'_{33} - A'^2_{13}A'_{22})/(A'_{22}A'_{33} - A'^2_{23}) \\
 \checkmark \quad S'_2 &= (A'_{12}A'_{23} - A'_{13}A'_{22})/(A'_{22}A'_{33} - A'^2_{23}) \\
 \checkmark \quad S'_3 &= A'_{22}/(A'_{22}A'_{33} - A'^2_{23}) \\
 \checkmark \quad S'_4 &= (A'_{13}A'_{23} - A'_{12}A'_{33})/(A'_{22}A'_{33} - A'^2_{23}) \\
 \checkmark \quad S'_5 &= -A'_{23}/(A'_{22}A'_{33} - A'^2_{23})
 \end{aligned}$$

Eq. 5

$S'_2$  &  $S'_4$  are dimensionless, whereas  $S'_1$  has dimensions [N/m<sup>2</sup>] and  $S'_3$  &  $S'_5$  are in terms of [m<sup>2</sup>/N].

According to these values and assuming that the external forces acting on the blade cross section can be defined as:

$$\begin{aligned}
 \checkmark \quad T_z &= c \oint N_z \cdot ds' \\
 \checkmark \quad M_x &= c^2 \oint y' N_z \cdot ds' \\
 \checkmark \quad M_y &= c^2 \oint y' N_z \cdot ds'
 \end{aligned}$$

Eq. 6

Substitution of  $N_z$  &  $\gamma_{zs}$  from Eq. 4 provides the following expressions:

$$\begin{aligned}
 \checkmark \quad T_z &= \varepsilon_z^0 \cdot t \cdot c \cdot S'_1 \oint ds' - \kappa_y t \cdot c^2 \cdot S'_1 \oint x' ds' + \kappa_x t \cdot c^2 \cdot S'_1 \oint y' ds' - \\
 &\quad M_z/2 \cdot A' \cdot c \oint S'_2 ds' \\
 \checkmark \quad M_x &= \varepsilon_z^0 \cdot t \cdot c^2 \cdot S'_1 \oint y' ds' - \kappa_y t \cdot c^3 \cdot S'_1 \oint x' y' ds' + \kappa_x t \cdot c^3 \cdot S'_1 \oint y'^2 ds' - \\
 &\quad M_z/2 \cdot A' \cdot c \oint y' S'_2 ds' \\
 \checkmark \quad M_y &= -\varepsilon_z^0 \cdot t \cdot c^2 \cdot S'_1 \oint x' ds' - \kappa_y t \cdot c^3 \cdot S'_1 \oint x'^2 ds' - \kappa_x t \cdot c^3 \cdot S'_1 \oint x' y' ds' + \\
 &\quad M_z/2 \cdot A' \cdot c \oint y x' S'_2 ds' \\
 \checkmark \quad \kappa_{xy} &= 1/2A \oint \gamma_{zs} \cdot ds = 1/2A' \left[ \varepsilon_z^0/c \oint S'_2 ds' - \kappa_y \oint x' S'_2 ds' + \kappa_x \oint x y' S'_2 ds' + \right. \\
 &\quad \left. M_z S'_3/2 \cdot A' \cdot c^3 \cdot t \oint ds' \right]
 \end{aligned}$$

Eq. 7

Rewriting the expressions of Eq. 7, the symmetric stiffness relation of the section [ $H_{ij}$ ] is obtained:

$$\begin{pmatrix} T_z \\ M_x \\ M_y \\ M_x \end{pmatrix} = \begin{bmatrix} H_{11} & H_{12} & H_{13} & H_{14} \\ H_{12} & H_{22} & H_{23} & H_{24} \\ H_{13} & H_{23} & H_{33} & H_{34} \\ H_{14} & H_{24} & H_{34} & H_{44} \end{bmatrix} \cdot \begin{pmatrix} \varepsilon_z^0 \\ \kappa_x \\ \kappa_y \\ \kappa_{xy} \end{pmatrix}$$

Eq. 8

As an alternative, [ $H_{ij}^*$ ] can be defined as the reduced stiffness matrix of the considered blade section and expressed independently of the dimensions  $t$  &  $c$ . The dimensions of [ $H_{ij}^*$ ] are in terms of [N/m<sup>2</sup>].

$$\begin{pmatrix} T_z \\ M_x \\ M_y \\ M_x \end{pmatrix} = \begin{bmatrix} H_{11}^* t \cdot c & H_{12}^* t \cdot c^2 & H_{13}^* t \cdot c^2 & H_{14}^* t \cdot c^2 \\ H_{12}^* t \cdot c^2 & H_{22}^* t \cdot c^3 & H_{23}^* t \cdot c^3 & H_{24}^* t \cdot c^3 \\ H_{13}^* t \cdot c^2 & H_{23}^* t \cdot c^3 & H_{33}^* t \cdot c^3 & H_{34}^* t \cdot c^3 \\ H_{14}^* t \cdot c^2 & H_{24}^* t \cdot c^3 & H_{34}^* t \cdot c^3 & H_{44}^* t \cdot c^3 \end{bmatrix} \cdot \begin{pmatrix} \varepsilon_z^0 \\ \kappa_x \\ \kappa_y \\ \kappa_{xy} \end{pmatrix}$$

Eq. 9

Where:

$$\begin{aligned}
 \checkmark \quad H_{11}^* &= S_1' \oint ds' + [\oint S_2' ds']^2 / S_3' \oint ds' \\
 \checkmark \quad H_{12}^* &= S_1' \oint y' ds' + \oint S_2' ds' \oint y' S_2' ds' / S_3' \oint ds' \\
 \checkmark \quad H_{13}^* &= -S_1' \oint x' ds' - \oint S_2' ds' \oint x' S_2' ds' / S_3' \oint ds' \\
 \checkmark \quad H_{14}^* &= -2A' \cdot \oint S_2' ds' / S_3' \oint ds' \\
 \checkmark \quad H_{22}^* &= S_1' \oint y'^2 ds' + [\oint y' S_2' ds']^2 / S_3' \oint ds' \\
 \checkmark \quad H_{23}^* &= -S_1' \oint y' x' ds' - \oint y' S_2' ds' \oint x' S_2' ds' / S_3' \oint ds' \\
 \checkmark \quad H_{24}^* &= -2A' \cdot \oint y' S_2' ds' / S_3' \oint ds' \\
 \checkmark \quad H_{33}^* &= S_1' \oint y x'^2 ds' + [\oint x' S_2' ds']^2 / S_3' \oint ds' \\
 \checkmark \quad H_{34}^* &= -2A' \cdot \oint x' S_2' ds' / S_3' \oint ds' \\
 \checkmark \quad H_{44}^* &= 4A'^2 / S_3' \oint ds'
 \end{aligned}$$

Eq. 10

$H_{14}^*$  defines the structural coupling for axial - torsion and  $H_{24}^*$  &  $H_{34}^*$  for bending - torsion respectively.

### 3.4.1.2 Validation

The accuracy of previous theory has been evaluated by direct comparison of the deflections obtained from cantilever beam models that account for H14, H24 & H34 Karalis terms with the results obtained from detailed FE models that are closer to the real behaviour.

The validation methodology applied starts from simple sectional geometries & lay-ups and ends with more complex situations.

For all of the scenarios, the beam model is fixed at one edge and loaded at the other with axial forces and bending & torsion moments.

#### 3.4.1.2.1 Circular cross section

The geometric and lay-up description of the models used for validation is described in Table 36 and Figure 115.

Table 36. **Geometry and lay-up for the circular cross section beam model**

Cantilever Beam with circular cross section					
Geometry		Lay-up			
Diameter [mm]	200	CONFIGURATION 01	Side 1	BIAX at +30°	e = 3.0mm
			Side 2	BIAX at +30°	e = 3.0mm
Length[mm]	2000	CONFIGURATION 02	Side 1	BIAX at +30°	e = 3.0mm
			Side 2	BIAX at -30°	e = 3.0mm

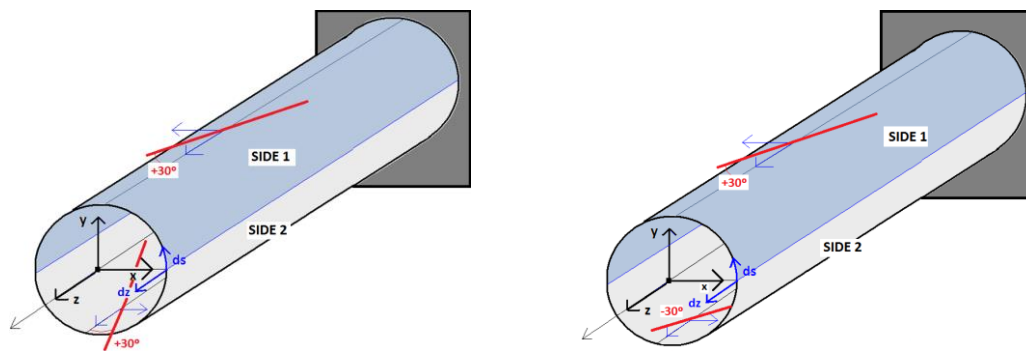


**Figure 115** Cantilever beam with circular cross section. CASE 01 & CASE 02

**Configuration 01**

For this configuration of the lay-up, Karaolis terms H24 and H34 are equal to 0.0. As a consequence, no bending - torsion structural coupling exists. The only non-zero coupling term is H14 = 5.34e8Nmm/rad. According to this value, maximum displacement and torsion of the cantilever free edge is detailed in Table 37.

**Table 37. Tip deflection & torsion for the circular cross section beam model (CASE01)**

Cantilever Beam with circular cross section (Configuration 01)						
LOAD CONDITION		TIP DISPLACEMENT & TORSION				
FZ [N]	1,0e3	KARAOLIS		FE model		Error
		$\delta z$ [mm]	8,2915e-2	$\delta z$ [mm]	8,2951e-2	-0,043%
		$\Theta z$ [rad]	-4.075e-4	$\Theta z$ [rad]	-4,102e-4	-0.661%

Following figure shows the deflection (torsion) of the cantilever beam under FZ = 1,0e3N

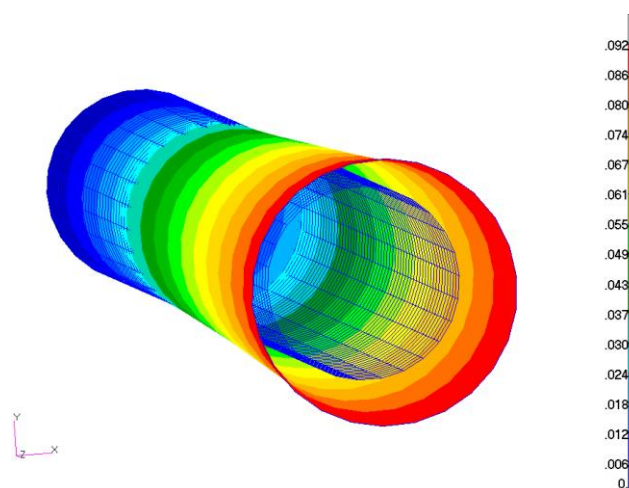


**Figure 116** Tip displacement of the cantilever beam with circular cross section (Configuration 01)

**Configuration 02**

According to the lay-up of configuration 02, Karaolis terms H14 and H34 are equal to 0.0. As a consequence, neither axial - torsion nor bending (along Y axis) – torsion structural coupling exists.

The only non-zero coupling term is  $H_{24} = 3.401e10 \text{ Nmm}^2$ . It represents the structural coupling between bending (along X axis) and torsion.

According to this value, maximum displacement and torsion of the cantilever free edge is detailed in Table 38.

**Table 38. Tip deflection & torsion for the circular cross section beam model (Configuration 02)**

Cantilever Beam with circular cross section (Configuration 02)						
LOAD CONDITION		TIP DISPLACEMENT & TORSION				
MX [Nmm]	1,0e6	KARAOLIS		FE model		Error
		$\Theta_x$ [rad]	1,659e-2	$\Theta_x$ [rad]	1,674e-2	-0,925%
		$\Theta_z$ [rad]	-5,190e-3	$\Theta_z$ [rad]	-5,246e-3	-1.082 %

Following figure shows the deflection (torsion) of the cantilever beam under  $M_X = 1,0e6 \text{ N.mm}$

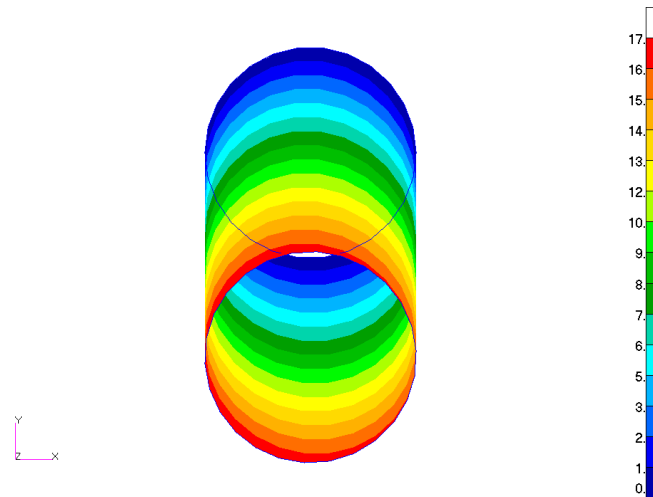


**Figure 117** Tip displacement of the cantilever beam with circular cross section (Configuration 02)

#### 3.4.1.2.2 DU25 airfoil section

For this geometry, three different configurations are analysed:

- ✓ Configuration 1: Lay-up of constant thickness of 3mm using BIAx material with a misalignment of  $+30^\circ$  at the pressure size and  $-30^\circ$  at the suction one
- ✓ Configuration 2: Lay-up of variable thickness, according to the following distribution:
  - Spar-Cap of 475mm and uniform thickness of 6mm. The material used is UD with a misalignment of  $+10\%$  at the pressure size and  $-10^\circ$  at the suction one from the PITCH axis.
  - Shell composed of BIAx material with 6mm of thickness. No misalignment.
- ✓ Configuration 3: Equal to configuration 2 but including a principal shear-web with BIAx material of 2mm thick and BALSA of 10mm width

These configurations are described in Table 39.

**Table 39. Geometry and lay-up for the circular cross section beam model**

Cantilever Beam with DU25 cross section						
Geometry		Lay-up				
Chord [mm]	1000	CONFIGURATION 01	Pressure	CAP	BIAX at +30°	e = 3.0mm
				SHELL	BIAX at +30°	e = 3.0mm
Length [mm]	6000		Suction	CAP	BIAX at -30°	e = 3.0mm
				SHELL	BIAX at -30°	e = 3.0mm
Airfoil thickness [mm]	250	CONFIGURATION 02	Pressure	CAP	UD at +10°	e = 6.0mm
				SHELL	BIAX at ±45°	e = 3.0mm
			Suction	CAP	UD at -10°	e = 6.0mm
				SHELL	BIAX at ±45°	e = 3.0mm
		CONFIGURATION 03	Pressure	CAP	UD at +10°	e = 6.0mm
				SHELL	BIAX at ±45°	e = 3.0mm
Suction	CAP		UD at -10°	e = 6.0mm		
	SHELL		BIAX at ±45°	e = 3.0mm		
		Shear WEB	-----	BIAX at ±45°	e = 2.0mm	
			-----	BALSA	e = 10mm	

The sign criterion used for fiber alignment is defined in the following figure.

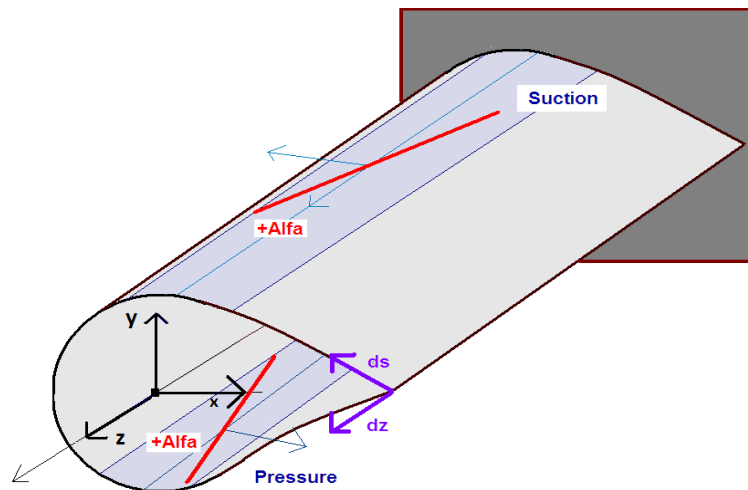


**Figure 118** Cantilever beam with DU25 cross section

At this section, only Karaolis terms related to the structural coupling between bending and torsion (H24 & H34) are computed considering that these terms are of significance for blade design.

**Configuration 01**

The values obtained for Karaolis terms are:

- ✓ H24= -1.834e11Nmm2/rad
- ✓ H34= 7.874e9Nmm2/rad

According to these values and for the cantilever model described in Table 39, maximum displacement and torsion of the cantilever free edge is detailed in Table 40.

**Table 40. Tip deflection & torsion for the DU25 cross section beam model (Configuration 01)**

Cantilever Beam with DU25 cross section (Configuration 01)						
LOAD CONDITION		TIP DISPLACEMENT & TORSION				
MX [Nmm]	1,0e6	KARAOLIS		FE model		Error
		Θx [rad]	1,053e-2	Θx [rad]	1,0597e-2	-0,613%
		Θz [rad]	2,672e-3	Θz [rad]	2,699e-3	-1,020%
MY [Nmm]	1,0e6	KARAOLIS		FE model		Error
		Θy [rad]	8,653e-4	Θy [rad]	8,617e-4	0,417%
		Θz [rad]	6,975e-5	Θz [rad]	7,606e-5	-8,296%

Following figure shows the deflection of the cantilever beam under  $MX = 1,0e6\text{Nmm}$  &  $MY = 1,0e6\text{Nmm}$  respectively.

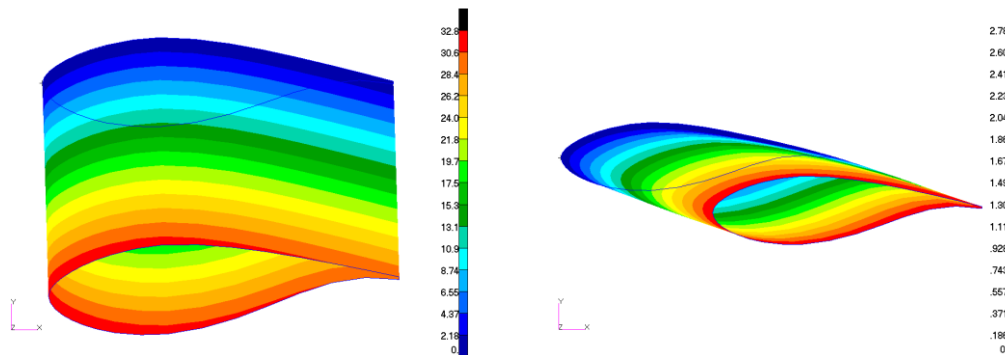


**Figure 119** Tip displacement of the cantilever beam with DU25 cross section (Configuration 01)

### Configuration 02

The values obtained for Karaolis terms are:

- ✓  $H24 = -6.796e11\text{Nmm}^2/\text{rad}$
- ✓  $H34 = +5.856e09\text{Nmm}^2/\text{rad}$

According to these values and for the cantilever model described in Table 39, maximum displacement and torsion of the cantilever free edge is detailed in Table 41.

**Table 41. Tip deflection & torsion for the DU25 cross section beam model (Configuration 02)**

Cantilever Beam with DU25 cross section (Configuration 02)						
LOAD CONDITION		TIP DISPLACEMENT & TORSION				
MX [Nmm]	1,0e6	KARAOLIS		FE model		Error
		Θx [rad]	2,794e-3	Θx [rad]	2,537e-3	10,15%
		Θz [rad]	2,100e-3	Θz [rad]	1,061e-3	97,9%
MY [Nmm]	1,0e6	KARAOLIS		FE model		Error
		Θy [rad]	6,469e-4	Θy [rad]	6,427e-4	0,637%
		Θz [rad]	6.772e-5	Θz [rad]	3,429e-5	97,5%

According to the results of Table 41, the structural coupling estimated by Karaolis approach is significantly different from that values predicted by the FE model. It is worth mentioning that one of the main assumptions is that the thickness of the lay-up is assumed to be constant.

Next figure shows the deflection of the cantilever beam under  $M_X = 1,0e6\text{Nmm}$  &  $M_Y = 1,0e6\text{Nmm}$  respectively.

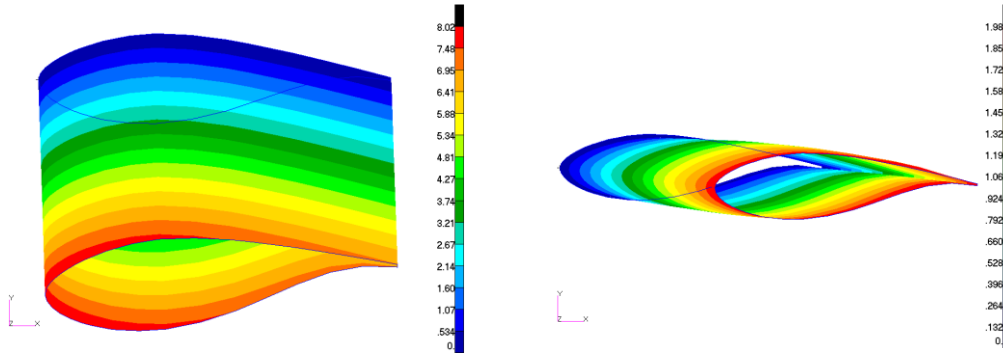


**Figure 120** Tip displacement of the cantilever beam with DU25 cross section (Configuration 02)

If the thickness of the spar-cap lay-up (with UD plies at  $\pm 10^\circ$ ) is reduced to 3mm (which is the same value as the thickness of the shell), the structural coupling effects predicted by Karaolis and the FE model give differences lower than 3.5%.

**Configuration 03**

The values obtained for Karaolis terms are:

- ✓  $H_{24} = -6.797e11\text{Nmm}^2/\text{rad}$
- ✓  $H_{34} = +5.836e09\text{Nmm}^2/\text{rad}$

The differences of these values in comparison with those ones from Configuration02 are almost negligible and they are only consequence of the elastic centre location change. Karaolis approach does neither consider the effect of the shear web on the structural coupling terms.

According to these values and for the cantilever model described in Table 39, maximum displacement and torsion of the cantilever free edge is detailed in Table 42.

**Table 42. Tip deflection & torsion for the DU25 cross section beam model (Configuration 03)**

Cantilever Beam with DU25 cross section (Configuration 03)						
LOAD CONDITION		TIP DISPLACEMENT & TORSION				
MX [Nmm]	1,0e6	KARAOLIS		FE model		Error
		$\Theta_x$ [rad]	2,794e-3	$\Theta_x$ [rad]	2,504e-3	11,57%
		$\Theta_z$ [rad]	2,099e-3	$\Theta_z$ [rad]	1,051e-3	99,8%
MY [Nmm]	1,0e6	KARAOLIS		FE model		Error
		$\Theta_y$ [rad]	6,469e-4	$\Theta_y$ [rad]	6,398e-4	1,104%
		$\Theta_z$ [rad]	6.771e-5	$\Theta_z$ [rad]	3,180e-5	112,9%

As it is checked, the errors of Karaolis prediction increase in comparison with the results from Configuration 02.

Next figure shows the deflection of the cantilever beam under  $M_X = 1,0e6\text{Nmm}$  &  $M_Y = 1,0e6\text{Nmm}$  respectively.

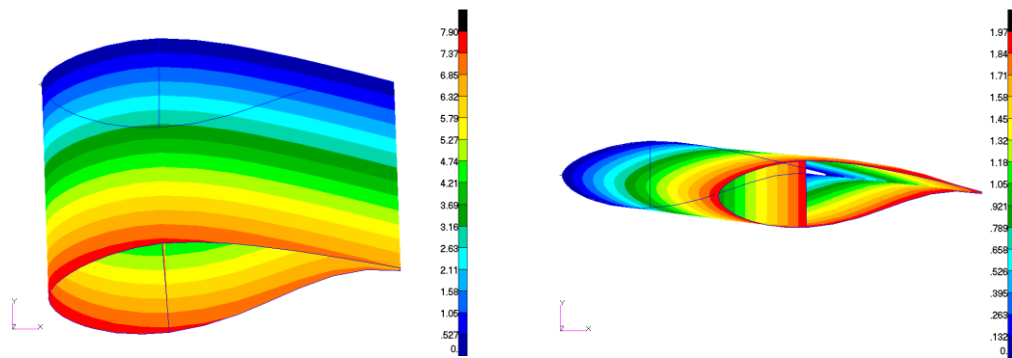


**Figure 121** Tip displacement of the cantilever beam with DU25 cross section (Configuration 03)

### 3.4.1.3 Conclusions on validation of the Karaolis approach

From the results obtained in section 3.4.1.2, it is concluded that Karaolis approach is not accurate enough to represent the structural coupling of a real blade.

The assumptions considered by the method, which limit its use to cross sections with constant lay-up thicknesses and mono-cell internal architecture, make this approach useless for build-in structural coupling blade designs.

An alternative is to tune the values of H14, H24 & H34 obtained with Karaolis with an optimization routine in order to reduce the differences in deflection between a BEAM model (that integrates these coupling terms) and a FE model with 2D elements where the PCOMP entries can consider the misalignment of the plies defined by the designer.

These updated values of H14, H24 & H34 can be used as an input for the beam model formulation that it is commonly used by software as BLADED and FAST for the aero-elastic loads computation according to the standard.

### 3.4.1.4 Karaolis Integration in BASSF

Although the method is not accurate enough according to the conclusions of 3.4.1.3, its formulation has been implemented in BASSF, so that it is possible to obtain the values of H14, H24 & H34 for every of the blade section where the structural analysis is being performed.

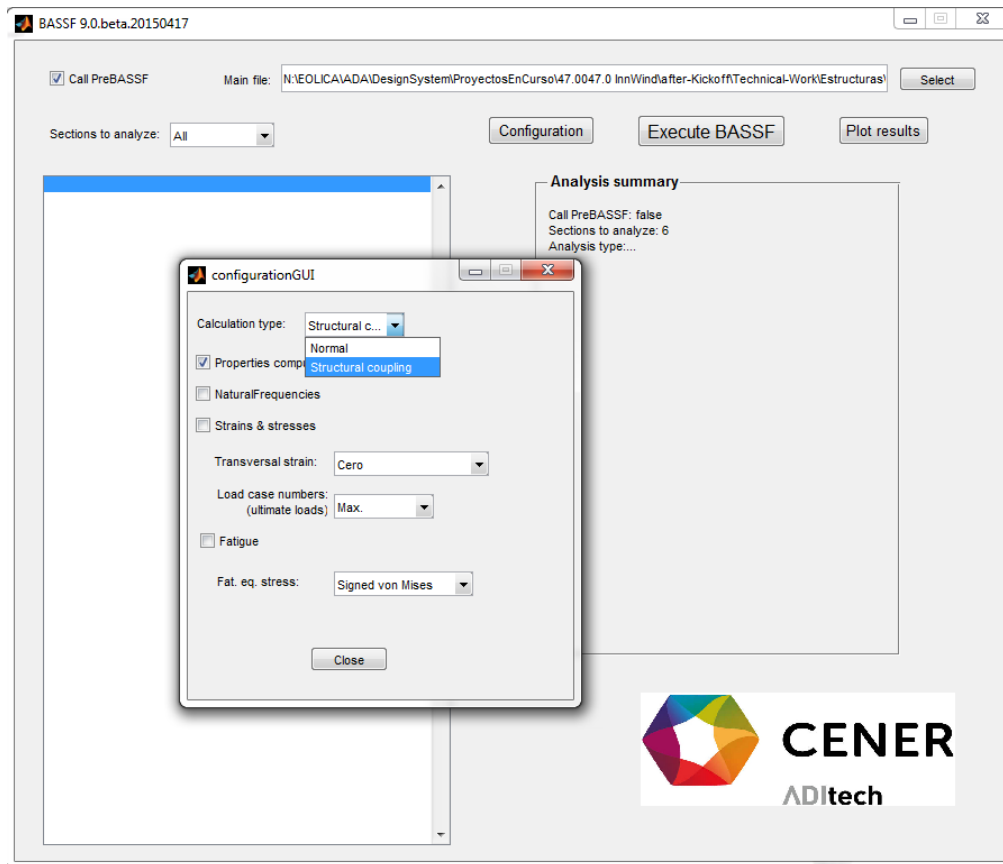


**Figure 122** BASSF new version interface including the structural coupling analysis

The validation of this new function of BASSF is performed using the examples defined in section 3.4.1.2. For all situations, BASSF gives the same numbers as those ones obtained from calculations with EXCEL.

#### 3.4.1.5 *Beam model to account for Structural Coupling*

Once the original or the updated values of Karaolis terms are calculated, it is necessary to integrate them into the FE model of the blade to understand how they influence its mechanical behaviour.

Among others, build-in coupling terms affect to:

- ✓ Blade Tip Deflection
- ✓ Blade natural frequencies and mode shapes
- ✓ Angle of attack of the relative wind direction velocity seen by every blade airfoil section: this effect can influence the load envelope supported by the wind turbine main and its energy production.

Next section defines the formulation used both in BASSF also in MSC.ADAMS to implement Karaolis terms.

##### 3.4.1.5.1 Stiffness Matrix Definition

###### Stiffness matrix definition at the elastic axis

The stiffness matrix of a BEAM element using Euler-Bernoulli theory is defined according to the following formula.

$$[K^{(e)}] = \begin{bmatrix} \mathbf{A}_1 & \mathbf{B}^T \\ \mathbf{B} & \mathbf{A}_2 \end{bmatrix}$$

$$\epsilon_1 = +1, \epsilon_2 = -1$$

$$[\mathbf{A}_i] = \begin{bmatrix} \frac{EA}{L} & 0 & 0 & 0 & 0 & 0 \\ 0 & \frac{12EI_x}{L^3} & 0 & 0 & 0 & \epsilon_i \frac{6EI_x}{L^2} \\ 0 & 0 & \frac{12EI_y}{L^3} & 0 & -\epsilon_i \frac{6EI_y}{L^2} & 0 \\ 0 & 0 & 0 & \frac{GJ}{L} & 0 & 0 \\ 0 & 0 & -\epsilon_i \frac{6EI_y}{L^2} & 0 & \frac{4EI_y}{L} & 0 \\ 0 & \epsilon_i \frac{6EI_x}{L^2} & 0 & 0 & 0 & \frac{4EI_x}{L} \end{bmatrix}$$

$$[\mathbf{B}] = \begin{bmatrix} -\frac{EA}{L} & 0 & 0 & 0 & 0 & 0 \\ 0 & -\frac{12EI_x}{L^3} & 0 & 0 & 0 & -\frac{6EI_x}{L^2} \\ 0 & 0 & -\frac{12EI_y}{L^3} & 0 & +\frac{6EI_y}{L^2} & 0 \\ 0 & 0 & 0 & -\frac{GJ}{L} & 0 & 0 \\ 0 & 0 & -\frac{6EI_y}{L^2} & 0 & \frac{2EI_y}{L} & 0 \\ 0 & \frac{6EI_x}{L^2} & 0 & 0 & 0 & \frac{2EI_x}{L} \end{bmatrix}$$

Figure 123 Formulation of Euler-Bernoulli beam

The terms of the stiffness matrix are defined at a local coordinate system where:

- ✓ Origin: Located at the elastic centre of the section
- ✓ X axis: Aligned with the element axis
- ✓ Y & Z axis: aligned with the principal elastic axis of the cross section

According to this stiffness matrix, H14 [Nm/rad], H24 [Nm<sup>2</sup>/rad] & H34 [Nm<sup>2</sup>/rad] are introduced at the following positions:

$$[K^{(e)}] = \begin{bmatrix} \mathbf{A}_1 & \mathbf{B}^T \\ \mathbf{B} & \mathbf{A}_2 \end{bmatrix}$$

$$\epsilon_1 = +1, \epsilon_2 = -1$$

$$[\mathbf{A}_i] = \begin{bmatrix} \frac{EA}{L} & 0 & 0 & \mathbf{H14} & 0 & 0 \\ 0 & \frac{12EI_x}{L^3} & 0 & 0 & 0 & \epsilon_i \frac{6EI_x}{L^2} \\ 0 & 0 & \frac{12EI_y}{L^3} & 0 & -\epsilon_i \frac{6EI_y}{L^2} & 0 \\ \mathbf{H14} & 0 & 0 & \frac{GJ}{L} & \mathbf{H24} & \mathbf{H34} \\ 0 & 0 & -\epsilon_i \frac{6EI_y}{L^2} & \mathbf{H24} & \frac{4EI_y}{L} & 0 \\ 0 & \epsilon_i \frac{6EI_x}{L^2} & 0 & \mathbf{H34} & 0 & \frac{4EI_x}{L} \end{bmatrix}$$

$$[\mathbf{B}] = \begin{bmatrix} -\frac{EA}{L} & 0 & 0 & -\mathbf{H14} & 0 & 0 \\ 0 & -\frac{12EI_x}{L^3} & 0 & 0 & 0 & -\frac{6EI_x}{L^2} \\ 0 & 0 & -\frac{12EI_y}{L^3} & 0 & +\frac{6EI_y}{L^2} & 0 \\ -\mathbf{H14} & 0 & 0 & -\frac{GJ}{L} & -\mathbf{H24} & -\mathbf{H34} \\ 0 & 0 & -\frac{6EI_y}{L^2} & -\mathbf{H24} & \frac{2EI_y}{L} & 0 \\ 0 & \frac{6EI_x}{L^2} & 0 & -\mathbf{H34} & 0 & \frac{2EI_x}{L} \end{bmatrix}$$

Figure 124 Formulation of Euler-Bernoulli beam including the structural coupling terms

#### Transformation to GL coordinate system

Considering that the direction of the principal axes varies from one blade section to another, it is recommended to rotate this matrix to a common coordinate system.

The rotation is done according to expression:

$$[K^{global}] = [R(\alpha)]^T \cdot [K^e] \cdot [R(\alpha)], \text{ where}$$

- ✓  $[K^e]$ : Stiffness matrix with the coupling terms for every blade element
- ✓  $\alpha$ : Rotation angle from the principal axis to the common global coordinate system

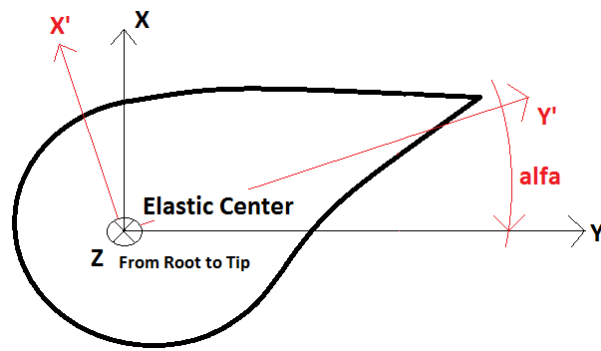


**Figure 125** Formulation of Euler-Bernoulli beam including the structural coupling terms

$$[R] = \begin{bmatrix} 1 & 0 & 0 & 0 & 0 & 0 & 0 & 0 & 0 & 0 & 0 & 0 & 0 \\ 0 & \cos(\alpha) & \sin(\alpha) & 0 & 0 & 0 & 0 & 0 & 0 & 0 & 0 & 0 & 0 \\ 0 & -\sin(\alpha) & \cos(\alpha) & 0 & 0 & 0 & 0 & 0 & 0 & 0 & 0 & 0 & 0 \\ 0 & 0 & 0 & 1 & 0 & 0 & 0 & 0 & 0 & 0 & 0 & 0 & 0 \\ 0 & 0 & 0 & 0 & \cos(\alpha) & \sin(\alpha) & 0 & 0 & 0 & 0 & 0 & 0 & 0 \\ 0 & 0 & 0 & 0 & -\sin(\alpha) & \cos(\alpha) & 0 & 0 & 0 & 0 & 0 & 0 & 0 \\ 0 & 0 & 0 & 0 & 0 & 0 & 1 & 0 & 0 & 0 & 0 & 0 & 0 \\ 0 & 0 & 0 & 0 & 0 & 0 & 0 & \cos(\alpha) & \sin(\alpha) & 0 & 0 & 0 & 0 \\ 0 & 0 & 0 & 0 & 0 & 0 & 0 & -\sin(\alpha) & \cos(\alpha) & 0 & 0 & 0 & 0 \\ 0 & 0 & 0 & 0 & 0 & 0 & 0 & 0 & 0 & 1 & 0 & 0 & 0 \\ 0 & 0 & 0 & 0 & 0 & 0 & 0 & 0 & 0 & 0 & \cos(\alpha) & \sin(\alpha) & 0 \\ 0 & 0 & 0 & 0 & 0 & 0 & 0 & 0 & 0 & 0 & -\sin(\alpha) & \cos(\alpha) & 0 \end{bmatrix}$$

**Consideration of the elastic & shear centres**

The influence of the elastic & shear centres is considered by the correction of the load values acting at the PITCH axis.

- ✓  $FX_{updated} = FX_{at\ PITCH\ axis}$
- ✓  $FY_{updated} = FY_{at\ PITCH\ axis}$
- ✓  $FZ_{updated} = FZ_{at\ PITCH\ axis}$
- ✓  $MX_{updated} = MX_{at\ PITCH\ axis} - FZ_{at\ PITCH\ axis} \cdot y_{ec}$
- ✓  $MY_{updated} = MY_{at\ PITCH\ axis} + FZ_{at\ PITCH\ axis} \cdot x_{ec}$
- ✓  $MZ_{updated} = MZ_{at\ PITCH\ axis} + FX_{at\ PITCH\ axis} \cdot y_{sc} - FY_{at\ PITCH\ axis} \cdot x_{sc}$

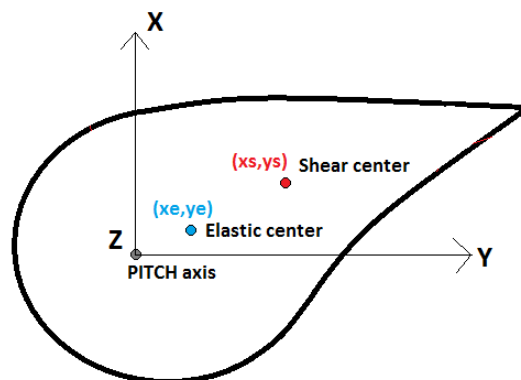


**Figure 126** Location of the elastic & shear centers from PITCH axis

### 3.4.2 Blade design with Build-In Structural Couplings

#### 3.4.2.1 Reference Blade Design

The reference blade developed by CENER is based on the baseline design provided by DTU [1] for the structural benchmark [22]. From this baseline, neither the aerodynamic design nor the material properties are modified. Main changes are related to the internal architecture and lay up used.

The motivation for the design of this reference blade is to handle a real lay-up book and a clear internal architecture that could bear the extreme loads defined in the reference case. In addition, from this reference blade it is easier to make small changes in the plies orientation in order to work with the advanced design that deals with build-in structural couplings.

##### 3.4.2.1.1 Lay-up description & mechanical properties

###### Lay-up description

The reference blade designed has the following internal architecture and lay-up distribution

###### ✓ Spar-Cap

- From Z=1.0m to Z=85m (distances from blade root)
- Position: symmetrically from the PITCH axis
- Material: UD-Glass Fibber (INWWIND properties)
- Width: 900 mm
- Maximum thickness: 67.2mm

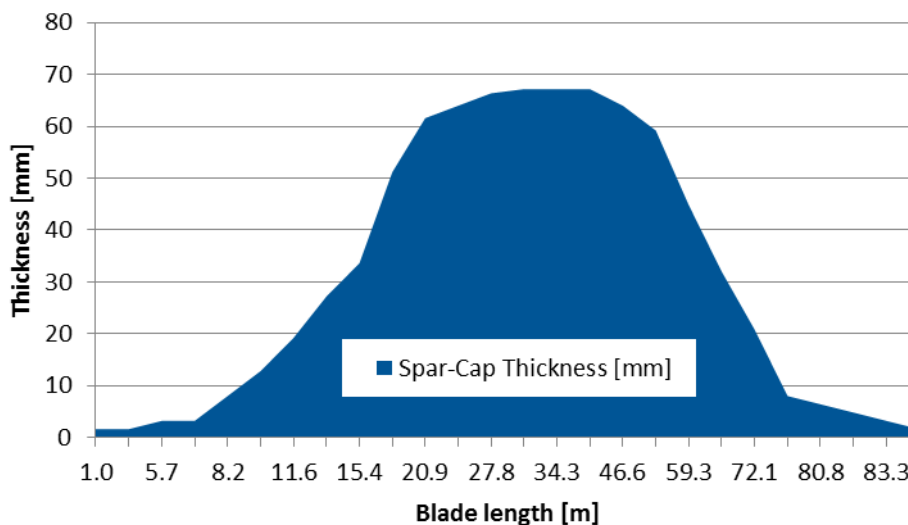


Figure 127 Thickness distribution of the spar-cap

###### ✓ LE reinforcement:

- From Z=1.0m to Z=72.1m (distances from blade root)
- Location: From Leading edge towards Trailing edge (at the pressure and suction sides)
- Material: UD-Glass Fibber (INWWIND properties)
- Width: 500mm at both sides (1000mm in total)
- Thickness:

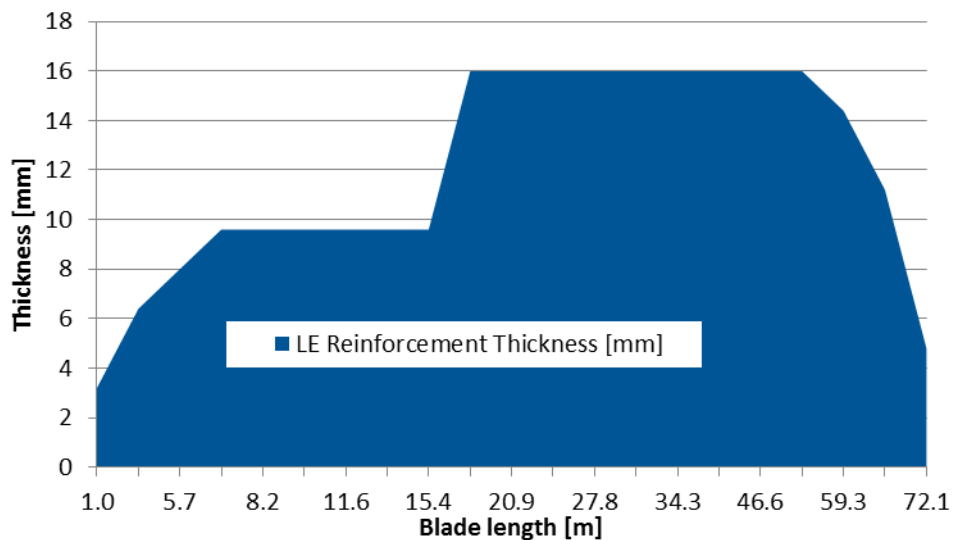


Figure 128 Thickness distribution of the LE reinforcement

✓ TE reinforcement:

- From Z=5.7m to Z=66.1m (distances from blade root)
- Location: From Trailing edge towards Leading edge with 50mm offset (at the pressure and suction sides)
- Material: UD-Glass Fibber (INWWIND properties)
- Width: 750mm at both sides
- Thickness:

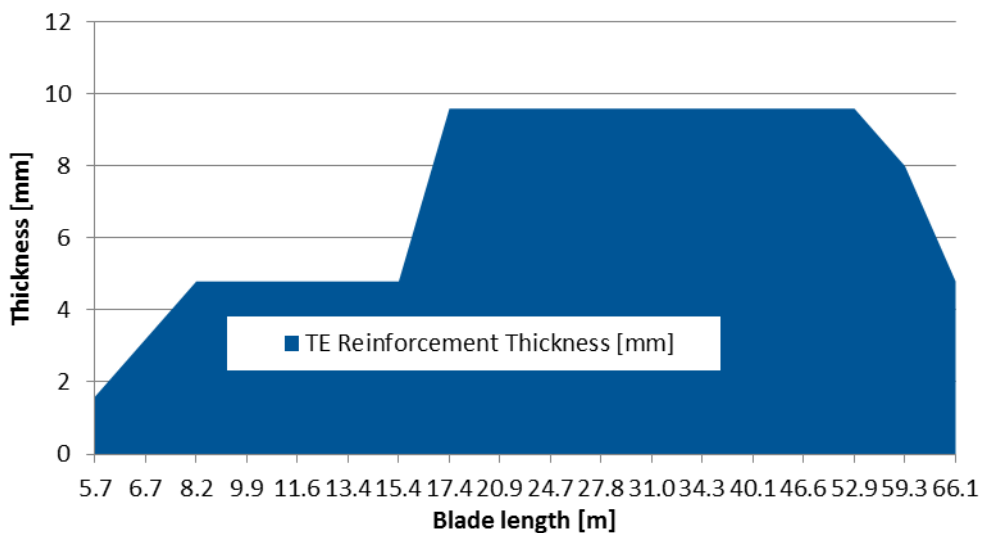


Figure 129 Thickness distribution of the TE reinforcement

✓ Principal Shear Webs (Two):

- From Z=2.95m to Z=83.3m (distances from blade root)
- Location: Symmetrically from PITCH axis and separated one another a constant distance of 750 mm
- Material: BIA-X-Glass Fibber and Balsa (INNWIND properties)

- Thickness:

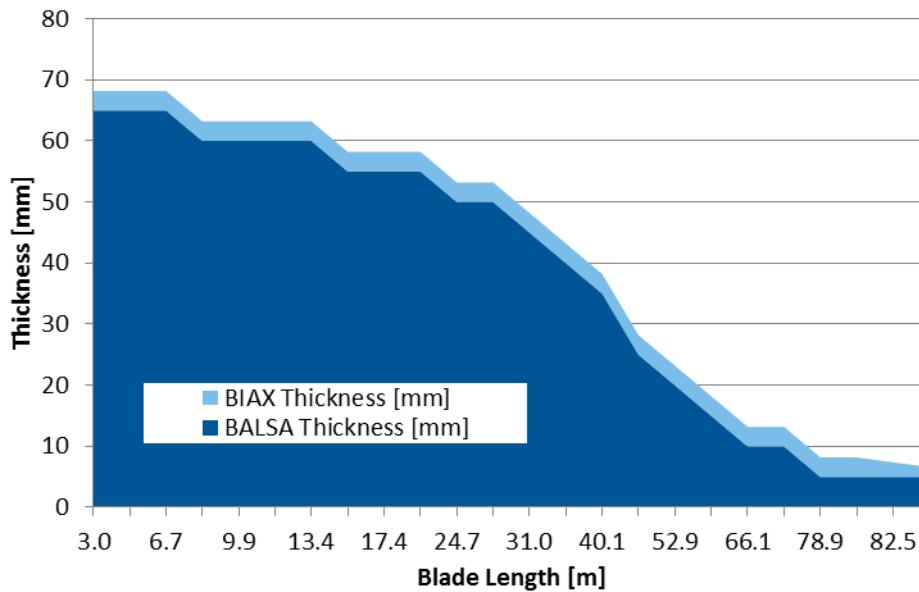


Figure 130 Thickness distributions of the shear-Webs (Principal)

- ✓ Secondary Shear Web:

- From Z=17.3m to Z=83.3m (distances from blade root)
- Location: At 87% of the chord line for every airfoil section – close to the trailing edge
- Material: BIAx-Glass Fibber and Balsa (INNWIND properties)
- Thickness:

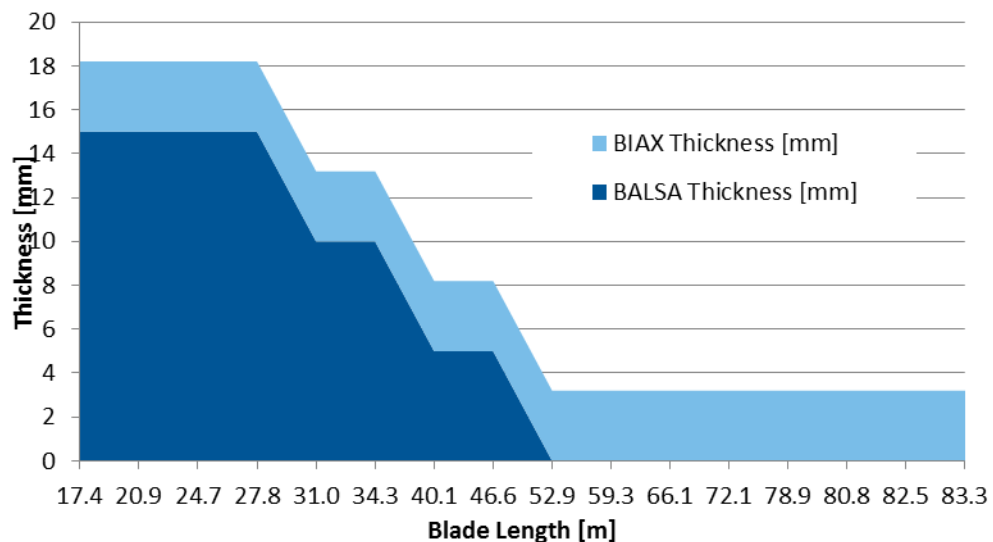


Figure 131 Thickness distribution of the shear-Web (Secondary)

- ✓ Shell:

- Material: TRIAX Glass Fibber, UD-Glass Fibber and Balsa (INNWIND properties)
- Thickness of Balsa: It varies from 5.0mm to 35mm at the leading panel and from 10.0mm to 70mm at the trailing panel
- Thickness of Glass Fibber:

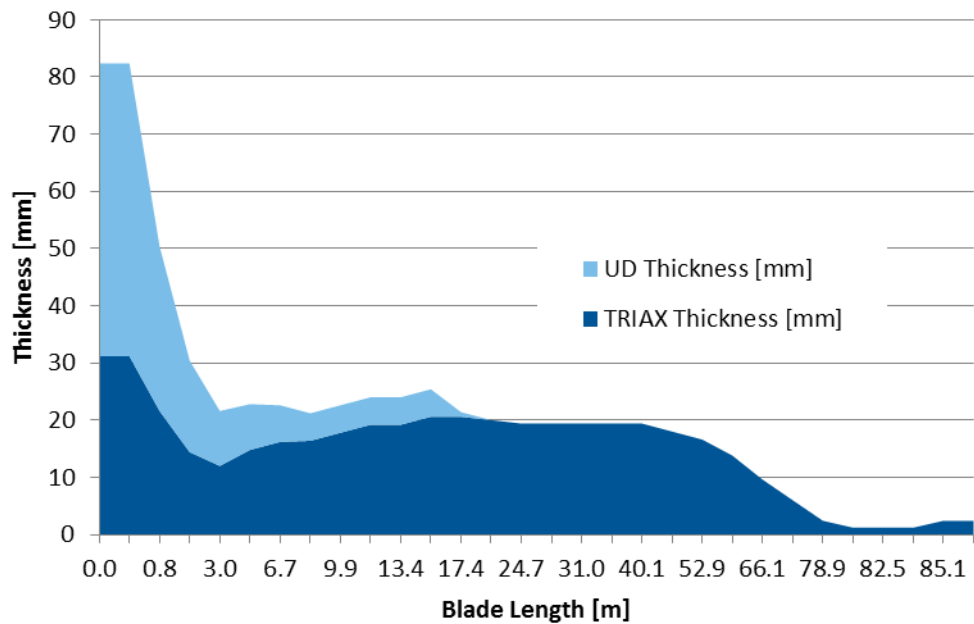


Figure 132 Thickness distribution of the shell

#### Mechanical properties

Table 43 and Table 44 define blade global mass properties, centre of gravity and main mechanical properties distribution.

Table 43. *Blade mass and center of gravity of the reference blade*

Blade definition by 30 sections	
Overall mass of the blade (Kg)	50465Kg
Location of centre of gravity from hub centre (z axis)	z: 30.415

Table 44. *Distribution of the reference blade mechanical properties*

Section ID	Distance from Root [m]	Mass/unit length [Kg/m]	Flapwise Stiffness [Nm <sup>2</sup> ]	Edgewise Stiffness [Nm <sup>2</sup> ]	Torsional Rigidity [Nm <sup>2</sup> ]	Centre of mass [%]	Elastic axis [-]
1	0.000	2658.0	1.67E+11	1.71E+11	6.49E+10	50.55	50.55
2	0.500	2658.0	1.67E+11	1.71E+11	6.49E+10	50.55	50.55
3	0.750	1622.7	1.00E+11	1.03E+11	4.15E+10	50.55	50.55
4	1.000	989.5	6.02E+10	6.16E+10	2.62E+10	50.24	50.16
5	2.950	830.7	4.51E+10	4.31E+10	1.87E+10	48.83	48.56
6	5.717	775.6	3.73E+10	3.86E+10	1.87E+10	47.92	47.60
7	6.691	772.3	3.58E+10	3.80E+10	2.03E+10	48.86	48.62
8	8.232	767.8	3.28E+10	3.75E+10	2.00E+10	48.97	48.86
9	9.869	789.5	2.94E+10	3.76E+10	1.77E+10	47.66	47.58
10	11.602	811.2	2.51E+10	3.76E+10	1.57E+10	46.39	46.32
11	13.430	833.7	2.20E+10	3.73E+10	1.23E+10	45.33	45.22
12	15.352	856.6	1.86E+10	3.72E+10	9.92E+09	44.71	44.49
13	17.364	864.5	1.52E+10	3.65E+10	7.39E+09	44.31	43.86
14	20.907	853.5	1.19E+10	3.49E+10	5.43E+09	43.78	42.92

Section ID	Distance from Root [m]	Mass/unit length [Kg/m]	Flapwise Stiffness [Nm <sup>2</sup> ]	Edgewise Stiffness [Nm <sup>2</sup> ]	Torsional Rigidity [Nm <sup>2</sup> ]	Centre of mass [%]	Elastic axis [-]
15	24.659	830.3	9.28E+09	3.34E+10	4.14E+09	43.53	42.38
16	27.788	822.8	7.73E+09	3.18E+10	3.33E+09	43.34	42.01
17	31.004	805.5	6.34E+09	2.93E+10	2.64E+09	43.26	41.79
18	34.282	786.4	5.18E+09	2.71E+10	2.11E+09	43.39	41.79
19	40.078	746.1	3.61E+09	2.17E+10	1.40E+09	43.22	41.57
20	46.624	659.0	2.27E+09	1.54E+10	8.23E+08	42.95	41.30
21	52.871	575.3	1.46E+09	1.07E+10	4.96E+08	42.64	41.02
22	59.316	433.3	8.09E+08	6.22E+09	2.80E+08	42.30	40.67
23	66.122	285.4	4.09E+08	2.83E+09	1.38E+08	41.04	39.32
24	72.088	159.3	1.89E+08	8.33E+08	6.11E+07	38.80	36.62
25	78.945	56.8	4.68E+07	1.82E+08	1.61E+07	40.15	38.50
26	80.810	39.0	2.95E+07	9.84E+07	8.86E+06	38.61	37.34
27	82.450	30.5	1.83E+07	7.33E+07	6.21E+06	39.26	37.81
28	83.322	22.5	1.10E+07	5.44E+07	4.38E+06	40.42	38.71
29	85.069	19.2	4.30E+06	3.72E+07	2.66E+06	44.12	42.16
30	85.944	9.6	7.48E+05	1.06E+07	8.93E+05	48.50	48.50

The reference blade designed is  $\approx 21.2\%$  heavier than the baseline provided by DTU [1]. The reason of this increase is because the lay-up has been reinforced in order the blade to bear the maximum loads defined in the reference case.

Main mechanical properties of DTU blade baseline [1] have been reported by CENER in [2] and are provided in APPENDIX B; estimated properties for DTU Reference blade (CENER) for completeness.

Figure 133 to Figure 135 show the distribution of mass, flapwise stiffness and edgewise stiffness of the reference blade defined by CENER and the baseline by DTU.

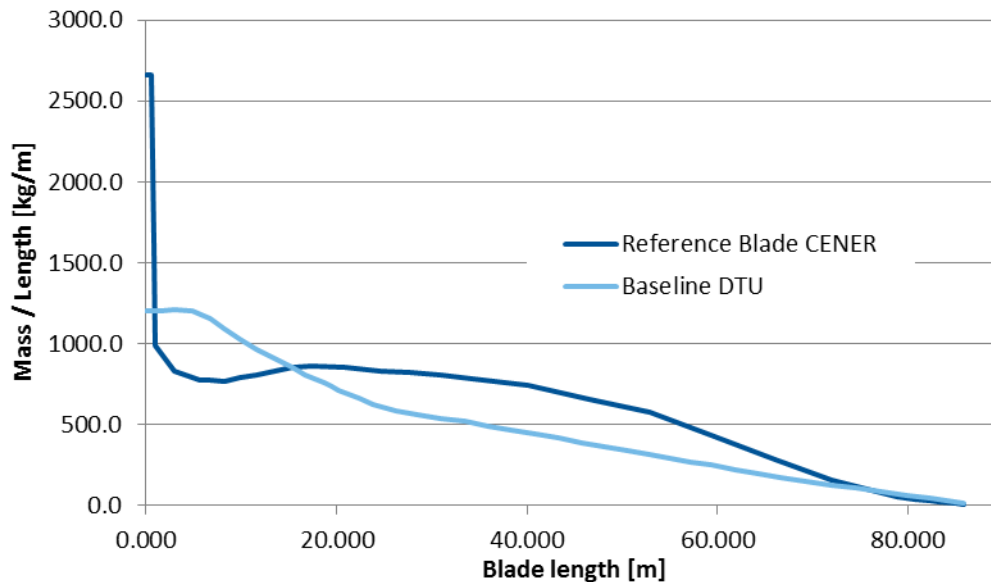
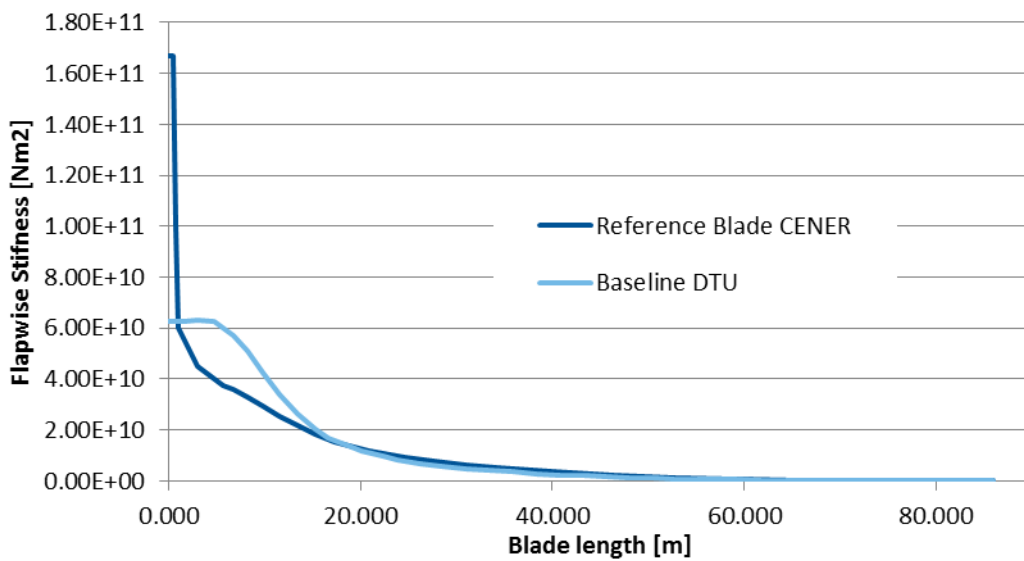
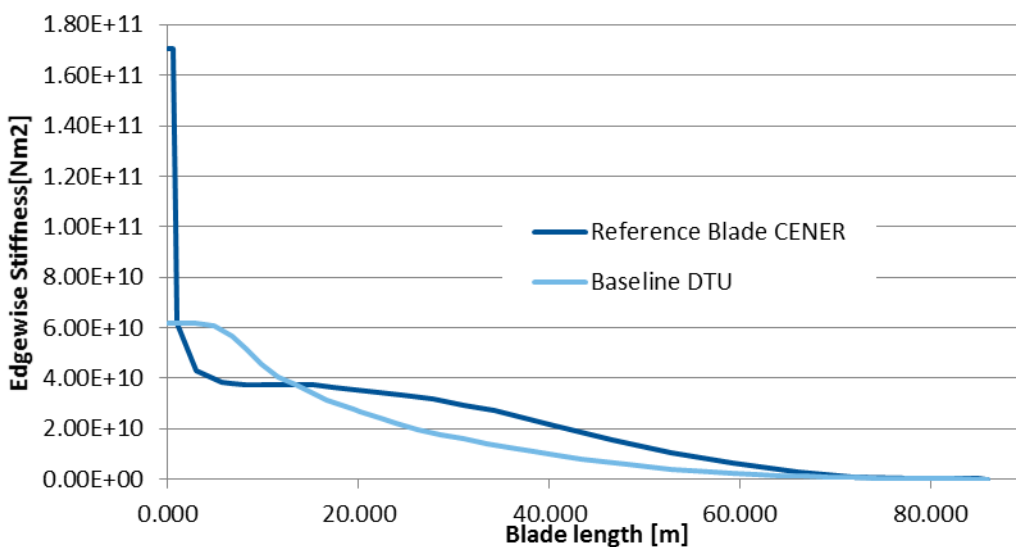


Figure 133 Blade mass distribution of CENER reference blade versus DTU baseline



**Figure 134** Flapwise stiffness distribution of CENER reference blade versus DTU baseline



**Figure 135** Edgewise stiffness distribution of CENER reference blade versus DTU baseline

### 3.4.2.2 Strength ratio for the static reference case

According to the design defined and the reference case, strength ratio distribution at every section is defined in Table 45.

**Table 45. Strength ratio distribution of CENER reference blade for reference load case**

Section	Strength ratio – Reference Load case				
n°	Distance from root [m]	Hill [-]	Hoffman [-]	Tsai-Wu [-]	Max-Strain [-]
1	0.000	1.635	1.669	2.070	2.698
2	0.00	3.844	3.931	4.907	6.088
3	0.50	3.881	3.969	4.956	6.149

Section	Strength ratio – Reference Load case				
n°	Distance from root [m]	Hill [-]	Hoffman [-]	Tsai-Wu [-]	Max-Strain [-]
4	0.75	2.345	2.398	2.994	3.717
5	1.00	1.412	1.444	1.803	2.244
6	2.95	1.009	1.032	1.040	1.340
7	5.72	1.005	1.027	1.038	1.324
8	6.69	1.005	1.027	1.032	1.328
9	8.23	1.007	1.030	1.038	1.338
10	9.87	1.012	1.035	1.036	1.324
11	11.60	1.051	1.075	1.075	1.373
12	13.43	1.032	1.056	1.060	1.363
13	15.35	1.041	1.063	1.063	1.415
14	17.36	1.008	1.005	1.005	1.341
15	20.91	1.008	1.005	1.005	1.397
16	24.66	1.008	1.005	1.005	1.417
17	27.79	1.010	1.020	1.027	1.467
18	31.00	1.021	1.034	1.050	1.495
19	34.28	1.016	1.027	1.049	1.506
20	40.08	1.010	1.019	1.064	1.562
21	46.62	0.996	1.000	1.067	1.591
22	52.87	1.024	1.022	1.111	1.528
23	59.32	0.995	0.998	1.083	1.476
24	66.12	1.011	1.000	1.115	1.526
25	72.09	1.008	0.999	1.061	1.311
26	78.95	1.213	1.183	1.229	1.370
27	80.81	1.206	1.173	1.203	1.246
28	82.45	1.179	1.160	1.167	1.180
29	83.32	1.180	1.168	1.171	1.180
30	85.07	2.073	2.070	2.070	2.072

### 3.4.2.2.1 Deflection

The deflection of the blade for the reference case load is obtained from two different FE models. The first one is based on CBEAM elements (NASTRAN format) and the second one is founded on the stiffness matrixes defined externally considering the formulation explained in section 3.4.1.5

For direct comparison, it is assumed that the elastic & shear centers of every section of the blade are coincident with the PITCH axis, and no torsional moments are introduced.

Due to the lay-up, that is oriented at 0° related to the PITCH axis of the blade, no structural couplings appear (H14, H24 and H34 are equal to 0.0) and as consequence, the torsional deflection of the blade is also equal to 0.0

Table 46 and Figure 136 shows the blade deflection values obtained for these two FE models.

**Table 46. Reference blade deflection values for the reference load case**

CENER reference blade deflections / GL Coordinate system					
CBEAM FE model			KAAX FE model		
Distance from Root [m]	Displacement X axis [m]	Displacement Y axis [m]	Distance from Root [m]	Displacement X axis [m]	Displacement Y axis [m]
2.80	0.00	0.00	2.80	0.00	0.00
3.30	0.00	0.00	3.05	0.00	0.00
3.55	0.00	0.00	3.43	0.00	0.00
3.80	0.00	0.00	3.68	0.00	0.00
5.75	0.00	0.00	4.78	0.00	0.00
8.52	0.02	-0.01	7.13	0.01	0.00
9.49	0.03	-0.01	9.00	0.02	-0.01
11.03	0.04	-0.02	10.26	0.03	-0.01
12.67	0.06	-0.03	11.85	0.05	-0.02
14.40	0.09	-0.04	13.54	0.07	-0.03
16.23	0.12	-0.05	15.32	0.10	-0.05
18.15	0.17	-0.07	17.19	0.14	-0.06
20.16	0.22	-0.10	19.16	0.19	-0.08
23.71	0.35	-0.15	21.94	0.28	-0.12
27.46	0.53	-0.22	25.58	0.43	-0.18
30.59	0.72	-0.28	29.02	0.62	-0.25
33.80	0.96	-0.36	32.20	0.83	-0.32
37.08	1.25	-0.45	35.44	1.10	-0.40
42.88	1.90	-0.62	39.98	1.55	-0.53
49.42	2.87	-0.85	46.15	2.34	-0.73
55.67	4.05	-1.09	52.55	3.40	-0.96
62.12	5.58	-1.37	58.89	4.76	-1.22
68.92	7.58	-1.67	65.52	6.53	-1.51
74.89	9.69	-1.95	71.90	8.64	-1.80
81.74	12.51	-2.27	78.32	11.17	-2.09
83.61	13.35	-2.36	82.68	13.17	-2.30
85.25	14.11	-2.44	84.43	14.04	-2.38
86.12	14.53	-2.48	85.69	14.67	-2.44
87.87	15.37	-2.57	87.00	15.34	-2.51
88.74	15.79	-2.61	88.31	16.03	-2.57
			88.74	16.25	-2.59

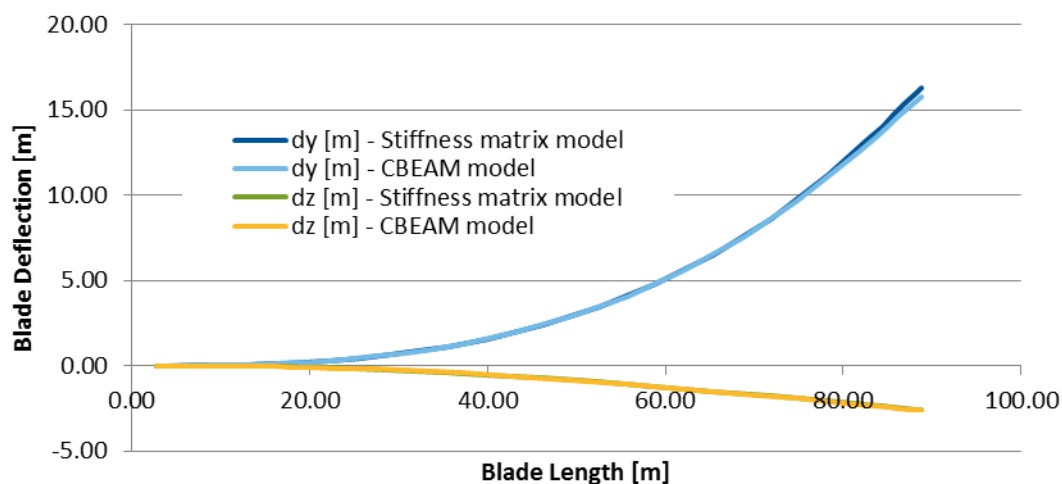


Figure 136 Blade deflections for the reference load case

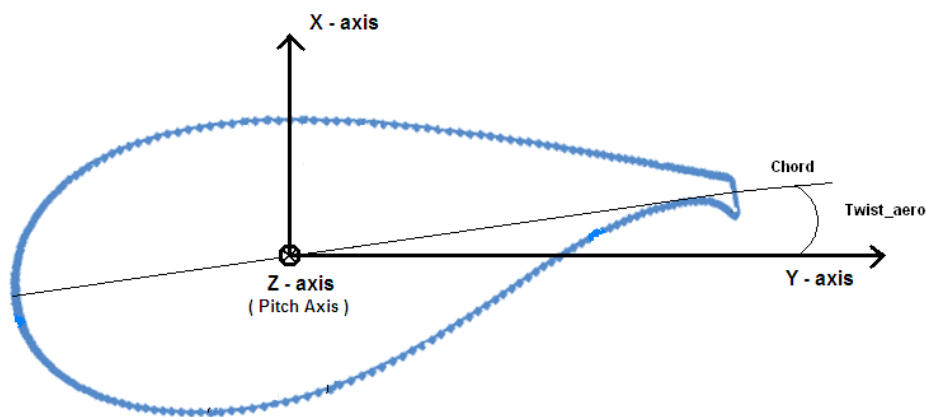


Figure 137 Coordinate system defined by GL-2010 [9]

The FE model defined with external stiffness matrixes predicts similar deflection as that one from the FE model with CBEAMS. However these matrixes include the possibility of considering the structural coupling effects by adding the cross terms H14, H24 & H34.

These stiffness matrixes can be also defined in MSC.ADAMS, which is the multi-body tool used by CENER for advanced aero-elastic load analyses.

### 3.4.2.3 Blade design for build –in structural coupling effects

To evaluate the influence of build-in structural coupling designs, the reference blade defined in section 3.4.2.1 is slightly modified by misaligning the orientation of the spar-cap UD layers to an angle of 5° with respect to the PITCH axis.

According to this new lay-up, the trailing edge moves towards the suction side of the blade as the flapwise moment increases. This effect should reduce the PITCH movement demanding and also increase the energy production at wind velocities different from nominal

#### 3.4.2.3.1 Lay-up description & properties

The lay-up description is identical to the lay-up for the reference blade described in paragraph 3.4.2.1.1.

The lay-up and internal architecture are coincident with the reference blade, so the overall mass and the centre of gravity are the same. However, the stiffness distribution changes slightly due to

the misalignment of the UD plies at the spar-cap. Table 47 shows these values.

**Table 47. Distribution of the blade's mechanical properties**

Section ID	Distance from Root [m]	Mass/unit length [Kg/m]	Flapwise Stiffness [Nm <sup>2</sup> ]	Edgewise Stiffness [Nm <sup>2</sup> ]	Torsional Rigidity [Nm <sup>2</sup> ]	Centre of mass [%]	Elastic axis [-]
1	0.000	2658.0	1.67E+11	1.71E+11	6.49E+10	50.55	50.55
2	0.500	2658.0	1.67E+11	1.71E+11	6.49E+10	50.55	50.55
3	0.750	1622.7	1.00E+11	1.03E+11	4.15E+10	50.55	50.55
4	1.000	989.5	6.02E+10	6.16E+10	2.62E+10	50.24	50.16
5	2.950	830.7	4.50E+10	4.31E+10	1.87E+10	48.83	48.56
6	5.717	775.6	3.72E+10	3.86E+10	1.87E+10	47.92	47.60
7	6.691	772.3	3.57E+10	3.79E+10	2.03E+10	48.86	48.62
8	8.232	767.8	3.27E+10	3.75E+10	2.00E+10	48.97	48.86
9	9.869	789.5	2.92E+10	3.76E+10	1.77E+10	47.66	47.58
10	11.602	811.2	2.49E+10	3.76E+10	1.58E+10	46.39	46.32
11	13.430	833.7	2.18E+10	3.73E+10	1.23E+10	45.33	45.23
12	15.352	856.6	1.83E+10	3.72E+10	9.93E+09	44.71	44.51
13	17.364	864.5	1.48E+10	3.65E+10	7.40E+09	44.31	43.91
14	20.907	853.5	1.16E+10	3.48E+10	5.43E+09	43.78	42.99
15	24.659	830.3	9.04E+09	3.34E+10	4.14E+09	43.53	42.47
16	27.788	822.8	7.52E+09	3.17E+10	3.34E+09	43.34	42.12
17	31.004	805.5	6.17E+09	2.93E+10	2.65E+09	43.26	41.91
18	34.282	786.4	5.04E+09	2.70E+10	2.12E+09	43.39	41.92
19	40.078	746.1	3.51E+09	2.16E+10	1.41E+09	43.22	41.71
20	46.624	659.0	2.21E+09	1.54E+10	8.24E+08	42.95	41.44
21	52.871	575.3	1.41E+09	1.06E+10	4.97E+08	42.64	41.15
22	59.316	433.3	7.85E+08	6.21E+09	2.81E+08	42.30	40.80
23	66.122	285.4	3.96E+08	2.82E+09	1.38E+08	41.04	39.42
24	72.088	159.3	1.83E+08	8.28E+08	6.12E+07	38.80	36.67
25	78.945	56.8	4.51E+07	1.80E+08	1.62E+07	40.15	38.60
26	80.810	39.0	2.84E+07	9.69E+07	8.91E+06	38.61	37.42
27	82.450	30.5	1.76E+07	7.21E+07	6.24E+06	39.26	37.90
28	83.322	22.5	1.06E+07	5.36E+07	4.40E+06	40.42	38.83
29	85.069	19.2	4.20E+06	3.68E+07	2.67E+06	44.12	42.30
30	85.944	9.6	7.48E+05	1.06E+07	8.93E+05	48.50	48.50

#### 3.4.2.4 Strength ratio for the static reference case

The strength ratio distribution for this misaligned version of the spar-cap lay-up under the reference case is defined in Table 48.

**Table 48. Strength ratio distribution of the updated blade (misaligned spar-cap) for the reference load case**

Section		Strength ratio – Reference Load case			
n°	Distance from root [m]	Hill [-]	Hoffman [-]	Tsai-Wu [-]	Max-Strain [-]
1	0.000	3.844	3.931	4.907	6.088
2	0.00	3.881	3.969	4.956	6.149
3	0.50	2.345	2.398	2.994	3.717
4	0.75	1.411	1.443	1.802	2.242
5	1.00	1.008	1.031	1.039	1.339
6	2.95	1.003	1.026	1.036	1.322
7	5.72	1.003	1.026	1.031	1.326
8	6.69	1.003	1.025	1.033	1.332
9	8.23	1.005	1.028	1.029	1.315
10	9.87	1.041	1.065	1.065	1.360
11	11.60	1.019	1.043	1.047	1.346
12	13.43	1.026	1.049	1.049	1.395
13	15.35	0.988	0.985	0.985	1.316
14	17.36	0.985	0.982	0.982	1.364
15	20.91	0.985	0.982	0.982	1.382
16	24.66	0.985	0.995	1.003	1.430
17	27.79	0.995	1.008	1.025	1.457
18	31.00	0.989	1.001	1.024	1.466
19	34.28	0.984	0.993	1.038	1.519
20	40.08	0.970	0.975	1.041	1.549
21	46.62	1.000	0.999	1.086	1.507
22	52.87	0.995	0.998	1.058	1.455
23	59.32	0.990	0.980	1.095	1.518
24	66.12	0.990	0.999	1.047	1.304
25	72.09	1.193	1.164	1.203	1.360
26	78.95	1.195	1.162	1.195	1.240
27	80.81	1.173	1.153	1.160	1.174
28	82.45	1.171	1.159	1.162	1.171
29	83.32	2.050	2.047	2.047	2.049
30	85.07	5.135	5.028	5.071	5.135

According to the results obtained, the structural performance of the blade with the misaligned spar-cap is decreased in comparison with the reference blade. As consequence this design must be reinforced to bear the loads defined in the reference load case.

From this conclusion, it does not make sense to work with this lay-up configuration. However, in order to accept or discard definitively this design it is necessary to evaluate the energy production, new loads envelope and also the demanding of PITCH that could balance the disadvantages associated to a slight higher blade weight.

### 3.4.2.4.1 Deflection

Due to the spar-cap lay-up, that is misaligned 5° related to the PITCH axis of the blade, structural coupling appear at those sections where the spar-cap exists. Table 49 shows the values for H14, H24 & H34 at every section of the blade.

Table 49. *Karaolis terms for the updated blade (misaligned spar-cap)*

Section n°	Distance from root [m]	Structural coupling terms		
		H14 [Nm/rad]	H24 [Nm <sup>2</sup> /rad]	H34 [Nm <sup>2</sup> /rad]
1	0.00	0.00E+00	0.00E+00	0.00E+00
2	0.00	0.00E+00	0.00E+00	0.00E+00
3	0.50	0.00E+00	0.00E+00	0.00E+00
4	0.75	2.32E+03	2.51E+07	5.74E+07
5	1.00	-2.43E+06	-3.13E+07	4.51E+07
6	2.95	-1.47E+04	5.73E+07	1.05E+08
7	5.72	1.75E+05	5.03E+07	1.09E+08
8	6.69	-5.05E+03	2.07E+08	3.12E+08
9	8.23	1.64E+03	2.44E+08	5.22E+08
10	9.87	6.15E+04	3.39E+08	7.73E+08
11	11.60	-2.85E+07	3.87E+08	9.91E+08
12	13.43	-2.93E+07	3.47E+08	1.06E+09
13	15.35	-1.70E+05	5.30E+08	1.79E+09
14	17.36	1.91E+04	4.37E+08	1.89E+09
15	20.91	9.08E+05	3.04E+08	1.61E+09
16	24.66	1.00E+05	2.36E+08	1.40E+09
17	27.79	-5.43E+05	1.78E+08	1.16E+09
18	31.00	3.14E+06	1.31E+08	9.63E+08
19	34.28	2.26E+06	7.25E+07	6.71E+08
20	40.08	-1.19E+04	3.39E+07	4.23E+08
21	46.62	-3.53E+04	1.39E+07	2.63E+08
22	52.87	-1.50E+04	3.52E+06	1.29E+08
23	59.32	-2.22E+04	3.54E+05	6.08E+07
24	66.12	1.98E+03	-3.43E+05	2.91E+07
25	72.09	1.10E+04	-2.16E+05	6.90E+06
26	78.95	-2.99E+03	-1.77E+05	4.69E+06
27	80.81	-5.99E+02	-1.02E+05	2.60E+06
28	82.45	-3.74E+02	-5.18E+04	1.36E+06
29	83.32	3.05E+01	-1.04E+04	2.88E+05
30	85.07	0.00E+00	0.00E+00	0.00E+00

The deflection of the blade under the reference case is detailed in Table 50. It is remarked that the elastic & shear centers are assumed to be coincident with the PITCH axis and no torsional moments are introduced. In this case, due to the coupling terms, the blade undergoes torsional deformation. Only the model defined with external stiffness matrixes is calculated.

**Table 50. Updated blade deflection values for the reference load case**

CENER updated blade deflections / GL Coordinate system			
KAAX FE model			
Distance from Root [m]	Displacement X axis [m]	Displacement Y axis [m]	Rotation Z axis [deg]
2.80	0.00	0.00	0.00
3.05	0.00	0.00	0.00
3.43	0.00	0.00	0.00
3.68	0.00	0.00	0.00
4.78	0.00	0.00	0.00
7.13	0.01	0.00	0.00
9.00	0.02	-0.01	0.00
10.26	0.03	-0.01	0.00
11.85	0.05	-0.02	0.00
13.54	0.07	-0.03	-0.01
15.32	0.10	-0.05	-0.02
17.19	0.14	-0.06	-0.04
19.16	0.19	-0.08	-0.07
21.94	0.28	-0.12	-0.20
25.58	0.44	-0.18	-0.47
29.02	0.63	-0.25	-0.81
32.20	0.86	-0.32	-1.16
35.44	1.14	-0.41	-1.58
39.98	1.63	-0.55	-2.23
46.15	2.49	-0.76	-3.33
52.55	3.66	-1.01	-4.79
58.89	5.17	-1.29	-6.46
65.52	7.14	-1.60	-8.19
71.90	9.49	-1.91	-9.97
78.32	12.31	-2.23	-11.97
82.68	14.54	-2.45	-13.61
84.43	15.50	-2.54	-14.14
85.69	16.21	-2.60	-14.39
87.00	16.96	-2.67	-14.52
88.31	17.71	-2.74	-14.55
88.74	17.97	-2.76	-14.55

### 3.4.3 Blade Design effect on loads and energy production

The effect of the blade design on the aero-elastic loads is done using MSC.ADAMS, although the multibody model of the wind turbine provided by DTU is defined making use of FAST2ADAMS tool (programmed by NREL).

Main characteristics of the wind turbine model are defined in Table 51.

**Table 51. Wind turbine model provided by DTU**

GENERAL CHARACTERISTICS OF THE WIND TURBINE model provided by DTU	
Wind Regime	IEC Class 1A
Rotor Orientation	Clockwise rotation - Upwind
Control	Variable Speed Collective Pitch
Cut in wind speed	4 m/s
Cut out wind speed	25 m/s
Rated wind speed	11.4 m/s
Rated power	10 MW
Number of blades	3
Rotor Diameter	178.3 m
Hub Diameter	5.6 m
Hub Height	119.0 m
Minimum Rotor Speed	6.0 rpm
Maximum Rotor Speed	9.6 rpm
Maximum Generator Speed	480.0 rpm
Gearbox Ratio	50.0
Maximum Tip Speed	90.0 m/s
Hub Overhang	7.1 m
Shaft Tilt Angle	5.0 °
Rotor Pre-cone Angle	-2.5 °
Rotor Delta3 (sweep) Angle	0.0 °

Up to now, the structural coupling effect has been considered using a parameter named in FAST as “Alpha” which is used to couple flapwise bending with torsion. This parameter has been tuned so that the torsion deformation of the blade fits with the values of Table 50.

Figure 138 shows the wind turbine model defined by DTU with the blade design that incorporates torsional coupling. When flapwise moment increases, blades’ trailing edges move towards the suction side.

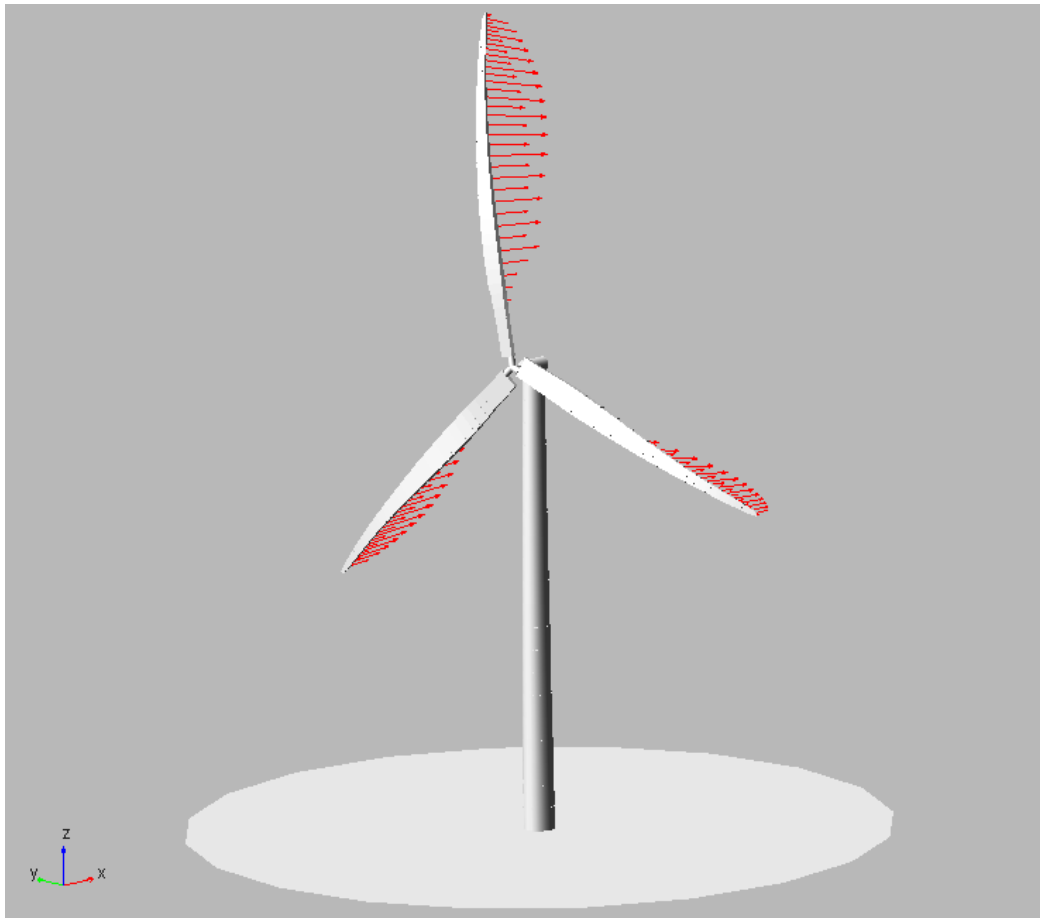


**Figure 138** DTU wind turbine model defined in MSC.ADAMS

Energy production and load envelope at blade root is checked at a stationary state where the wind speed is 8.4m/s (lower values than the rated wind speed)

Following main results are obtained:

- ✓ Flapwise bending moment at blade root: This value is reduced from 23500kNm to 19000kNm ( $\approx 20\%$ ) for the blade design which includes build-in structural coupling.

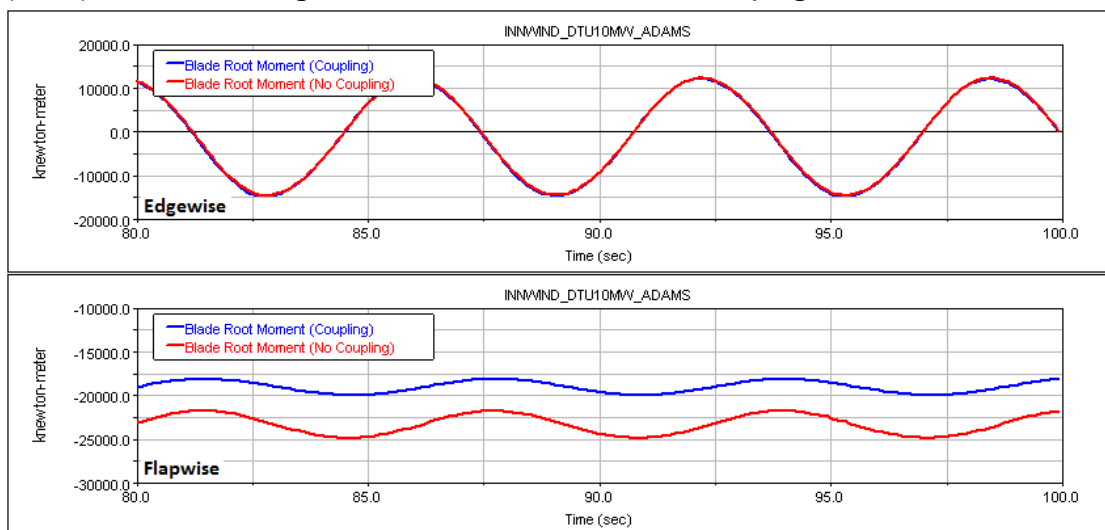


**Figure 139** Flapwise bending moments at blade root for both blade designs

- ✓ Wind turbine power: This values is increased from 3.3MW to 3.8MW ( $\approx 15\%$ ) at this working condition. PITCH demand is almost the same at both configurations

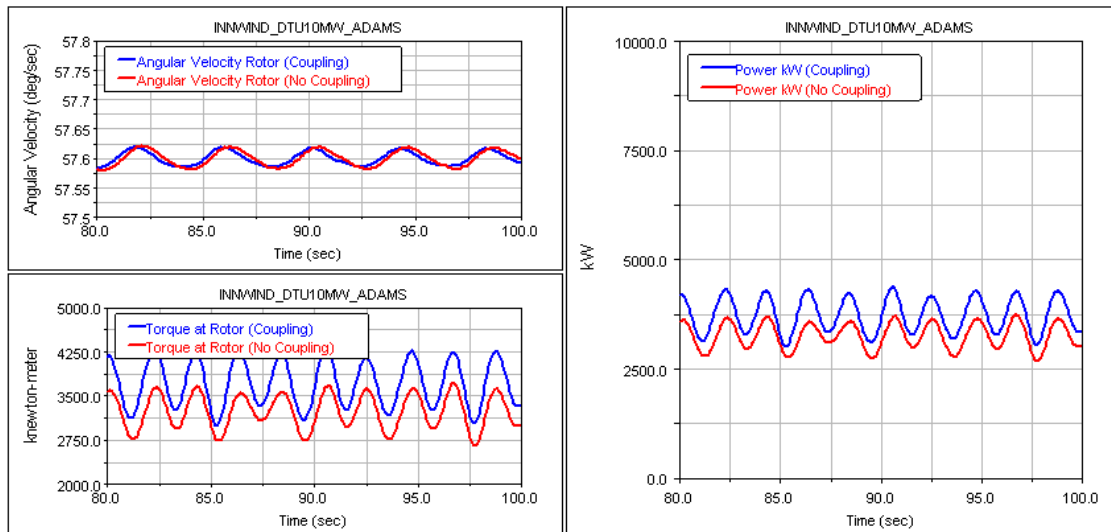


**Figure 140** Wind turbine power for both blade designs

Although these first results are attractive, further work should be done to evaluate the performance of the wind turbine under all of the cases defined by the standard in order to understand exactly how the build-in structural blade design is affecting the performance of the wind turbine, and as a consequence take a decision about the feasibility and effectiveness of this solution.

## 4 INTEGRATED STRUCTURAL DESIGN SOLUTIONS

In the present chapter solutions relevant to the structural design optimization performed through an integrated aeroelastic and structural solution environment are described.

The structural design to verify the integrity of the blade in the case of low induction rotor blades is presented first. The low induction rotor has been studied by CRES as a solution through aerodynamic analysis within task 2.1 of the INN WIND.EU project. In the present work package the material configuration is adapted properly, in order to accommodate the constraints posed regarding stiffness, strength and dynamic response in the operation of the reference wind turbine. In order to maintain the mass of the blade for a feasible design part of the unidirectional glass reinforcement was replaced with carbon fibres. This was needed since by elongating the blade (increasing the length of the reference blade) the natural frequencies dropped significantly and the mass of the blade increased substantially. To enable the increased energy capture through the longer rotor, while keeping the rest of the wind turbine components, the blade mass had to return to comparable values as for the reference.

In this chapter also the work of WMC is presented relevant to optimizing the placement of material in the reference wind turbine blade, by use of the integrated aeroelastic-structural optimization code FOCUS6. The design or redesign of the blade is performed by keeping the same material as well as the same aerodynamic shape.

Finally, in this chapter PoliMI presents three different integrated structural solutions based on the blade “PoliMI 10MW BTC SC+05” presented in section 3.1. These blades are:

- “PoliMI 10MW 182m BTC SC+05”: a longer blade (+4m with respect to the reference one) with the Bend-Twist Coupling (BTC). This solution is based on the idea that since the BTC is able to reduce the loads on the hub and tower (as seen in section 3.1), one may stretch the blade keeping almost constant the loads on these components and increasing, at the same time, the Annual Energy Production;
- “PoliMI 10MW BTC SC+05 IPC”: a blade with the same shape and size of that presented in section 3.1, but designed including also an Individual Pitch Control (IPC), an advance control law able to reduce the fatigue load as well as the ultimate ones;
- “PoliMI 10MW 188m BTC SC+05 + IPC”: a longer blade (+10m with respect to the reference one) with also the IPC. In this case thanks to the advance controller, the blade length is about 10m longer than the reference one.

All the blades proposed here have been re-designed within an optimization design framework in order to account for all the design constraints (i.e. frequencies placements, maximum tip deflection, ultimate and fatigue stress and buckling). The final goal is to reduce the Cost of Energy which accounts for the mass of the blade as well as for the Annual Energy Production (AEP).

Within this delivery, the aerodynamic shape of the blade is the same of the reference one; the longer blades (for the 182, 188m and 200m rotors) have been only stretched.

### 4.1 Structural solution for Low Induction Rotor (LIR) blade (CRES)

The structural design of the Low Induction Rotor (LIR) blade performed by CRES is presented in the current section. The aerodynamic investigations relevant to the blade have been performed within the INN WIND.EU project and reported in the frame of WP2, Task 2.1.

#### 4.1.1 State of the art and motivation

Short description of the state of the art for the solution and motivation for the structural concept selected.

#### 4.1.2 Brief description of the concept/solution

For the structural investigations performed and presented in here the LIR blade is based on the geometric characteristics of the reference INN WIND.EU blade. The modification concerned the prolongation of the z-axis node coordinates (along the blade length) of the reference blade by a factor of 1.13 resulting in a new blade of 100.758 m (LIR blade).

The optimized design of the LIR blade was achieved with the introduction of carbon uniaxial layers on selective locations along the blade length to improve the stiffness of the blade keeping at the same time the mass of the blade as low as possible. Additionally, glass fibre layers with 90° fiber orientation in relation to the blade axis were introduced mainly on the suction side of the blade to increase strength against transverse stresses.

The description of the materials and the lamination schemes used in the blade structure is presented in the next sections. Further, the performance of the blade with respect to modal, strength, buckling analysis (extreme loading) is also demonstrated.

It should be stated that the suction side is mainly subjected to compressive loading and thus it is prone to elastic instabilities as well as to structural failures because the compressive failure strengths are lower than the tensile ones. Taking this into account, the blade was purposely enforced to a greater extend in its suction side while material was subtracted from the pressure side to keep the overall mass of the blade as low as possible. Thus, regarding the cap, the introduction of carbon layers was to increase stiffness in the flap direction as well as to strengthen the blade. Additionally, 90° glass UNIAX layers were introduced to increase strength against transverse stresses. Further, carbon layers were added in tail A to augment the blade stiffness in the edge direction, to reduce the tip displacement in the same direction as well as to enhance the eigen-frequency related to vibration in the edge direction. For the same reasons, the growth of the glass UNIAX thickness was performed in tail B. Finally, for the web A & B, the balsa and the BIAx layers were augmented to withstand more efficiently the developed shear stresses.

#### 4.1.3 Anticipated PROS and CONS

The carbon fabrics ensure greater stiffness and strength of the blade structure keeping its mass in low values. On the other hand, the use of these carbon layers certainly increases the cost of the structure.

#### 4.1.4 Assessment of the structural integrity of the proposed design

##### 4.1.4.1 Design layout and dimensioning

Material properties: The three glass fabrics manipulated in the INN WIND.EU reference blade namely UNIAX, BIAx and TRIAX were also adopted herein. BALSa was used in the various sandwich panels. Additionally, carbon uniaxial layers were further introduced in the specific blade design while their property values were retrieved by a literature research in the area of carbon reinforced fibres for use in the wind energy sector e.g. [66], as well as from experiments performed within the EERA JP-Wind PrePreg miniproject [67]. The material properties for every fabric as well as its density are presented in Table 52. Note that the strength properties depicted in this table correspond to the design values and they have already been multiplied with the appropriate safety factors defined by GL [9].

Table 52. *Design values for the material properties of the Glass and Carbon fabrics*

Parameter	[Unit]	UNIAX	BIAx	TRIAx	BALSa	CARBON
E <sub>1</sub>	[GPa]	41.63	13.92	21.79	0.05	115.00
E <sub>2</sub>	[GPa]	14.93	13.92	14.67	0.05	7.56
v <sub>12</sub>	[-]	0.24	0.53	0.48	0.50	0.30
G <sub>12</sub>	[GPa]	5.05	11.50	9.41	0.017	3.96
X <sub>T</sub>	[MPa]	396.44	100.99	217.38	0.31	596.20
X <sub>C</sub>	[MPa]	283.17	94.68	177.85	0.18	280.60
Y <sub>T</sub>	[MPa]	33.50	100.99	40.90	0.31	9.86
Y <sub>C</sub>	[MPa]	85.69	94.68	69.10	0.18	34.50
S	[MPa]	25.60	63.50	51.60	0.14	20.60
ρ	[kg/m <sup>3</sup> ]	1915.50	1845.00	1845.00	110.00	1578.00

Lamination scheme: The LIR blade design is based on the design of the reference INN WIND.EU blade. The notation used to describe the various location in the reference blade e.g. Tail A, Tail V

etc. was also adopted herein. The new design involves the following modifications with respect to the design of the reference blade.

**Tail A** (pressure and suction side): The glass UNIAX fabrics were replaced with carbon layers of 0° fiber orientation (along the blade axis). The thickness of the carbon layers was set equal to 0.6 of the thickness of the glass UNIAX fabric.

**Tail B** (pressure and suction side): The thickness of the glass UNIAX fabrics were increased twice.

**Cap** (pressure side): The thickness of the glass UNIAX layers were reduced to 0.3 of their initial thickness while carbon layers were added to the lamination scheme with thickness equal to 0.4 the initial thickness of the glass UNIAX layers.

**Cap** (suction side): Glass UNIAX layers of 90° fiber orientation were added to the lamination scheme symmetrically with respect to the Balsa position. The thickness of the 90° layers were set equal to 0.3 and 0.2 the thickness of the initial glass UNIAX layers from the root up to 9.019 m and from 9.019 m to the blade tip respectively. Further, starting from the blade root up to 9.019 m, the glass UNIAX layers were replaced with carbon layers with the same thickness. From 9.019 m to the blade tip, the thickness of the carbon layers were set equal to 0.5 of the initial thickness of the glass UNIAX fabrics while the thickness of the glass UNIAX layers were reduced to 0.3 their original thickness.

**LP** (suction side): The glass UNIAX layers were reduced to 0.7 and 0.4 of their initial thickness from 9.019 m to 24.635 m and 24.635 m to 32.442 m from the blade root respectively. Glass UNIAX layers with 90° fiber orientation were introduced in the lamination scheme from 24.635 m up to 32.442 m from the blade root. The thickness of the 90° layers was gradually increased from 0.4 to 7.2 the initial thickness of the glass UNIAX layers at this span. BIAx layers were also added in the lay-up with thickness equal to 0.2 the initial thickness of the glass UNIAX layers.

**Web A & B**: The thickness of the glass BIAx layers were augmented and set equal to 4 mm from 87.095 m to the blade tip. In the same locations, the thickness of the Balsa was set equal to 8 mm.

The lamination scheme for the other location e.g. Web C, tail V etc. was kept the same with the reference INN WIND.EU blade.

**Mass**: The mass of the new blade design as well as the mass of the carbon layers used in the lamination schemes can be seen in the first two columns of Table 53. In the same table, the center of gravity for the whole blade is also superimposed while a comparison with the reference blade is also performed. The x, y, and z axis correspond to the global coordinate system introduced in the benchmark of the structural analysis tools within INN WIND.EU project [2]. It is highlighted that the new blade design is heavier compared to the reference one about 2415 kg while the ratio of the carbon-layer mass to the overall blade mass is 15.92%. Concerning the spar caps, the mass of the carbon layers is 6332.5 kg close to the mass of the unidirectional glass fabric (6477.95 kg).

Table 53. *Global blade properties*

Blade	Overall mass [kg]	Carbon [kg]	C.G. z [m]	C.G. x [m]	C.G. y [m]
LIR blade	44785.90	7127.89	31.69	-0.21	0.11
INN WIND.EU blade	42371.20	—	28.80	-0.16	0.04

#### 4.1.4.2 Load cases considered

The loading of the LIR blade was estimated by the reference wind turbine blade loading. Following the aerodynamic design of the blade the solution to be acceptable for the reference wind turbine would mean that the root bending moments for the longer blade would be kept the same as the reference blade. Therefore, for deflection and strength estimations the LIR blade was subjected to 13% lower concentrated loads in both the edgewise and flapwise directions.

#### 4.1.4.3 Structural integrity verification

To verify the suitability of the blade design for the wind turbine, as well as to verify the structural integrity, modal analysis, static strength analysis and buckling analysis were performed. The

constraints set in order to have a feasible solution for the reference 10MW wind turbine, were as follows:

**Dynamic behaviour:** natural frequencies of the blade were to be as close as possible to the reference wind turbine blade. Avoidance of 6p, 9p, etc. of the reference wind turbine.

**Stiffness, Strength:** Stiffness and strength of the LIR blade should be comparable to the reference blade.

**Elastic stability:** The LIR blade should perform comparable to the reference blade or even better. The loading applied to verify the structural design was the same as that of the stiffness and the strength.

The results of the final solution proposed are presented in the following.

**Modal analysis:** The first six natural frequencies of the blade are presented in Table 54. It is obvious that all the calculated frequencies of the LIR blade are close to the ones of the reference INNWIND.EU blade with the LIR blade frequencies however to be below the reference blade frequency values (except for the first natural frequency which are equal).

Table 54. *Natural frequencies of the blade (all frequencies in Hz)*

Mode No.	LIR blade	INNWIND.EU blade
1	0.640	0.640
2	0.897	0.959
3	1.807	1.849
4	2.686	2.863
5	3.644	3.763
6	5.469	5.824

Results of the tip displacement in the x (edge) and y (flap) direction can be seen in the following table. The LIR blade is stiffer both in flap- and edge-wise direction comparing with the reference blade.

Table 55. *Tip deflection*

Blade	Ux (edge) [m]	Uy (flap) [m]
LIR	1.817	15.556
INNWIND.EU	2.322	18.529

Strength analysis was performed calculating the Tsai-Wu failure index. Contour plots of the maximum Tsai-Wu value among the various layers for every element is presented in Figure 141 for both sides of the rotor blade (pressure and suction side). Critical part of the blade comprises the suction side especially in the spar cap, see Figure 141d. More specifically, the Tsai Wu failure index for the elements from 38.79 m to 61.30 m from the blade root varies between 1.09 and 1.11. The failure mode is related to the failure of the carbon layers in the fiber direction. Reminding that the INNWIND.EU reference blade indicated a maximum Tsai-Wu failure index equal to 2.756 (using CRES calculations) [2], the current blade design is considered adequate.

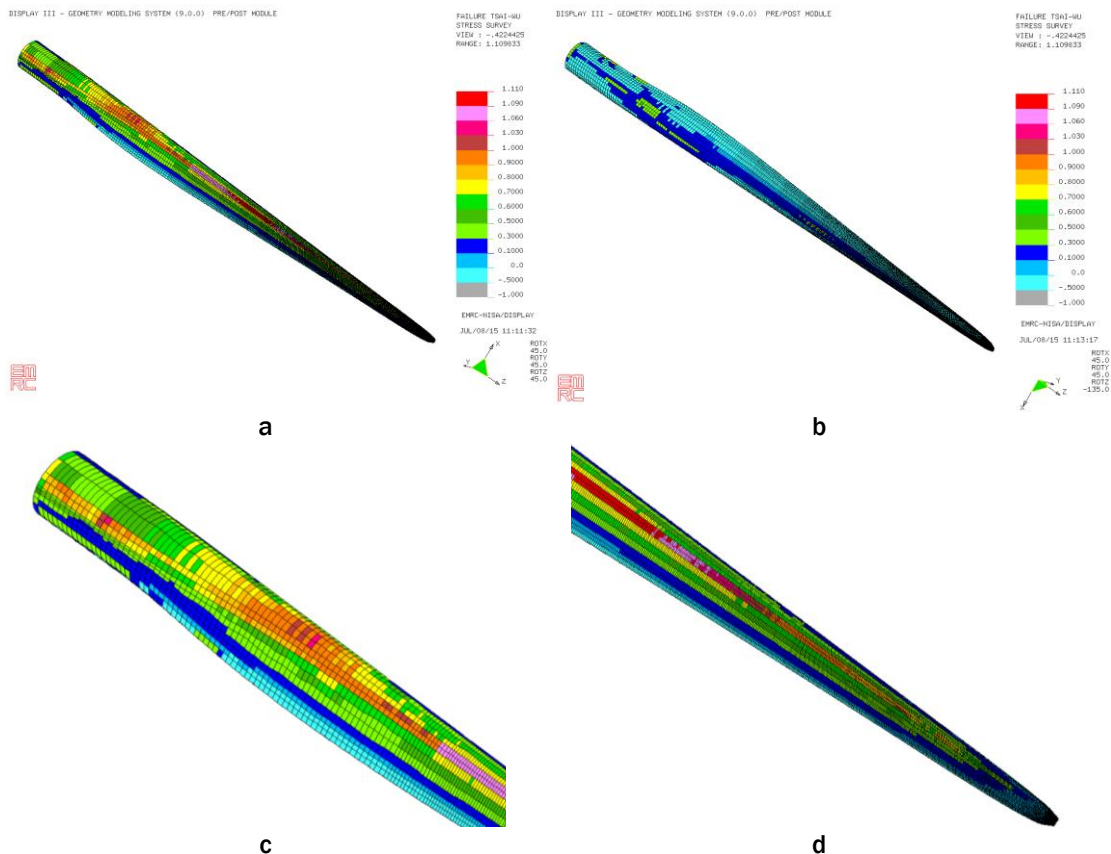


**Figure 141. Tsai-Wu failure criterion a) at the suction side b) at the pressure side c) a detail in the Inboard part of the suction side d) a detail in the outboard part in the suction side of the LIR blade**

Buckling analysis was performed considering safety factors for the stiffness properties of the glass and carbon fabrics as also done within the benchmark. More specifically, the values of the stiffness properties of Table 52 were divided by a factor 2.042. The value of the factor was adopted by [2] following GL [9] requirements. The first critical buckling load factor was calculated equal to 0.97 while the respective eigen-mode is presented in Figure 142. The critical location comprises the suction side of the blade, see Figure 142b, as well as the shear webs (A & B), see Figure 142c. More specifically, buckling is observed in the spar cap of the blade root and in the spar cap, leading and trailing panels in the outboard part (near the tip) at the suction side of the blade. Moreover, the shear webs in the outboard part (near the tip) of the blade also buckle. Regarding the failure in the outboard part, it should be said that concentrated forces of high value were applied at this location in the FE blade model and thus the respective failure mode correspond to this modelling defect. A direct comparison with the reference blade (buckling load factor 0.875) indicates that the LIR blade is quite adequate considering elastic stability.

DISPLAY III - GEOMETRY MODELING SYSTEM (9.0.0) PRE/POST MODULE

DISPLACED-SHAPE  
 MX DEF= 1.96E-04  
 NODE NO. = 60470  
 SCALE = 1.0  
 (MAPPED SCALING)

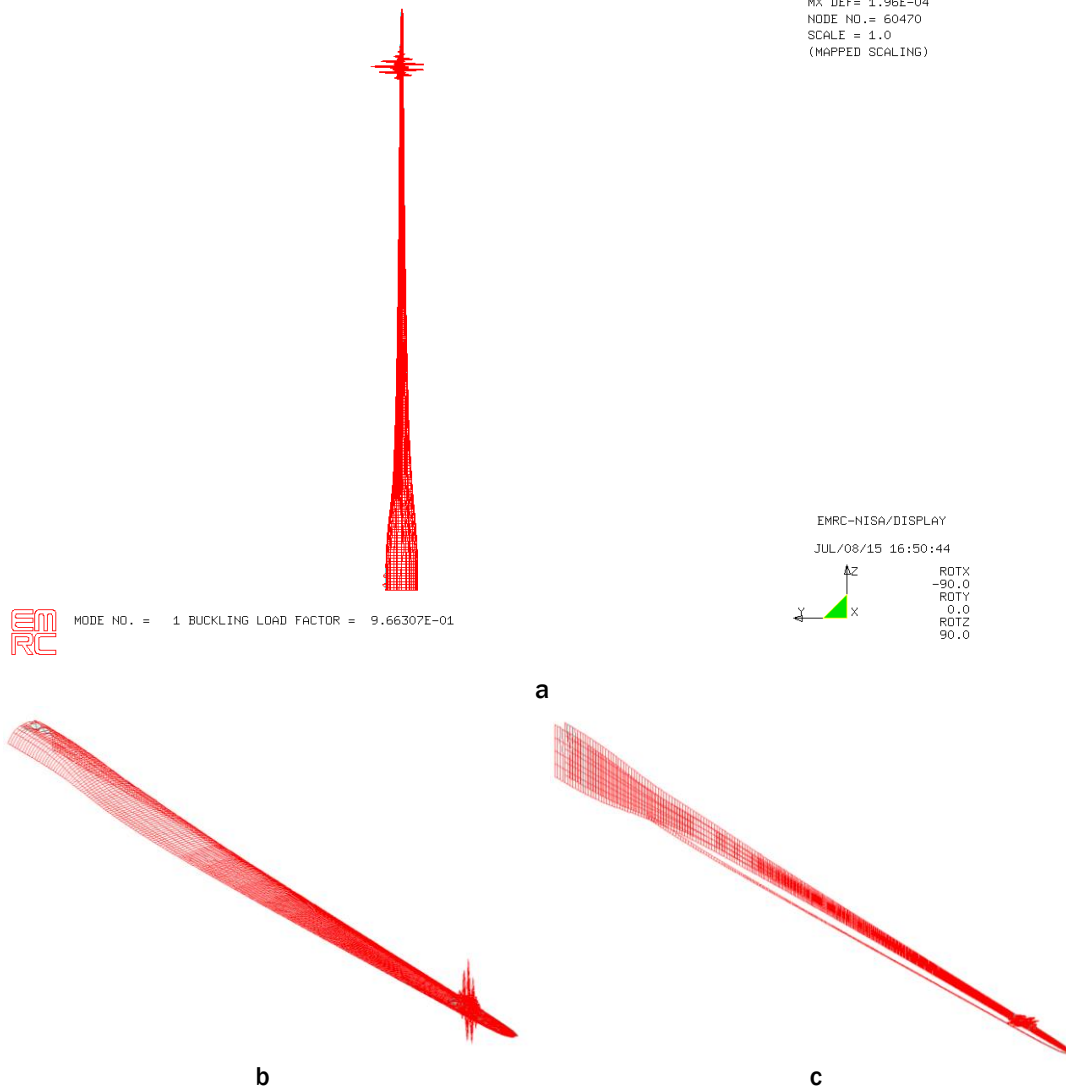


Figure 142. First eigen-mode of the LIR blade a) left side b) suction side c) shear webs (A & B & C)

#### 4.1.5 Conclusions and recommendations

The introduction of carbon fabrics permitted an efficient design of a 100 m rotor blade with respect to modal, stiffness, strength and buckling analysis. At the same time, the mass of the blade was kept in low values, increased only 5.6% in comparison to the mass of the 90 m INN WIND.EU reference blade design.

## 4.2 Integrated structural optimization using FOCUS6 (WMC)

### 4.2.1 State of the art and motivation

The design solution in the present section is developed by performing an optimization in FOCUS6. We started with the reference turbine and calculated load cases. The loads from these load cases were applied to the reference blade. Next the thickness distributions along the blade were modified using the parameterization method described in [66].

The optimization procedure in FOCUS6 has led to optimized thickness distributions, which are described below.

The solution presented is based on the design of the reference blade and does not require any new concepts.

#### **4.2.2 Brief description of the concept/solution**

The optimization procedure has led to a design where the spar cap is heavier than in the reference blade, but a reduced material usage elsewhere in the blade. The net mass reduction is approximately 1700 kg.

#### **4.2.3 Anticipated PROS and CONS**

Strengthening the spar cap is not generally applicable to an arbitrary blade design.

However, the reference blade design is the result of upscaling from a smaller blade. It makes sense that different parts of the blade have their own scaling rules.

The flap wise bending moments are carried mainly by the spar caps. On the other hand, the trailing and leading panels do not play a large role in that. Therefore they can be allowed to grow less fast with the length of the blade.

#### **4.2.4 Assessment of the structural integrity of the proposed design**

##### **4.2.4.1 Design layout and dimensioning**

The optimized design and the reference design only differ in the layer thickness as a function of the radius as shown in the figure below.

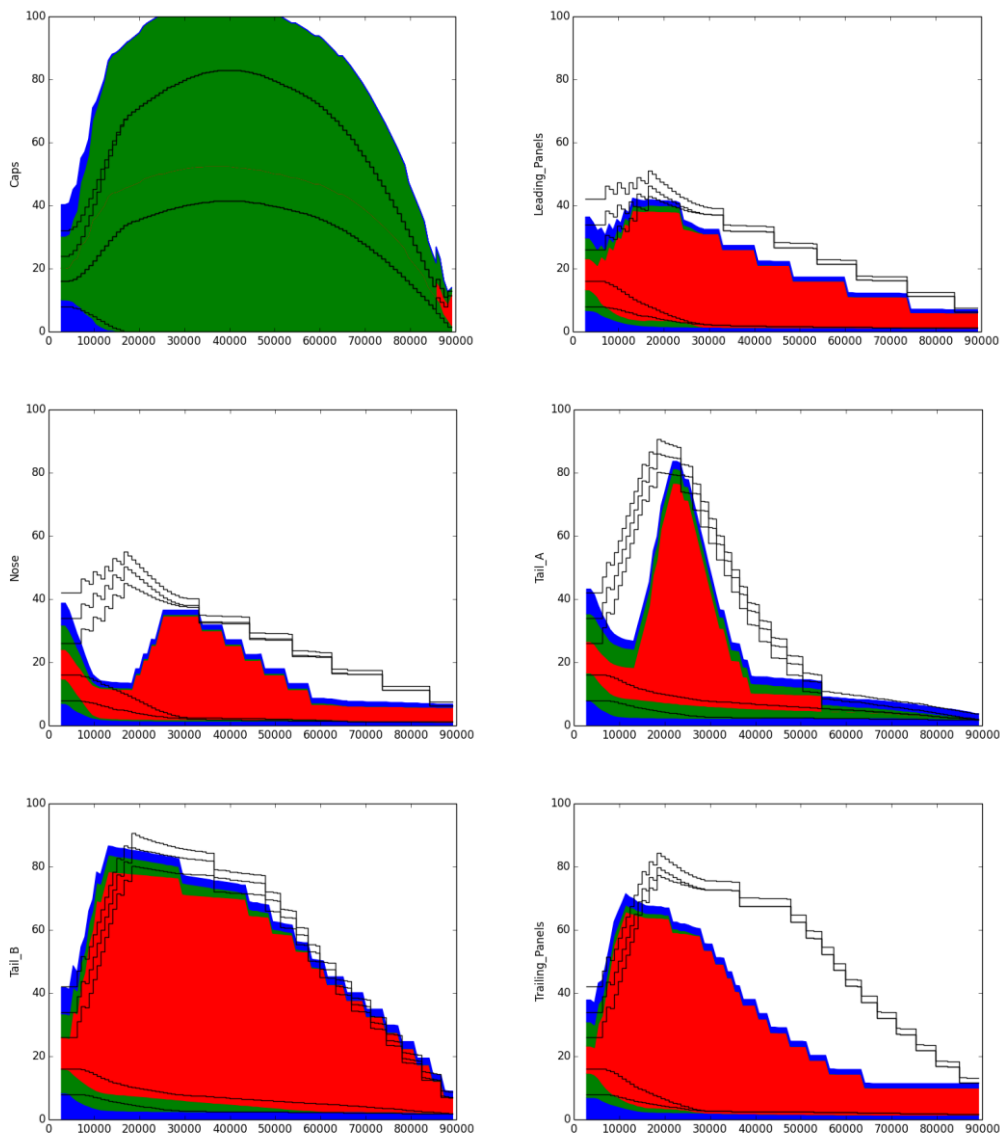


**Figure 143. Comparison of the thickness distributions of the optimized and reference blade**

#### 4.2.4.2 Structural integrity verification

The weight of the optimized blade is 1700 kg less than the weight of the reference blade. The resistance against buckling has been reduced from 1.21 to 1.05, but is still acceptable, i.e. larger than 1. The minimum safety factor for stress is increased to a safe value from 0.86 to 1.01. The maximum tip deflection is reduced from 12.51 to 10.54 m. Furthermore, the maximum fatigue damage has been decreased from the unsafe value of 4.61 to the safe value of 0.73.

**Table 56. Comparison of the structural constraints of the reference and the optimized blades**

Name	Reference blade	Optimized blade
Minimum critical load factor	1.21	1.05
Minimum safety factor for stress	0.86	1.01
tip_deflection [m]	12.51	10.54
total_mass [kg]	42024.47	40318.28
Maximum damage	4.61	0.73

Besides the overall weight reduction, the optimized blade has a better structural performance than the reference blade.

#### 4.2.5 Conclusions and recommendations

We have observed that the thickness of the layers in the spar cap should increase. The weight increase can be compensated by decreasing thicknesses in the other parts of the blade. This suggests that the knowledge of scaling rules for different parts of the blade can help the development of designs of large blades for offshore wind turbines.

The reference blade can be made stronger by strengthening the spar cap. The weight increase is more than compensated by decreasing layer thicknesses in trailing and leading panels. Besides the overall weight reduction the optimized blade has a better structural performance and meets all applied constraints.

The reference blade is designed by upscaling a smaller blade. Our investigation suggests that the required strength of the spar caps increases faster than the secondary structural parts of the blade.

### 4.3 PolIMI 10MW 182m BTC SC+05 (PolIMI)

The integrated structural design of the PolIMI 10MW 182m rotor incorporating Bend-Twist-Coupling is presented in this section. In relation to the “PolIMI 10MW BTC SC+05” solution presented earlier, this solution includes stretching of the blade length.

#### 4.3.1 State of the art and motivation

The re-design of the RWT blade inner structure, with the adoption of bend-twist coupling as presented in section 3.1, shows the potential advantages of this passive load reduction technique in terms of ultimate and fatigue loads. The blade mass therefore reduces, but, since the AEP is almost the same, the CoE drops slightly.

As observed in [67], the cost of energy model has a very high influence on the wind turbine rotor design: on dependence of the cost model adopted one can obtain a significant different optimal rotor design. The solution here proposed is based on the INN WIND cost model [68]. This model is mainly dependent on the annual energy production, while the blade total mass has a very small influence and the loads on the fixed frame (hub and/or tower) are not taken into account at all.

In order to influence more and more the CoE, (i.e. to increase the AEP) one solution could be to stretch the blade keeping constant the hub and tower loads (i.e. maintaining the same structure of the turbine).

#### 4.3.2 Brief description of the concept/solution

A series of parametric studies is done increasing the rotor diameter of the structural solution proposed in 3.1 (“PolIMI 10MW BTC SC+05”). For each solution the blade design is performed with a constrained optimization-based procedure that sizes the structural blade elements by minimizing a cost function [28], [29] and [30] through the procedure indicated in section 3.1.2.

Since the BTC is able to reduce the loads on the hub (and on the tower), the diameter is increased as long as the maximum combined bending moment on the hub does not exceed the one computed for the RWT.

The increase in blade length is done by stretching all the properties to a major extension. No other element of the wind turbine is touched, i.e. non changes to hub height or rotor cone, etc. The distribution of chord, twist, airfoil thickness is unchanged, but it is now stretched to adapt to a longer blade.



Figure 144. PoliMI BTC SC+05, blade length increased

### 4.3.3 Anticipated PROS and CONS

The main goal of this solution is to increase the AEP increasing the rotor diameter but keeping frozen the load on the hub and tower, i.e. keeping frozen the other components of the WT. The constraint used in this solution is not to exceed the maximum combined bending moment on the hub based on the assumption that this is a design load. The fatigue loads are computed but not constrained so that in some case may exceed the reference values. The impact of this loads on the structure (and hence on the final real CoE) should further investigated in the other WPs.

The blade total mass, and its cost, increases, but this seems to have a little impact on the final cost of energy. On the other hand, the longer blade affects heavily the AEP and hence the final cost of energy.

Aerodynamic distribution of twist, chord and thickness remains the same of the RWT, but the longer blade probably changes the local Reynolds number so that this impact on the aerodynamic performance has to be further investigated.

Nevertheless we expect a sensible increase of annual energy production and hence a lower cost of energy.

### 4.3.4 Assessment of the structural integrity of the proposed design

#### 4.3.4.1 Design layout and dimensioning

The same concept for the design layout as for the “PoliMI 10MW BTC SC+05”, as described under section 3.1.4.1 was used for the present structural solution.

The following table reports the global data of the optimal blade POLIMI 182m BTC SC+05 compared with the reference one.

Table 57. PoliMI 182m BTC SC+05, comparison against RWT

	RWT	PoliMI 182 m BTC SC+05	Difference
Rotor Diameter	178.3 m	182 m	+ 2.07 %
Blade Total Mass	42422 kg	44473 kg	+ 5.02 %
Blade 1 <sup>st</sup> modal freq (flap)	0.6123 Hz	0.5522 Hz	-
Blade 2 <sup>nd</sup> modal freq (edge)	0.9124 Hz	0.6303 Hz	-
Max Blade Tip Deflection	13.04 m	12.90 m	-
AEP	45.760 GWh	46.765 GWh	+ 2.19 %
CoE	75.911 \$/kWh	74.632 \$/kWh	- 1.68 %

The following table reports the mass breakdown computed for each structural components including the Non-Structural Masses (NSM). The figures below report the thickness distributions

along the blade span of the internal sub-components and the mass, flapwise and edgewise stiffness.

Table 58. *PolIMI 182m BTC SC+05, bill of material*

Structural Component	Mass [kg]	% of total blade mass
Skin	9069	20.39
Spar Cap	19092	42.93
Web A + B	2356	5.31
Web C	91	0.20
LE & TE Reinforcement	1825	4.10
Root Reinforcement	3006	6.76
<b>Total Structural Mass</b>	<b>35439</b>	<b>79.69</b>
<b>NSM</b>	<b>9034</b>	<b>20.31</b>
<b>Total blade mass</b>	<b>44473</b>	<b>100.00</b>

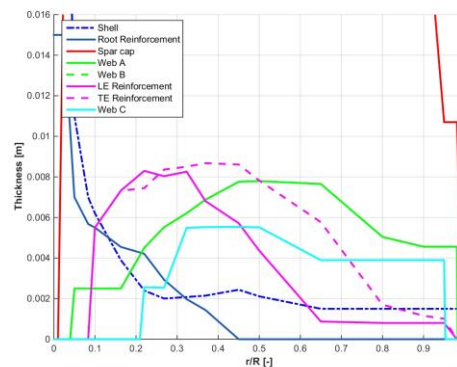
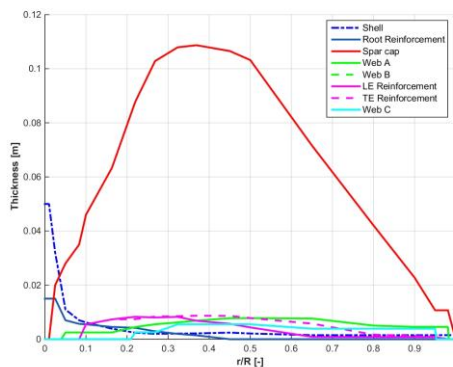


Figure 145. PolIMI 182m BTC SC+05, structural thickness distributions

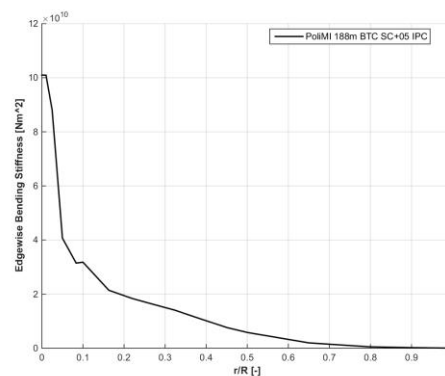
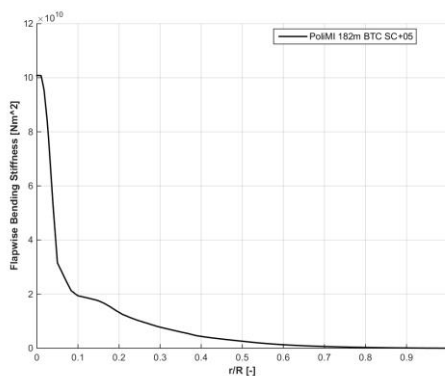
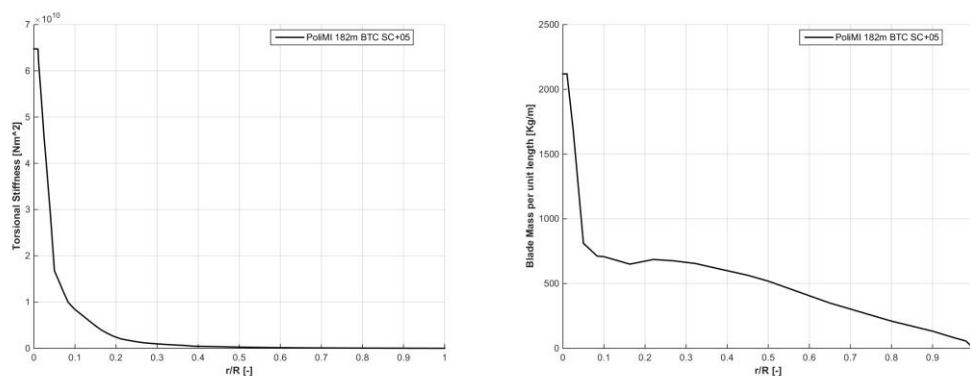
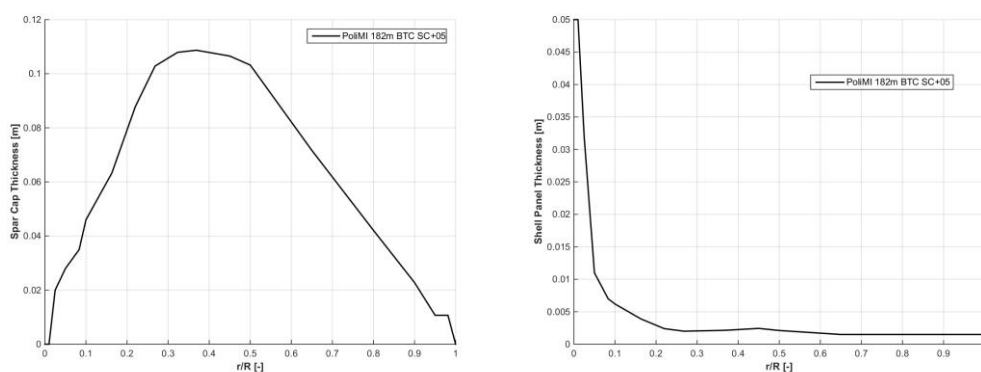


Figure 146. PolIMI 182m BTC SC+05, flapwise (left) and edgewise (right) stiffness distributions



**Figure 147. PolIMI 182m BTC SC+05, torsional stiffness (left) and blade mass (right) distributions**



**Figure 148. PolIMI 182m BTC SC+05, spar cap (left) and skin (right) distributions**

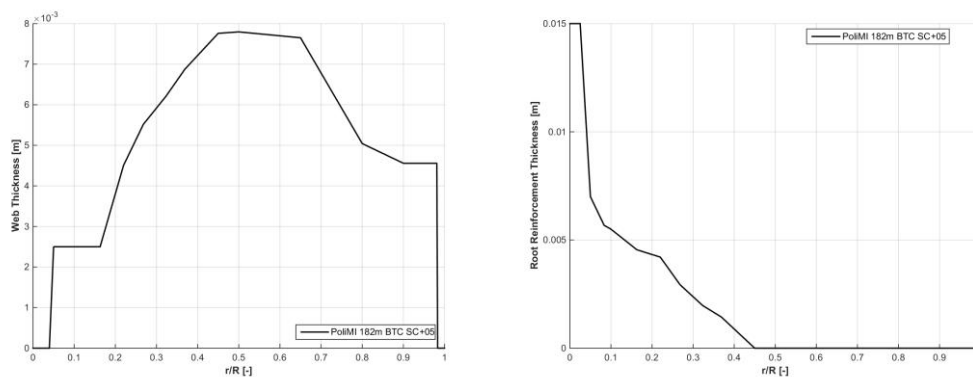


**Figure 149. PolIMI 182m BTC SC+05, web (left) and root reinforcement (right) distributions**

The next figures show the deflection of the blade in the out of plane direction in correspondence of the first mode of vibration (at left) and the corresponding torsion associated to the blade (at right) mainly due to the bend-twist coupling.

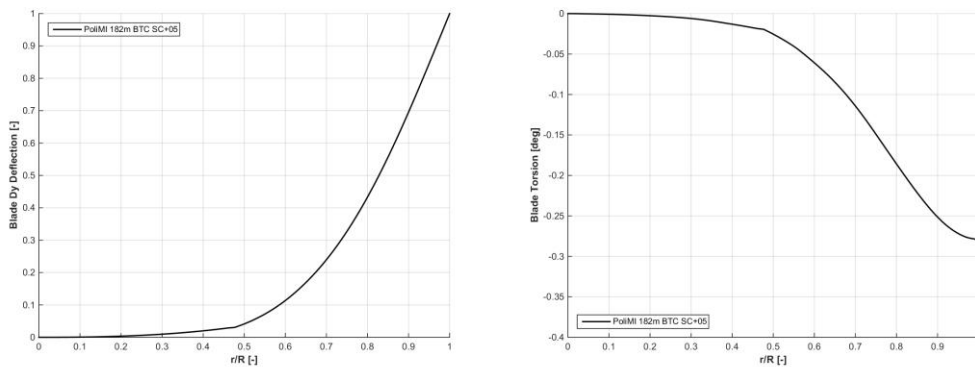


**Figure 150. Polimi 182m BTC SC+05, first flapwise mode: flapwise (left) and torsion (right) deflections**

#### 4.3.4.2 Load cases considered

The blade is designed according to IEC 61400-1 Ed.3. The load cases selected for the design are the same defined in section 3.1.4.2.

#### 4.3.4.3 Structural integrity verification

The proposed blade satisfies all the design constraints, as can be seen from the following figures, which report the constraint margin for stress, strain and fatigue analysis in all the structural components of the blade as described in sections 3.1.

A constraint value is considered active when its value reaches 0. If  $> 1$  the constraint is violated, if  $< 0$  the constraint is non-active. As one can see, only the fatigue constraint is active in the first 3 figures, which are relatives to skin, spar cap and webs.

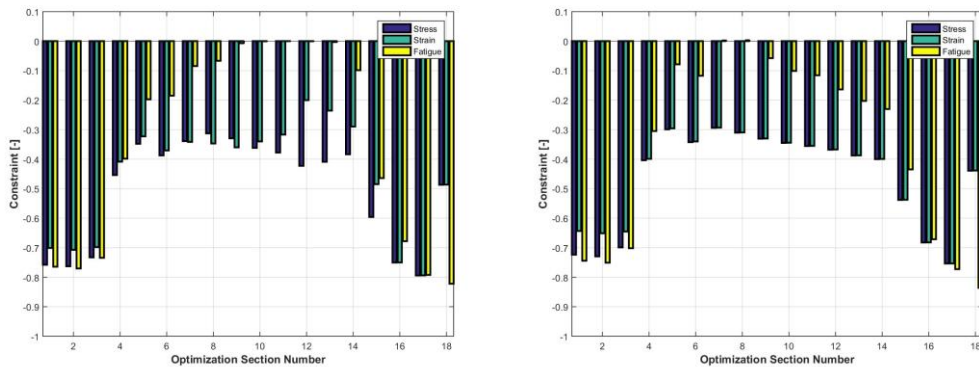


**Figure 151. Polimi 182m BTC SC+05, skin (left) and spar cap (right) constraints**

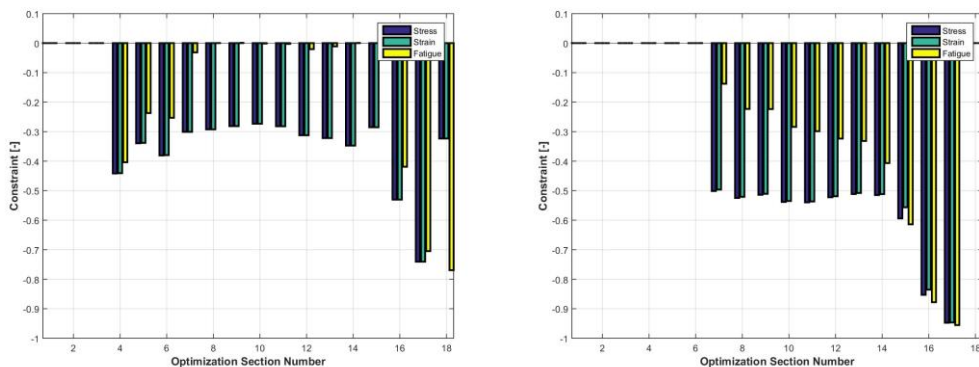


**Figure 152. Polimi 182m BTC SC+05, web (left) and TE reinforcement (right) constraints**

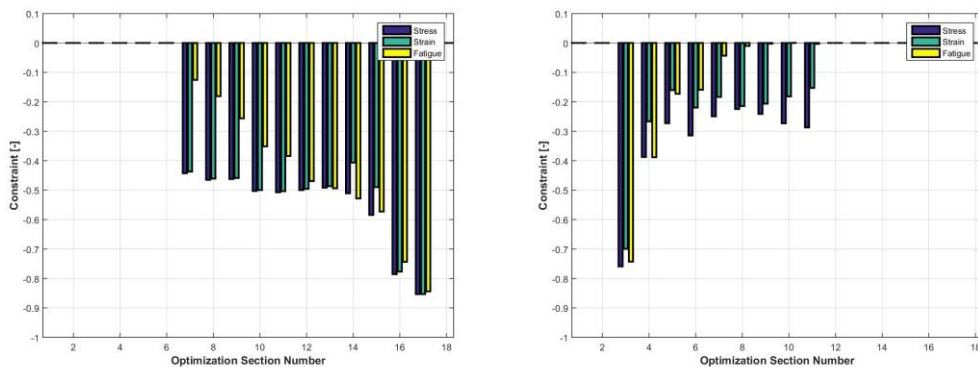


Figure 153. PoliMI 182m BTC SC+05, LE reinforcement (left) and root reinforcement (right) constraints

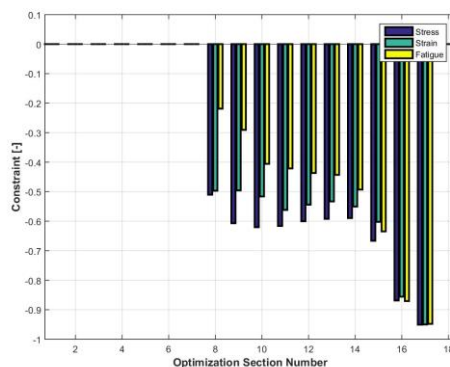


Figure 154. PoliMI 182m BTC SC+05, third web constraints

The following table shows the ultimate loads on the hub and tower compared with the ones computed (with the same conditions) for the RWT. In this analysis the hub combined bending moment is constrained to be equal to the reference one (-049%), but as one can see the loads on the tower are still lower than the reference values.

Table 59. PoliMI 182m BTC SC+05, comparison of ultimate loads against RWT

	RWT	PoliMI 182 m BTC SC+05	difference
Hub Nodding Moment	57097 kNm	57428 kNm	+ 0.58 %
Hub Yaw Moment	53046 kNm	46066 kNm	- 13.15 %
Hub Combined Moment	58271 kNm	57982 kNm	- 0.49 %
Hub Axial Force	3560 kN	3059 kN	- 14.07 %
Tower Bottom Fore-Aft Moment	491819 kNm	486450 kNm	- 1.09 %
Tower Bottom Combined Moment	495794 kNm	486997 kNm	- 1.77 %
Tower Bottom Torsional Moment	59056 kNm	48556 kNm	- 17.78 %
Tower Top Fore-Aft Bending Moment	59244 kNm	56335 kNm	- 4.91 %
Tower Top Torsional Moment	58688 kNm	48500 kNm	- 17.36 %

Relevant to the fatigue loading, the next table shows the cumulative damage equivalent loads computed considering only DLC12 cases (power production in turbulent wind), as in the case presented for the “PoliMI 10MW BTC SC+05” and described in 3.1.4.3.

It can be seen that the optimal blade with BTC with this longer blade is able to limit the increase in the fatigue loads of about 4% on the hub despite the increase in the blade length and its mass.

Since tower and hub have not been re-designed in this deliverable, the real effects on the CoE of this optimal blade have to be further investigated.

Table 60. *PoliMI 182m BTC SC+05, comparison of fatigue DEL against RWT*

	RWT	PoliMI 182 m BTC SC+05	Difference
DEL Hub Nodding Moment	27950 kNm	29096 kNm	+ 4.10 %
DEL Hub Yaw Moment	26192 kNm	27243 kNm	+ 4.01 %
DEL Tower Bottom Side-Side Moment	59828 kNm	56462 kNm	- 5.63 %
DEL Tower Bottom Fore-Aft Moment	136805 kNm	140107 kNm	+ 2.41 %

#### 4.3.5 Conclusions and recommendations

In this section PoliMI has presented an integrated structural solution based on the so called Bend-Twist Coupling (BTC) plus a blade stretch. The BTC is a passive load mitigation solution obtained by exploiting the anisotropic mechanical properties of composite materials. BTC implies that, when the blade bends because of increased loads, the ensuing change of twist will affect the aerodynamic loading through a change in angle of attack. The load reduction obtained by this solution has been used here to increase the rotor diameter without exceeding the hub and tower loads with respect to the reference ones.

The structural solution is computed throughout a blade design procedure based on a novel comprehensive multi-level constrained optimization approach. The design process alternates between a multibody beam model augmented with a 2D FEM cross sectional sub-models and a fine scale 3D FEM detailed model of the blade. The former enables the numerous transient aero-servo-elastic analyses required to compute loads and deflections throughout the lifetime of the machine, while the latter makes it possible to conduct detailed local verifications of the design.

The use of a constrained optimization-based approach to design is crucial and allows comparing different solutions that satisfy the same design requirements, and hence permitting to choose the optimal solution. The control set-points have been changed in order to improve the annual energy production.

The optimal blade presented here is 2% longer with respect to the RWT and is heavier (+5%), but the ultimate loads on the hub are the same (by constraints) and on the tower are lower. Since the AEP is 2.19% more than the RWT the final CoE is reduced by 1.68%.

The only point to be further investigated is the fatigue loads on the hub which increase by 4%. Since these components have not been re-designed within this task the actual final effect on the CoE of this optimal blade has to be further investigated.

The possibility to adopt an individual pitch control strategy [69], [70] and [71], permits to further lower the loads on the hub and hence to have more space to increase further the rotor diameter.

## 4.4 PoliMI 10MW BTC SC+05 IPC (PoliMi)

### 4.4.1 State of the art and motivation

Active load control systems exploit a power source to move the whole blade, or a part of it, so as to reduce loads due to turbulence, gusts and asymmetry in the inflow. Generally these systems require sensors to measure the wind turbine response and drive, through a feedback loop, a suitable motion strategy. Recently, several IPC formulations have been proposed, demonstrating a significant potential for fatigue load reduction [69], [70], [71], [72], [73], [74], [75] and [76]. In fact, changing the pitch of each blade independently allows for the reduction of the lowest load harmonics, including their mean value. However, one of the possible drawbacks of active load control is its effect on the actuators and their design: constantly pitching the blade increases the actuator duty cycle, and hence its wear. This, in turn, requires more expensive and larger actuators, inducing a tradeoff with the advantages brought by IPC.

Since the longer BTC blades were shown to allow for a reduction in ultimate and fatigue loads (see section 3.1), it seems interesting to combine the two load control technologies. In fact, since both BTC and IPC can reduce loads, by combining them one may obtain a synergistic effect. On the other hand, since BTC tends to reduce ADC and IPC to increase it, by combining the two one can obtain significant load reductions without increase ADC too much.

#### 4.4.2 Brief description of the concept/solution

In this section, PoliMI further investigates the solution presented in 3.1, the solution with bend-twist coupling obtained rotating the fibers of spar cap unidirectional integrated with an Individual Pitch Control (IPC).

This controller is based on the architecture proposed in Ref. [69]; it is driven by blade root moments, which are Coleman transformed in a nacelle-fixed frame of reference to yield the rotor tilt and yaw moments. Two independent proportional integral derivative (PID) controllers compute two fixed frame control inputs by trying to drive the tilt and yaw moments to zero. In turn, the fixed frame inputs are back-transformed into the rotating frame using the inverse Coleman transformation, an operation that generates the individual pitch control inputs. Such inputs are superimposed to the ones computed by a collective pitch and torque controller, whose roles are the regulation of the machine around a given set point and the reaction to gusts.

By adjusting the gains of the IPC PID controllers, one can tune within a certain range the level of individual blade pitch activity, consequently affecting the level of load reduction and of ADC increase.

This integrated BTC and IPC solution is investigated within a design framework where the blade design is performed with a constrained optimization-based procedure that sizes the structural blade elements by minimizing a cost function [28], [29] and [30] through the procedure indicated in section 3.1.2.

#### 4.4.3 Anticipated PROS and CONS

The adoption of an individual pitch controller is aimed at the reduction of loads on the fixed frame, the solution expected should have ultimate and fatigue loads on the hub significantly lower than the loads on the RWT. Since the use of such controller type permits also to decrease the value of loads on blade root, reductions of loads are expected not only on the hub, but also on tower top and bottom.

IPC on the other hand tends to increase significantly the actuator duty cycle and a possible drawback can be the reduction of annual energy production, as already observed in [27].

As per the model cost adopted [68] the influence of energy production is higher than that of blade mass, it should be interesting to see if a multi-megawatt wind turbine equipped with an individual pitch controller has a cost of energy higher or lower than a wind turbine with standard collective pitch controller.

#### 4.4.4 Assessment of the structural integrity of the proposed design

##### 4.4.4.1 Design layout and dimensioning

The same concept for the design layout as for the “PoliMI 10MW BTC SC+05”, as described under section 3.1.4.1 was used for the present structural solution.

The following table reports the global data of the optimal blade POLIMI BTC SC+05 IPC compared with the reference one.

Table 61. *Polimi BTC SC+05 IPC, comparison against RWT*

	RWT	Polimi BTC SC+05 IPC	Difference
Blade Total Mass	42422 kg	40385 kg	- 4.80 %
Blade 1 <sup>st</sup> modal freq (flap)	0.6123 Hz	0.5543 Hz	-
Blade 2 <sup>nd</sup> modal freq (edge)	0.9124 Hz	0.6101 Hz	-
Max Blade Tip Deflection	13.04 m	12.98 m	

	RWT	PoliMI BTC SC+05 IPC	Difference
AEP	45.760 GWhy	46.078 GWhy	+ 0.69 %
CoE	75.911 \$/kWh	75.214 \$/kWh	- 0.92 %

The following table reports the mass breakdown computed for each structural components including the Non-Structural Masses (NSM). The figures below report the thickness distributions along the blade span of the internal sub-components and the mass, flapwise and edgewise stiffness.

Table 62. *PoliMI BTC SC+05 IPC, bill of material*

Structural Component	Mass [kg]	% of total blade mass
Skin	8840	21.89
Spar Cap	16666	41.27
Web A + B	2287	5.66
Web C	73	0.18
LE & TE Reinforcement	1234	3.05
Root Reinforcement	2518	6.24
<b>Total Structural Mass</b>	<b>31618</b>	<b>78.29</b>
<b>NSM</b>	<b>8767</b>	<b>21.71</b>
<b>Total blade mass</b>	<b>40385</b>	<b>100.00</b>

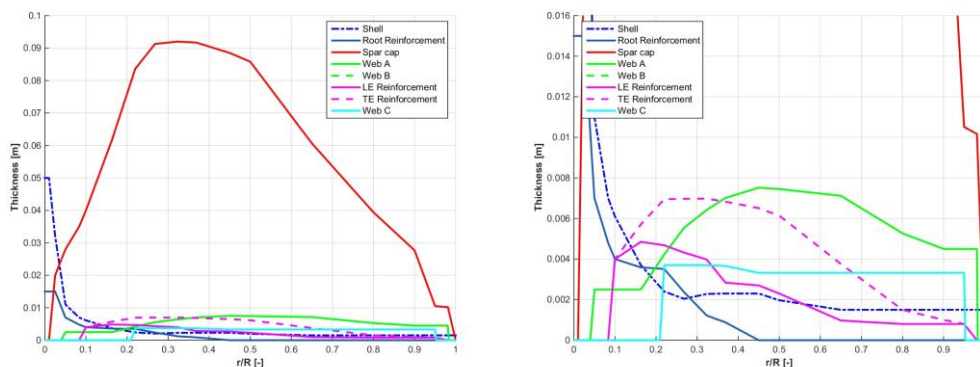


Figure 155. PoliMI BTC SC+05 IPC, structural thickness distributions

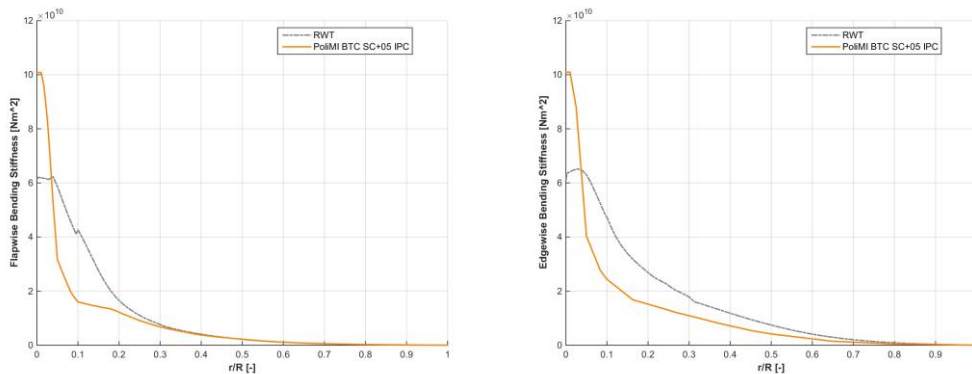


Figure 156. PoliMI BTC SC+05 IPC, flapwise (left) and edgewise (right) stiffness distributions

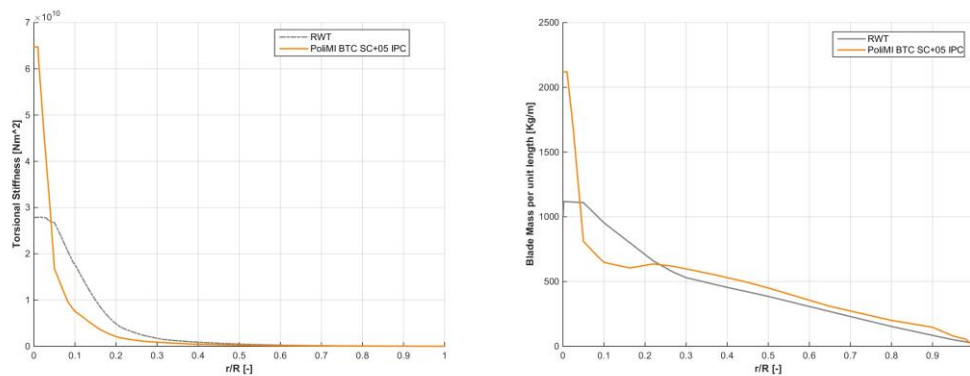


Figure 157. PolIMI BTC SC+05 IPC, torsional stiffness (left) and blade mass (right) distributions

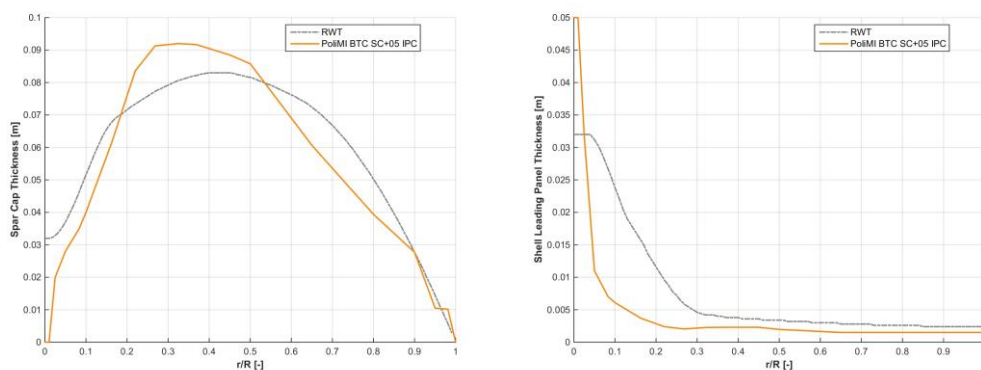


Figure 158. PolIMI BTC SC+05 IPC, spar cap (left) and skin (right) distributions

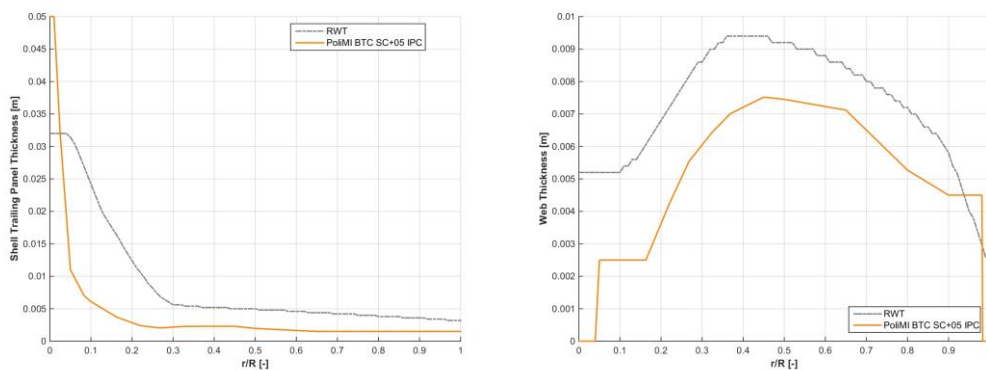


Figure 159. PolIMI BTC SC+05 IPC, web (left) and root reinforcement (right) distributions

The next figures show the deflection of the blade in the out of plane direction in correspondence of the first mode of vibration (at left) and the corresponding torsion associated to the blade (at right) mainly due to the bend-twist coupling.

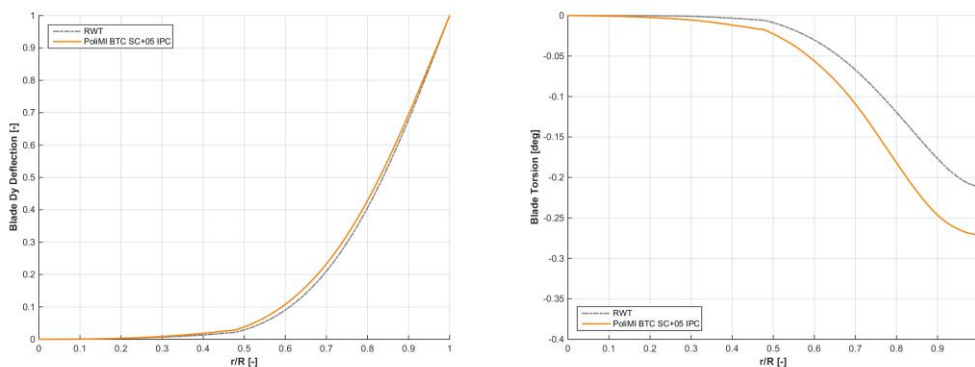


Figure 160. PolIMI BTC SC+05 IPC, first flapwise mode: flapwise (left) and torsion (right) deflections

#### 4.4.4.2 Load cases considered

The blade is designed according to IEC 61400-1 Ed.3. The load cases selected for the design are the same defined in section 3.1.4.2.

#### 4.4.4.3 Structural integrity verification

The proposed blade satisfies all the design constraints, as can be seen from the following figures, which report the constraint margin for stress, strain and fatigue analysis in all the structural components of the blade as described in sections 3.1.

A constraint value is considered active when its value reaches 0. If  $> 1$  the constraint is violated, if  $< 0$  the constraint is non-active. As one can see, only the fatigue constraint is active in the first 3 figures, which are relatives to skin, spar cap and webs.

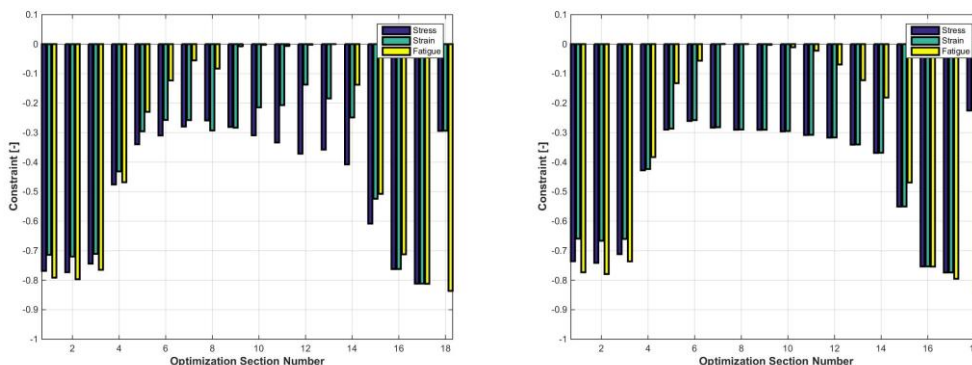


Figure 161. PolIMI BTC SC+05 IPC, skin (left) and spar cap (right) constraints

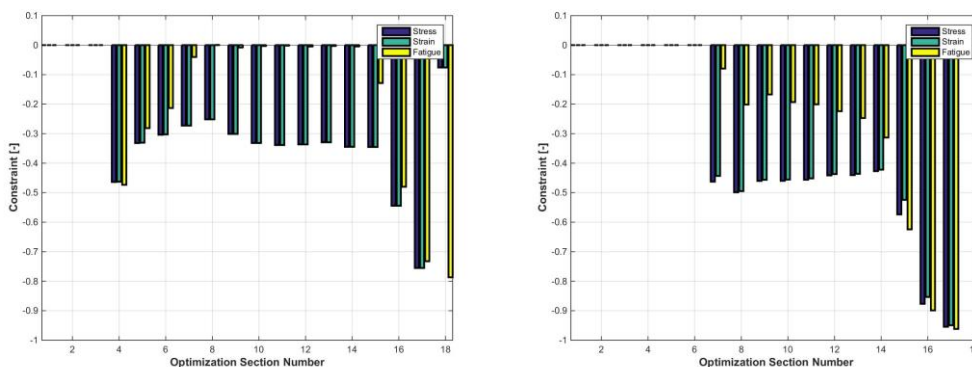
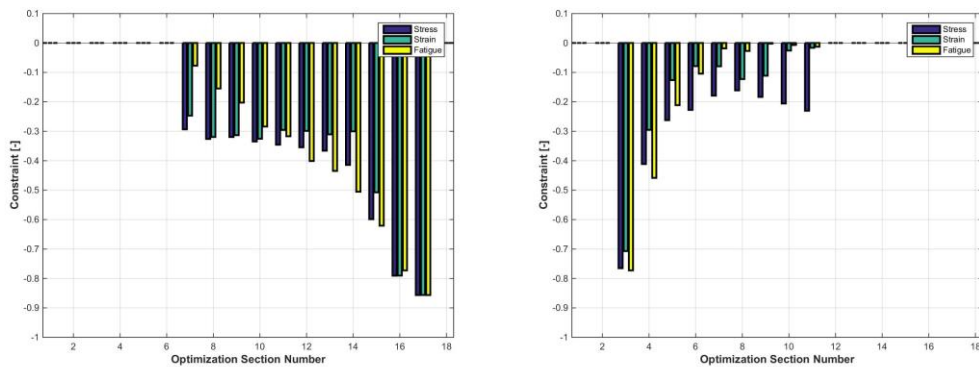
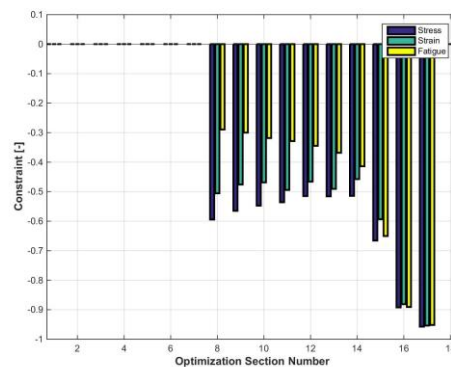


Figure 162. PolIMI BTC SC+05 IPC, web (left) and TE reinforcement (right) constraints



**Figure 163. PoliMI BTC SC+05 IPC, LE reinforcement (left) and root reinforcement (right) constraints**



**Figure 164. PoliMI BTC SC+05 IPC, third web constraints**

The following table shows the ultimate loads on the hub and tower compared with the ones computed (with the same conditions) for the RWT. As one can see the effect of IPC is evident on the reduction of ultimate loads. Comparing these results with that of solution 3.1 (without IPC controller) now the difference is nearly double in terms of reduction of loads, for example the hub combined moment passes from a -7.13 % of saving to a -12.53%.

**Table 63. PoliMI BTC SC+05 IPC, comparison of ultimate loads against RWT**

	RWT	PoliMI BTC SC+05 IPC	Difference
Hub Nodding Moment	57097 kNm	50578 kNm	- 11.42 %
Hub Yaw Moment	53046 kNm	42948 kNm	- 19.04 %
Hub Combined Moment	58271 kNm	50972 kNm	- 12.53 %
Hub Axial Force	3560 kN	3376 kN	- 5.17 %
Tower Bottom Fore-Aft Moment	491819 kNm	414224 kNm	- 15.77 %
Tower Bottom Combined Moment	495794 kNm	464314 kNm	- 6.35 %
Tower Bottom Torsional Moment	59056 kNm	47660 kNm	- 19.30 %
Tower Top Fore-Aft Bending Moment	59244 kNm	50826 kNm	- 14.21 %
Tower Top Torsional Moment	58688 kNm	47470 kNm	- 19.11 %

Relevant to the fatigue loading, the next table shows the cumulative damage equivalent loads computed considering only DLC12 cases (power production in turbulent wind), as in the case presented for the “PoliMI 10MW BTC SC+05” and described in 3.1.4.3.

It can be seen that the optimal blade with BTC and IPC controller is able to further reduce the fatigue loads to - 5% on the hub. This can be used to further extend the concept idea showed in section 4.3.

Table 64. *Polimi BTC SC+05 IPC, comparison of fatigue DEL against RWT*

	RWT	Polimi BTC SC+05 IPC	Difference
DEL Hub Nodding Moment	27950 kNm	26399 kNm	- 5.55 %
DEL Hub Yaw Moment	26192 kNm	24902 kNm	- 4.93 %
DEL Tower Bottom Side-Side Moment	59828 kNm	59513 kNm	- 0.53 %
DEL Tower Bottom Fore-Aft Moment	136805 kNm	136430 kNm	- 0.28 %

#### 4.4.5 Conclusions and recommendations

In this section Polimi has presented an integrated structural solution based on the so called Bend-Twist Coupling (BTC) plus the Individual Pitch Control (IPC). The BTC is a passive load mitigation solution obtained by exploiting the anisotropic mechanical properties of composite materials. BTC implies that, when the blade bends because of increased loads, the ensuing change of twist will affect the aerodynamic loading through a change in angle of attack. IPC is an active load mitigation solution, whose advantages are widely known, and is here explored the possibility offered by the combination of these two technologies. Load reductions obtained are higher than it would be possible by the use of each single one of the two approaches. In the end, the limit of achievable load reduction is also probably due to the physics of the mitigation mechanism itself, that in both cases is due to a change of angle of attack.

The wind turbine, as expected, shows lower loads on hub and tower top and bottom, either maximum or fatigue loads. The lower loads on the blade lead to a designed blade which is significantly lighter than the RWT, this traduces itself in a lower blade cost and hence a lower cost of energy. The reduction of loads experienced is obtained by a change in angle of attack, to which correspond a lower value of lift and hence of loads on the blade. On the other hand, the reduction of angle of attack brings to a less production of energy and so to an increase of cost of energy. To increase as much as possible the value of AEP a tuning of lower bound of pitch regulation versus wind is done.

The final blade is significantly lighter than the RWT (-4.80%), produces more energy (+0.69%) and has a lower cost of energy (-0.92%). This CoE reduction is lower than the one obtained with only BTC (-0.99%, see 3.1). This is mainly due to a lower increase in the AEP which heavily affects the CoE. Nevertheless this integrated solution is interesting since its main advantage is more evident if we consider the difference on the ultimate loads on the wind turbine (which do not affect the CoE). This important load reduction (from 10% to 20%) may be used in other WPs to re-design a lighter substructure and/or can be used to re-design the blade increasing the rotor diameter in order to keep these loads constant but, at the same time, increasing the AEP as done (without IPC) in section 4.3. This integrated (BTC + IPC + higher rotor diameter) solution will be investigated in section 4.5.

### 4.5 Polimi 10MW 188m BTC SC+05 + IPC (Polimi)

#### 4.5.1 State of the art and motivation

The re-design of the RWT blade inner structure, with the adoption of bend-twist coupling as presented in section 3.1, shows the potential advantages of this passive load reduction technique in terms of both ultimate and fatigue loads. The blade mass therefore reduces, but, since the AEP is almost the same, the CoE drops slightly.

As observed in [67], the cost of energy model has a very high influence on the wind turbine rotor design: on dependence of the cost model adopted one can obtain a significant different optimal rotor design. The solution here proposed is based on the INN WIND cost model [68]. This model is mainly dependent on the annual energy production, while the blade total mass has a very small influence and the loads on the fixed frame (hub and/or tower) are not taken into account at all.

In order to influence more and more the CoE, (i.e. to increase the AEP) one solution could be stretching the blade while keeping constant the hub and tower loads (i.e. maintaining the same structure of the turbine), as in the solution presented under section 4.3.

To further limit the increase of ultimate loads on the hub, due to the extension of blade length, within a certain value, PoliMI considers in this integrated solution also the combined adoption of an individual pitch controller (IPC), as presented in the previous section (section 4.4).

#### 4.5.2 Brief description of the concept/solution

A series of parametric studies is done increasing the rotor diameter of the structural solution proposed in 3.1 (“PoliMI 10MW BTC SC+05”) as presented under section 4.3. For each solution the blade design is performed with a constrained optimization-based procedure that sizes the structural blade elements by minimizing a cost function [28], [29] and [30] through the procedure indicated in section 3.1.2.

In parallel, since the combined adoption of BTC and IPC, as shown in 4.4, is able to reduce the loads on the hub (and on the tower), the diameter is increased as long as the maximum combined bending moment on the hub does not exceed the one computed for the RWT.

The increase in blade length is done by stretching all the properties to a major extension, similar to the solution investigated under section 4.3.

The individual pitch controller is based on the architecture proposed in Ref. [69], as also used under section 4.4.

#### 4.5.3 Anticipated PROS and CONS

The main goal of this solution is to increase the AEP increasing the rotor diameter keeping frozen the load on the hub and tower, i.e. keeping frozen the other components of the WT. The constraint used in this integrated solution is not to exceed the maximum combined bending moment on the hub based on the assumption that this is a design load. The fatigue loads are computed but not constrained so that in some case may exceed the reference values. The impact of this loads on the structure (and hence on the final real CoE) should further investigated in the other WPs.

The blade total mass, and its cost, increases, but this seems to have a little impact on the final cost of energy. On the other hand, the longer blade affects heavily the AEP and hence the final cost of energy.

Aerodynamic distribution of twist, chord and thickness remains the same of the RWT, but the longer blade probably changes the local Reynolds number so that this impact on the aerodynamic performance has to further investigated.

Possible drawbacks of active load control are the reduction of AEP and its effect on the actuators and their design: constantly pitching the blade increases the actuator duty cycle, and hence its wear. This, in turn, requires more expensive and larger actuators, inducing a tradeoff with the advantages brought by IPC. The combined adoption of BTC and IPC should mitigate the increment of actuator duty cycle [27].

Nevertheless it is expected a sensible increase of annual energy production and hence a better cost of energy.

#### 4.5.4 Assessment of the structural integrity of the proposed design

##### 4.5.4.1 Design layout and dimensioning

The same concept for the design layout as for the “PoliMI 10MW BTC SC+05”, as described under section 3.1.4.1 was used for the present structural solution.

The following table reports the global data of the optimal blade PoliMI 188m BTC SC+05 IPC compared with the reference one.

Table 65. *PoliMI 188m BTC SC+05 IPC, comparison against RWT*

	RWT	188m BTC SC+05 IPC	Difference
Rotor Diameter	178.3 m	188 m	+ 5.44 %
Blade Total Mass	42422 kg	49281 kg	+ 16.16 %
Blade 1 <sup>st</sup> modal freq (flap)	0.6123 Hz	0.5529 Hz	-

	RWT	188m BTC SC+05 IPC	Difference
Blade 2 <sup>nd</sup> modal freq (edge)	0.9124 Hz	0.6085 Hz	-
AEP	45.760 GWhy	47.70 GWhy	+ 4.24 %
CoE	75.911 \$/kWh	73.791 \$/kWh	- 2.80 %

The following table reports the mass breakdown computed for each structural components including the Non-Structural Masses (NSM). The figures below report the thickness distributions along the blade span of the internal sub-components and the mass, flapwise and edgewise stiffness.

Table 66. *PolIMI 188m BTC SC+05 IPC, bill of material*

Structural Component	Mass [kg]	% of total blade mass
Skin	9554	19.38
Spar Cap	22585	45.83
Web A + B	2349	4.77
Web C	95	0.19
LE & TE Reinforcement	2040	4.14
Root Reinforcement	3320	6.74
<b>Total Structural Mass</b>	<b>39943</b>	<b>81.05</b>
<b>NSM</b>	<b>9338</b>	<b>18.95</b>
<b>Total blade mass</b>	<b>49281</b>	<b>100.00</b>

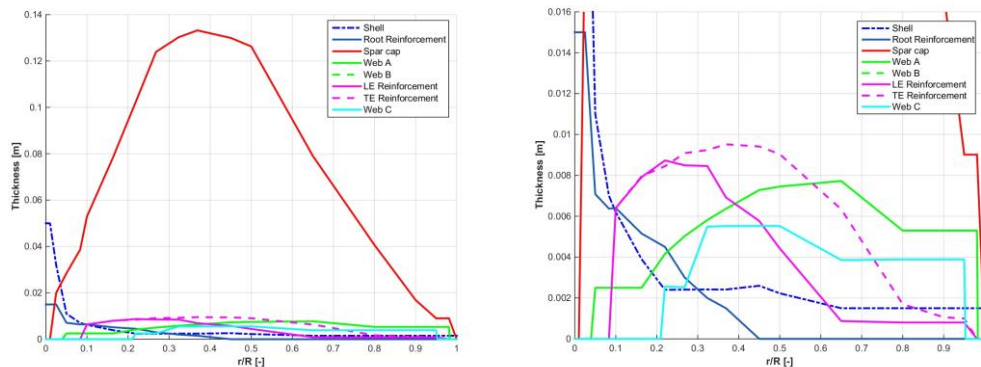


Figure 165. PolIMI 188m BTC SC+05 IPC, structural thickness distributions

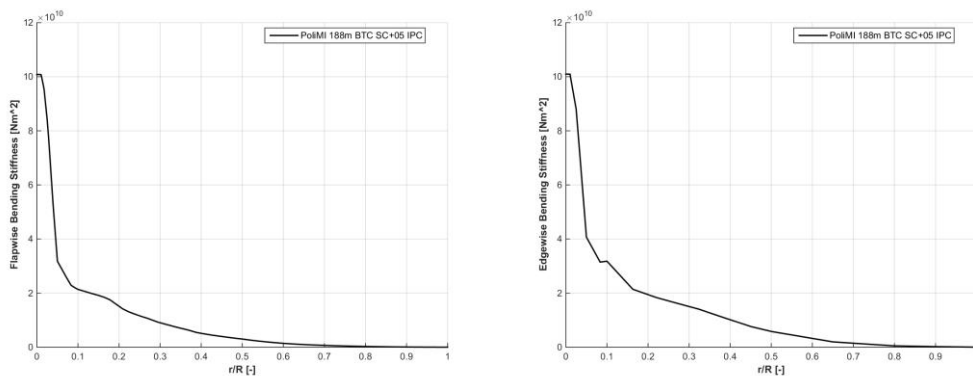


Figure 166. PolIMI 188m BTC SC+05 IPC, flapwise (left) and edgewise (right) stiffness distributions

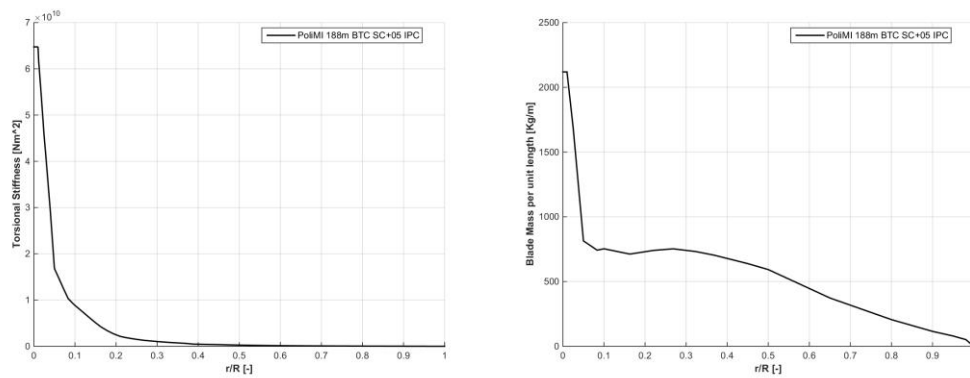


Figure 167. PolMI 188m BTC SC+05 IPC, torsional stiffness (left) and blade mass (right) distributions

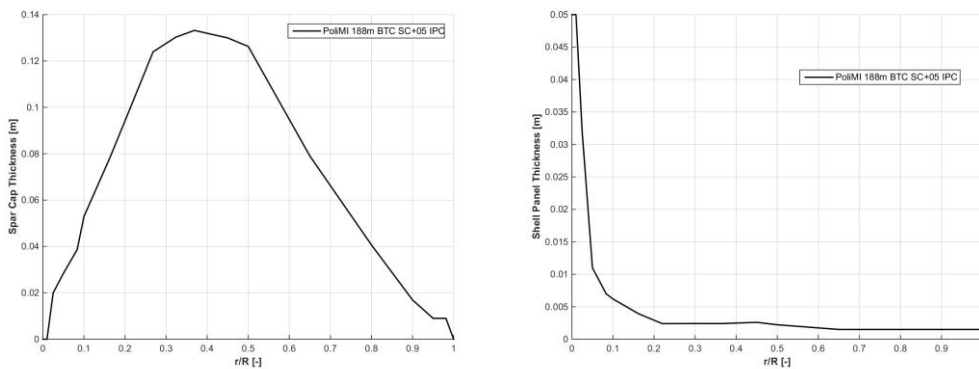


Figure 168. PolMI 188m BTC SC+05 IPC, spar cap (left) and skin (right) distributions

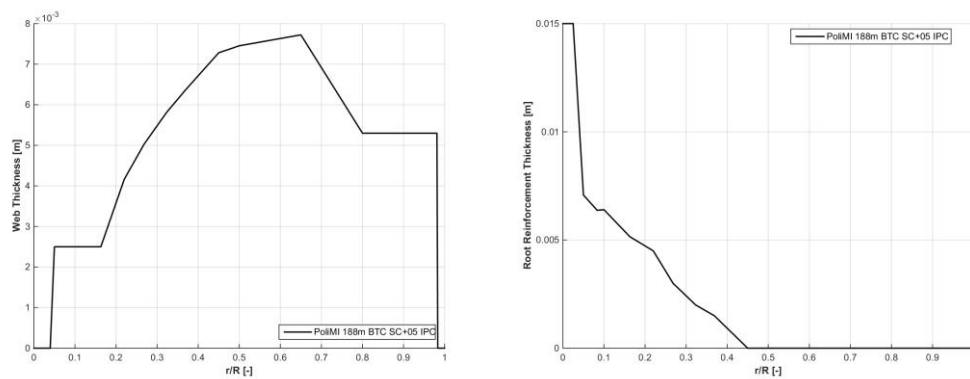
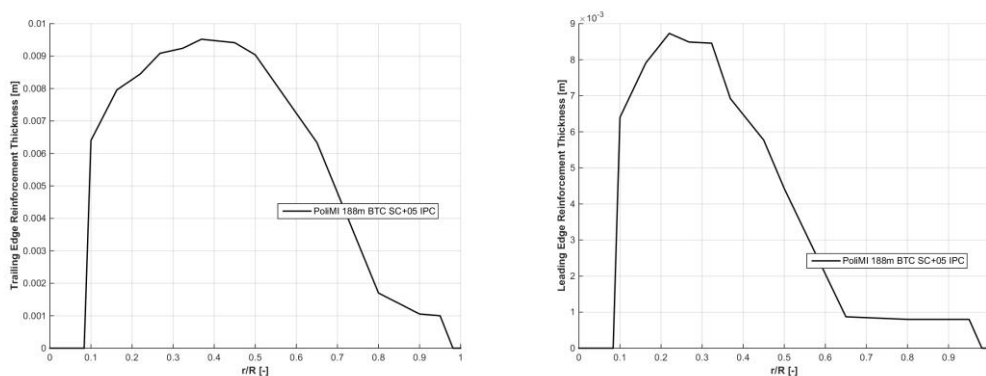
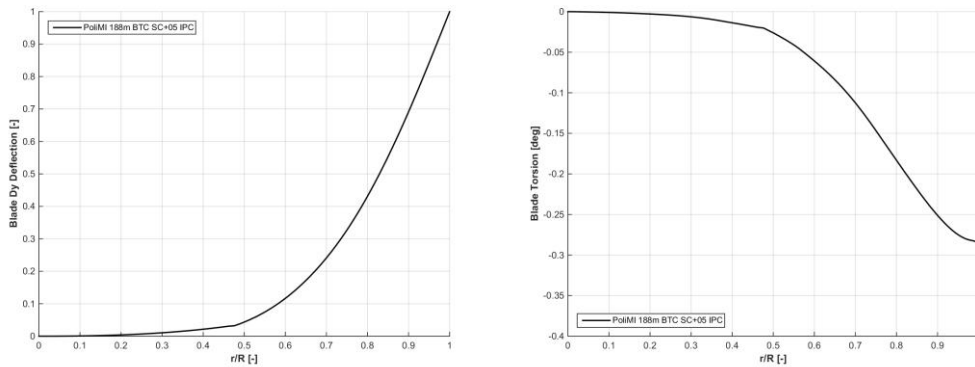


Figure 169. PolMI 188m BTC SC+05 IPC, web (left) and root reinforcement (right) distributions



**Figure 170. PolIMI 188m BTC SC+05 IPC, TE reinforcement (left) and LE reinforcement (right) distributions**

The next figures show the deflection of the blade in the out of plane direction in correspondence of the first mode of vibration (at left) and the corresponding torsion associated to the blade (at right) mainly due to the bend-twist coupling.



**Figure 171. PolIMI 188m BTC SC+05 IPC, first flapwise mode: flapwise (left) and torsion (right) deflections**

#### 4.5.4.2 Load cases considered

The blade is designed according to IEC 61400-1 Ed.3. The load cases selected for the design are the same defined in section 3.1.4.2.

#### 4.5.4.3 Structural integrity verification

The proposed blade satisfies all the design constraints, as can be seen from the following figures, which report the constraint margin for stress, strain and fatigue analysis in all the structural components of the blade as described in sections 3.1.

A constraint value is considered active when its value reaches 0. If  $> 1$  the constraint is violated, if  $< 0$  the constraint is non-active. As one can see, only the fatigue constraint is active in the first 3 figures, which are relatives to skin, spar cap and webs.

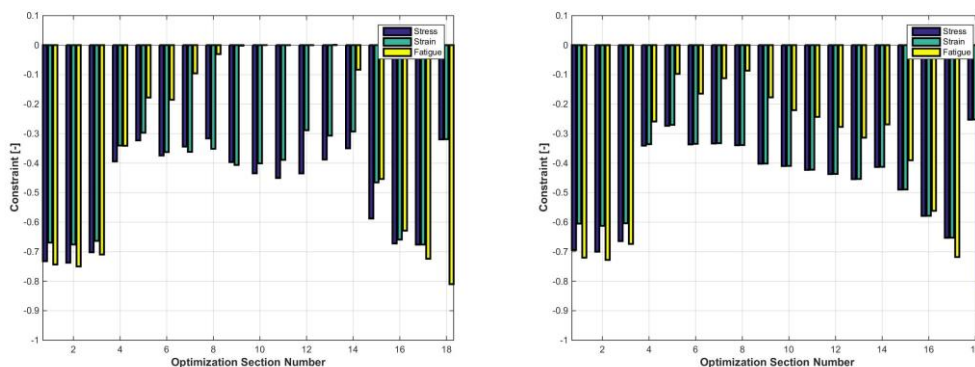


**Figure 172. PolIMI 188m BTC SC+05 IPC, skin (left) and spar cap (right) constraints**

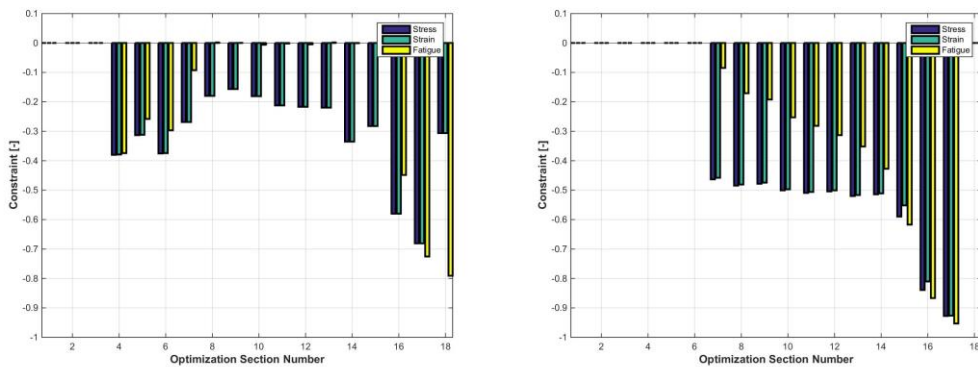


Figure 173. PolIMI 188m BTC SC+05 IPC, web (left) and TE reinforcement (right) constraints

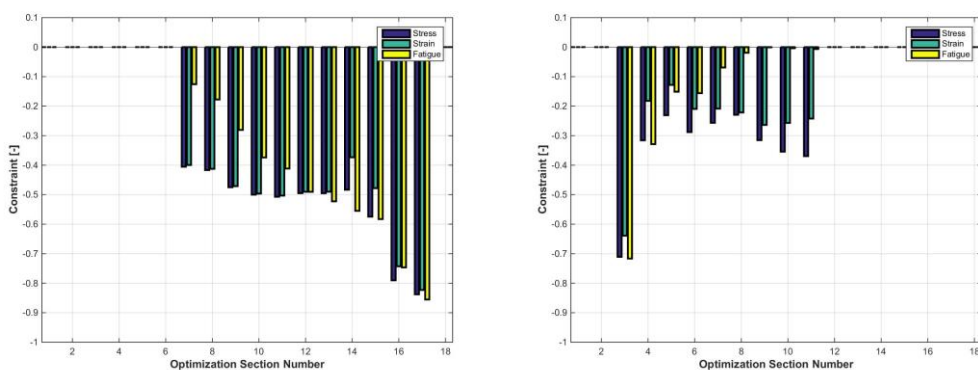


Figure 174. PolIMI 188m BTC SC+05 IPC, LE reinforcement (left) and root reinforcement (right) constraints

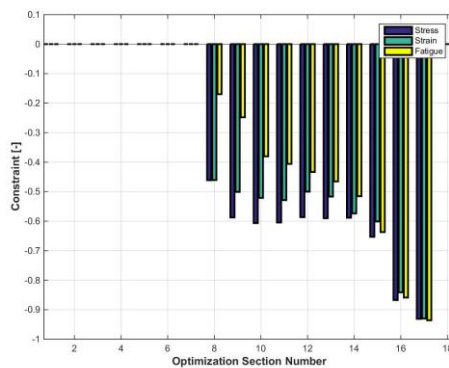


Figure 175. PolIMI 188m BTC SC+05 IPC, third web constraints

The following table shows the ultimate loads on the hub and tower compared with the ones computed (with the same conditions) for the RWT. In this analysis the hub combined bending moment is constrained to be equal to the reference one (- 0.50%), but, as one can see, the loads on the tower are slightly higher (+ 1.73% for the tower bottom combined bending moment) than the reference values.

Table 67. *PolIMI 188m BTC SC+05 IPC, comparison of ultimate loads against RWT*

	RWT	188m BTC SC+05 IPC	Difference
Hub Nodding Moment	57097 kNm	56863 kNm	- 0.41 %
Hub Yaw Moment	53046 kNm	52120 kNm	- 1.74 %
Hub Combined Moment	58271 kNm	57975 kNm	- 0.50 %

	RWT	188m BTC SC+05 IPC	Difference
Hub Axial Force	3560 kN	3322 kN	- 6.68 %
Tower Bottom Fore-Aft Moment	491819 kNm	504378 kNm	+ 2.55 %
Tower Bottom Combined Moment	495794 kNm	504390 kNm	+ 1.73 %
Tower Top Fore-Aft Bending Moment	59244 kNm	53966 kNm	- 8.90 %
Tower Top Torsional Moment	58688 kNm	64144 kNm	- 9.29 %

Relevant to the fatigue loading, the next table shows the cumulative damage equivalent loads computed considering only DLC12 cases (power production in turbulent wind), as in the case presented for the “PoliMI 10MW BTC SC+05” and described in 3.1.4.3.

It can be seen that the optimal blade with combined BTC and IPC with this longer blade increases the fatigue loads of about 15% on the hub. Since tower and hub have not been re-designed in this deliverable, the real effects on the CoE of this optimal blade have to be further investigated.

Table 68. *Polimi BTC SC+05 IPC, comparison of fatigue DEL against RWT*

	RWT	188m BTC SC+05 IPC	Difference
DEL Hub Nodding Moment	27950 kNm	32192 kNm	+ 15 %
DEL Hub Yaw Moment	26192 kNm	29941 kNm	+ 14.3 %
DEL Tower Bottom Side-Side Moment	59828 kNm	57920 kNm	- 3.19 %
DEL Tower Bottom Fore-Aft Moment	136805 kNm	149055 kNm	+ 8.95 %

The following figures show the power curve computed in turbulent condition for both the PoliMI 188m BTC SC+05 IPC and the RWT. In region II the power of the new re-designed blade is, as expected, significantly higher. The final AEP is in fact + 4.24 % higher. The figure on the right reports the standard deviation (STD) of the power curve compared against the STD of the RWT. This curve shows that, mainly in region III, the STD of the PoliMI blade is much lower.

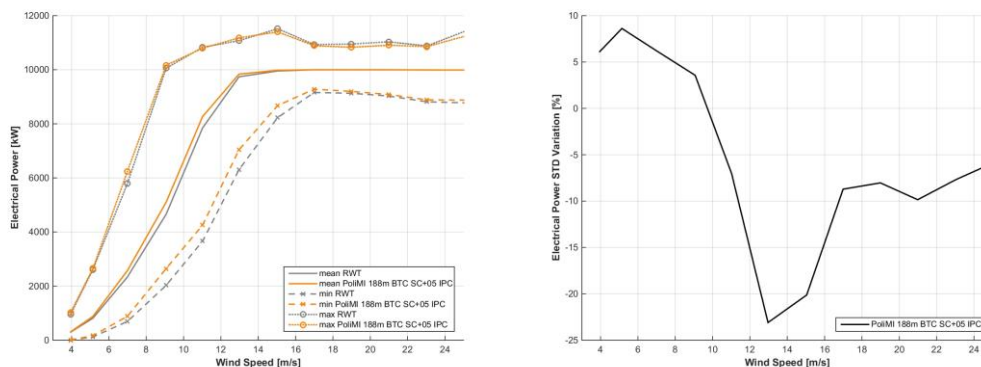


Figure 176. *Polimi 188m BTC SC+05 IPC, turbulent power curve (left) and power STD variation (right), comparison against RWT*

#### 4.5.5 Conclusions and recommendations

In this section PoliMI has presented an integrated structural solution based on the so called Bend-Twist Coupling (BTC), Individual Pitch Controller (IPC) plus a blade stretch. The BTC is a passive load mitigation solution obtained by exploiting the anisotropic mechanical properties of composite materials. BTC implies that, when the blade bends because of increased loads, the ensuing change of twist will affect the aerodynamic loading through a change in angle of attack. IPC is an active load mitigation solution which exploits a power source to move the whole blade, or a part of it, so as to reduce loads due to turbulence, gusts and asymmetry in the inflow. It is here explored the

possibility offered by the combination of these two technologies. The load reduction obtained by this solution has been used here to increase the rotor diameter without exceeding the hub loads with respect to the reference ones.

The structural solution is computed throughout a blade design procedure based on a novel comprehensive multi-level constrained optimization approach. The design process alternates between a multibody beam model augmented with a 2D FEM cross sectional sub-models and a fine scale 3D FEM detailed model of the blade. The former enables the numerous transient aero-servo-elastic analyses required to compute loads and deflections throughout the lifetime of the machine, while the latter makes it possible to conduct detailed local verifications of the design.

The use of a constrained optimization-based approach to design is crucial and allows comparing different solutions that satisfy the same design requirements, and hence permitting to choose the optimal solution. The control set-points have been changed in order to improve the annual energy production.

The possibility offered by the synergetic adoption of BTC and IPC of lowering the loads allowed to increase as much as possible the rotor diameter, operation that concerns a worsening of loads, but that has the main goal of increase the energy production.

The optimal blade presented here is significantly longer, +5.44%, and heavier, +16.16%, with respect to the RWT, but produces more energy, +4.24%, and, at the end, has a lower cost of energy, -2.80%. The larger rotor diameter permits also to reduce the oscillations in power production, permitting to improve the quality of power production.

Ultimate loads on hub are quite close to that of the RWT, tower top moment is 8.90% lower, and also the torsional moment is significantly lower, -9%. For tower bottom loads the situation is opposite, the RWT is subjected to lower loads, even if the difference is small, at about 2%.

On the other side, fatigue loads increase, both on the hub and on the tower. The solution proposed here is constrained to keep the maximum loads on the hub constant, not the fatigue loads, based on the assumption that these ultimate loads are design-driven. Since these components have not been re-designed within this task, the actual final effect on the CoE of this optimal blade has to be further investigated. In order to try to mitigate also these fatigue loads one could use a different IPC setting (changing the IPC-PID gains).

Alternatively a lower rotor diameter can be selected. These parametric analysis (changing the rotor diameter with BTC+IPC) has been investigated and summarize in the following table and figures.

**Table 69. Comparison of increasing rotor diameter solution against RWT**

	RWT	PoliMI BTC SC+05 + IPC	PoliMI 182m BTC SC+05 + IPC	PoliMI 185m BTC SC+05 + IPC	PoliMI 188m BTC SC+05 + IPC
Rotor Diameter	178.3 m	178.3 m	182 m	185 m	188 m
Blade Total Mass	42422 kg	- 4.80 %	+ 2.80 %	+ 9.40 %	+ 16.16 %
AEP	45.760 GWhy	+ 0.69 %	+ 2.12 %	+ 3.01 %	+ 4.24 %
CoE	75.911 \$/kWh	- 0.92 %	- 1.71 %	- 2.11 %	- 2.80 %
Hub Combined Moment	58271 kNm	- 12.53 %	- 9.80 %	- 4.74 %	- 0.50 %
Tower Bottom Combined Moment	495794 kNm	- 6.35 %	- 3.21 %	- 0.03 %	+ 1.73 %
DEL Hub Nodding Moment	27950 kNm	- 5.55 %	+ 2.05 %	+ 8.34 %	+ 15 %
DEL Hub Yaw Moment	26192 kNm	- 4.93 %	+ 2.33 %	+ 7.35 %	+ 14.3 %

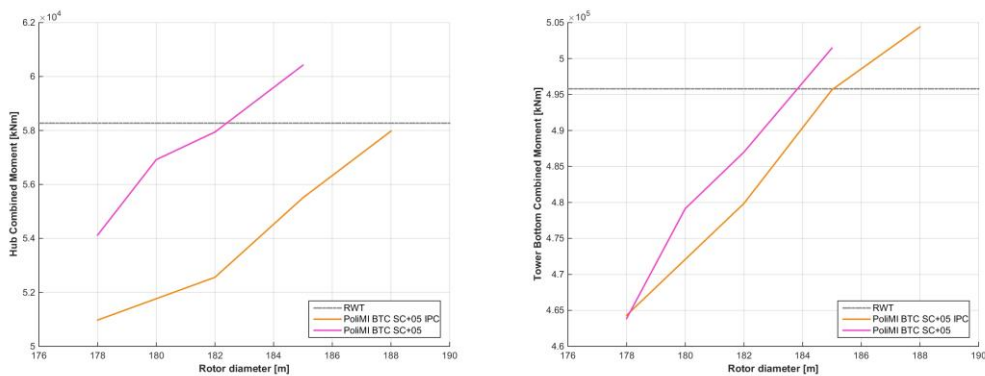


Figure 177. Comparison of hub (left) and tower bottom (right) combined moments wrt rotor diameter

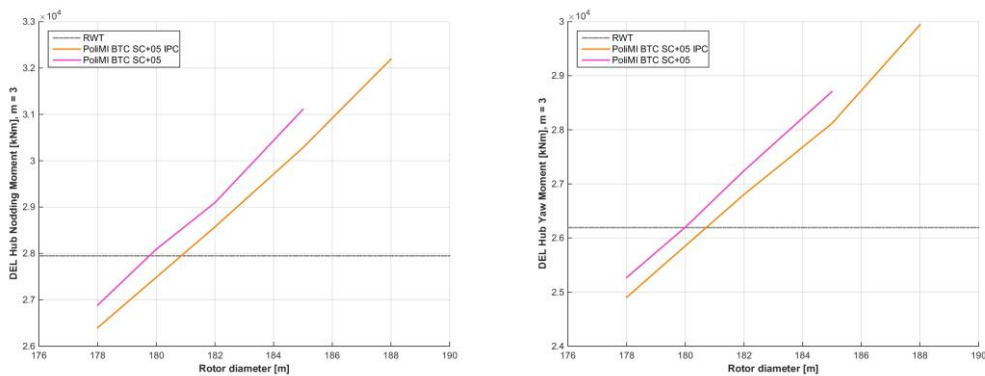


Figure 178. Comparison of hub nodding (left) and yawing (right) DEL moments wrt rotor diameter

Finally, the next table summarize PoliMI's (integrated) solutions compared with the RWT.

Table 70. Comparison of different solutions against RWT

	RWT	PoliMI BTC SC+05	PoliMI 182m BTC SC+05	PoliMI BTC SC+05 + IPC	PoliMI 188m BTC SC+05 + IPC
Rotor Diameter	178.3 m	178.3 m	182 m	178.3 m	188 m
Blade Total Mass	42422 kg	- 3.65 %	+ 5.02 %	- 4.80 %	+ 16.16 %
AEP	45.760 GWh	+ 0.87 %	+ 2.19 %	+ 0.69 %	+ 4.24 %
CoE	75.911 \$/kWh	- 0.99 %	- 1.68 %	- 0.92 %	- 2.80 %
Hub Combined Moment	58271 kNm	- 7.13 %	- 0.49 %	- 12.53 %	- 0.50 %
Tower Bottom Combined Moment	495794 kNm	- 6.44 %	- 1.77 %	- 6.35 %	+ 1.73 %
DEL Hub Nodding Moment	27950 kNm	- 3.82 %	+ 4.10 %	- 5.55 %	+ 15 %
DEL Hub Yaw Moment	26192 kNm	- 3.52 %	+ 4.01 %	- 4.93 %	+ 14.3 %

## 5 CONCLUSIONS

More than 15 solutions were presented for the blade structural configuration in this report. These are the result of individual work of the partners contributing, having nevertheless a common reference point: the 10MW DTU wind turbine blade along with the reference load case used during the benchmark at the first stage of the INN WIND.EU project. Carefully chosen solutions will be communicated to work package WP1 in order to evaluate the effect of the solution on the cost of wind energy. Yet, for some of the solutions cost analysis has been performed and was presented in this report, revealing a large potential for improvements on the blade structure.

The technological readiness level of the investigated solutions ranges from 4 to 7, providing a broad range of concept maturity.

Beginning with the concepts of the lowest technology readiness level (TRL 4-5) chapter 2 discussed the pure structural solutions to improve the internal configuration of the blade in terms of manufacturing procedure and quality consistency. Specifically for the truss structure concept, this was pursued also to allow for new smart blade concepts developed within Task 2.3 of the InnWind.EU project. Aim of the studies was to investigate the feasibility of the alternative manufacturing methods in paper, by reaching on blade designs that comply with the set specifications. Use of truss structures, use of grid reinforced panels as well as a structural modification by offsetting the shear webs were investigated. In total 5 complete solutions were presented. These were the output of several design iteration to a) validate the numerical analysis tools for use with the new concepts and b) to optimize the structure complying with set constraints. Among the solutions presented, the solution investigated by UPAT, employing a truss structure to replace the traditional shear web configuration showed the highest potential and maturity in design complying to set requirements. An almost 30% mass reduction was achieved for this, despite the frozen load cases investigated, whereby the mass reduction was neglected. Thus, despite the potential cost increase due to joining of the truss members and the use of a more expensive material (Carbon/Epoxy), the significant mass saving is expected to lead also to reduction of cost of energy. A similar trend was observed also by the work performed on the rib reinforced blade, i.e. replacing the traditional shell of the blade with truss members, although the procedure followed needs further analysis to reach the final result. Similar mass savings in the order of 20% were also obtained by replacing the sandwich panel of the trailing edge with grid reinforced panels; a solution that was investigated by TUD. It is obvious that as the large of the wind turbine blade is not comparable with that of the blades ten years ago, new manufacturing concepts for the internal blade structure are becoming more relevant.

In chapter 3 the solutions to achieve passive load alleviation were discussed. These are technologically more mature than those presented in chapter 2. The technology readiness level for this solutions is 5 to 6. For the passive control of the wind turbine 10 solutions have been presented. PoliMi optimized the structure of the blade, running the complete design circle to achieve a structure complying with all design requirements including fatigue, while introducing passive load reduction through the incorporation of bend-twisting coupling. A 3% mass reduction was achieved with an about 1% increase in Annual energy production, leading to a minimal reduction of the levelized cost of energy. Nevertheless, the effect of the load reduction achieved on other than the blade wind turbine components was not taken into account. DTU investigated 7 different solutions, combining the concept of bend-twist coupling, swept blade, and single shear web (reduced torsional stiffness). Pros and cons were discussed for each of those solutions. UBRISTOL and CENER each investigated the concept of bend-twist coupled blade from different perspectives.

Additional 5 solutions were presented under chapter 4 discussing integrated aerodynamic-structural solutions. One structural solution regarded the low induction rotor blade, performed by CRES. This was done in support of the aerodynamic solution reported under Task 2.1. Three solutions were investigated by PoliMi combining the bend-twist coupled blade with and without an individual pitch controller and taking into consideration longer rotor blades. Additional optimization of the blade structure was performed by WMC.

From the complete set of solutions described, at least 7 solutions were compliant with all constraints set for the blade design by work package 1. Of these solutions **three were selected**,

basically one of each group of solutions presented in chapters 2 to 4, to be further processed under INN WIND.EU work package WP1 (Deliverable 1.24). These are:

- The blade having an internal truss structure replacing the shear webs (UPAT)
- The bend-twist coupled blade (PoliMi)
- The structural solution for the low induction rotor (CRES)

Overall, new structural concepts were identified as feasible for implementation in the wind turbine blade. These have been also combined with load alleviation solutions, which in turn affect the design of more components on the wind turbine. The effect of the latter falls beyond the objectives of work package 2 and has to be investigated by other research groups and/or work packages. Especially for the innovative structural solutions presented, to assess the cost of the final product additional design efforts are needed for the details of the structure, such as the joints. At this stage of investigations this was neglected. Further to that, some of the proposed configurations will be also investigated within the INN WIND.EU project on a 20MW rotor.

## 6 REFERENCES

- [1] C. Bak, F. Zahle, R. Bitsche, T. Kim, A. Yde, L. C. Henriksen, A. Natarajan and M. H. Hansen, "Description of the DTU 10MW Reference Wind Turbine," DTU Wind Energy Report, I-0092, Roskilde, Denmark, 2013.
- [2] D. J. Lekou, K. C. Bacharoudis, D. Chortis, A. B. Farinas, C. Amezueta, I. Nuin, C. Pavese, P. Berring, K. Branner, C. L. Bottasso, A. Croce, F. Gualdoni, T. P. Philippidis, I. T. Masmanidis, G. A. Roukis, G. D. de Winkel and H. Dekker, "Benchmark on structural design methods for composite wind turbine rotor blades," in *Deliverable D2.21 Benchmarked aerodynamic-structural design methods*, INNWIND.EU project, Grant Agreement No. 308974, 2015.
- [3] D. J. Lekou, "Information on the benchmark of blade structural fatigue models," INNWIND.EU project report, July 2014.
- [4] P. W. Christensen and A. Klarbring, *An introduction to Structural Optimization*, Netherlands: Springer, 2008.
- [5] "Lightweight composite truss wind turbine blade". Patent US 20070217918 A1.
- [6] "Efficient wind turbine blades, wind turbine structures and associated systems and methods of manufacture, assembly and use". Patent US 8500408 B2.
- [7] H. A. Eschenauer and N. Olhoff, "Topology optimization of continuum structures: A review," *Appl. Mech. Rev.*, vol. 54, no. 4, pp. 331-390.
- [8] "Matlab theory manual".
- [9] Germanischer Lloyd, *Guideline for the certification of wind turbines*, Germanischer Lloyd, 2010.
- [10] T. Ashwill, "Materials and innovation for large blade structures: Research opportunities in wind energy technology," in *50th AIAA Structures, Structural Dynamics & Materials Conference*, Palm Springs, 2009.
- [11] T. Ashwill, "Innovative design approaches for large wind turbine blades: Final Report," Sandia National Laboratories, 2004.
- [12] S. Joncas, "Thermoplastic composite wind turbine blades: An integrated design approach," TU Delft, 2010.
- [13] F. Jensen, "Ultimate strength of a large wind turbine," Technical University of Denmark, 2008.
- [14] N. Buckney, A. Pirrera, S. D. Green and P. M. Weaver, "On the structural topology of wind turbine blades," *Wind Energy*, pp. 545-560, 2013.
- [15] Altair Engineering, *HyperWorks 10.0 Release Notes*, 2009.
- [16] M. Ashby, *Materials Selection in Mechanical Design*, 3rd ed., Elsevier, 2008.
- [17] R. Birmingham and J. A. Wilcox, "Charting the links between material selection and elemental form in structural design," *Journal of Engineering Design*, pp. 127-140, 1993.
- [18] M. Ashby, "Overview no 92: Materials and shape," *Acta Metallurgica et Materialia*, pp. 1025-1039, 1991.
- [19] D. Griffith and T. D. Ashwill, "The Sandia 100-meter all-glass baseline wind turbine blade:SNL100-00," Sandia National Laboratories, Albuquerque, NM, 2011.
- [20] D. T. Griffith, T. D. Ashwill and B. R. Resor, "Large offshore rotor development; Design and analysis of the Sandia 100-meter wind turbine blade," in *53rd AIAA Structures, Structural Dynamics and Materials Conference*, Honolulu, HI, 2012.
- [21] D. T. Griffith, B. R. Resor and T. D. Ashwill, "Challenges and opportunities in large offshore rotor development: Sandia 100-meter blade research," in *AWEA WINDPOWER 2012 Conference and Exhibition*, Atlanta, GA, 2012.
- [22] D. J. Lekou, "Information on the Benchmark of blade structural models," INNWIND.EU project report, July 2013.
- [23] P. S. Veers, G. Bir and D. W. Lobitz, "Aeroelastic tailoring in wind-turbine blade application," in *Windpower '98, AWEA Annual Conference and Exhibition*, Bakersfield, CA, April 27- May 1, 1998.

- [24] D. W. Lobitz, P. S. Veers, G. R. Eisler, D. J. Laino, P. G. Migliore and G. Bir, "The use of twist-coupled blades to enhance the performance of horizontal axis wind turbines," Sandia Report, SAND 2001-1301, Albuquerque, NM, May 2001.
- [25] D. W. Lobitz and D. J. Laino, "Load mitigation with twist-coupled HAWT blades," in '99 ASME Wind Energy Symposium, Reno, January 11-14, 1999.
- [26] D. W. Lobitz, P. S. Veers and D. J. Laino, "Performance of twist-coupled blades on variable speed rotors," in AIAA 2000-0062, 2000 ASME Wind Energy Symposium, Reno, NE, January 10-13, 2000`.
- [27] C. L. Bottasso, F. Campagnolo, A. Croce and C. Tibaldi, "Optimization-based study of bend-twist coupled rotor blades for passive and integrated passive/active load alleviation," *Wind Energy*, vol. 16, no. 8, pp. 1149-1166, 2013.
- [28] C. L. Bottasso, F. Campagnolo and A. Croce, "Multi-Disciplinary Constraint Optimization of wind turbines," *Multibody System Dynamics*, vol. 27, no. 1, pp. 21-53, 2012.
- [29] C. L. Bottasso, F. Campagnolo, A. Croce, S. Dilli, F. Gualdoni and M. B. Nielsen, "Structural optimization of wind turbine rotor blades by multi-level sectional/multibody/3DFEM analysis," *Multibody System Dynamics*, vol. 32, no. 1, pp. 87-116, 2014.
- [30] V. Giavotto, M. Borri, P. Mantegazza and G. L. Ghiringhelli, "Anisotropic beam theory and applications," *Computers & Structures*, vol. 16, pp. 403-413, 1983.
- [31] O. A. Bauchau, "Flexible multibody dynamics," *Solid Mechanics and its Applications*, vol. 176, 2011.
- [32] O. A. Bauchau, C. L. Bottasso and L. Trainelli, "Robust integration schemes for flexible multibody systems," *Computer methods in applied mechanics and engineering*, vol. 192, pp. 395-420, 2003.
- [33] C. L. Bottasso and A. Croce, "CP-Lambda: User's Manual," Dipartimento di Ingegneria Aerospaziale, Politecnico di Milano, 2006-20011.
- [34] N. W. M. Bishop and F. Sherratt, "Finite element based fatigue calculations," NAFEMS, 2000.
- [35] T. P. Philippidis and A. P. Vassilopoulos, "Complex stress state effect on fatigue life of GRP laminates. Part I, experimental," *International Journal of Fatigue*, vol. 24, pp. 813-823, 2002.
- [36] T. P. Philippidis and A. P. Vassilopoulos, "Complex stress state effect on fatigue life of GRP laminates. Part II, theoretical formulation," *International Journal of Fatigue*, vol. 24, pp. 825-830, 2002.
- [37] T. D. Ashwill, "Blade technology innovations for utility-scale turbines," Sandia National Laboratories , Albuquerque, NM, 2006.
- [38] M. Capuzzi, A. Pirrera and P. M. Weaver, "A novel adaptive blade concept for large-scale wind turbines. Part I: Aeroelastic behavior," *Energy*, vol. 73, pp. 15-24, 2014.
- [39] M. Capuzzi, A. Pirrera and P. M. Weaver, "A novel adaptive blade concept for large-scale wind turbines. Part II: Structural design and power performance," *Energy*, vol. 73, pp. 25-32, 2014.
- [40] G. Ingram, "Wind turbine blade analysis using the blade element momentum method v.1.1," Durham University, 2011.
- [41] M. Buhl, "NWTC Design Codes (WT\_Perf by Marshall Bull)," 2011. [Online]. Available: <http://wind.nrel.gov/designcodes/simulators/wtperf/>.
- [42] D. A. Peters, D. D. Boyd and C. J. He, "Finite-state induced-flow model for rotors in hover and forward flight," *Journal of the American Helicopter Society*, vol. 34, no. 4, pp. 5-17, 1989.
- [43] D. M. Pitt and D. A. Peters, "Theoretical prediction of dynamic inflow derivatives," *Vertica*, vol. 5, pp. 21-34, 181.
- [44] E. Madenci and A. Barut, "Dynamic response of thin composite shells experiencing nonlinear elastic deformations coupled with large rapid overall motions," *International Journal for Numerical Methods in Engineering*, vol. 39, no. 16, pp. 2695-2723, 1996.

- [45] F. J. Tarzanin, "Prediction of control loads," *Journal of the American Helicopter Society*, vol. 17, pp. 33-46, 1972.
- [46] M. Capuzzi, A. Pirrera and P. M. Weaver, "Structural design of a novel aeroelastically tailored wind turbine blade," *Thin-Walled Structures*, vol. 95, pp. 7-15, 2015.
- [47] T. Ashwill, P. S. Veers, J. Locke, I. Contreras, D. Griffin and M. D. Zuteck, "Concepts for adaptive wind turbine blades," in *ASME 2002 Wind Energy Symposium*, Reno, NE, 2002.
- [48] T. D. Ashwill, G. Kanaby, K. Jackson and M. Zuteck, "Development of the swept twist adaptive rotor (STAR) blade," in *Proceedings of the 48th AIAA Aerospace Sciences Meeting*, Orlando, Florida, 2010.
- [49] M. H. Hansen, "Aeroelastic properties of backward swept blades," in *Proceeding of the 49th AIAA Aerospace Sciences Meeting*, Orlando, FL, 2011.
- [50] D. R. S. Verelst and T. J. Larsen, "Load consequences when sweeping blades - A case study of a 5MW pitch controlled wind turbine," Risø-DTU technical report Risø-R-1724, Roskilde, Denmark, 2010.
- [51] M. Zuteck, "Adaptive blade concept assessment: Curved planform induced twist investigations," Sandia National Laboratories Report SAND2002-2996, Albuquerque, NM, 2002.
- [52] Knight & Carver Wind Group, "Sweep-twist adaptive rotor blade: Final project report," Sandia National Laboratories report SAND2009-8037, Albuquerque, NM, 2009.
- [53] I. Sønderby and M. H. Hansen, "Open-loop frequency response analysis of a wind turbine using high-order linear aeroelastic model," *Wind Energy*, 2013.
- [54] C. Tibaldi, L. C. Henriksen, M. H. Hansen and C. Bak, "Effects of gain-scheduling methods in classical wind turbine controller on wind turbine aeroservoelastic models and loads," in *Proceedings of the 52th AIAA Aerospace Science Meeting*, National Harbor, Maryland, USA, 2014.
- [55] T. Kim, A. M. Hansen and K. Branner, "Development of an anisotropic beam finite element for composite wind turbine blades in multibody system," *Journal of Renewable Energy*, vol. 59, pp. 172-183, 2013.
- [56] F. Vorpahl, M. Strobels, J. M. Jonkman, T. J. Larsen and P. Passon, "Verification of aeroelastic offshore wind turbine design codes under IEA wind task XXIII," *Wind Energy*, 2013.
- [57] W. Popko, F. Vorpahl, A. Zuga, M. Kohlmeier, J. Jonkman, A. Robertson, T. J. Larsen, A. Yde, K. Stertr and K. M. Okstad, "Offshore code comparison collaboration continuation (OC4), PHASE I - Results of coupled simulations of an offshore wind turbine with jacket support structure," in *Proceedings of the International Offshore and Polar Engineering Conference 2012*, 2012.
- [58] T. J. Larsen, A. H. Madsen, G. C. Larsen and K. S. Hansen, "Validation of the dynamic wake meander model for loads and power production in the Egmond Aan Zee wind farm," *Wind Energy*, vol. 16, no. 4, pp. 605-624, 2013.
- [59] J. P. Blasques and R. Bitsche, "User's Manual for BECAS," DTU Wind Energy Report, Roskilde, Denmark, 2014.
- [60] R. D. Bitsche, "Airfoil2BECAS: A preprocessor for the cross-section analysis software BECAS," DTU Wind Energy Report, Roskilde, Denmark, 2014.
- [61] R. Bitsche, "Shellexpander: A preprocessor for the cross-section analysis software BECAS," DTU Wind Energy Report, Roskilde, Denmark, 2013.
- [62] M. H. Hansen and L. C. Henriksen, "Basic DTU Wind Energy Controller," DTU Wind Energy Technical Report E-0018, Roskilde, Denmark, 2013.
- [63] M. H. Hansen, K. Thomsen, A. Natarajan and A. Barlas, "Design load basis for onshore turbines - rev.0," DTU Wind Energy report E-0074(EN), Roskilde, Denmark, 2015.
- [64] IEC, IEC 61400-1: Wind Turbines - Part 1: Design Requirements, 2005.
- [65] V. Fedorov and C. Berggreen, "Bend-twist coupling potential of wind turbine blades," *Journal of Physics; Conference Series*, vol. 524, p. 012035, 2014.
- [66] Gurit, WE91-2 PrePreg, PDSWE-WE91-2-2-0907.

- [67] R. Nijssen, R. Rodriguez and C. Amezcua, "Tests on pre-preg glass and carbon fibre," in *EERA/IRPWIND conference 2014*, Amsterdam, The Netherlands, 2014.
- [68] J. Dekker, J. Kuiken, C. Lindeburg and G. de Winkel, "Optimization of internal layout structure of the blade of the DTU-10 WM RWT using FOCUS6," INN WIND.EU project report, 2015.
- [69] O. Duran Lucas, Influence of cost of energy models on wind turbine rotor design, Master Thesis, 2015.
- [70] P. Chaviaropoulos, *Cost Models V1.01 Oct 2014.xls*, INN WIND.EU project report, 2014.
- [71] E. Bossanyi, "Individual blade pitch control for load reduction," *Wind Energy*, vol. 6, pp. 119-128, 2003.
- [72] E. Bossanyi, "Developments in individual blade pitch control," in *The Science of Making Torque from Wind*, Delft, The Netherlands, April 19-21, 2004.
- [73] M. Geyler and P. Caselitz, "Individual blade pitch control design for load reduction on large wind turbines," in *European Wind Energy Conference (EWEC 2007)*, Milano, Italy, May 7-10, 2007.
- [74] E. Bossanyi, "Wind turbine control for load reduction," *Wind Energy*, vol. 6, pp. 229-244, 2003.
- [75] E. Bossanyi, "Further load reductions with individual pitch control," *Wind Energy*, vol. 8, pp. 481-485, 2005.
- [76] T. van Engelen, "Design model and load reduction assessment for multi-rotational model individual pitch control," in *European Wind Energy Conference (EWEA 2006)*, Athens, Greece, February 27-March 1, 2006.
- [77] S. Kanev and T. van Engelen, "Exploring the limits in individual pitch control," in *European Wind Energy Conference (EWEA 2009)*, Marseille, France, March 16-19, 2009.
- [78] W. Leithead, V. Neilson and S. Dominguez, "Alleviation of unbalanced rotor loads by single blade controllers," in *European Wind Energy Conference (EWEC 2009)*, Marseille, France, March 16-19, 2009.
- [79] Gurit, "Balsa wood core material," PDSWE-Balsaflex-3-0412, [www.gurit.com](http://www.gurit.com).
- [80] S. Larwood and M. Zuteck, "Swept wind turbine blade aeroelastic modelling for loads and dynamic behavior," *Windpower*, 2006.
- [81] C. Tibaldi, L. C. Henriksen, M. H. Hansen and C. Bak, "Wind turbine fatigue damage evaluation based on a linear model and a spectral method," *Wind Energy*, 2015.
- [82] European Wind Energy Association, *Wind Energy Factsheets*, 2010.

## APPENDIX A; STRENGTH PLOTS FOR CONFIGURATIONS OF SECTION 3.3

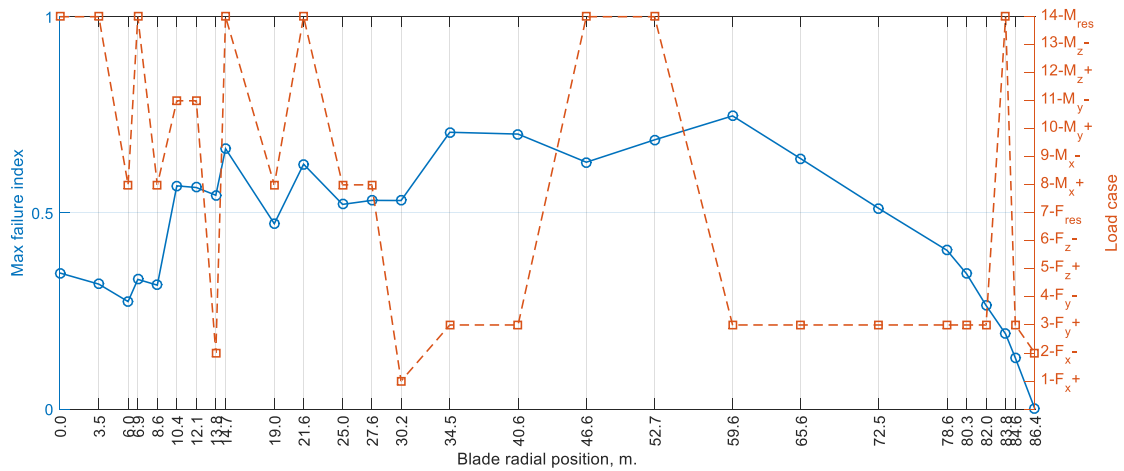


Figure 179 - Strength characteristics of the baseline blade design (Baseline).

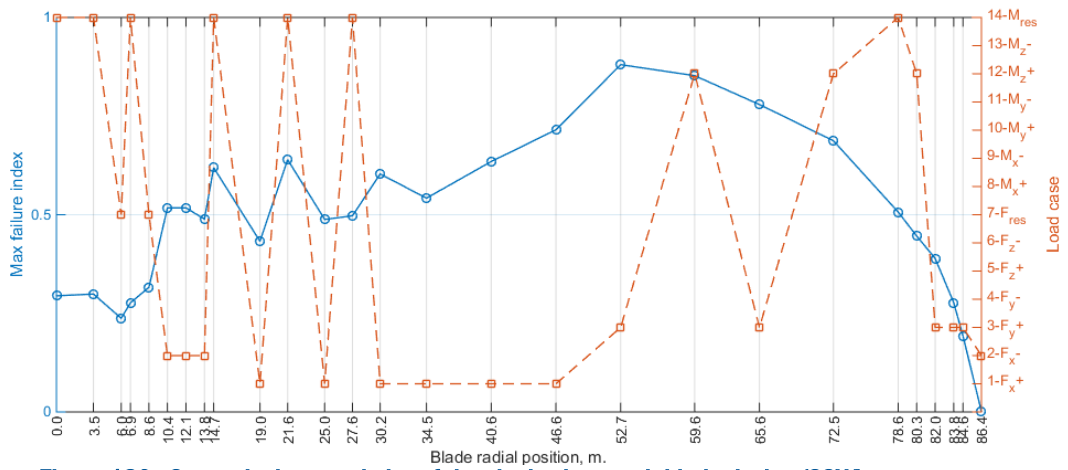


Figure 180 - Strength characteristics of the single shear web blade design (SSW).

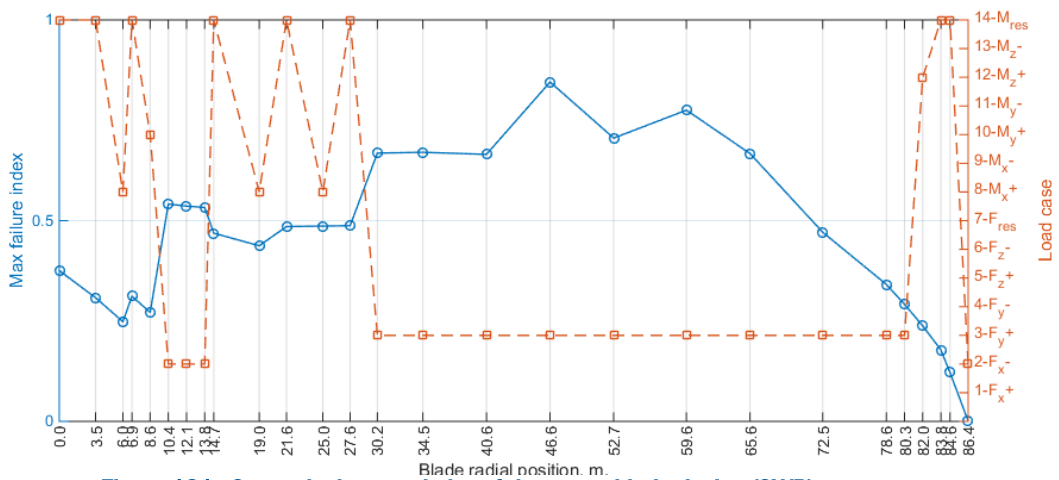
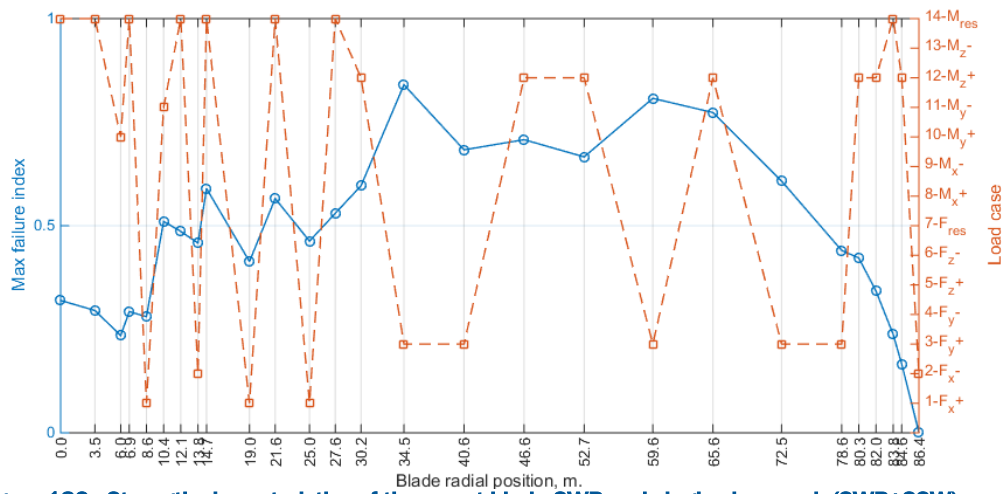
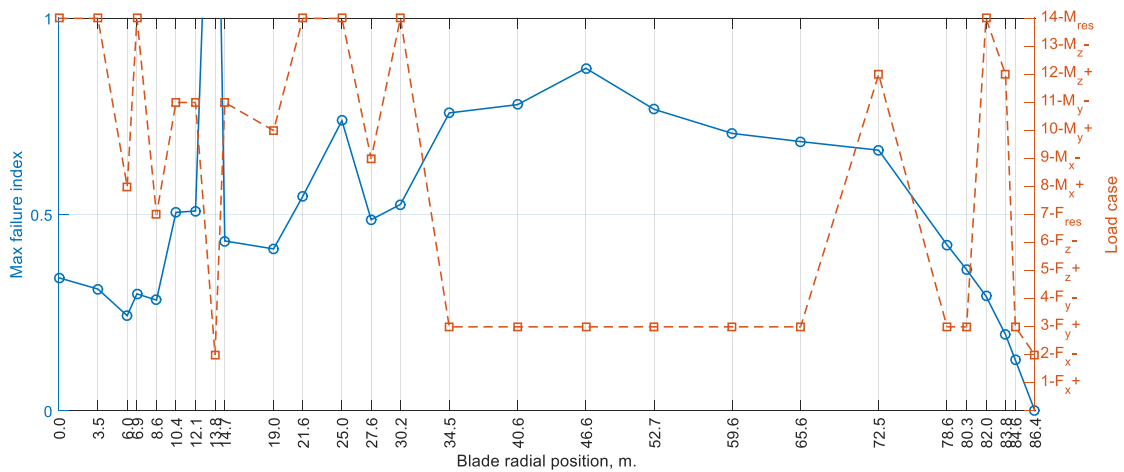


Figure 181 - Strength characteristics of the swept blade design (SWP).



**Figure 182 - Strength characteristics of the swept blade SWP and single shear web (SWP+SSW).**



**Figure 183 - Strength characteristics of the blade with BTC (BTC).**

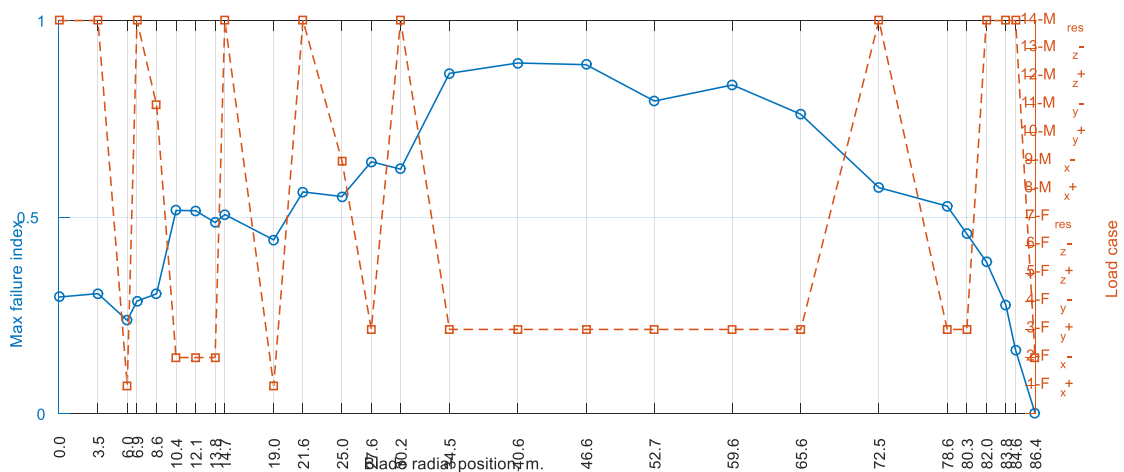


**Figure 184 - Strength characteristics of the blade BTC and single shear web (BTC+SSW).**

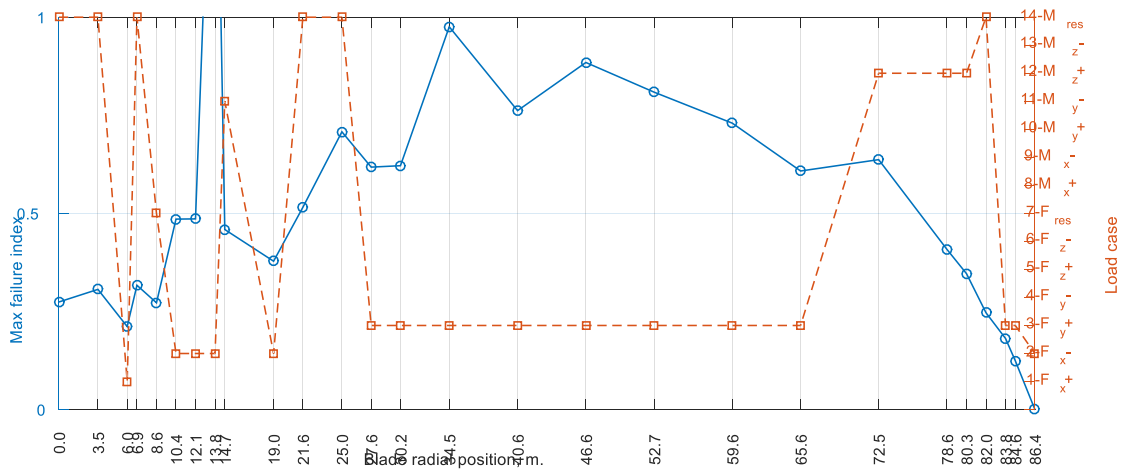


**Figure 185 - Strength characteristics of the swept blade with BTC (SWP+BTC).**

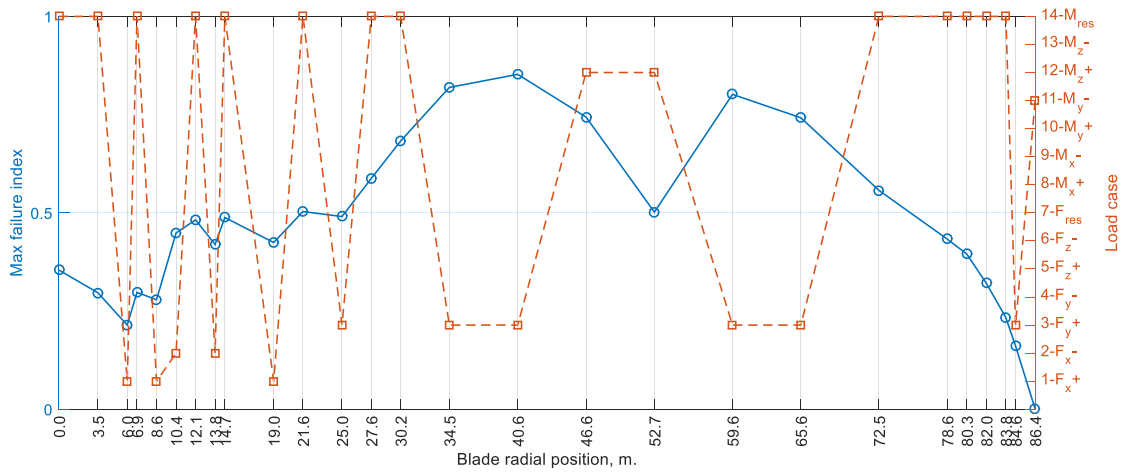


**Figure 186 - Strength characteristics of the swept blade with BTC and single shear web (SWP+BTC+SSW).**

## APPENDIX B; ESTIMATED PROPERTIES FOR DTU REFERENCE BLADE (CENER)

Following tables collect the mechanical properties of the DTU reference (baseline) blade as calculated by CENER. Also included is the reference load case used and the relevant strength ratio results obtained.

Table 71. *DTU baseline global mass properties*

Blade definition by 41 sections	
Overall mass of the blade (Kg)	41643Kg
Location of centre of gravity from hub centre (z axis)	z: 28.638

Table 72. *DTU baseline mechanical properties distribution*

Section ID	Distance from Root [m]	Mass/unit length [Kg/m]	Flapwise Stiffness [Nm <sup>2</sup> ]	Edgewise Stiffness [Nm <sup>2</sup> ]	Torsional Rigidity [Nm <sup>2</sup> ]	Centre of mass [%]	Elastic axis [-]
1	0.000	1203.33	6.276E+10	6.163E+10	2.731E+10	50.06	50.07
2	1.502	1203.53	6.277E+10	6.169E+10	2.731E+10	50.08	50.09
3	2.950	1208.21	6.332E+10	6.181E+10	2.729E+10	50.13	50.14
4	4.784	1205.56	6.259E+10	6.076E+10	2.625E+10	50.45	50.36
5	6.691	1152.64	5.721E+10	5.663E+10	2.321E+10	50.47	50.24
6	8.232	1093.24	5.106E+10	5.171E+10	2.011E+10	50.40	50.08
7	9.869	1026.22	4.267E+10	4.567E+10	1.568E+10	49.32	48.84
8	11.602	962.13	3.410E+10	4.059E+10	1.153E+10	48.28	47.60
9	13.430	907.40	2.661E+10	3.714E+10	8.246E+09	47.09	46.17
10	15.352	855.96	2.031E+10	3.360E+10	5.776E+09	45.60	44.50
11	16.684	809.74	1.684E+10	3.117E+10	4.378E+09	45.08	43.69
12	18.754	755.97	1.356E+10	2.874E+10	3.280E+09	44.20	42.54
13	19.463	734.31	1.259E+10	2.764E+10	3.066E+09	44.19	42.26
14	20.180	713.30	1.172E+10	2.655E+10	2.746E+09	43.93	41.92
15	22.384	664.79	9.547E+09	2.418E+10	2.105E+09	43.00	40.67
16	23.894	627.96	8.341E+09	2.198E+10	1.702E+09	42.21	39.68
17	26.211	586.25	6.923E+09	1.949E+10	1.294E+09	41.32	38.46
18	28.585	565.04	5.853E+09	1.767E+10	1.063E+09	40.65	37.65
19	31.004	541.63	4.931E+09	1.604E+10	8.934E+08	40.49	37.21
20	33.458	519.39	4.167E+09	1.412E+10	7.390E+08	39.98	36.58
21	35.934	492.46	3.506E+09	1.253E+10	6.192E+08	39.64	36.32
22	38.421	468.42	2.924E+09	1.084E+10	5.104E+08	39.37	36.02
23	40.906	443.04	2.424E+09	9.388E+09	4.206E+08	39.44	35.96
24	43.375	418.58	2.008E+09	8.079E+09	3.516E+08	39.54	35.84
25	45.818	388.56	1.653E+09	6.792E+09	2.853E+08	39.22	35.64
26	48.222	366.86	1.376E+09	5.775E+09	2.396E+08	39.14	35.51
27	50.576	339.68	1.138E+09	4.863E+09	1.956E+08	38.93	35.42
28	52.871	314.75	9.484E+08	4.086E+09	1.652E+08	38.82	35.39
29	55.098	291.85	7.972E+08	3.400E+09	1.385E+08	38.51	35.22
30	57.248	268.63	6.645E+08	2.858E+09	1.166E+08	38.52	35.38
31	59.316	251.43	5.612E+08	2.395E+09	1.001E+08	38.55	35.33
32	61.936	224.25	4.461E+08	1.893E+09	8.108E+07	38.56	35.39
33	64.391	199.14	3.540E+08	1.492E+09	6.654E+07	38.69	35.63
34	66.677	176.88	2.776E+08	1.184E+09	5.405E+07	38.97	35.83
35	69.294	152.43	2.084E+08	8.976E+08	4.292E+07	38.97	36.05

Section ID	Distance from Root [m]	Mass/unit length [Kg/m]	Flapwise Stiffness [Nm <sup>2</sup> ]	Edgewise Stiffness [Nm <sup>2</sup> ]	Torsional Rigidity [Nm <sup>2</sup> ]	Centre of mass [%]	Elastic axis [-]
36	72.088	129.79	1.503E+08	6.605E+08	3.359E+07	39.69	36.52
37	74.520	107.38	1.076E+08	4.947E+08	2.595E+07	40.34	37.24
38	77.247	86.60	7.178E+07	3.462E+08	1.988E+07	40.95	38.08
39	79.930	66.85	4.293E+07	2.256E+08	1.379E+07	42.04	39.12
40	82.450	46.28	2.081E+07	1.320E+08	8.552E+06	44.20	41.27
41	85.944	16.48	1.165E+06	1.546E+07	8.537E+05	48.81	47.97

Table 73. *Reference load case*

Reference Sections	Reference Load case - Cumulative loads						
	GL 2010 coordinate system						
n°	z [m]	FX [kN]	FY [kN]	FZ [kN]	MX [kNm]	MY [kNm]	MZ [kNm]
1	2,80	1299,18	-667,86	978,88	25458,86	65745,20	457,94
2	5,80	1306,94	-545,14	1020,74	25871,15	60950,99	415,18
3	8,80	1302,92	-541,42	1034,74	24054,71	57104,09	420,20
4	9,80	1300,24	-541,95	1027,75	23492,07	55811,76	430,23
5	11,50	1295,19	-543,00	1023,97	22577,68	53601,58	423,57
6	13,20	1289,12	-543,80	1016,32	21677,17	51390,95	421,81
7	15,00	1282,11	-542,78	1005,14	20690,43	49078,08	408,58
8	16,00	1277,19	-542,48	996,33	20170,97	47790,20	398,77
9	17,80	1265,12	-542,16	980,45	19301,93	45462,83	367,97
10	21,00	1245,52	-540,16	945,64	17670,11	41499,88	333,59
11	24,20	1226,14	-530,43	907,13	15839,40	37615,69	323,04
12	26,69	1218,24	-490,63	873,36	13605,61	34952,25	334,35
13	27,40	1216,21	-477,79	863,33	12941,33	34218,40	337,80
14	30,60	1197,35	-418,34	801,54	10286,23	31012,36	320,81
15	33,80	984,02	-251,71	594,75	8374,18	28093,94	213,85
16	37,00	943,63	-235,75	538,15	7111,32	25194,55	210,49
17	37,91	932,62	-229,95	521,14	6785,71	24461,77	208,53
18	43,00	871,00	-196,78	425,28	4985,59	20391,34	190,29
19	49,40	790,07	-158,41	316,54	3199,87	15325,07	147,23
20	54,15	725,06	-135,68	240,31	2201,36	11875,88	116,52
21	55,80	701,86	-127,31	214,55	1861,16	10695,79	105,78
22	62,20	578,32	-68,77	154,31	879,07	7138,96	81,34
23	68,60	405,78	-34,92	73,18	478,44	4151,34	30,99
24	71,59	352,73	-31,57	46,60	357,15	3090,84	17,61
25	75,00	294,62	-28,90	17,90	226,43	1929,07	4,04
26	81,80	147,65	-17,93	-11,32	70,25	494,99	3,10
27	83,30	112,28	-14,33	-11,25	44,88	303,43	2,07
28	84,80	78,88	-10,30	-9,42	24,37	160,46	1,01
29	86,30	47,35	-6,63	-5,73	10,51	64,61	-0,07
30	87,80	19,16	-2,20	-2,57	2,05	13,05	0,13
31	89,14	0,02	0,05	0,16	0,02	-0,01	0,006

**Table 74. DTU baseline strength ratios under the reference load case**

Section	Strength ratio – Design Load Cases						
	n°	Distance from root [m]	Hill [-]	Hoffman [-]	Tsai-Wu [-]	Max-Strain [-]	Puck – FF [-]
1	0.000	1.635	1.669	2.070	2.698	5.673	2.113
2	1.502	1.688	1.723	2.136	2.791	5.867	2.179
3	2.950	1.764	1.800	2.231	2.919	6.138	2.274
4	4.784	1.849	1.887	2.339	3.052	6.416	2.378
5	6.691	1.846	1.884	2.334	3.021	6.351	2.373
6	8.232	1.796	1.833	2.270	2.922	6.144	2.305
7	9.869	1.686	1.720	2.130	2.675	5.625	2.034
8	11.602	1.561	1.592	1.969	2.392	5.030	2.241
9	13.430	1.442	1.458	1.745	2.120	4.456	1.496
10	15.352	1.275	1.286	1.527	1.852	3.894	1.269
11	16.684	1.164	1.171	1.381	1.681	3.534	1.120
12	18.754	1.069	1.072	1.252	1.559	3.277	0.984
13	19.463	1.039	1.041	1.210	1.522	3.198	0.942
14	20.180	1.015	1.015	1.176	1.497	3.145	0.906
15	22.384	0.956	0.954	1.095	1.449	3.044	0.827
16	23.894	0.911	0.907	1.032	1.413	2.967	0.763
17	26.211	0.865	0.859	0.968	1.384	2.909	0.809
18	28.585	0.844	0.837	0.938	1.316	2.896	0.782
19	31.004	0.830	0.821	0.917	1.267	2.882	0.766
20	33.458	0.815	0.806	0.895	1.212	2.882	0.745
21	35.934	0.802	0.792	0.877	1.169	2.879	0.728
22	38.421	0.789	0.778	0.858	1.129	2.870	0.707
23	40.906	0.772	0.761	0.837	1.085	2.851	0.688
24	43.375	0.783	0.772	0.851	1.072	2.865	0.701
25	45.818	0.767	0.755	0.829	1.013	2.831	0.681
26	48.222	0.774	0.762	0.831	0.993	2.853	0.684
27	50.576	0.763	0.751	0.811	0.954	2.845	0.672
28	52.871	0.774	0.761	0.809	0.943	2.875	0.663
29	55.098	0.793	0.783	0.819	0.948	2.962	0.660
30	57.248	0.796	0.788	0.820	0.946	2.995	0.653
31	59.316	0.809	0.801	0.838	0.960	3.064	0.667
32	61.936	0.841	0.832	0.871	0.989	3.181	0.675
33	64.391	0.870	0.861	0.900	1.021	3.257	1.084
34	66.677	0.892	0.883	0.919	1.054	3.334	1.085
35	69.294	0.977	0.966	0.996	1.147	3.654	1.135
36	72.088	1.075	1.064	1.096	1.269	4.002	1.194
37	74.520	1.237	1.223	1.237	1.424	4.682	1.286
38	77.247	1.407	1.396	1.460	1.739	5.157	1.364
39	79.930	1.811	1.799	1.866	2.227	6.715	1.564
40	82.450	3.029	2.998	2.998	3.278	14.464	2.103
41	85.994	-----	-----	-----	-----	-----	-----